Middle East Regional Cooperation Program
Grant No.: TA-MOU-07-M27-050

Project M27-050 Israel (GII, TAU) and Jordan (BAU)

Sinkhole Hazard Assessment of the Dead Sea area in Israel and Jordan: Multidisciplinary Study

Final Technical Report

(December 1, 2009 - September 30, 2013)

Principal Investigators

Dr. Michael Ezersky, PI
Geophysical Institute of Israel (GII),
Lod, Israel

Prof. Abdallah Al-Zoubi, Co-PI
Al-Balqa Applied University (BAU),
Salt, Jordan

Dr. Shmariahu Keydar, Co-PI
Geophysical Institute of Israel (GII),
Lod, Israel

Prof. Lev Eppelbaum, Co-PI
Tel Aviv University (TAU),
Tel-Aviv, Israel

Managerial Institution:

Geophysical Institute of Israel (GII), Lod Israel

Submitted to:
US Agency for International Development; Bureau for Global Programs, Field Support and Research; Center for Economic Growth and Agricultural Development

Washington D.C.

Contents *Page no.*

1. Executive summary 4
2. Research Objectives 7
3. Methods and Results 11
3.1. Sites under investigation 11
3.1.1. General description 11
3.1.2. Ghor Al-Haditha (site I, Jordan) 11
3.1.3. Mineral Beach (site II, Israel) 13
3.1.4. Nahal Ze'elim (site III, Israel) 15
3.1.5. Ein Boqeq (site IV, Israel) 16
3.1.6. Boreholes drilled for the Project 17

3.2. Methods results of studies 19
3.2.1. Development 2D and 3D Seismic Reflection methods for Fault mapping 19
3.2.1.1. Background 19
3.2.1.2. The 3D zero offset stacking method 19
3.2.1.3. Multipath summation 20
3.2.1.4. Results of 2D, 3D seismic reflection studies 21
3.2.1.5. Conclusions on Section 3.2.1 25
3.2.2. Mapping of salt layers using MASW method 26
3.2.2.1. Introduction 26
3.2.2.2. Results of previous Vs studies 26
3.2.2.3. The MASW method – brief description 27
3.2.2.4. MASW for bed rock 27
3.2.2.5. Data acquisition 31
3.2.2.6. Results of surface-wave surveys 32
3.2.2.7. Discussion 32
3.2.2.8. Conclusions on Section 3.2.2 36
3.2.3. Salt – Fault relations as applied to mechanism of sinkhole forming 36
3.2.3.1. Tectonic setting 36
3.2.3.2. DS sinkholes - Salt edge hypothesis 37
3.2.3.3. Salt layer 38
3.2.3.4. Salt layer deposition and salt edge concepts 38
3.2.3.5. Structural hypothesis 40
3.2.3.6. Combined model 41
3.2.3.7. Conclusions on Section 3.2.3 43
3.2.4. Mapping of groundwater salinity (aggressiveness) using TEM method 43
3.2.4.1. Introduction 43
3.2.4.2. Hydrogeology 45
3.2.4.3. Archie's Law 45
3.2.4.4. The TEM method 46
3.2.4.5. The new approach of TEM mapping 47
3.2.4.6. Resistivity-salinity calibration near boreholes 48
3.2.4.7. Water Resistivity – Salinity relationship 49
3.2.4.8. Bulk Resistivity salinity relationships 50
3.2.4.9. Constructing a salinity map based on bulk resistivity 53
3.2.4.10. Evaluation of groundwater salinity and aggressivity using bulk resistivity 53
3.2.4.11. Conclusions on Section 3.2.4 58
3.2.5. Microgravity and Micromagnetic Methods 58
3.5.2.1. Background 58
3.2.5.2. Removing Regional Trends in microgravity complex environments: testing on 3D models and field investigations in the eastern Dead Sea

coast (Jordan) 60
3.2.5.3. Data acquisition 67
3.2.5.4. Investigation of Physical Properties 68
3.2.5.5. Results of magnetometry in the western DS coast (Site 2, Israel) 69
3.2.5.6. Results of magnetometry in the Ghor Al-Haditha (Site 1, Jordan) 71
3.2.5.7. Results of Microgravity in the Ghor Al-Haditha (Site 1, Jordan) 72
3.5.2.8. Combined Modeling of Gravity and Magnetic Fields 77
3.5.2.9. Conclusions to section 3.2.5 77
3.2.6. Surface Geophysical Methods (In Jordan) 77
3.2.6.1. General 77
3.2.6.2. Electrical Resistivity Tomography (ERT) 79
3.2.6.3. Electro Magnetic Radiation (EMR) Method 83
3.2.6.4. Ground Penetrating Radar (GPR) Method 84
3.2.6.5. Conclusions on Section 3.2.6 87
3.2.7. Laboratory and in-situ testing of Dead Sea soil 87
3.2.7.1. General 87
3.2.7.2. Methods 88
3.2.7.3. Boreholes 89
3.2.7.4. Laboratory study 90
3.2.7.5. Interpretation and Discussion 93
3.2.7.6. Conclusions on Section 3.2.7 97
3.2.8. Laboratory and in-situ testing of DS salt 97
3.2.8.1. General 98
3.2.8.2. In situ salt properties 98
3.2.8.3. Salt specimens 98
3.2.8.4. Methods 100
3.2.8.5. Results of the laboratory studies 104
3.2.8.6. Results of the borehole study 107
3.2.8.7. Discussion 108
3.2.9. In-situ Shear Wave Velocity – Resistivity versus Hydraulic Conductivity Inter-relationships in the Dead Sea Salt Layers 109
3.2.9.1. General 109
3.2.9.2. Main Methods 110
3.2.9.3. Results 117
3.2.9.4. Discussion 108
3.2.10. Implementation of MASW method at the Dead Sea Dam 5/8 (Southern Basin) 116
3.2.10.1. General 116
3.2.10.2. Geological context 116
3.2.10.3. Geophysical measurements layouts 116
3.2.10.4. Results 117
3.2.10.5. Conclusion on Section 3.2.10 118
3.2.11. Discussion and conclusions on Section 3.2 119
References 121
4. Impact relevance and technology transfer 132
5. Project activities/outputs 133
5.1. Presentation of Project results at scientific meetings 133
5.2. Training, publications, patents for entire project 133
6. Project productivity 136
6.1. Project accomplishments 136
6.2. Future work 138
Acknowledgements 138
Appendix 1. List of publications and presentations 139

1. Executive summary

1. ***Objective:***
The studying of the fault distribution using high-resolution 3D seismic reflection (SRFL) method at the sites of the sinkhole groups oriented along the lineaments.

***Study results*:**
We have studied the sinkhole hazardous zones on new 2-D and 3-D techniques developed during the Project (Keydar and Mikenberg, 2010; Keydar et al., 2011, Keydar et al., 2012, Keydar et al., 2013a, Keydar et al., 2013b; Medvedev et al., 2012).

2. ***Objective:***
The mapping of the salt layer edge and its top using seismic methods. The study has been focused on two shear wave techniques both Multichannel Analysis of Shear Wave (MASW) and seismic refraction methods (SRFR).

***Study results*:**
We have suggested Vs estimation using surface-wave prospecting methods, based on the surface-wave dispersion measurements and inversion. Along the Israeli shoreline, Vs mapping has been performed to discriminate weak and hard zones within salt layers, after the calibration of the inverted Vs near boreholes. It has been shown that there is a Vs increase in the DS direction. Initially examined weak zones, located near the salt edge, associated with karstified salt, are characterized by Vs values of 760-1050 m/s, and extend 60 -100m from salt edge in the DS direction. Hard salt zones with velocity Vs values greater than 1500 m/s are located at distances of more than 100-220m from salt edge. Finally, transition zones (1050 <Vs <1500 m/s) have a 40-160m spread. On a Jordanian site, we used previous studies including roll-along acquisition and dispersion stacking. Inverted pseudo-2D Vs sections present low Vs anomalies in the vicinity of existing sinkholes and made it possible to detect decompacted sediments associated with potential sinkholes occurrences. Moreover, Vs profiles showed a high velocity unit at 40-50m depth that can be interpreted as a salt layer. (Ezersky et al., 2012; 2013a)

3. ***Objective:***
Salt – Fault-Sinkhole relations based on results of the seismic reflection and MASW study

***Study results*:**
As a result of two above studies we have proved the salt presence in the Ghor Al-Haditha (Frumkin et al., 2011) and proposed general model of the Dead Sea sinkhole formation based on salt distribution around the DS (Ezersky et al., 2013b, Ezersky and Frumkin, 2013).
Sinkholes are formed along the edge of the salt layer that, in his turn, is formed either along faults or sediments brought by wadies (Ezersky 2006; Frumkin et al., 2011; Ezersky et al., 2012c; Ezersky and Frumkin, 2013).

4. ***Objective:***
The detailed study of the bulk ground resistivity (interpreted in terms of salinity) and its 3D distribution in the shallow subsurface based the Transient Electromagnetic (TEM) method in his fast technology modification.

***Study results*:**

We suggested a new approach to use the Transient Electromagnetic (TEM) method in its FAST modification. This approach is based on separate studying of both characteristics of the salt layer and evaluation of groundwater salinity. The key point of the new methodology is delineating salt distribution, in particular the salt edge, using seismic refraction method (Ezersky et al., 2010). Then we can separate the investigation area into two “sub-areas” (Levi et al., 2011): (1) “salt” area, where the measured resistivity is influenced by the salt porosity (estimated from the Archie’s law); (2) “no-salt” area, where the measured resistivity is

influenced by the groundwater salinity estimated using the resistivity-salinity inter-relations obtained for the Dead Sea region (Ezersky and Levi, 2013). In Israel, west of the salt edge resistivity of aquifer is associated with the aquifer salinity, whereas east of that salt layer resistivity is related to its porosity. In Jordan it works reversely. New methodology enables the avoiding of 3-D effects in vicinity of salt edge. We have mapped areas in the Mineral Beach, Nahal Zeelim and Ghor Al-Haditha sites.

5. ***Objective:***

Multidisciplinary study of Ghor Al-Haditha area (Jordan) using the Micromagnetic and Microgravity methods developed for subsurface cavities detection in combination with surface geophysical methods

Result of study:

We tested number of transformation methods (including computing gravity field derivatives, self-adjusting and adaptive filtering, Fourier series, wavelet, and other procedures) on a 3D model (complicated by randomly distributed noise) (Al-Zoubi et al., 2011, Al-Zoubi et al., 2013; Eppelbaum, 2013). Field Microgravity and Micromagnetic investigations were carried out in Ghor Al-Haditha (Jordan). We show that the most effective methods for regional trend removal (at least for the theoretical and field cases here) are the bilinear saddle and local polynomial regressions. Application of these methods made it possible to detect the anomalous gravity effect from buried targets in the theoretical model and to extract the local gravity anomaly at the Ghor Al-Haditha site. The local anomaly was utilized for 3D gravity modeling to construct a physical-geological model (PGM) **(**Al-Zoubi et al., 2012, Eppelbaum, 2013). Al-Zoubi et al. (2012) integrated Microgravity and Micromagnetic methods into surface geophysical methods to reveal sinkhole hazards. Electromagnetic Radiation (EMR) method was tested through the Ghor Al-Haditha area (Akkawi et al., 2012). Electrical Resistivity Tomography (ERT) in 2D and 3D mode was applied in Jordan (Frumkin et al., 2011).

6. ***Objective: Borehole and laboratory testing of DS salt and soil***

6.a.

Site characterization, stratigraphic, evaluation of soil engineering parameters by using borehole drilling and laboratory testing of samples. Selected samples of the undisturbed structure were used to determine geotechnical and geophysical properties of the tested section and their dependence on the DS water.

6.b.

Salt and soil properties with respect to the sinkhole problem were studied using ultrasonic (US) and resistivity methods in the laboratory conditions

6.a. Results:

Two types of lithology were studied in-situ and laboratory conditions to reveal geotechnical and geophysical properties of these soils. Two boreholes MN-5E and EB-3E, of clayey and sandy-gravel, respectively lithology, were drilled in the Mineral Beach and Ein Boqeq sites.

We have revealed following features of the DS soil properties (Ezersky, 2013; Ezersky and Livne, 2013). Sandy-gravel sediments are presented by coarse sands, which are characterized by Vs = 300 – 650 m/s. Brine saturated lime carbonates (DS mud) are characterized by low Vs values of 120 – 250 m/s. They do not exhibit cohesion when saturated in the DS brine. It is explained by mineralogical composition of the Dead Sea material, composed predominantly of calcite and not clay minerals, whereas other Israeli clays are comprised largely of montmorillonite (spectite) clay minerals. This feature allows considering of saturated lime carbonate as cohesionless soil like fine sands. Lime carbonates demonstrate also very low cation exchange capacity (CEC) that allows use of TEM resistivity method for determining of porosity of both sands and DS mud (Ezersky and Levi, 2013). Note also that significant difference of Vs in sands and lime carbonates allows mapping of different lithology along DS coastal areas.

6.b. Results:

(a) Salt porosity-permeability, their mutual inter-relationships and correlations with ultrasonic compression wave velocity (Vp), shear wave velocity (Vs) and resistivities (ρ_x) were studied in laboratory conditions (Ezersky and Eppelbaum, 2013). These relationships were interpolated into range of in-situ values using MASW method and Magnetic Resonance Sounding (MRS) permeability, carried out in past. Thus, mapping of salt permeability based on Vs values was performed in 3 sites under investigation. (Ezersky and Legchenko, 2013).

7. Results of the study were implemented in the Dam 5/8 separating the Southern DS basin from the Northern one

The Project accomplishments.

The studies that were carried out in the framework of the Project have shed light to the problem of sinkholes as a regional process peculiar to both sides of the DS.

The study has allowed the reconciling of two competition models: "Structural" the one associating sinkholes with neo-tectonic faults and "Salt edge" model, associating sinkholes with the salt dissolution along salt outer border. Joint model associated salt development along faults, whereas sinkholes form in the 60-100m zone along the salt edge.

We specified the geological structure of the subsurface in all studied sites and identified the origin of sinkholes as result of evaporation karst (It was accepted earlier that origin of sinkholes in Israel and Jordan is different).

We have shown the spatial distribution of salt elastic properties connected with the salt voidness. This distribution confirms formation of karstified zones (responsible for sinkholes) along the outer salt edge. We have suggested methodology of quantitative assessment of salt layer permeability based on laboratory ultrasonic measurements and in-situ MASW ones.

We suggested estimation of groundwater aggressiveness relatively salt layers using quasi-3D TEM mapping of aquifer bulk resistivity.

The methodology application of microgravity and magnetometry in combination with surface geophysical methods has permitted the detecting of sinkholes through wide coastal areas in Jordan.

New geophysical methodology will allow mapping of sinkhole hazardous zones either through mapping of salt or using potential geophysical methods.

The numerous publications in the international scientific journals (8 articles have been published and 3 are in the reviewing) during project lifetime, presentations at the international (20) and local (3) meetings have made the visibility of the project results to worldwide and Israeli scientific and engineering community.

In spite of the very complicated political situation in the Middle East region generally and, specifically, in Jordan, our communication and cooperation continued during the entire project, we presented joint publications and even an organized section on the problem of arid karst at the 2012 EGU General Assembly (Vienna, Austria). The Project has been successfully completed.

Skills and awareness

We assume that new approaches tested in the scientifical and engineering aspects developed during project activity will remain in the future. One new PhD B. Medvedev and two other post-graduate students (E. Levi and A.-R. Abueladas) will transfer the knowledge to the students. A mutual transfer of information between the participants will enrich our knowledge on the geological conditions of both countries. Moreover, there is a great interest to the results of the project from the Regional Councils and engineers of the Dead Sea Works and Arab Potash plants.

Origin of the Arab-Israeli cooperation on the Project

In spite of the complicated political situation in our region (that is constantly worsened) the Israeli and Jordanian participants of the Project continued the contact during the reported period. Our usual communications are done by regular means and phone conversations between the leaders of the collaborating groups. E-mails are also an important element of communicating. However, the situation in Jordan made difficult even phone conversations and e-mail communication. Therefore, the meeting with the partners were the most effective mean of fast exchange of materials, ideas, plans and publications.

***Strengthening of the Middle Eastern Institution*.**

During the Project life, GII (Israel) purchased equipment, new software and upgraded the available one, as follows:

1. OYO SonicViewer - SX Model 5251C was used for ultrasonic measurements on salt and soil specimens;
2. Resistance Meter Nilsson #400 (Farwest Corrosion Control Company, USA) was used for resistance measurements of soil and salt specimens;
3. Low frequency geophones SN4_2.5Hz (Gisco Ltd, Minneapolis, USA) were used for the MASW measurements in the field.
4. Software RadExPro (Deco Ltd, San Petersburg, Russia) was upgraded.
5. We upgraded also SurfSeis 3 software for MASW data processing and RadExPro software for reflection data processing.
6. TAU has purchased a magnetic susceptibility meter during the field magnetometry mapping of the Mineral Beach area.
7. The purchase of the densitometer for TAU enabled the measuring of salt specimen density;
8. BAU (Jordan) received the CG-5 Gravity Meter (by Scintrex a division of LRS, Canada) and mapped the north of the Ghor Al-Haditha area.
9. The equipment produced at GII (7-transducered Ultrasonic Probe for borehole) was successfully used during the borehole investigations.

Impact relevance and technology transfer

The new knowledge and methodology obtained during the Project met the interest of scientists and parallel programs which were carried out in the Dead Sea region. Based on our results, The Geological Service of Israel specifies the maps of sinkhole hazard generated intuitively through the areas where the sinkholes have been formed, whereas no maps were generated throughout areas where no sinkholes are visible at the surface.

We have advised the Leading Researcher, Dr. G. Shamir who is dealing with the Program of Defense of the Dead Sea Hotels. Our results were used by the Geological Survey of Israel (Dr. A. Salomon) and the Ben-Gurion University (Prof. Y. Hatzor), in estimation of the liquefaction potential of the Dead Sea area. The MSc thesis by E. Livne was written based on the boreholes data. The Israel National Roads Company Ltd (MAATZ) ordered from GII in 2011 seismic surveys in the Mineral Beach and Ein Gedi areas, to search salt and estimate sinkhole hazards.

2. Research Objectives

Reason for the project performing

The Project has been performed in the Region where an intensive industrial activity (Potash Facilities in Jordan and Dead Sea Work in Israel) takes place. The agricultural activity takes place along the Dead Sea shore (Ghor Al-Haditha in Jordan and Qalia, Ein Gedi, Mizpe Shalem, etc. in Israel). Archeological and Historical objects are being visited by numerous tourists. In addition, the Dead Sea region is an international resort zone, where buildings of numerous hotels have been constructed and exploited. At the same time, the sinkhole developing along the DS shore in Israel and Jordan (Fig. 1) has already caused considerable damage to the infrastructure, and some peoples have fallen into sinkholes which collapsed under their feet. The agricultural fields in the Ghor Al-Haditha are affected by great sinkholes. There is an obvious potential for further collapses beneath the main highways and other human structures. Thus, high sinkholes hazard threatens human lives and economic development in the Dead Sea basin. In addition the drop in the Dead Sea level accelerates the sinkhole developing.

Addisional factor is the seismic hazards from earthquakes. It is clearly there is a great interest of the business community, local administrations and different researchers to the sinkhole hazard assessment that should play a crucial role in planning and development of areas susceptible to sinkhole formation. In order to protect human life and infrastructure, it is necessary to understand how sinkholes form and to produce reliable sinkhole susceptibility and hazard maps, identifying the most dangerous areas that should be avoided or properly engineered.

The problems addressed. The overall aim of the Project is to understand the sinkhole mechanism and to develop a methodology for the combined application of several geophysical methods for delineating those areas, which are at high risk of potential sinkhole collapse, thus endangering human life and infrastructure and limiting economic development. The principal research objectives of the project may be defined as follows:

1. A detailed integrated study of the subsurface geological and geophysical structure and properties of the sites were sinkholes have occurred, to develop a better understanding of the processes causing them to occur. The following problems are considered:
   a. Mapping of the salt layer (its boundary and top depth location) using two shear wave velocity (Vs) techniques – Seismic refraction and Multichannel Analysis of Surface Waves (MASW); (Al-Zoubi A., Akkawi E., Ezersky M., Frumkin A.)
   b. Detection of the faults and other structural elements using 3D high resolution seismic reflection; (Keydar S., Medvedev B., Al-Zoubi A.)
   c. Estimation of water salinity distribution (through geoelectrical resistivity) – using TEM FAST technology; (Ezersky M., Frumkin A., Levi E.)
   d. Detection of large underground cavities (mass deficit) using Microgravity and Micromagnetic methods (BAU, Jordan); (Al-Zoubi A., Abueladas A.-R., Eppelbaum, L.)
   e. Study of the subsurface soil mass properties at the sinkhole development sites using geotechnical methods in combination with geophysical ones (Ezersky M., Livne E.,)
   f. Study of salt properties and their relationships with geophysical parameters in the laboratory and in-situ (Ezersky M., Eppelbaum, L)
   g. Generating of the model of DS sinkholes based on findings discovered during the Project (Al-Zoubi A., Ezersky M., Eppelbaum L., Frumkin A., Keydar S.)

The study has resulted in 3-D geological models and collapse hazard assessments for the Dead Sea coastal areas where this geologic hazard is endemic in Israel and Jordan. (Al-Zoubi et al., 2013, Eppelbaum 2013, Ezersky and Livne, 2013; Frumkin et al, 2011, Ezersky and Levi, 2013)

2. Development and verification of an optimal methodology for sinkhole hazard assessment (Frumkin et al, 2011: Ezersky, Bodet et al., 2013a).

3. Implementation and strengthening of relationships between the Government Institutions and professionals as part of the Middle East Peace process.

4. Technology transfer between the investigators, their students, and the international Engineering and geological community, who can utilize this data.

The success has been achieved through the integrated use of geological, geophysical and hydrogeological approaches in their 2(3)-D modification and a comprehensive analysis of the data.

The Project summary looks like the following:

(1) The mapping of the salt layer edge and its top using seismic methods. The study has been focused on two shear wave techniques both Multichannel Analysis of Shear Wave (MASW) and seismic refraction methods (SRFR)

(2) The studying of the fault distribution using high-resolution 3D seismic reflection (SRFL) method at the sites of sinkhole groups oriented along the lineaments.

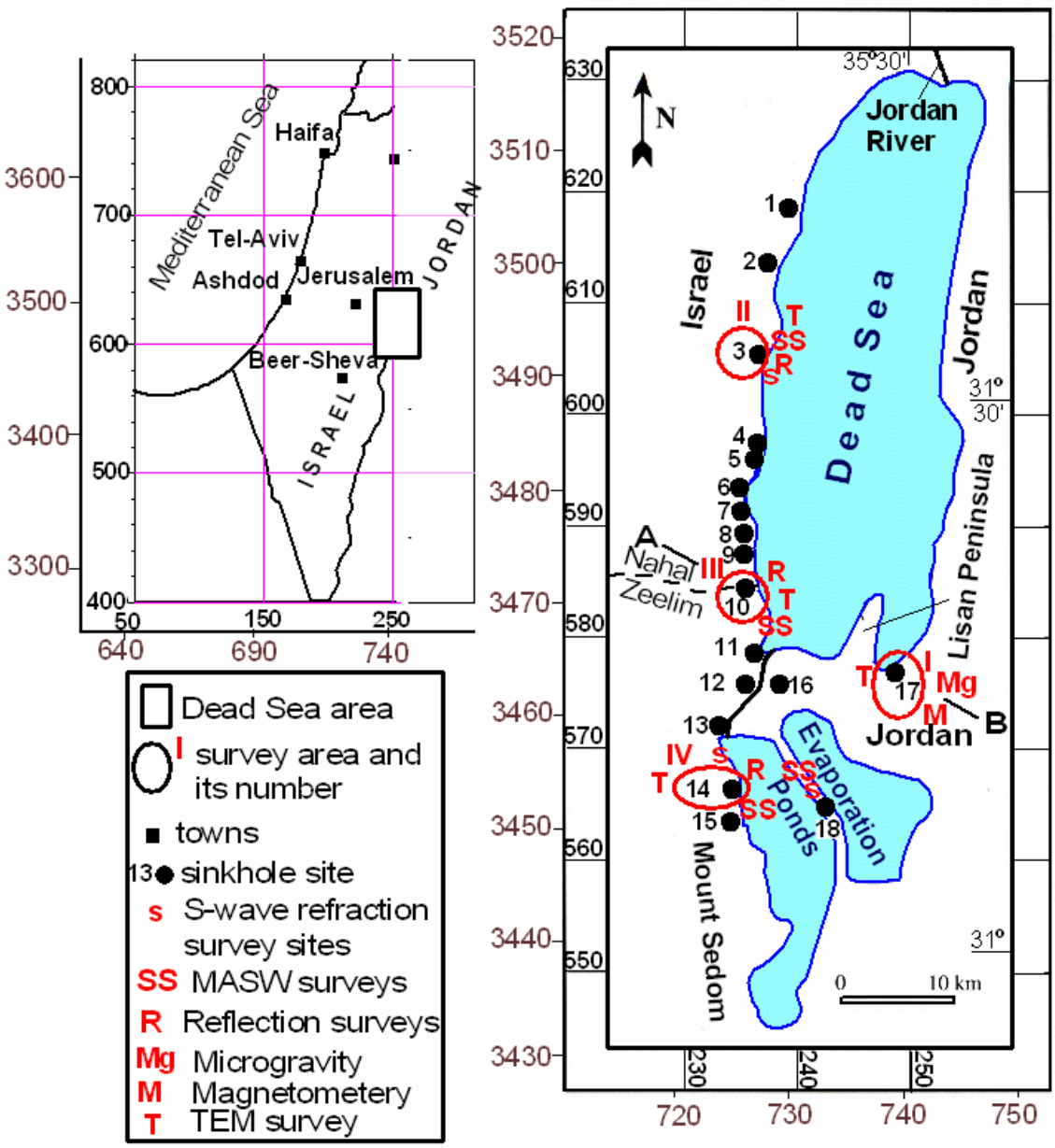

Figure 1.
Sinkhole sites along Dead Sea shore: 1- Palms, 2 – Samar Spring, 3 –Mineral Beach, 4 – Ein Gedi and Nahal Arugot, 5 – Yesha, 6 – Zeruya, 7 – Nahal Hever northern, 8 – Nahal Hever southern, 9 – Asa'el, 10 – Nahal Zeelim, 11 - Mezada, 12 – Rahaf, 13 – Mor, 14 – Ein Boqeq, 15 – Newe Zohar, 16-Lisan Peninsula, 17-Ghor Al-Haditha, 18 – Dam-2. I-IV – sites under investigation. AB - line of the generalized geological section. (The coordinates in the frame are new Israel Mercator grid in km, the outer coordinates are Universal Transverse Mercator grid, in km).

(3) *The detailed study of the bulk ground resistivity (interpreted in terms of salinity) and its 3D distribution in the shallow subsurface based the Time Domain Electromagnetic (TDEM) method in his fast technology modification.*

(4) *Site characterization, stratigraphic, evaluation of soil engineering parameters by using borehole drilling and laboratory testing of samples. We suggest that selected samples of the undisturbed structure will be used to determine geotechnical and geophysical properties of the tested section and their dependence on the water saturation.*

(5) The Micromagnetic and Microgravity methods have been developed for subsurface cavities detection (Microgravity method will be performed in the Jordan only).
(6) Salt and soil properties with respect to the sinkhole problem have been studied using ultrasonic (US) and resistivity methods

The Importance of the problem for development.
The resolving of the sinkhole phenomena through the whole DS region generalizes the knowledge on the problem mechanism and the new methodologies will allow the delineating of the dangerous zones. That is why the cooperation between Israeli and Jordanian researchers has a significant scientific impact to the problem decision.

Fitting the Project into the on-going research by other scientists and reference pertinent literature
The Project is well fit into the on-going researches by other scientists (Abelson et al., 2013, Avni et al., 2013; Closson et al, 2009; Filin et al., 2011; Legchenko et al., 2009). These studies comprise detection and collapse prediction (Abelson et al., 2013; Aksinenko et al., 2013). Avni et al. (2013) and Filin et al. (2011) develop mapping of sinkholes using high resolution air-born laser. Closson and Abu Karaki (2009) investigate faults and earth displacements using high resolution satellite images analysis. Legchenko et al. (2009) use Magnetic Resonance Sounding (MRS) method to reveal hydrological problems of sinkhole hazard. Note, most of the studies are aimed to predict sinkhole collapse based on subsidence of an earth surface, whereas our study has the goal to delineate sinkhole hazardous zone based on the understanding of subsurface processes.

The Innovative aspects of the project
During the Project life, the following innovative aspects of the sinkhole hazard were addressed:
(1) We have developed the new Seismic Reflection technique (S. Keydar and B. Medvedev) allowing the studying of the shallow subsurface;
(2) Removing Regional trends in a complex environment has been developed (A. Al-Zoubi and L. Eppelbaum;
(3) Mapping of buried salt layers and evaluation of their permeability in-situ using MASW method has been developed for a first time (M. Ezersky);
(4) TEM resistivity mapping of separately salt and aquifer areas suggested by E. Levi and M. Ezersky allows avoiding of 3D effects. The determining of salt layer parameters (depth to top, thickness of layer and its resistivity is the first result of that. Mapping of the aquifer resistivity and the estimation of its salinity and aggressivity is a second result.
(5) Finally, geotechnical characteristics of the DS soil (especially, lime carbonate) shed light to the sinkhole forming mechanism (M. Ezersky and E. Livne).
All these novelties were tested in the laboratory and in-situ and results and conclusions were subjected to peer reviewing and published in the relevant scientific journals.
We have suggested the model of the DS sinkholes based on geophysical, geotechnical and geological findings .

Support the project by other organizations:
During the project life we cooperated with the different organizations that supported us in different aspects of the activity. DS Works (Israel) and Potash Facility (Jordan) permitted performing surveys on the Dam. We implemented our MASW methodology to construct the geological section along the Dam. The Geological Survey of Israel and the Ben-Gurion University assisted us in the borehole drilling, description of lithology. They sponsored the borehole drilling and one of students (Livne E.) made the M. Sc thesis, whereas we obtained two boreholes instead one that was planned, without any increase of the budget. The Tamar Regional Council provided us with the permission for performing of works, drilling, studies. MAAZ provided geological data of drilling in the Mineral Beach. The administration of the Mineral SPA – permitted performing of studies through and within a private area. The great support was rendered us by the Ministry of Energy and Water Resources of Israel.
We should also point out the great support rendered to us by the International scientific community that during previous years carried out researches in the DS area. With their assistance we got materials of previous investigations and generalized our conclusions. Such organizations and researchers are
Dr. L. Bodet from University of Pierre and Marie Curie (Paris 6 University, France),

Dr. A. Legchenko from Institute for research and development (Grenoble University, France), Dr. D. Closson from Belgium Military Academy etc.

3. Methods and Results

3.1. Sites under investigation

3.1.1. General description

The survey areas are located between the DS shoreline and the western and eastern borders of the DS rift within the graben area. Most of those sites are situated on alluvial fans. The surficial deposits are composed of gravels (from pebbles to boulders), as well as of fine-grained facies (clay and silt), and a salt layer. A general geological W-E section through the DS is shown in Fig. 2 (see Fig. 1 for location).

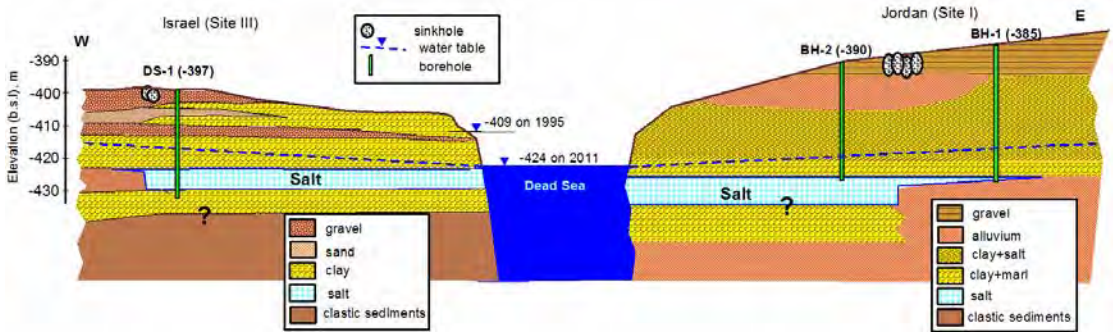

Figure 2. Generalized geological W-E section (along line A-B in Fig. 1) through the southern part of the Dead Sea. Four representative sites were selected for the present study: Ghor Al-Haditha (site I in Fig. 1) on the eastern coast in Jordan and three sites on the western coast in Israel: Mineral Beach (site II), Nahal Ze'elim (site III) – both northern DS basin and Ein Boqeq (site IV) on the southern one (see Fig. 1 for location). These sites include some of the most common sinkhole features of the Dead Sea region.

The Ghor Al-Haditha (site I) is located in Jordan, along the eastern shore of the Dead Sea, near its southern tip (Fig. 1). All the Israeli sites (II-IV, see Fig. 1 for location) under investigation are located between the DS shoreline and Route #90 (the main road along the western DS shore). The sites are well-studied by boreholes and geophysical methods, such as seismic refraction, transient electromagnetic (TEM) surveys, etc. (Yechieli et al. 2004; Frumkin et al. 2011). Salt layers of 6-30m thickness are located at depths of 20-50m (top). Salt is usually sandwiched between clay layers from below and from above, especially when approaching the DS shoreline. The salt edge to the west of the DS is often in contact with the sandy-gravel sediments. Sinkholes developed along a North linear trend following a salt layer edge (Fig. 2). The largest sinkholes (20-30m in diameter) developed at Mineral Beach (site II), while sinkholes of smaller size (5-10m in diameter) appeared at Nahal Ze'elim (site III). Very few sinkholes (some 4-6) have been detected at Ein Boqeq (site IV). During recent years, sinkhole development has progressed northward along the western DS shore (Frumkin et al. 2011).

3.1.2. Ghor Al-Haditha (site I, Jordan)

The Ghor Al-Haditha area is located south-east of the northern Dead Sea basin (Site I in Fig. 1). Alluvial fan deposits of the Wadi Ibn Hammad cover southern part of this area (Fig. 3). The sinkholes at the eastern coast of the Dead Sea can be dated by middle of 1980s (Taqieddin et al., 2000). The sinkhole layouts through the Ghor Al-Haditha area are shown in Fig. 3.

The area of the sinkhole formation is gently inclined wave eroded platform, about 3km width east of Lisan Peninsula. This area formed the bed of the Dead Sea during a period of higher Dead Sea level (390m b.s.l.). One can see from Fig. 3 that sinkholes are arranged along the tortuous line extended from the north-east to the south-west of the area. Note that line of sinkholes slowly migrate toward the DS, especially, in the northern part of the area.

The typical geological section shown in Fig. 4 is based on the boreholes BH-1 and BH-2 presented by Taqieddin et al. (2000). Boreholes sections indicate that the geological materials of the shallow subsurface consist of laminated sand interbedded with layers calcareous silts and possibly clay or marl.

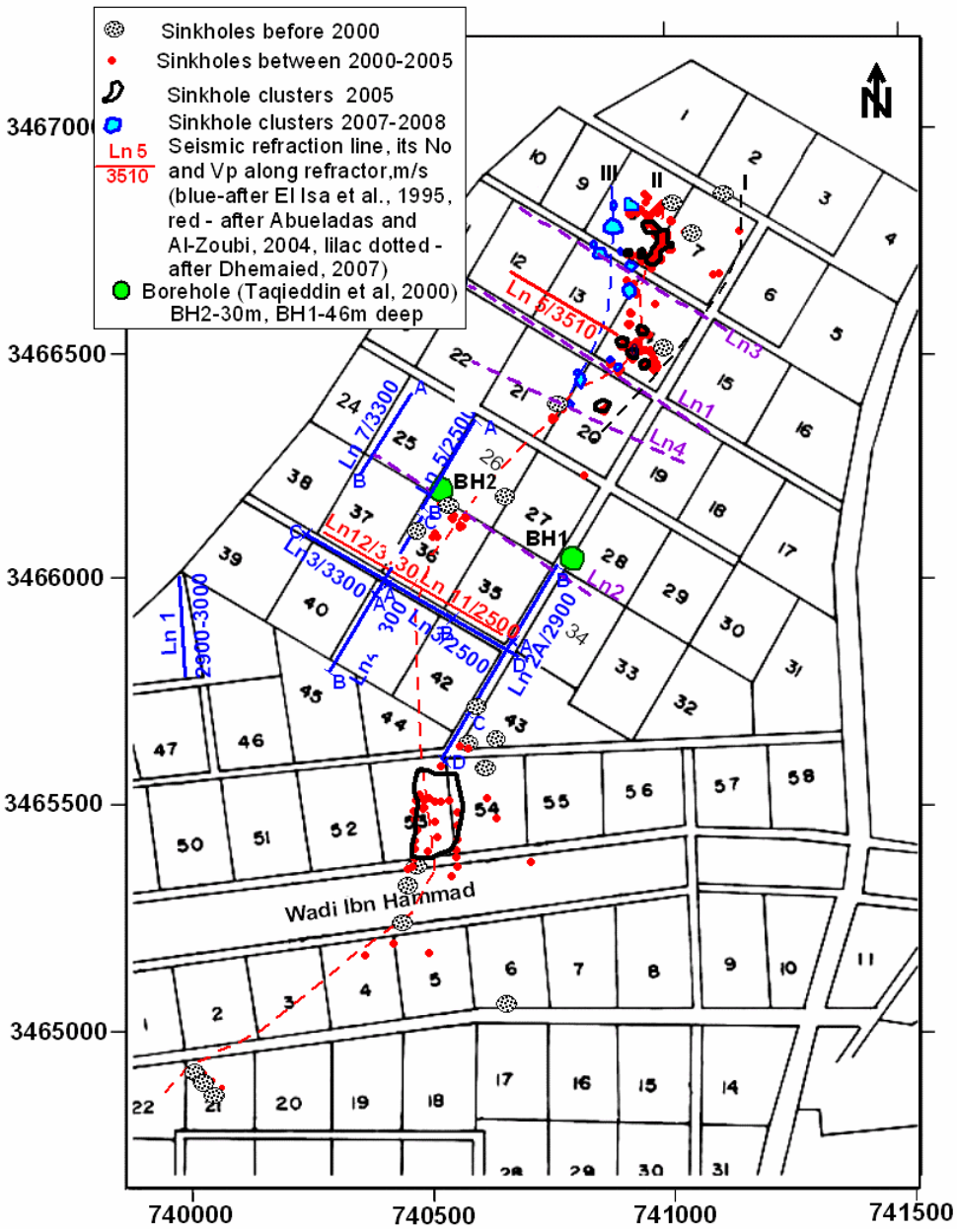

Figure 3. A Ghor Al-Haditha layout map. There are shown: seismic refraction lines (after El-Isa et al. 1995, Abueladas and Al-Zoubi 2004, Dhemaied 2007), boreholes and sinkholes before 2000 (after Taqieddin *et al. 2000), sinkholes between 2000 and 2008 (after Abueladas, person. commun), sinkhole clusters in 2005 and 2008 (after Bodet et al. 2010). I, II, and III are sinkhole lines, respectively, in 2000, in 2005 and in 2008. Coordinates are in m, Universal Transverse Mercator grid.*

Salt unit was not revealed by both boreholes because drilling was carried out using fresh water (A. Abueladas, personal communication). Authors suggested presence of a massive halite layer presumed to exist at some 25-50 m depth (Taqieddin et al., 2000, p.1248). However, geological structure of the site and especially salt layer location would be specified based on results of the seismic refraction surveys carried out by El-Isa (1995) and Abueladas and Al-Zoubi (2004). Seismic refraction lines (185-235 m long) shot by El-Isa et al. (1995) and Abueladas and Al-Zoubi (2004) are also presented in Fig. 3. The authors have distinguished in longitudinal wave velocity (V_p) section 3-5 layers. Lowermost layer (refractor) is mainly characterized by high velocity of 2900-3500 m/s. This layer is located at 38-50m deep.

This section is conformed to the Taqieddin et al. (2000) with all comments above, seismic refraction data of El-Isa et al. (1995), Abueladas and Al-Zoubi (2004), TEM study of Akkawi (2010). We should add also recent studies carried out by Bodet et al. (2010) revealed the shear wave velocity (V_s) of more than 1000 m/s at the depth of ~40-50m. These velocities undoubtedly characterize hard unit that we identify as salt. We suggest here additionally only salt featheredge masking the underlain sediments, which are characterized by lower than salt velocity and therefore are unseen for seismic refraction method.

Velocity of 2500m/s is explained by insufficient penetration of the seismic rays, which did not reach the refractor because of limited line long. First authors interpreted refractor as clay saturated with DS brine (El-Isa et al., 1995). Abueladas and Al-Zoubi (2004) associated refractor with the salt unit. This interpretation is consistent with our salt velocity criterion. Thus, SRFR testifies that there is a salt layer with a top located at 38-50m. Thickness of the salt layer cannot be determined using SRFR method. However we suggest that salt unit discovered in the Ghor Al-Haditha that was formed in the Earlier Holocene (Yechieli et al., 1995) should be consistent with the similar salt layers revealed by numerous boreholes drilled along the western DS shore. Depth of these layers varies between 20 and 50 meters and thickness is in range of 10-30 m. The shallow salt layers located at 100-200 m deep were suspected also by seismic reflection lines carried out Al-Zoubi and ten Brink (2001). Recently E. Akkawi (Personal Communication) performed Transient Electromagnetic (TEM) surveys revealed high resistive layer at a depth of 85-120 m that can be interpreted as massive salt layer. With these data we can suggest modified geological section through the Ghor Al-Haditha study site (Fig. 4).

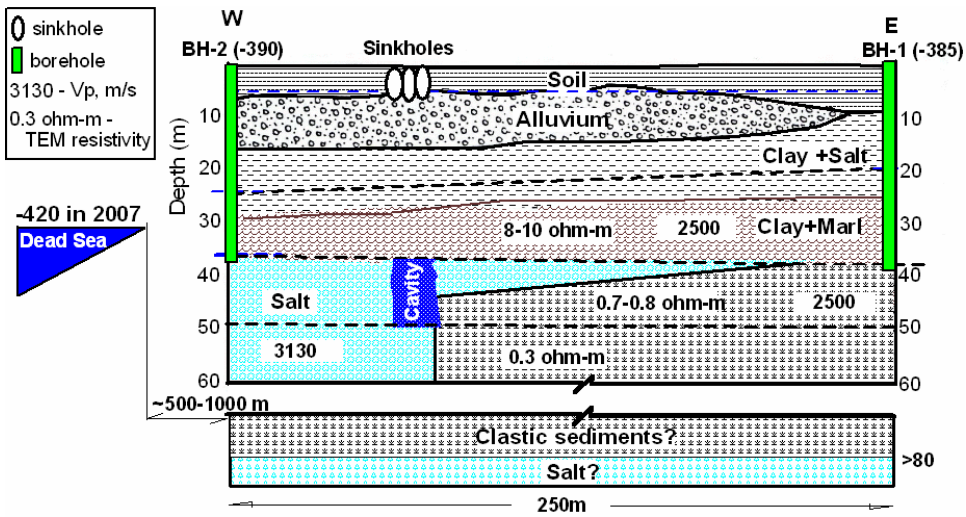

Figure 4. Hypothetic geological W-E section of the Ghor Al-Haditha site based on the BH-1 and BH-2 boreholes

TEM measurements show following zonation of bulk resistivity along the borehole axis: from surface to 20-25m deep sediments are characterized by high resistivity of $100\,\Omega m$. At depth interval from 20-25m to 35-38m resistivity is of 8-10$\,\Omega m$. It characterizes evidently sediments saturated with fresh water. At depth of 35-38m the sharp drop in resistivity from 8-10$\,\Omega m$ to 0.8$\,\Omega m$ is observed. Resistivity of 0.8-0.7$\,\Omega m$ characterizes the depth interval between 35-38m and 50m. The sediments in this depth range are saturated probably with the brackish water. We suggest also that salt unit is karstified at this depth range. Finally, deeper than 50m the resistivity decreased to 0.1-0.3$\,\Omega m$ value, which is typical for clay saturated by the Dead Sea brine (Legchenko et al. 2009).

3.1.3. Mineral Beach (site II, Israel)

The Mineral Beach area, covering ~1 km^2, is located at the western coast of the central part of the northern DS basin (II in Fig. 1). The study site is located between the Dead Sea shoreline and Route #90 (the main road along the western DS shore) (Fig. 5a). The area comprises the Mineral Spa, where natural black mud and sulphur-rich hydrothermal water with a temperature of 39 °C, attracts tourists

from Israel and abroad. Around Mineral Spa, sinkholes develop in both mudflat (south) and alluvial fan (north) areas (Figs. 5c and 5d, respectively). Fig. 5a illustrates that sinkhole development is mainly linear, along a salt layer edge or controlled by a fault (Frumkin et al., 2011, Ezersky, 2010). A salt layer with a cavity was intersected by Mn-2 borehole (Fig. 5c). Borehole MN-2 crossed DS mud from surface to 18 m deep. Groundwater sampled from the cavity indicated salt dissolution; Na/Cl ratio of 0.55–0.60 compared with 0.30 in Dead Sea brines (Yechieli et al., 2006). Borehole MN-1 (Fig. 5c) crossed sandy-gravel section. It did not discover salt layer. Soon after drilling, the borehole MN-2 collapsed into a newly developed sinkhole which was then east of the salt layer front.
Ezersky (2010) has delineated the salt layer edge in the Mineral Beach study site (lilac line in Fig. 5b). Because the area north of dyke (Fig. 5b) is located in the Hazazon Wadi it is very broken by gullies and ditches. In addition it is complicated by stones and large cobbles hampering performing of the field study. It is why during MERC project performing we have added survey by some refraction lines shown in Fig. 5b by dashed black lines. The specified salt border is shown in Fig. 5b. Frumkin et al. (2011) have shown the western border of the salt at the north of the area is located in alluvium composed of sandy-gravel sediments.

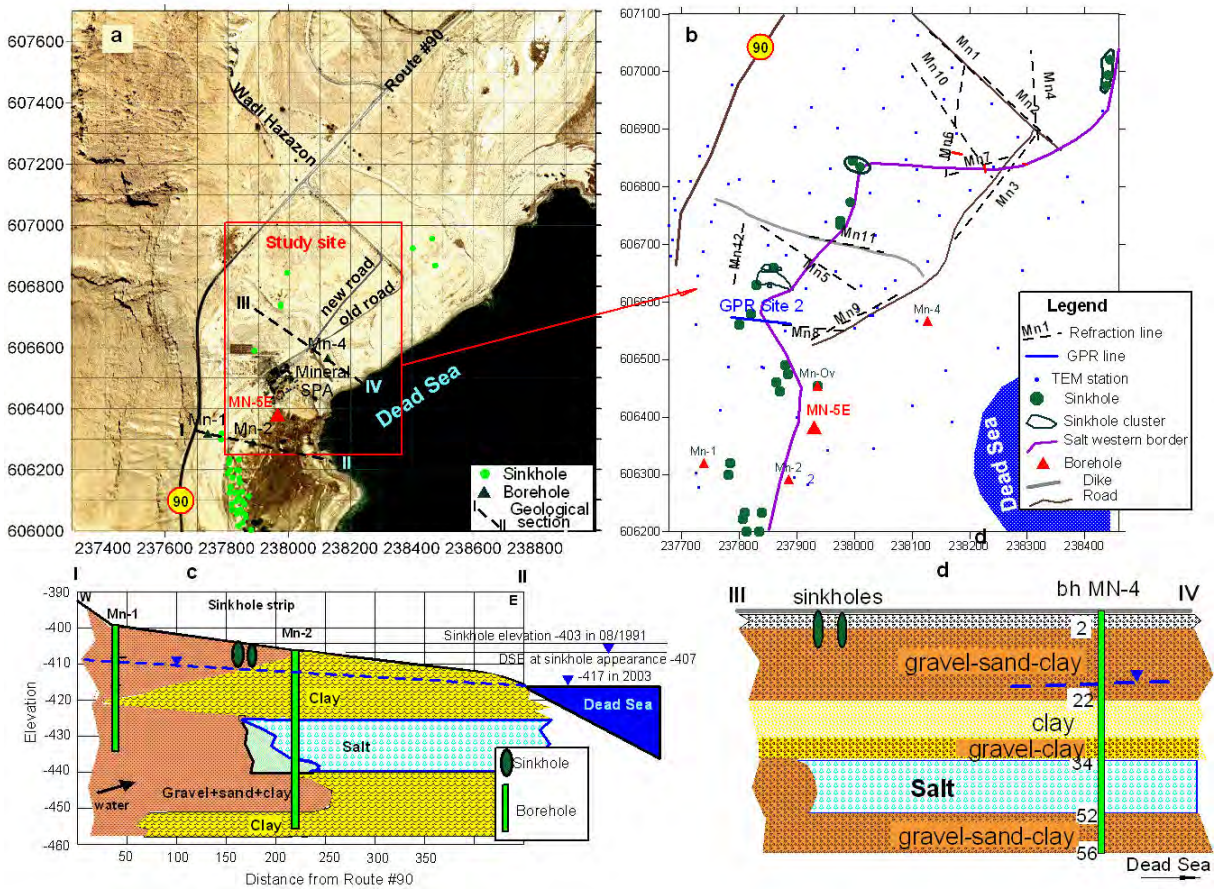

Figure 5. Mineral Beach area: (a) study site location; and (b) geophysical measurements layouts, recent sinkholes and salt western border; (c) geological section I-II via mud flat (MN-1 – MN-2 boreholes; (d) geological section I-II via sandy-gravel sediments (MN-4 borehole). See (a) for sections location

These sediments permit direct contact of the salt layer with highly mineralized rising water (200 g/l chloride) at a temperature of 29-40° C. Southern part of the salt border is sandwiched by DS mud.
Sinkholes are located close to the salt front. Borehole Mn-1 revealed aggressive water with relatively low chloride concentration - 120 g/l (Yechieli et al., 2006). Fig. 6 presents a large sinkhole between boreholes Mn-1 (W) and Mn-2 (E) as observed on January 2008.

Figure 6. Photography of the Mineral site between boreholes Mineral-1 and Mineral-2 (I-I' section) in October 2008

The large cluster of sinkholes south of Mineral Spa started to develop in 1992 (Fig. 5a). During recent years sinkhole development progressed northward.

3.1.4. Nahal Ze'elim (site III, Israel)

Study area is located at the southern part of the northern DS basin (site III in Fig. 1) some 2-3 km from Judea Mountains. Geological section is composed of pebbles, cobbles and clayey-sandy sediments.

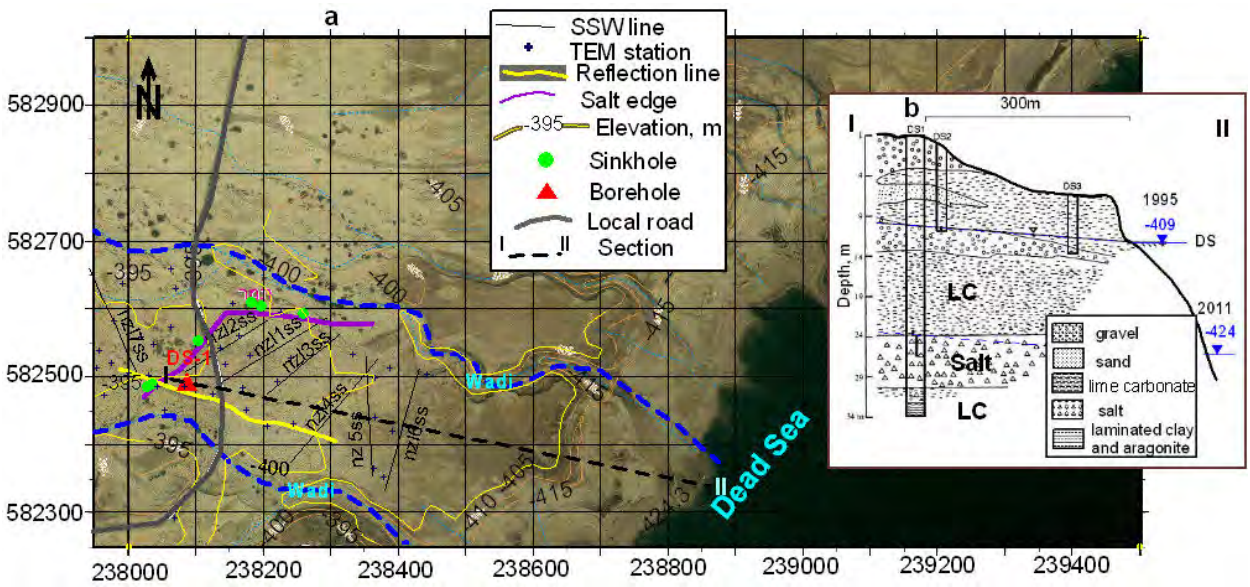

Figure 7. Nahal Ze'elim study site and geophysical measurements layouts. (a) Study site aerial map; (b) geological section via DS-1 borehole (see (a) for location) (Yechieli et al., 1995)

Borehole DS-1 (See Figs. 1 and 7a for location) drilled in the Nahal Ze'elim study site in 1993 was first borehole revealed the shallow salt unit of 10,000-11,000 year old in the Dead Sea coastal area (Yechieli et al., 1995). The thickness of salt layer is of 7 m in the borehole.

Salt layer located at 24m deep is enveloped by massive lime carbonate layer from above and from below (Fig. 7b) and very saline DS brine with chloride content varying from 82 g/l found in the water table at 11m deep (in 1993) up to 210g/l chloride after penetrating the salt layer at 24m deep. The water table in borehole DS-1 on 2011 declined to 24m deep (e.g., almost depth of salt top). However, geophysical measurements show very low electrical resistivity of 0.1-0.3 Ωm testifying that salt unit is enveloped by clayey sediments still saturated with the DS brine.

Study site is located some 300m from the Dead Sea between two wadies. Salt location was determined by the seismic refraction method (Ezersky and Legchenko, 2008). Western salt border is shown in Fig. 7a by lilac line. First sinkhole appeared in the study site between 2005 and 2007, considerably later than in all other sites (Fig. 8).

Figure 8. Two small sinkholes formed along the local road in the Nahal Ze'elim site (see Fig. 7 for location)

Hereafter 5 sinkholes were appeared in the studied area. Note also that sinkholes of the Nahal Ze'elim are characterized by small sizes: 2-5m diameter and 1-2 m depth. Sinkholes are arranged along the salt edge shown Fig. 7a.

3.1.5. Ein Boqeq (site IV, Israel)

Ein Boqeq area of 1.5-2.0 km long and 250-300m width is extended along the southern DS basin (recently evaporation ponds artificially filled by pumping DS water from the northern basin (site IV in Fig. 1). Numerous hotels are located through Ein Boqeq that named also Hotel area. The study area is located at the north of Ein Boqeq some 2-3 km east of Judea Mountains. Geological section is composed of pebbles, cobbles and clayey-sandy sediments.

Figure 9. Ein Boqeq study site and geophysical measurement layouts

Geology of the Ein Boqeq site is presented by borehole EB-1, EB-2 (Yechieli et al. 2004). Borehole EB-3E was drilled for this project in order to collect salt samples. The borehole crossed sandy-gravel alluvium overlain the salt unit at 26m deep. At depth of 32 m borehole met crushed salt and at 35m deep drilling was stopped. The sediments revealed by EB-3E borehole are conformed to those from boreholes EB-1 and EB-2 located some 200-400m south of the study site. The thickness of salt unit is of 28m. The alluvium is saturated with very saline groundwater varying from 209 g/l chloride at a top of borehole to 233 g/l at its bottom.

Salt layer was delineated by seismic refraction study (Ezersky, 2009, 2010). Embryos of 6 small shallow sinkholes were detected during drilling of the EB-1 borehole. No other sinkholes were detected. Images of Ein Boqeq sinkholes are shown in Fig. 10.

Figure 10. Embryos of sinkholes developed in the of Ein Boqeq amphitheatre on 2008

The feature of the Ein Boqeq as against other sites is a high elevation of groundwater located some 3-4 m from surface.

3.1.6. Boreholes drilled for the Project

Two boreholes MN-5E and EB-3E were drilled in the Mineral Beach and Ein Boqeq sites (Israel) jointly by the Geophysical Institute of Israel (GII), Geological Survey of Israel (GSI) and Ben-Gurion University of the Negev (BGU) to completely study clayey and sandy-gravel lithology using geotechnical and geophysical methods.

MN-5E borehole (site II in Fig. 1) was drilled in the northern DS basin in the margin of an alluvial fan near Mineral Beach SPA (Fig. 11).

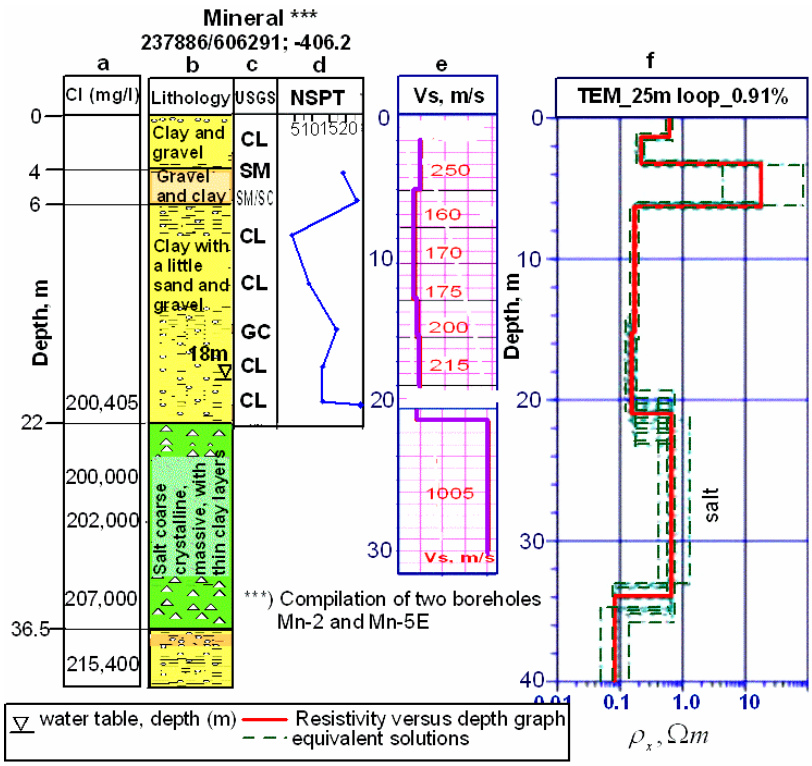

Figure 11. Borehole Mn-5E and results of its testing: (a) Chloride concentrations in the groundwater (mg/l) (after Yechieli et al. 2004), (b) lithology section; (c) soil classification based Unified Soil Classification System (USCS) (d) N_{SPT} blows; (e) Shear wave velocity (Vs) versus depth profile based on downhole measurements; (f) inverted resistivity vs depth function. Thick line (in Fig. 11f) denotes the inverted resistivity vs. depth graph, whereas thin dashed lines are equivalent solutions. (Lithology and SPT sounding has been interpreted by Livne (2012))

This section consists mainly of fine grain sediments, silts with a little clay (named after Frydman et al. (2008) *lime carbonates*) with few inter-layers of gravels. The consistency of lime carbonate can be related to firm – stiff (based on N_{SPT} values of range 4-16 and unconfined strength 50-220 kPa). The lime carbonate sediments are typically comprised of laminated, clay to silt size clastic sediments (predominantly calcite), and authigenic aragonite and gypsum. The clastic detrital material was brought into the basin by seasonal floods. The DS lime carbonate sediment is made up of about 95% calcite, with the other 5% being aragonite, quartz and gypsum. Brine saturated lime carbonates (DS mud) are characterized by low Vs values of 120 – 250 m/s. They do not exhibit cohesion (Frydman et al. 2008). This feature allows considering saturated lime carbonate as cohesionless soil, like fine sands (Ezersky and Livne 2013).

EB-3E borehole (site IV in Fig. 1) was drilled in the alluvial fan of the Ein Boqeq site (Fig. 12). The section consists mainly of coarse clastic sandy-gravel sediments (Livne 2012). Note the section is typical of the DS fans. Similar coarse sandy-gravel lithology is reported by Taqieddin et al. (2000) on the Jordanian shore.
In both boreholes a Standard Penetration Test (SPT) was carried out in addition to *in-situ* downhole and TEM measurements. Samples from the boreholes were tested in the laboratory to determine density, water content, Atterberg limits and USCS classification (Livne 2012). Hydrogeological conditions of these sites have been studied by GSI using ground water salinity monitoring (Yechieli et al. 2007). Results of SPT are presented in Figs. 11d and 12d.

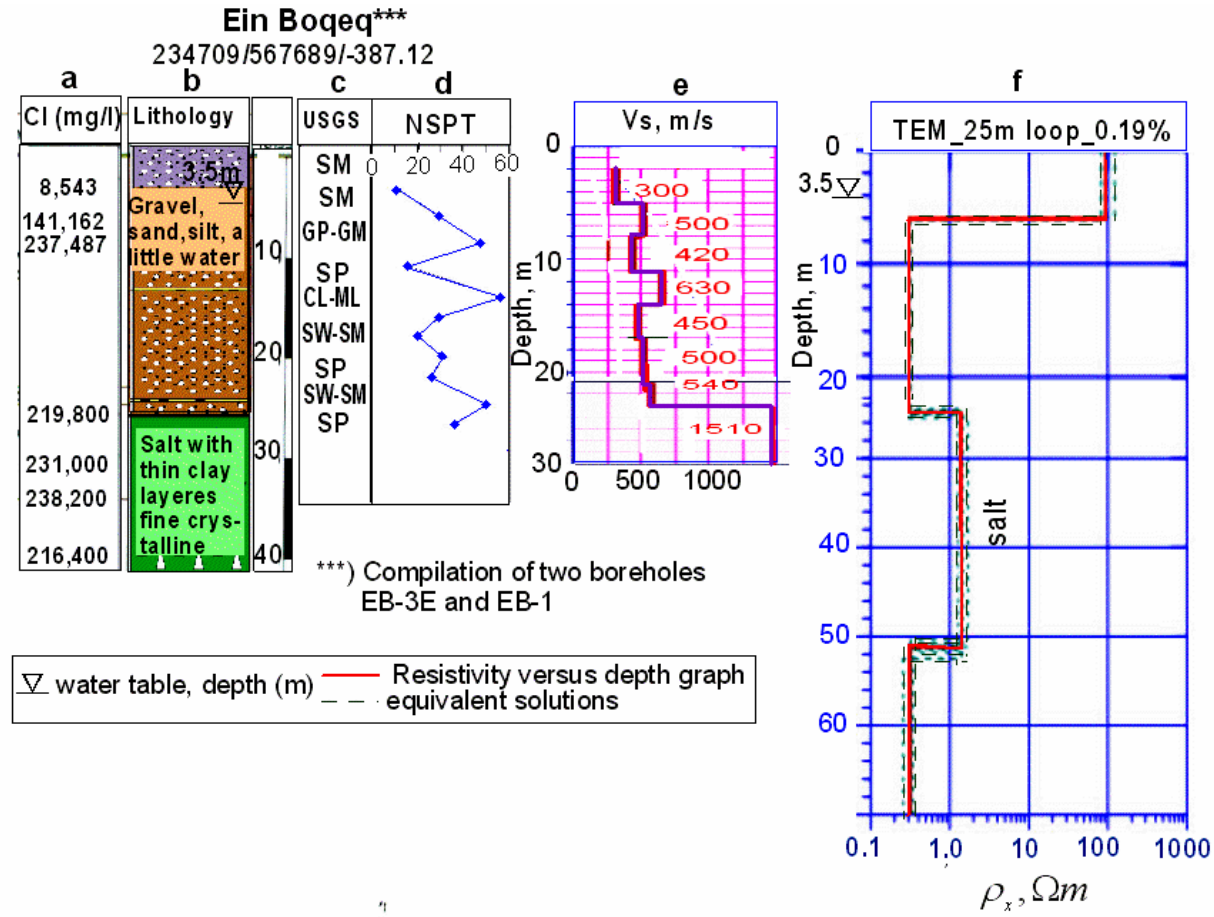

Figure 12. Borehole EB-3E and results of its testing. Denotations are as in Fig. 11

The boreholes were used during the Project for: (1) Determining of in-situ geophysical (Vp and Vs) and geotechnical (N_{SPT}) properties of two lithology types of the DS coastal area; (2) Studying of salt geophysical properties (Vp, Vs and ρ) within boreholes; (3) Calibration of shear wave velocities (Vs) revealed from MASW measurements, (4) Calibration of resistivity salinity relationships within 28 boreholes available in the area; (5) extraction of undisturbed samples of soil and salt for the

laboratory testing. All these tests were carried out during the Project and results are reported in corresponding Sections in continuation

3.2. Methods and results of studies

3.2.1. Development 2D and 3D Seismic Reflection methods for Fault mapping

This section is based on new 2-D and 3-D techniques developed during the Project *(The method and results have been published and are presented in details in Keydar and Mikenberg, 2010, Keydar et al., 2011; Keydar et al. 2012a; Keydar et al. 2013a, Keydar et al., 2013b, Medvedev et al., 2012)*

3.2.1.1. Background

The high-resolution seismic reflection method is intended for the study faults and conduits in the shallow subsurface (down to 100-200m deep), which could bring the fresh water to the salt layer presumably from below. The conventional processing technique, so-called CMP (Common Mid Point) method essentially consists of a "stack" (summation) of properly corrected traces thus increasing the signal-to-noise ratio. However, in the shallow subsurface the conventional CMP method causes a loss of information because of the problem of "stretching" of data caused by NMO time correction formula. That is why a new 2D and 3D free stretch imaging approach had been applied in the framework of the MERC project M27-050 in order to examine tectonic hypothesis connecting the sinkholes with tectonic faults (Keydar et al., 2011, Keydar et al., 2012a). We have carried out several new seismic surveys along line crossing the sinkhole lineaments and reinterpreted number of previous reflection sections. The 2D imaging technique has been presented in (Keydar et al., 2012a).

A new approach for imaging shallow subsurface combines several recently developed imaging techniques. The first one is zero-offset Common Shot Point (CSP) stacking (Keydar et al., 1996). The other one is a diffraction imaging technique (Landa and Keydar, 1998; Keydar et al., 2010).

Imaging of subsurface using those methods is performed by a spatial summation of seismic waves along time surfaces. The summation can be implemented using either of two approaches. In the first, conventional, approach, the target waves are stacked along the time surfaces defined by some "optimal" parameters such as velocity or wavefront parameters. These parameters are estimated by a time-consuming procedure of parameters analysis involving visual examination and interpretation of intermediate seismic images. In our new approach we use an alternative, a more formal recently proposed multipath summation with proper weights (Keydar, 2004; Keydar and Shtivelman, 2005; Shtivelman and Keydar, 2005; Landa et al., 2006; Shitevelman et al.,2009). The multipath summation is performed by stacking the target waves along all possible time surfaces having a common apex at the given point. This approach does not require any explicit information on parameters since the involved multipath summation is performed for all possible parameters values within a wide specified range.

In order to get a more reliable image of shallow subsurface a three dimensional (3D) seismic reflection technique was developed. This technique was applies to 3D data from the western shoreline of the Dead Sea. The CSP stack and diffraction method are complementary to each other and reveal useful information about the subsurface. The diffraction method serves as a tool for detection of faults and voids, while the CSP stacking contains information about the structure of the subsurface. We give here a short description of 3D zero offset stacking and multipath weighted summation. For a more comprehensively discussion of the methods one can read in the relevant papers.

3.2.1.2. The 3D zero offset stacking method

The basis of the 3D zero offset stacking method is a new normal moveout (NMO) time correction formula for three-dimensional media as function on wavefront parameters (Keydar and Mikenberg, 2008; 2010). One of this parameters on which the proposed time correction formula is based is the emergence angle β, defined as the acute angle between the wavefront normal and the normal to the acquisition plane at the CSP. Let consider a central ray and its associated wavefront arriving at a Common Shot Point (CSP) (Fig.13.). An ellipsoidal wavefront emerges at the CSP location *O*. It has two independent tangent vectors **e1** and **e2** tangent to the wavefront and the normal **n**. The emergence angle β is the angle between **n** and the normal to the acquisition plane, k. Additional fundamental parameters on which the time correction formula is based are the curvatures of the wavefront. It is well

known from the differential geometry of surfaces that at each point of the wavefront two principal curvatures can be defined, being the eigenvalues of the 2×2 matrix of second derivatives. These curvatures are the minimal and maximal curvatures, and related to the mean and Gaussian curvatures. The principal curvatures are associated to two perpendicular principal directions, which together with the wavefront normal form a rectangular system of axes. The curvature of the wavefront is completely described by the two principal curvatures and the angle the principal directions make with the general coordinate system. This is denoted in Fig.13a as **i, j, k**. The principal curvatures can be expressed in terms of principal radii of curvature, which play an important role in the traveltime correction expressions derived in this paper. Fig. 13b illustrates the case where one of the principal directions is normal to **k**. Based on those principles and eikonal equation only, the following formula 3-D travel-time correction formula in for an arbitrary system of coordinates was obtained.

$$t = \frac{1}{V}(a_{31}x + a_{32}y) + \frac{1}{2VR_1}(a_{11}x + a_{12}y)^2 + \frac{1}{2VR_2}(a_{21}x + a_{22}y)^2] + \ldots, \tag{1}$$

$$a31 = \sin\beta\sin\phi,\ a32 = -\sin\beta\cos\phi,\ a11 = \cos\phi,$$
$$a12 = \sin\phi,\ a21 = -\cos\beta\sin\phi,$$
$$a22 = \cos\beta\ \cos\phi\ .$$

Where β is the emergence angle of the wavefront at point O, ϕ azimuth angle, defined as the angle between the axis *OX* and the principal direction of the wavefront at point O, $\breve{x}$ and $\breve{y}$ are the offsets along the axis *OX* and *OY*. For a given source-receiver gather the moveout equations express the moveout correction with respect to a zero-offset trace by five parameters measured at the central point.

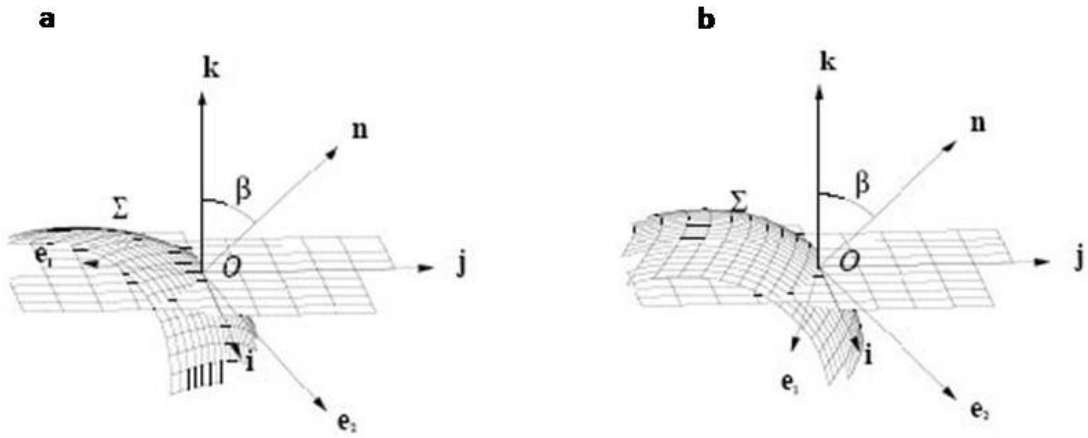

Figure 13. (a) Scheme of wavefront arriving at a Common Shot Point; (b) The same as (a) in case of one direction is normal to vector ***k***

3.2.1.3. Multipath summation

The summation of 3D stacking is performed along time surfaces defined by equation 1. The summation can be implemented using either of the two approaches. In the first, conventional, approach the target waves are stacked along the time surfaces defined by wavefront parameters and velocity in case. These optimal parameters usually are estimated using optimization problem which consists of finding parameters which maximize some correlation functional. We use an alternative, a more formal recently proposed multipath summation with a proper weighting (Keydar, 2004; Keydar and Shtivelman, 2005; Landa et al., 2006; Schleicher and Costa, 2012). The weighted multipath summation allows us to replace the complex optimization problem of estimating the optimal parameters, by summation along all possible surfaces that are created from small variations of those

parameters. The weighted multipath summation (WMPS) can be described by the following expressions:

$$I_{WMPS} = \sum_P I_P W(I_P) / \sum_P W(I_P) \qquad (2)$$

$$I_P = \sum_P \sum_S \sum_R U_{SR}(T_{SR}(P)) \qquad (3)$$

$W(I_p)=exp(\lambda I_P)$ is an "optimal" weighting function , λ is an dimensionless large number. I_p is the image obtained for fixed parameters P namely, for radii of curvature azimuth and emergence angles. $U_{SR}(T_{SR})$ is a seismic trace for a given source-receiver pair. T_{SR} is travel time from shot S to receiver R. The summation (2) with the proper weight $W(I_p)$ is performed for all possible parameter values within a specified range. The imaging defined by I_p means that for every point to be imaged, seismic amplitudes are stacked together along all possible time surfaces defined by equation (1). The constructive and destructive interference of the amplitudes contributed by each time surface produces an image close to that obtained by stacking with the "correct" parameter (Shtivelman et al., 2009). Parameters are: principal radii of the wavefront $R1$ $R2$, the azimuth angle ϕ , the emergence angle β and the reference velocity V. In the following we give a short description of weighted multipath summation

3.2.1.4. Results of 2D, 3D seismic reflection studies

Ghor Al-Haditha (site 1 in Fig.1, Jordan) (Ezersky and Frumkin, 2013)

An E-W 2-D seismic reflection section along line 4 through the Ghor Al-Haditha site is shown in Fig. 14b (see Fig. 14a for location). The dataset was originally collected by Bodet et al. (2010) in order to analyze surface-wave dispersion. Field records were acquired using a 72-channel Geometrics seismic recorder with a 24-geophone spread (4.5 Hz, vertical component). Receiver spacing was 5 m, shot location was 5 m away from the nearest trace (off-end shooting east side), and the move up between shots was one receiver interval. The recorded seismograms were also compiled and processed by Keydar et al. (2011) in order to extract Common Shot Point (CSP) stacking and diffraction images along the lines.

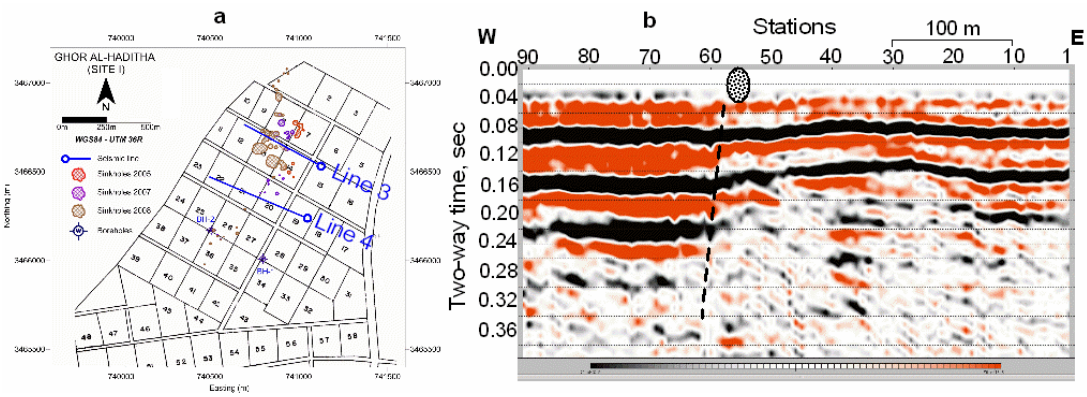

Figure 14. Ghor Al-Haditha (site I in Fig. 1a, Jordan) (a) Location map; (b) E-W 2-D reflection section along line GH-4 (Bodet et al., 2010, Keydar et al., 2011; permission of L. Bodet). Grey ellipse indicates sinkholes cluster.

The black dashed line divides the section into two parts differing in their reflection pattern. The line evidently separates zones of different lithology. We suggest that the western reflector might be a salt layer characterized by strong reflections. The eastern part of the section might represent clastic sediments. The separation between the two parts of the section could also be a fault although the evidence seen in the section is not conclusive.

Nahal Ze'elim (site III, in Fig. 1, Israel) (Ezersky and Frumkin, 2013)

Nahal Ze'elim area (site III in Fig. 1a) is located at the south of the northern DS basin. A 340 m-long W-E 2D seismic reflection profile was shot across the sinkhole line (Fig. 15a). The dataset was originally collected using a 96-channel Summit II seismic recorder (GMT, Germany) with a 60-geophone spread (10 Hz, vertical component). Receiver spacing was 2.5 m, shot location was 5 m away from the nearest trace (off-end shooting west side), and the move up between shots was a two receiver interval.

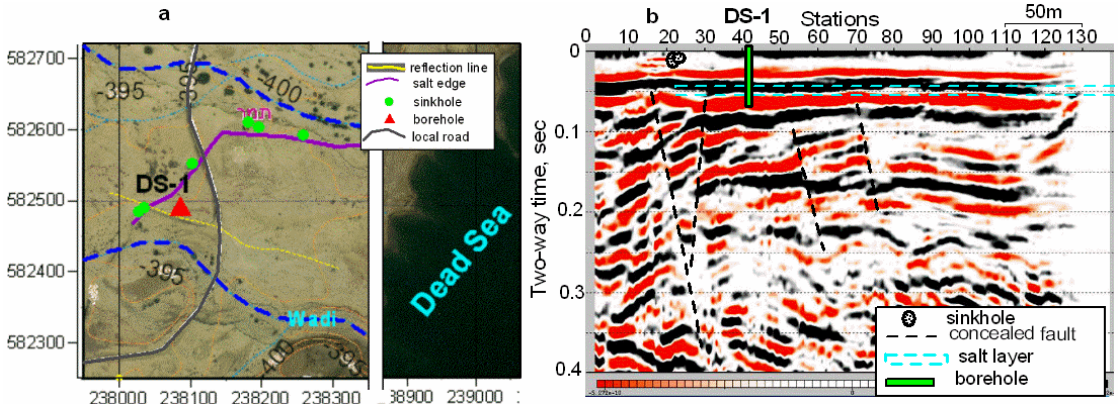

Figure 15. Nahal Ze'elim site (a) Location map: Reflection line (yellow) crosses the salt layer edge and a small sinkhole which is a part of a sinkhole line. (b) W-E 2-D seismic reflection section through the site

The edge of a 7-10 m-thick salt layer has been delineated by seismic refraction study and verified by borehole DS-1 (Fig. 15a). A distortion zone is evident where the reflection profile intersects the sinkhole line (Fig. 15b). The results show the presence of faults close to the sinkhole zone. The upper reflector is smooth but distorted between stations 10 and 30. Two sinkholes and the salt edge coincide with the fault site.

Mineral Beach 2D reflection line along dyke (Keydar et al., 2012a)

To specify the structural geological conditions of the site, a 345m multi channel reflection survey have been acquired (dashed black line in Fig. 18). Field parameters of this survey included 71 shot points with 5m interval and 48 receivers for each shot with 2.5m interval between the receivers. As a source was used an accelerated weightdrop ('Digipulse'). The data was recorded using 0.5msec sample rate and 0.5 sec record length. Typical common shot gathers seen on Fig.16a.

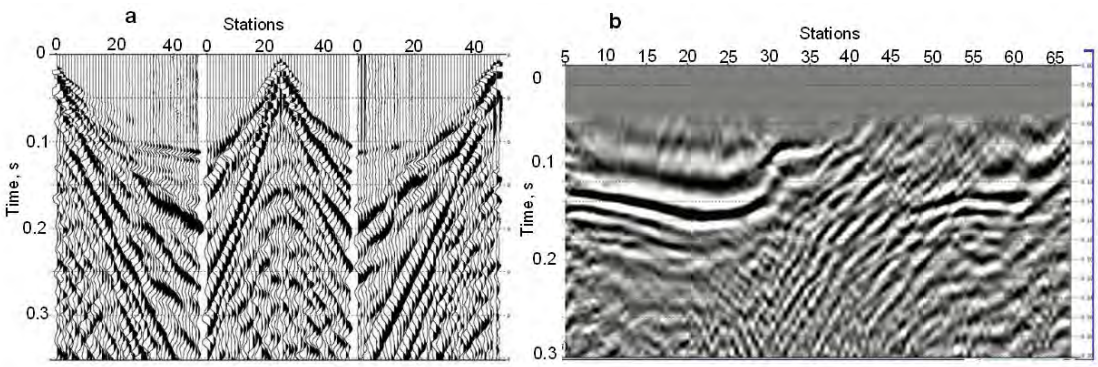

Figure 16. (a) Example of three Common Shot gathers; and (b) Stacked section obtained using conventional processing.

The time sections, obtained using conventional CMP (Fig. 16b) and CSP methods (Fig. 17a), reveal a complex structure at subsurface that can be interpreted as two blocks separated by a normal fault at ~ sp 30. Both sections were processed using the same flow including bandpass filter, gain and static correction. The CMP stacked section include 269 traces with 1.25m interval and can be divided to three zones, till sp 30, sp 30-45 and 45 to the end (sp71). The first zone includes a clear coherent reflector at time 125-155 ms with a dominant frequency of 40Hz. On the second zone data quality is poor and the reflector disappears and can be seen again at the third zone till sp 65. The CSP section

includes 71 traces with 5m interval. In general this section is similar to the CMP stacked section but it is different in details. A reflector is clearly seen and unlike in the CMP stacked section this reflector is continuous along all the line (sp-1-65). The dominant reflector has a similar character but with lower

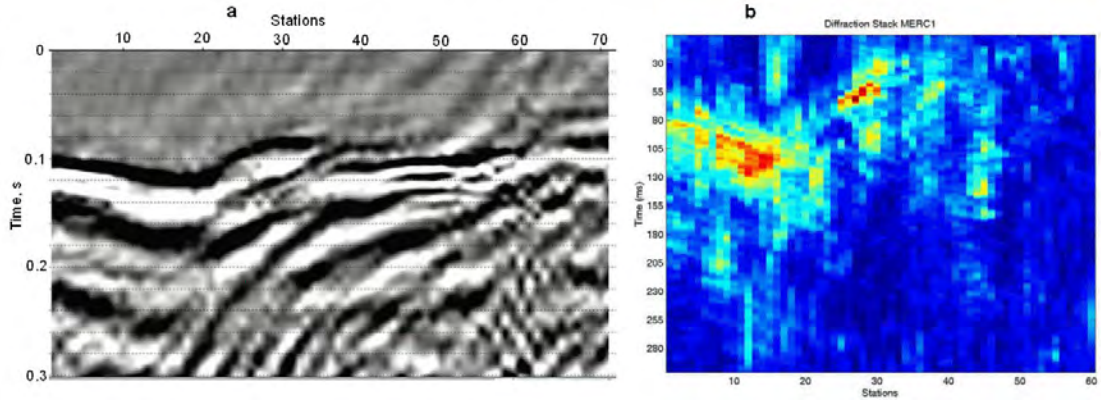

Figure 17. (a) CSP time section obtained using the weighted multipath summation; and (b) Diffraction image obtained by diffraction method using weighted multipath summation.

frequency contain. The main event appears on the conventional CMP stacked section at time ~140ms the same event appears on CSP section at time ~110ms.One of the possible explanations is that in case of CSP stacking the NMO time correction is stretch free and therefore it allows to image the first arrivals of the event. In case of CMP stack the NMO time correction is not stretch free and the stacking along NMO curve destroy the first arrivals of the event and only the later phase of the event appears on the CMP stacked section.

In addition, a diffraction imaging was applied in order to detect the fault. The strong anomalies on the diffraction image located between shots 22-30 (Fig. 17b) are consistent with the discontinuities of the reflector on both the CSP and the CMP time sections.

Mineral Beach 3D survey (site II in Fig. 1, Israel) (Keydar et al., 2013)

A 3D survey of a DS sinkholes site was conducted for the first time at Mineral Beach (site II in Fig. 1a). The site is located between the Dead Sea shoreline and Route #90, where sinkholes develop in an alluvial fan and lacustrine deposits (Frumkin et al., 2011).

Layouts of data acquisition are shown in Fig. 16. The field acquisition covers 120m by 60m and consists of seven receiver lines in a 10 m interval between them. Shooting was carried out using six shot lines (288 shots in total) and each shot includes 96 channels in 2.5m interval between them. The distance between shot lines is 10 m. (Fig. 16)

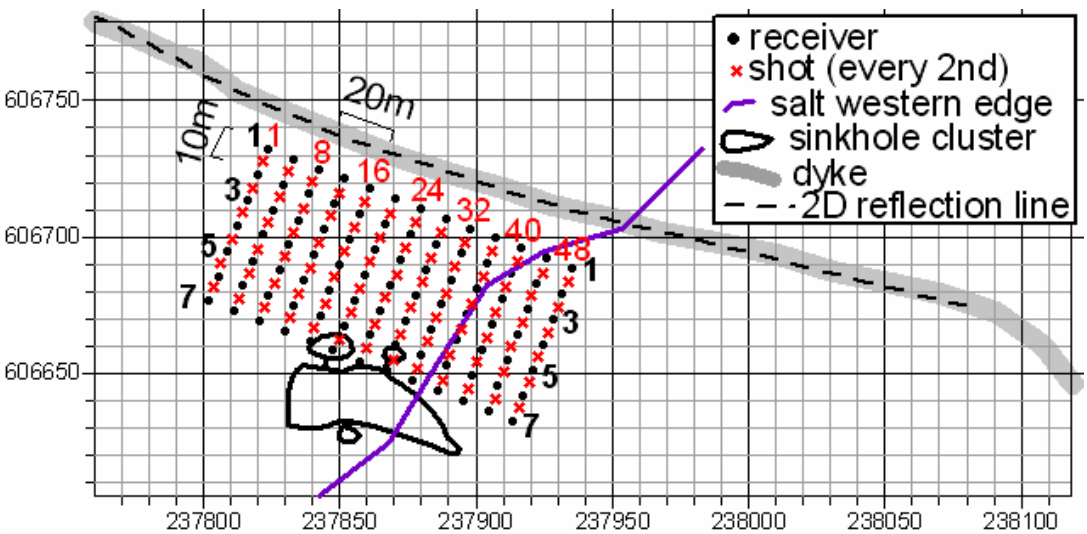

Figure 18. The geometry of 3D seismic survey

We used truck mounted accelerated weight ("Digipulse") as an energy source and single 10Hz geophone per station. In order to image the new developing fault in details the survey was designed with a full azimuth cover for offsets less than 30m (Fig. 19).

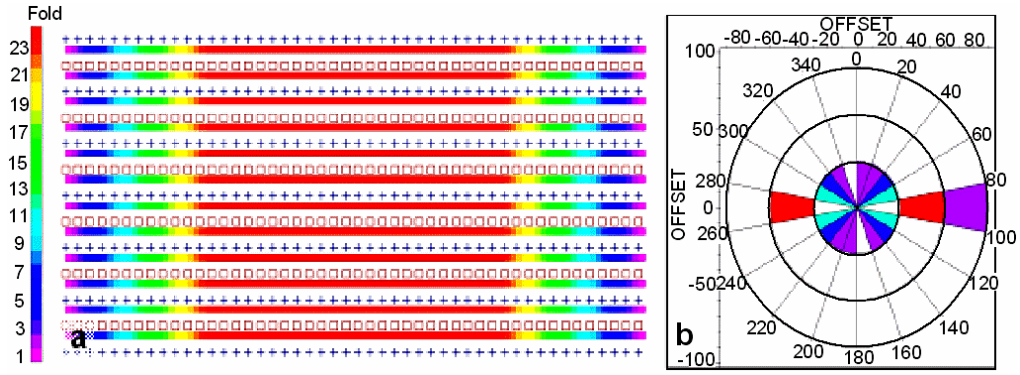

Figure 19. Fold scheme. (a) The shots location are marked by '+' and receivers location are marked by squares.(b). fold as function of azimuth.

The data was recorded using 0.5msec sample rate and 0.5 sec record length. Typical common shot gathers seen on Fig. 20.

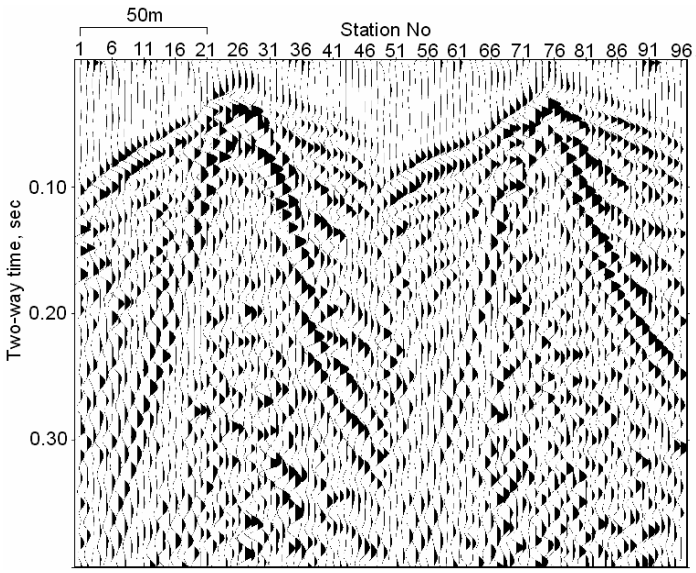

Figure 20. Typical common shot gather including 96 channels

The data were recorded using a Summit II seismograph (GMT, Germany). Two-way time reflection sections along reflection lines from 1 to 7 are presented in Fig. 21b.

On all the figures sub-horizontal coherent reflectors are clearly seen at approximate depth of 50-80 m, close to the exposed sinkhole cluster. In addition, two faults are seen on all sections (Fig. 21b from 1 to 7). These faults have found expression in the time surface of the upper reflector in Fig. 21c as lineaments of increased time (depth). One can see in Fig. 21c that one of the faults (directed NW-SE) crosses the salt western edge near a large sinkhole cluster. Moreover, this fault seems to be a boundary between two geological units. Boreholes located on both sides of the fault show that the salt layer discovered by the southern (to fault) borehole is approximately 10 m higher than the salt layer crossed by the borehole to the north of fault. There is also a change in the lithology: south of the fault the shallow subsurface is composed of 18 m-thick DS mud layer, whereas north-east of the fault a sandy lithology predominates. The second fault would presumably be at the north-eastern border of the sunken unit. However, the geological evidence is not conclusive.

Examples of 2-D seismic reflection surveys (Abelson et al., 2003, 2006) show disturbance zones interpreted as faults in the close vicinity of sinkholes. These faults affect sinkholes in various ways:

reflection sections show variable structural damages close to the sinkholes and salt edge locations. However, there is no evidence that sinkholes are a surface manifestation of concealed faults

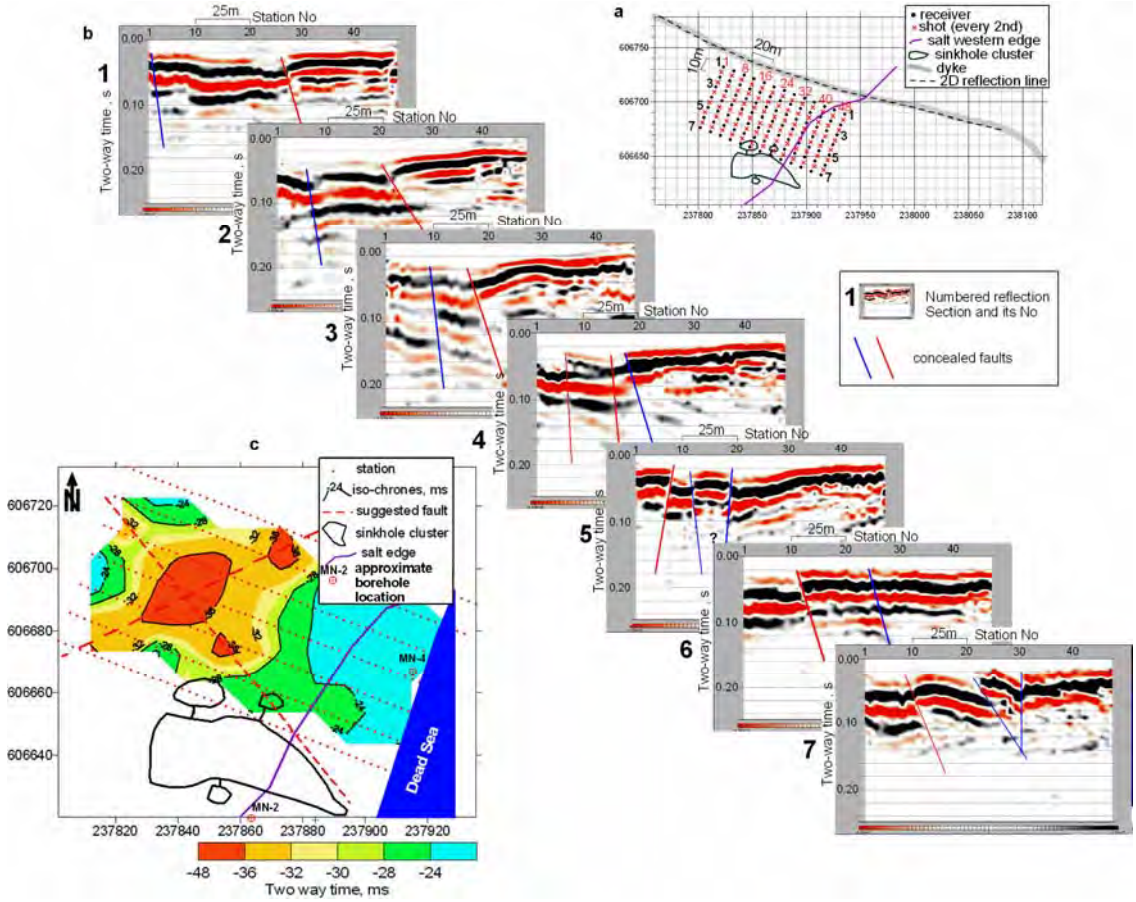

Figure 21. Results of 3D seismic reflection in Mineral Beach area. (a) Layout map of the study area with salt edge and faults; (b) seven 2D reflection sections, (c) two-way time map of the upper reflector, approximate location of two boreholes is shown. Two faults clearly seen in all sections are expressed in the time surface of the reflector (Keydar et al., 2013)

Our 3-D study at Mineral Beach (Fig. 21) shows that a fault crossing the salt facilitates the entrance of undersaturated water to the salt edge. This was confirmed by TEM resistivity mapping (Frumkin et al., 2011). In addition, the available boreholes show that this fault is the boundary of salt units displaced mutually for 10 m in sub-vertical direction (Fig. 21c).

3.2.1.5. Conclusions on Section 3.2.1.

In order to understand the relationship between a developing sinkhole and its tectonic environment, a high-resolution (HR) 2-D and 3-D seismic reflection surveys were carried out at the western shoreline of the Dead Sea. In addition previous reflection lines carried out in the Ghor Al-Haditha were processed using new technique.

The 2D and 3D images of the subsurface were obtained by the use of recently developed imaging approaches. The core of this approach is a new 3D NMO time correction surface formula. Imaging of subsurface is performed by a spatial summation of seismic waves along these time surfaces using recently proposed multipath summation with proper weights.

The multipath summation is performed by stacking the target waves along all possible time surfaces having a common apex at the given point. This approach does not require any explicit information on parameters since the involved multipath summation is performed for all possible parameters values within a wide specified range. The results from processed 3D time volume show sub-horizontal coherent reflectors at approximate depth of 50-80m which incline on closer location to the exposed sinkhole and suggest a possible linkage between revealed fault and the sinkholes.

3.2.2. Mapping of salt layers using MASW method

(The method and results are presented in details in Ezersky et al., 2013a; Ezersky and Bodet, 2012; Ezersky and Legchenko, 2014; Keydar et al., 2011) *Comments: During the MERC Project MASW survey was carried out in Israeli site only. However, to generalize our findings we have invited French scientists carried out the surface-waves prospecting through the Ghor Al-Haditha jointly with A. Al-Zoubi in 2007 to write joint article. We submitted this paper to the Special Issue on Geotechnical Assessment and Geoenvironmental Engineering in EAGE journal of Near Surface Geophysics and EEGS Journal of Environmental and Engineering Geophysics (JEEG). The article by Ezersky M., Bodet L., Al-Zoubi, A., Akkawi, E. et al. (2013a) has been published. In this report we present results obtained in Israel only.*

3.2.2.1. Introduction

Most researchers associate the sinkhole phenomenon with the formation of dissolution cavities within 10-30m thick salt layers located at depths of 25-50m with consequential gradual collapse of surface sediments. Both the timing and location of sinkholes suggest that the salt weakens as a result of increasing circulation of unsaturated (with respect to halite) water, thus enhancing the karstification process (Bernabe et al. 2003; Shalev et al. 2006). The location, depth, thickness and weakening of salt layers along the DS shorelines, as well as the thickness and mechanical properties of the upper sedimentary deposits, are thus considered as controlling factors of this on-going process.

It is known that shear-wave velocities (Vs) are associated with porosity, fracturing, and correspondingly, with the mechanical properties of soil and rocks (Stokoe et al. 1994; Dvorkin 2008). It is most important if target layers are located under the groundwater table where pressure-wave velocities (Vp) are strongly affected by pore saturation, whereas Vs principally characterizes properties of the medium without fluid filling. However, from a practical point of view, the measurement of Vs remains delicate because of well-known generation and picking issues in shear-wave refraction seismic methods (Palmer 1986). As an alternative to S-wave refraction method, we have suggested using surface-wave prospecting techniques based on surface-wave dispersion measurements and inversion (see for instance, comprehensive reviews in Socco and Strobbia 2004; Socco et al. 2010) to characterize near-surface Vs.

The main objective of the study is to use Vs in order to detect decompaction zones in the salt unit and in the overlying layers, which could be the marker of forthcoming sinkhole development. Two approaches have been used: (1) In Israel, Vs mapping has been performed to discriminate weak and hard zones within salt layers, after calibration of inverted Vs near boreholes (deep target); (2) In Jordan, roll-along acquisition and dispersion stacking have been performed to achieve multi-modal dispersion measurements along linear profiles to map decompaction zones in the clastic sediments overlying salt layers (shallow target) (This part of study was carried out by French researchers acquired seismic data in previous project). Note that the latter issue in the context of sinkhole hazard has been recently studied numerically and applied to real data analysis (O'Neill et al. 2008), whereas salt mapping using surface-wave prospecting methods is carried out for the first time.

3.2.2.2. Results of previous Vs studies

Eleven seismic refraction lines (P- and SH-wave surveys) were carried out during the last 15 years by different researchers along the DS shore in Israel. We selected the SH-data allowing unambiguous interpretation. The corresponding SH-wave refraction lines are shown by the letter "S" in Fig.1. Lines were located within the salt area delineated by P-wave seismic refraction surveys (Ezersky et al. 2010). Generally, 2-3 layers above the salt layer can be distinguished on Vs depth sections. The 3-layer parameters deduced from the 11 seismic refraction surveys are summarized in Table 1.

Table 1 gives us reference for soil and salt velocities measured using S-wave refraction method. However, taking into account complications in the measuring Vs using refraction method (mentioned in the paragraph 5.2.2.1) we suggested application of surface wave prospecting using MASW technique. One can familiarise this technique, its advantages and disadvantages, data acquisition and processing in paragraph 5.1.2. and, in more details, in Ezersky et al. (2013a).

Table 1. Elastic dynamic parameters of the Dead Sea salt layers based on seismic refraction surveys

Layer/ Lithology	Depth, m	Vp, m/s min-max	Vp, m/s Average	Vs, m/s min-max	Vs, m/s Average	Vp/Vs min-max	Vp/Vs Average	Poisson's Ratio min-max	Poisson's Ratio Average
Upper/ Alluvium dry	0-12	550-890	734	200-380	375	1.65 -3.15	2.03	0.21-0.44	0.34
Middle/ Alluvium saturated	2-12 to 12-50	1470-2500	1964	350-800	626	1.92 -4.73	3.29	0.32-0.48	0.45
Lower/ Salt saturated	Under 12-50	2900-4080	3365	930-1680	1182	1.89 -2.42	2.15	0.29-0.40	0.36

3.2.2.3. The MASW method – brief description

Surface-wave dispersion inversion is a standard approach to infer 1D Vs structure for global earth seismology, near-surface geophysics, geotechnical, and civil engineering applications (see for instance: Nazarian and Stokoe 1984; Socco and Strobbia 2004). The technique has grown in popularity among practitioners in the early 2000's with their access to multichannel equipment, and the development of dedicated techniques and associated software, such as Multichannel Analysis of Surface Waves (MASW) (Miller et al. 1999; Park et al. 1999; Xia et al. 1999). Active-source surface-wave dispersion measurements can be indeed quite easily achieved using typical seismic shot gathers. The wavefield is transformed to the frequency-wavenumber (or frequency-slowness) domain in which maxima should correspond to surface waves. On such generated dispersion images, several dispersion curves can be picked if propagation modes are well separated. Dispersion curves are then inverted for a 1D Vs profile with depth. When data are collected in a roll-along mode, each 1D profile is represented at its corresponding spread midpoint allowing a pseudo-2D Vs section to be drawn.

The maximum penetration depth $Z_{\max}$ and thickness H_1 of the uppermost (irresolvable) layer limiting the resolution of sub-surfaces are determined by the wavelength and parameters of the data acquisition according to the half-wavelength criterion (Rix and Leipsky 1991). The normally accepted criterion is that maximum depth ($Z_{\max}$), for which *Vs* can be reasonably calculated (penetration depth), is about half the longest wavelength ($\lambda_{\max}$) measured:

$$Z_{\max} = \lambda_{\max} / 2 = 0.5 V_{ph_{\max}} / f_{\min} \qquad (4)$$

At the same time, the minimum penetration H_1 is determined by:

$$H_1 \geq 0.5\lambda_{\min} = 0.5 V_{ph_{\min}} / f_{\max} \qquad (5)$$

where $V_{ph_{\max}}$ and $V_{ph_{\min}}$ are the maximum and minimum phase velocities of the fundamental mode, respectively, and $f_{\min}$ and $f_{\max}$ are corresponding frequencies at the phase velocity measured. Note that $\lambda_{\max}$ also relates to the maximum spread length (L), whereas $\lambda_{\min}$ relates to the minimum distance (*2dx*) between geophones (O'Neill 2003).

One well known limitation of the method is its trade-off between lateral resolution and investigation depth (Gabriels et al. 1987). On one hand, the inverse problem formulation imposes the investigated medium to be assumed 1D under the spread. Additionally, the spread itself has to be short enough to achieve lateral resolution if profiling is performed. On the other hand, long spreads are required to record wavelengths great enough to increase investigation depth and to mitigate near-field effects (Bodet et al. 2005). However, several countermeasures exist to overcome such drawbacks, particularly when the seismic set-up provides redundant data. Specific processing techniques (offset moving windows and dispersion stacking) can be successfully used to narrow the lateral extent of dispersion measurements (Grandjean and Bitri 2006). When applied, it is possible to extract more local information about the investigated medium along the line and thus to retrieve its lateral variations.

3.2.2.4. MASW for bed rock

(The method and results are presented in details in Ezersky et al., 2013a; Ezersky and Bodet, 2012; Keydar et al., 2011)

The problem of investigating shallow bedrock using surface-wave methods has been described in a number of publications (Banab and Motazedian 2010; Casto et al. 2009).

1. All researchers agree that investigation of shallow structures (down to 30m from surface) when the Vs contrast between the overburden (loose soil Vs < 200 m/s) and firm bedrock (Vs > 2300 m/s) is very large, is not a trivial procedure. Inversion of the fundamental-mode Rayleigh wave in this case could result in Vs of the bedrock much lower than the expected values (Casto et al. 2009). This is a case in the Dead Sea area where a high velocity salt layer is overlain and underlain by clastic sediments.
2. The general problem is selection of the proper equipment and methodology of the data acquisition
3. Another problem is the selection of the number of layers for inversion to avoid the non-uniqueness solution (Cercato 2009; Renalier et al. 2010). This problem is associated with the obtaining of the additional information on subsurface.

To overcome these problems the MASW method was preliminary investigated using modeling, the data calibration to the borehole measurements, use of low frequency geophones etc.
Thus the MASW method was improved to map salt layers located at 25-50m (top) with a 7-30m thickness.

Modeling. The goal of forward modelling is to show how structure and properties of the subsurface affect the phase-wave-velocity spectrum, which is input data used for inversion. Here we show the influence of salt layer thickness *L*, depth *H* and Vs on the spectrum of phase velocity V_{ph}. We used real parameters of the subsurface layers based on borehole data and field acquisition results. Fig. 22a shows the dispersion curves calculated for the 3-layer model depicted in Fig. 22a-1. Parameters of the model are as follows: H = 25m, Vp = 3500m/s and Vs = 1650 m/s. Salt thickness *L* varies in the range of 1.0-125m. In the range of 7-30Hz, the dispersion curves are identical (Fig. 22a), but they diverge below 7Hz. The salt thickness then affects the phase velocity curves in the frequency range 3–7Hz. While 4.5Hz geophones filter below 4.5Hz, 2.5Hz geophones cover the entire frequency range where dispersion curve is sensitive to salt layer thickness variations. Seeking salt layer thickness from dispersion curves will then be strongly dependent on the quality of the data in the low frequency range. The sensitivity of dispersion curves to Vs in the salt layer is presented in Fig. 22b. The 10m thick salt layer is located at 25 m depth and characterized by Vp = 3500 m/s. Vs varies in the range of 750 m/s to 2350 m/s. At frequencies higher than 7Hz, dispersion curves are identical. As in the previous model, differences between phase velocities are observed in the frequency range of 3 – 7 Hz, requiring low geophone frequency (2.5 Hz). Therefore, results acquired with 4.5 Hz geophones will strongly depend on medium properties.

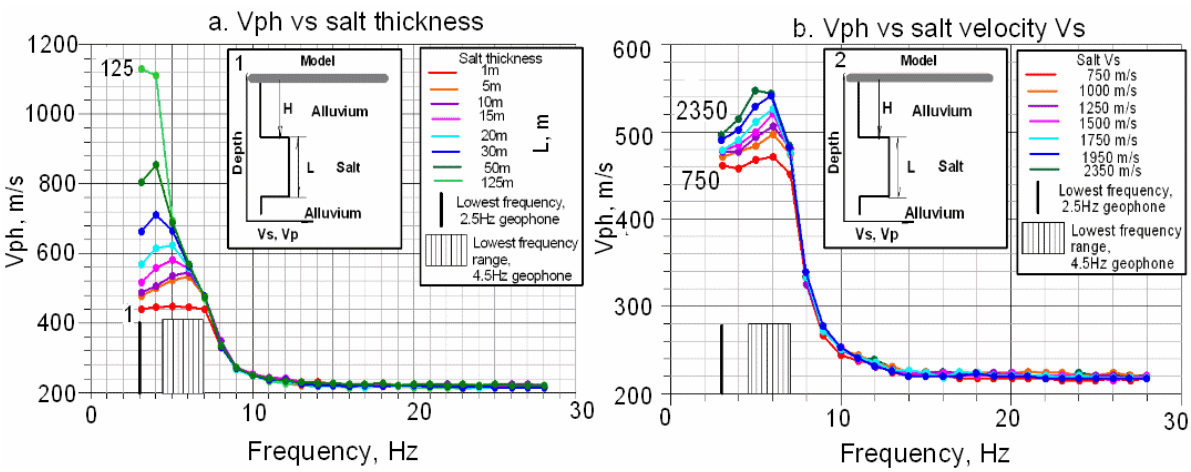

Figure 22. Salt layer forward model: Top depth H=25m, Vs = 1650m/s, Vp = 3500m/s. The salt layer thickness L is changed. Calculated dispersion curves in dependence on: (a) salt layer thickness L. Parameter of curves is L; (b) salt layer velocity, parameter of curves is Vs of salt layer.

We have also checked the influence of the salt layer depth *H* upon dispersion curves. Results showed that V_{ph} is mostly sensitive to *H* variations in the shallow part of the section (*H* = 15m), whereas differences in the phase velocity significantly decrease for greater *H* values. In the parameter conditions of the DS area (10 m< *L*< 20 m; 750 m/s< Vs< 1500 m/s; 20m<*H* <40 m) the dispersion curves are more affected by changes in layer thickness than by Vs variations, which is different from the conclusions of Xia et al. (1999), who used a model with a linear velocity increase. These examples show that sensitivity studies can be influenced by the overall velocity model used.

Although this parametric study cannot be considered as complete, the results show that investigation of the salt layer (high velocity layer sandwiched in low velocity clastic sediments) by surface waves (Rayleigh fundamental mode) requires the use of low frequency geophones (2.5 Hz). Geophones of 4.5 Hz, typically used for surface-wave recordings can be inadequate in the shallow geological conditions of the DS.

Calibration. We obtained Vs values consistent with borehole measurements which provided confidence in the inversion results, using calibration of the method near two boreholes where other methods were applied to reveal the Vs structure of the subsurface. As a result, we have mapped the salt layers through three Israeli sites.

Two boreholes were drilled for the project at Ein Boqeq (Site IV) and at Mineral Beach (Site II) (see Figure 1 for location). Borehole EB-3E crossed sandy gravel sediments and met the salt layer at a depth of 26m (Fig. 23b). Borehole MN-5E , located at the southern margin of the Mineral Beach site on a mud flat found the DS clay (mud) overlaying and underlying a 20m thick salt layer located at a depth of 22m depth (Fig. 23e). Depth-Velocity graphs are presented in Figs. 23a and 23d, respectively, along with two vertical electrical resistivity profiles derived from TEM soundings (Figs. 23c and 23f). Downhole (DH) surveys within boreholes and close seismic refraction surveys were used for calibration measurements, the objectives of which are: (1) to compare Vp and Vs velocities measured by different methods with those from surface-wave prospecting, and to distinguish Vs in the different lithologies; (2) to select model parameters for inversion; (3) to estimate the resolution of the surface-wave method.

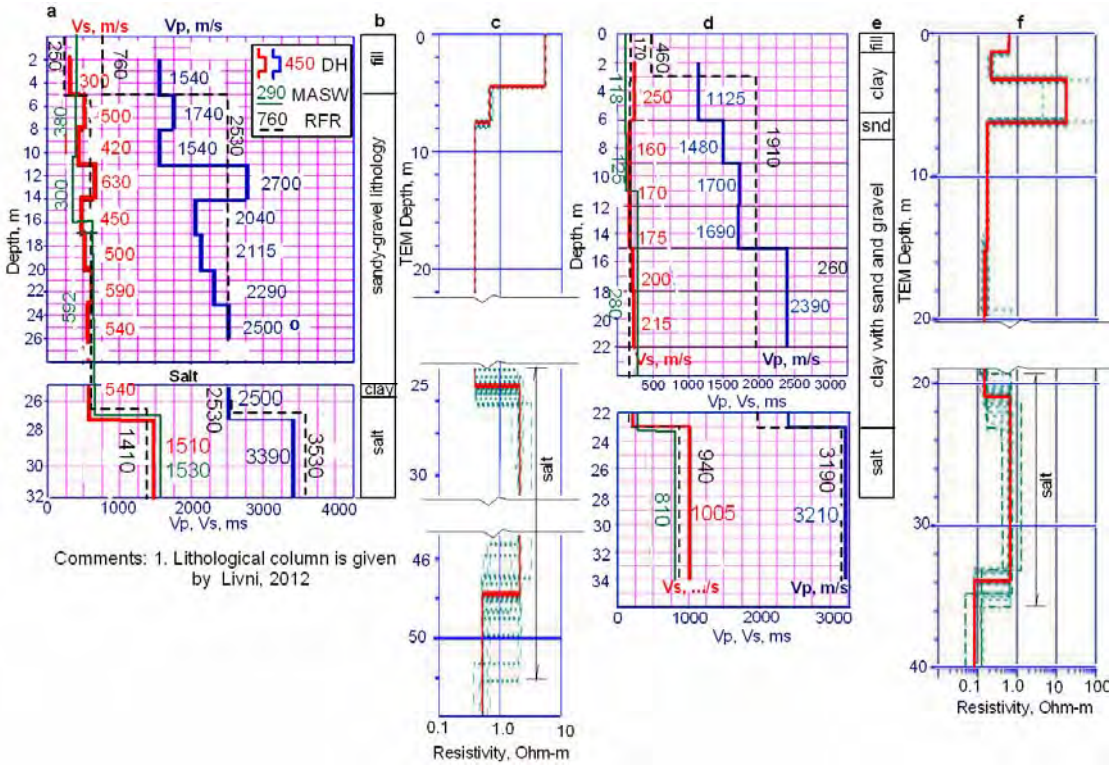

Figure 23. Results of the calibration measurements in the EB-3E and MN-5E boreholes: downhole data are combined with surface-wave and seismic refraction graphs (a and d, respectively); corresponding lithological columns of the EB3E and Mn-5E boreholes (b and e, respectively); TEM resistivity-depth functions of the EB-3E and MN-5E boreholes (c and f, respectively), scale of TEM depth is distorted.

Constraints. We used all available information for the parameterization of the initial model before inversion in order to reduce the non-uniqueness of solutions, as far as possible. Every seismic line was accompanied by seismic refraction and TEM surveys, enabling to determine the salt layer depth, thickness and Vp values. We have also discussed the maximum penetration depth. We used low frequency geophones, a power Digipulse and long seismic line on the western DS shore, where linearized inversion was used.
Example of data inversion of borehole EB-3E (Site IV in Fig. 1a, sandy-gravel lithology) is shown here.

Borehole shows a depth of 26m to the salt top. Seismic refraction method shows the salt top at 27m depth and a compression wave velocity of Vp = 3400-3530 m/s for the salt layer. TEM resistivity-depth graph (Fig. 8c) comprises high resistivity ($2.0\,\Omega m$) unit at the depth range of 24-52m on the background of very low resistive soil ($0.4\text{-}0.5\,\Omega m$). This high resistive unit is a salt layer. Ezersky et al. (2011) have shown that such a high resistive unit at the DS conditions can be detected with high resolution. Green graphs in Fig. 23c are equivalent solutions, which lead to the same apparent resistivity graph. Thus, we can select parameters constraining the model for inversion of dispersion curves: Depth of 25m to salt layer; salt thickness of 18m; salt layer Vp = 3400 m/s, salt density at 2000-2100 kg/m^3, Poisson Ratio 0.4 for water-saturated soil and a 0.33 ratio for water-saturated salt. The latter parameters have been revealed by laboratory tests.

Inversion. Then inversion of the surface-waves records can be performed using selected constraints. Results of surface-wave surveys near borehole EB-3E are presented in Fig. 24.

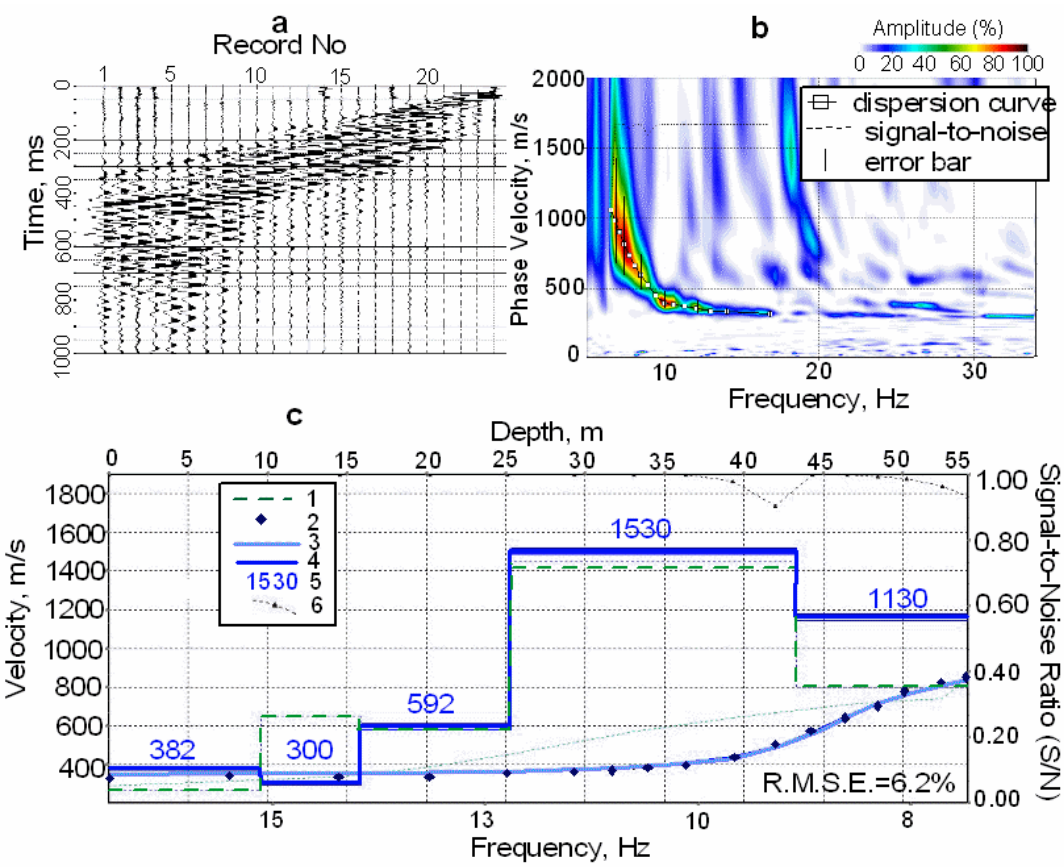

Figure 24. Results of Surface Wave Prospecting along line near EB-3E borehole in the Ein Boqeq (site IV). (a) Signal; (b) Dispersion image; (c) Vs inversion model (3 layers above salt). 1 – initial Vs – depth model, 2 - experimental extracted points (see in Fig. 24b), 3 – dispersion curve matching the experimental points, 4 – final inverted Vs versus depth layered model, 5– inverted Vs of the salt layer [m/s], 6 – S/N ratio graph.

The seismograms (Fig. 24a) and dispersion image with extracted dispersion curve (Fig. 24b) characterize data with a high S/N ratio of 0.85-1.0 (Fig. 24c). The fundamental mode dispersion curve

is clearly expressed in the frequency range $f_{\min}$ = 6.0 $f_{\max}$ = 16.9Hz (Fig. 24b). Phase velocity varied between $V_{ph\max}$ = 860 m/s and $V_{ph\min}$ = 320 m/s, corresponding to wavelengths $\lambda_{\max}$ = 143m and $\lambda_{\min}$ = 19m. With these values and the profile length, the minimum and maximum penetration depths are H_1 = 9.5m and $Z_{\max}$ = 57m, respectively. Inversion of the dispersion curve was carried out, fixing Vp = 3400 m/s in the salt layer. The inverted Vs profile (Fig. 24c), obtained with a RMS of 6.2% consists of 5 layers (3 layers above high velocity layer). In the depth range between 9.5 m and 26 m (sandy-gravel layers) Vs varies between 300 m/s and 590 m/s, and increases up to 1530 m/s in the salt layer (lithology given by borehole data; Fig. 23b). Below the salt, Vs decreases to 1130 m/s in clay layer (Fig. 24c). We tested the robustness of inversion results in relation to the starting model. It was determined that Vs in the salt layer varies within limits of $\pm$8% of average value depending upon the starting model.

Borehole drilling was halted at 6 m within the salt layer, but closely located borehole EB-2 (Yechieli et al. 2004) encounters 25m of salt. Transient electromagnetic sounding (Fig. 23f) shows 20-26m salt thickness. Inversion at 26m salt thickness was carried out at minimum root-mean-square error (R.M.S.E.) of 6.2%. The velocity profiles obtained by the different methods are compared in Fig. 23a. Although the velocity logs are characterized by different resolution, they are very similar, exhibiting variations within limits of $\pm$8%.

The DH and surface-wave methods show consistent Vs values, both in the sandy-gravel overburden (300-630 m/s with the DH method and 260–590 m/s with the surface-wave method), and in the salt unit (1510 m/s for DH and 1530 m/s for surface-wave method). The difference in the Vs values is less than 6-8%. The Vs profile obtained from the seismic refraction survey varies also within the same velocity range. Vp is 1540-1750m/s in the upper water-saturated sediments (2-11m deep) and 2040–2700 m/s in the sediments of lower part of the overlaying salt layer (11-26m deep). The salt unit is characterized by Vp = 3390-3530 m/s.

Similar results were obtained for MN-5E borehole (Site II, clayey lithology). The results of the down-hole survey are presented in Fig. 23d. All depth velocity graphs are compared in Fig. 23c. Despite the velocity logs obtained by various methods characterized by different resolutions, they are very similar and vary within limits of $\pm$10%.

Thus, based on analysis of the modeling, borehole calibration and constrained inversion procedure we selected parameters of data acquisition that allowed us measuring the salt layer shear wave velocities with a accuracy of 8-10%. The decisive factor of the methodology are low frequency geophones allowing reaching of $\lambda_{\max}$=150-180 m and respectively investigation depth of 75 – 90 m. Such depth is reached at the line length of 115 – 150 m.

3.2.2.5. Data acquisition

In the western DS sites, we used conventional seismic data (i.e., the vertical component of the wavefield from common shot records obtained in shallow refraction surveys). Data acquisition is shown in Fig. 25. Data excitation was carried out using Digipulse hydraulic source (Fig. 25) mounted on a Chevrolet pickup truck (a and b). A 96-channel Summit II plus seismic recorder was used with a 24-geophone spread (vertical 2.5 Hz geophones – 6 in Fig. 25c). Receiver spacing was 5m; shot location was 5-10m away from nearest trace (off-end shooting), and move-up between shots was a one – two receiver interval.

One can compare source for Surface Wave exciting (2 in Fig. 25b) with that for SH-wave exciting (4 in Fig. 25d). The first one of ~100 kg mass as well as by special resin drive, whereas second hammer of ~30 kg mass is accelerated by only his own weight. That allows exciting of surface waves of very high energy.

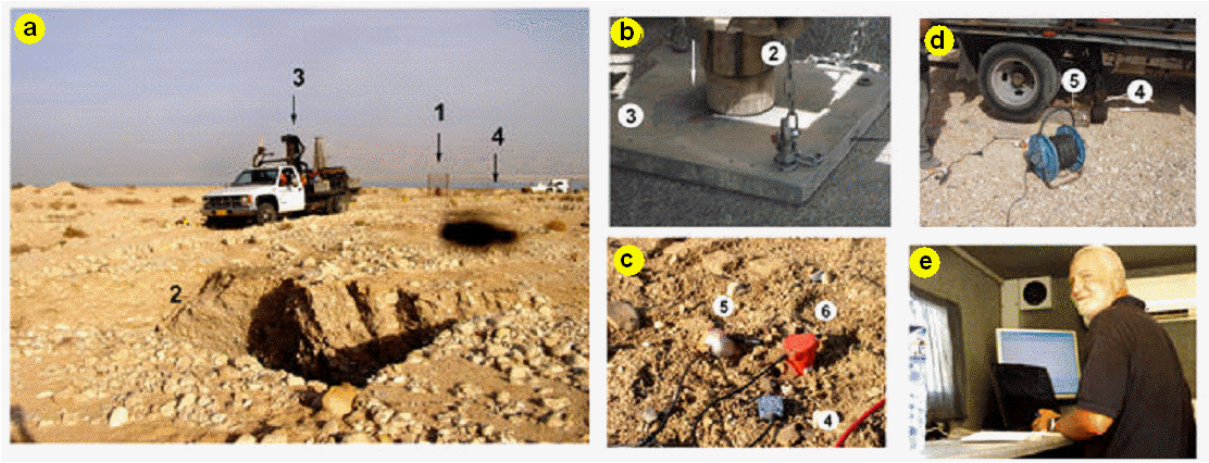

Figure 25. MASW data acquisition in the Nahal Zeelim site. (a) Digipulse seismic source: 1 – borehole DSIF1, 2 – sinkhole, 3 – vertical Digipulse hammer, 4 – Dead sea; (b) vertical hammer (2) stroking on the metallic plate (3) to excite compression and surface waves; (c) geophones used: 4 – vertical 10Hz geophone for P-wave refraction, 5 – horizontal 8.5Hz geophone for S-wave refraction, 6 – vertical 2.5Hz geophone for Surface Wave (MASW) survey; (d) hammer (4) stroking on horizontal beam (5) to excite SH shear waves; (e) field recording for registration and preliminary processing of acquired data

3.2.2.6. Results of surface-wave surveys

Israeli sites (II-IV). The salt layer in the DS area was characterized at 3 sites. The measured parameters (Table 2) are maximum and minimum frequencies, phase velocities, maximum penetration depths (Z), root-mean-square error (R.M.S.E.), Vs, Vp, depths limited by the line length, the distances of each line to the salt edge and to Dead Sea shoreline. Lines located in the sinkhole area are highlighted in grey.

To investigate the spatial variations in the salt Vs, maps from surface-wave measurements (Fig. 26) have been constructed for 3 sites on the western Dead Sea shore.

In the Mineral Beach area (site II), the Vs map in salt, which is based on surface-wave measurements along 10 profiles (Fig. 26a), shows a gradual eastward increase in Vs from 810 m/s near the salt edge to more than 1600 m/s near the Dead Sea. The geological cross-section A-B (Fig. 26d) shows similar WE variation Vs with distance from the salt edge to the DS. Large sinkholes (about 30m diameter) are located in the low velocity zone Vs = 850-950 m/s, whereas latent karstic cavities (revealed by borehole Mn-O, Fig. 26a) are located in the low- velocity zone Vs = 950–1050 m/s. A similar seismic structure is observed in the Nahal Ze'elim area (site III) where the Vs map (Fig. 26b) was drawn from 6 seismic lines with a SE-NW direction. As above, the Vs gradually increases from 760–950 m/s close to the salt edge to more than 1600 m/s near eastern line nzl6ss, located 300m west of the Dead Sea. Note the presence of superficial, relatively small sinkholes (3–5 m diameter) arranged along the salt edge mapped by Seismic Refraction method (Ezersky et al. 2010).

In the Ein Boqeq area (Site IV) the Vs map is less detailed as it based on surface-wave dispersion measurements along 4 profiles (Fig. 26c). Again, the Vs quickly increases from 850 m/s near the salt edge to more than 1600 m/s at Dead Sea shoreline (some 150m east of the salt edge). This area is close to the Evaporation Pond where the salt layer was found at a depth of 26m below sandy-gravel sediments. According to the borehole data, very high mineralized water (~230 g/l chloride) envelops the salt layer (Yechieli et al. 2004). Sinkholes have not been detected in this area.

3.2.2.7. Discussion

Investigation of shallow structures (down to 30m from surface) when the Vs contrast between the overburden (loose soil Vs < 200 m/s) and firm bedrock (Vs > 2300 m/s) is very large, is not a trivial procedure (Banab and Motazedian 2010; Casto et al. 2009).

Inversion of the fundamental-mode Rayleigh wave in this case could result in Vs of the bedrock much lower than the expected values (Casto et al. 2009). Another problem is the selection of the number of layers for inversion to avoid the non-uniqueness solution (Cercato 2009; Renalier et al. 2010).

Table 2. Shear wave velocities measured in the Dead Sea shore area in Israel using MASW method

Site [1]	Line No	Salt depth (m) [2]	Phase velocity, $V_{ph\max}$ / $V_{ph\min}$ (m/s)	Frequency, $f_{\min}$ / $f_{\min}$, (Hz)	$Z_{\max}$ (m)	MRSE [3] %	Vs in salt [4] (m/s)	Vp in salt (m/s)	Distance from MASW line to salt edge (Dead Sea)
Site II	1SSL	35-40	503/353	4.8/14.16	54	6	975	2900	30 (350)
Site II	MN5E	22.3	290/130	3.0/6.4	48.5	6.9	810	3200	20(360)
Site II	17SS	35-40	528/363	4.8/10.9	55	4.2	1215	3000	50 (330)
Site II	8SS	35-40	526/348	4.6/13.1	58	7.9	990	2940	30 (350)
Site II	2LSS	35-40	585/409	4.4/14.7	66.2	5.4	1350	3420	110 (270)
Site II	5SS	35-40	541/362	4.9/14.0	56	9.6	1070	3080	50 (330)
Site II	18SS	34	588/176	3.6/17.1	88	24	1650	3470	250 (130)
Site II	19SS	20	578/259	3.7/17.3	78	29	1670	3780	340 (40)
Salt edge-DS									0(380)
Site III	2SS	22-25	555/271	4.89/17.1	57	3.1	904	2930	40 (600)
Site III	1SS	22-25	601/246	5.8/16.9	51	6.2	1430	3100	100 (540)
Site III	3SS	22-25	634/257	5.77/15.1	55.3	4.9	1492	3200	160 (480)
Site III	4SS	22-25	615/221	5.59/24.6	55.8	6.1	1710	3500	220 (420)
Site III	5SS	22-25	631/214	4.97/12.1	63.5	9.9	1730	3600	280 (360)
Site III	6SS	22-25	615/208	4.56/10.7	67.4	15.4	1830	3600	320 (320)
Salt edge-DS									0 (640)
Site IV	9ss	26-30	640/381	5.12/18.2	61.7	7.9	880	3400	25 (145)
Site IV	7ss	26-30	718/335	5.57/19.8	65	6.06	984	3570	70 (90)
Site IV	EB3E	26	930/320	7/17	57.5	36	1540	3530	95 (30)
Site IV	2ss	26-30	848/357	6.08/20.6	69.8	9.03	1655	3430	180 (80)
Salt edge-DS									0(~125-160)

[1] Site II – Mineral Beach; Site III – Nahal (Wadi) Ze'elim; Site IV – Ein Boqeq (see Fig. 1 for location); [2] depth to salt top; [3] R.M.S.E. variations along the SW spread; [4] Average Vs $\pm$ (8-10%) variation along the SW spread. Comment: Lines located in the sinkhole area are highlighted in grey

We used all available information for the parameterization of the initial model before inversion in order to reduce the non-uniqueness of solutions, as far as possible. Every seismic line was accompanied by seismic refraction and TEM surveys, enabling to determine the salt layer depth, thickness and Vp values. We have also discussed the maximum penetration depth. We used low frequency geophones, a power Digipulse and long seismic line on the western DS shore, where linearized inversion was used. We obtained Vs values consistent with borehole measurements which provided confidence in the inversion results, using calibration of the method near two boreholes where other methods were applied to reveal the Vs structure of the subsurface. As a result, we have mapped the salt layers through three Israeli sites.

The Vs map of Israeli sites (II-IV) shows the increase of Vs from the salt edge (that is coincident with sinkhole area) to the DS shoreline (Figs. 26). The Vs variation with distance for the 3 investigated sites in Israel is displayed in Fig. 27. The curves show that there are correlations between Vs value and distance from measurement point to the salt edge. Note that principally all dependences between Vs and distance from the salt edge are similar, although they slightly differed for different sites. Data were updated using a linear function for sites III and IV, and a power of that for site II. The r-squared coefficient of correlation varies from D = 0.65 (in site IV) to D = 0.93-0.95 (in two other sites). The latter show well the relative relationships between measured values.

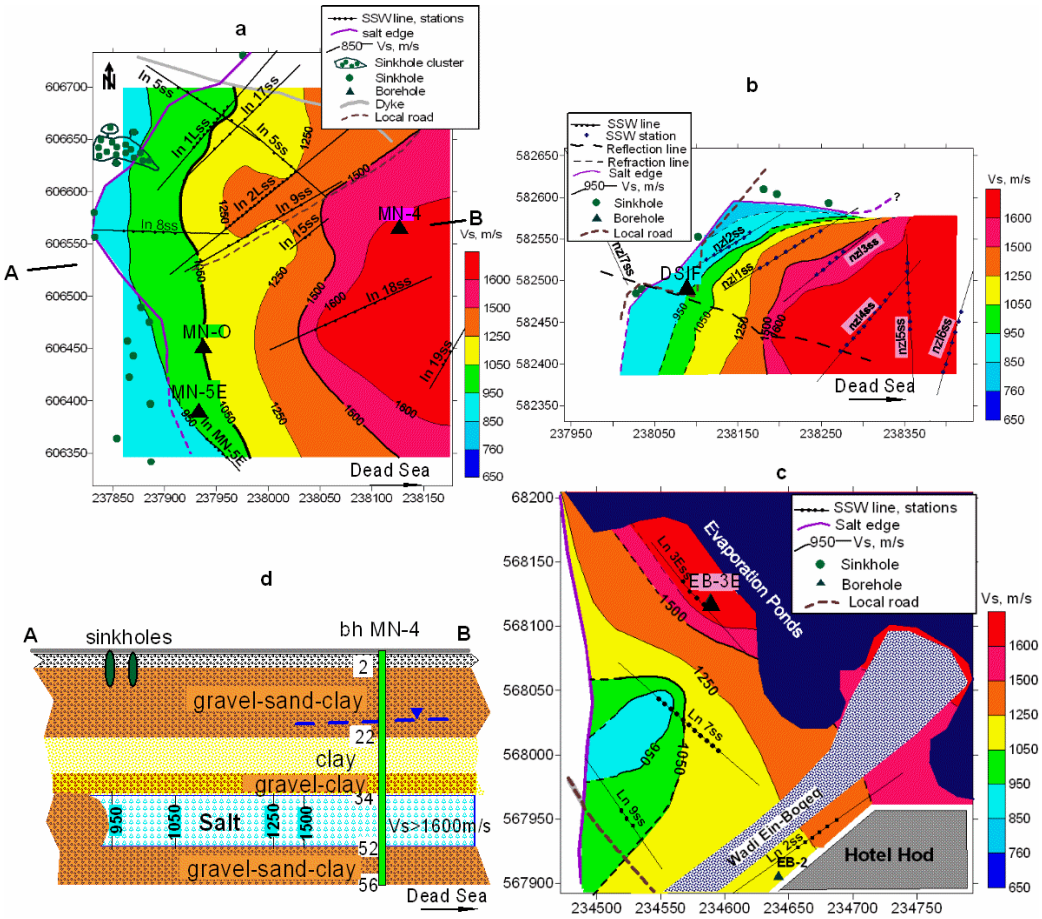

Figure 26. Vs maps in the salt unit at (a) Mineral Beach (site II), (b) Nahal Ze'elim (site III), and (c) Ein Boqeq (site IV). (d) Mineral Beach WE geological section along A-B line via borehole MN-4.

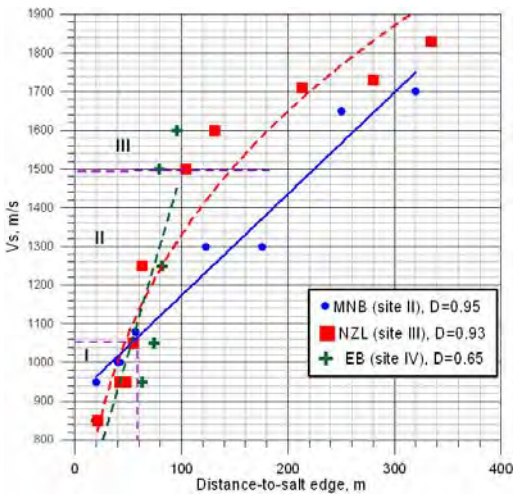

Figure 27. Variations of Vs versus distance to salt edge for 3 sites of the western Dead Sea shore (based on Table 2). D – coefficient of correlation (r-squared) in separate site. (See Fig. 1 for site location).

All graphs converged in the area nearest the sinkholes (salt edge). Vs values vary from 760 m/s at the salt edge and rising to 1500 m/s and more with the distance from the salt edge in the direction of the Dead Sea. Such variation could be caused by a change of either salt voidness or lithological changes; e.g., in clay content. Analysis of the borehole logs has shown that clay content in the salt layer does not exceed 3-5%, which could lead to a Vs decrease of 10-15% (Dvorkin 2008). Since Vs variations of 200% are observed, they probably result from variations in salt porosity. The circulation of under-

saturated water with respect to chloride causes salt dissolution. This water circulation is more intensive near the salt edge and attenuates with distance from it. Correspondingly, karstification (voidness) of salt is active near the layer edge and gradually decreases towards the Dead Sea. This process fits the sinkhole formation along the salt edge (Ezersky et al. 2010; Frumkin et al. 2011; Legchenko et al. 2008) and is supported by the salt dissolution model proposed by Shalev et al. (2006). The dissolution belt along the salt edge is wide at the western side, and in the northern and southern parts of the Jordanian side of the DS. It can become narrow and even completely disappear in the central part of the Jordanian side. As a result of the heterogeneous dissolution, the seismic properties in salt should strongly vary along (e.g., parallel to DS shoreline) and gradually change (increase) perpendicular to shoreline (i.e., towards the DS direction).

Moreover, the seismic velocities in the sediments above karstified salt should also decay because of the subsidence and decompaction processes (Frumkin et al. 2011). This has been confirmed by our studies in Israel and Jordan. Thus, two different strategies should be used to study shallow (decompaction of shallow sediments) and deep targets (karstified salt). To study shallow sinkholes, dangerous parts of the subsurface lines should cross the sinkhole lineaments. They have to be as short as possible to increase lateral resolution. In contrast, to characterize salt properties, lines should be put along zones of karstification (i.e., parallel to the DS shoreline). The entire surface-wave line in this case characterizes average properties of the karstified salt zone. Data presented in the Table 2 show that average Vs values within hazardous sinkhole zones vary slightly along the seismic spread. For example, Vs variation at Mineral Beach is within a range of 900-1150 m/s (1SSL line), 1100 to 1320 m/s (Line 17ss); i.e., in limits of 15-20% between min and max values. At the same time, variations of Vs through the entire area are 1.5 to 2 fold. From Vs values in the salt layer, we propose a classification of the sinkhole prone zones based on the analysis of the field data and on the National Earthquake Hazards Reduction Program (NEHRP) classification (Romero and Rix 2001). The data available shows that sinkholes are located in the velocity zone of 760-950 m/s. A number of latent cavities discovered by boreholes are located in the velocity zone of 950-1050m/s. It would reasonably suggest that velocity less than 1050 m/s is a zone of the present or forthcoming sinkhole hazard. This is also confirmed by graphs depicted in Fig. 27. Indeed, all Vs versus distance-to-salt edge graphs are converged in the 60-100 m zone with velocity Vs<1050 m/s. We will designate this zone as I-sinkhole hazardous one. After Romero and Rix (2001), zones with Vs > 1500 m/s characterizes hard rock (hereafter, hard salt). Respectively, a velocity zone of Vs > 1500 m/s can be characterized at first approach as a safe area with respect to sinkhole hazard. In Fig. 27 this zone (numbered III) is located at distance of more than 100m to 200m from the salt edge (in dependence of site). Finally, a velocity zone in the range of Vs = 1050–1500 m/s (numbered as II in Fig. 27) can be determined as a transition zone where the degree of salt karstification attenuates with distance from salt edge to the Dead Sea. The suggested zonation of the sinkhole hazardous area is based of course on some empirical assumptions and is a first approach. Quantitative estimation should be based on taking into consideration of salt voidness and permeability. That is the objective for the near future when results of salt velocity – permeability testing will be finalized. Note also that such classification is relevant only for present conditions (when DS brine envelops salt layers from above and from below). Velocity criterions will change when the DS level will drop under the salt top surface and the process of salt dissolving by surface waters will begin.

Results obtained in the Ghor-Al-Haditha area (Site I) (Fig. 28) deserve to be considered in light of the results obtained from the western DS shore. Despite obvious high uncertainties at depth, velocity of a half space greater than 1000 m/s (Fig. 28b and 28c) would characterize the salt layer in accordance with the classification accepted here and derived during calibration measurements in Israel.

It also seems logical, in light of the above mentioned seismic refraction data by El-Isa et al. (1995) and Abueladas and Al-Zoubi (2004), who mapped salt layers at depths of 40-50m. If our suggestion were right, a wide degradation zone in Fig. 28b (Line 3) would be interpreted as dissolved salt and a hazardous sinkhole zone. Degradation of high Vs values in the western (DS) direction seen on both lines would be caused by the inclination of the salt layer in the DS direction. Such inclination is associated with more subsidence of the central part of the DS relative to its margins as resulting from tectonics (Garfunkel and Ben-Avraham 1996).

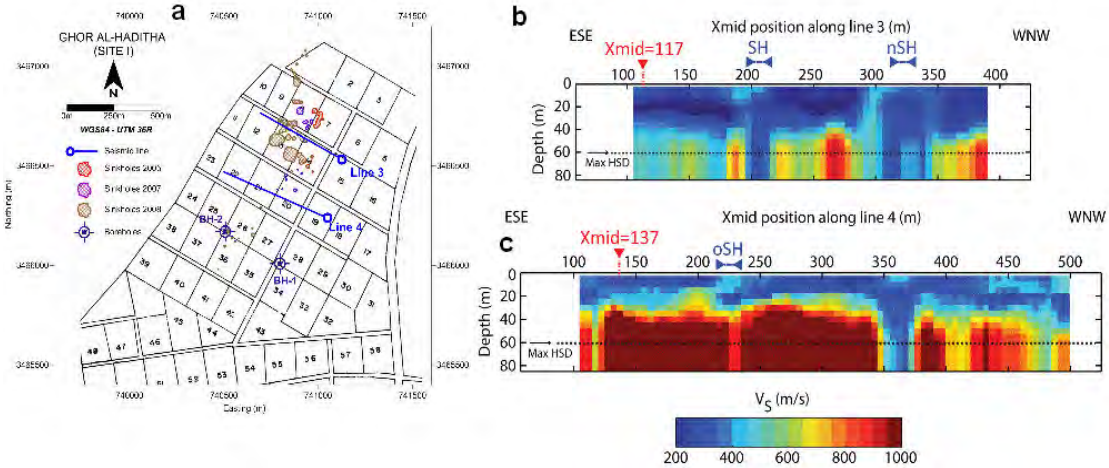

Figure 28. Surface-wave profiling sections implemented in Ghor Al-Haditha (site I). (a) Location map of lines The "O" marks the origins of the lines. Sinkholes occurrences were tracked in 2005 and in 2007, during the survey. An accelerated development of sinkholes occurred toward the north in 2008. The background image corresponds to former agricultural land division; (b) Pseudo-2D Vs sections along Line 3 (top) and (c) Line 4 (bottom), constructed from all 1D profiles. The dotted lines correspond to the maximum half space depth (max HSD).

3.2.2.8. Conclusions on Section 3.2.2.

The main objective of the study was to use Vs for detecting decompaction zones in the salt unit and in overlying layers, which could be the marker of forthcoming sinkhole development. It has been shown in the Ghor Al-Haditha site (I) that inverted pseudo-2D Vs sections present low Vs anomalies near existing sinkholes and made it possible to detect decompacted sediments associated with potential sinkholes occurrences. Moreover, Vs profiles show high velocity unit (Vs > 1000 m/s) at a depth of 40-50m that can be interpreted as a salt layer. In the Israeli sites, a regular Vs increase is observed in the salt layer from its edge in the DS direction. Soft zones (sinkhole hazardous areas) located near the salt edge and associated with karstified salt, are characterized by Vs values of 760-1050 m/s and extend 60-100m from salt edge in the DS direction. Hard-salt zones with velocity Vs values greater than 1500 m/s are located at distances of more than 100-220m from salt edge. Finally, transition zones (1050<Vs<1500 m/s) have a 40-160m spread.

3.2.3. *Salt – faults - sinkholes relations as applied to mechanism of sinkhole forming*

(The discussion has been published in details in Ezersky and Frumkin, 2013; Ezersky et al., 2012b)

3.2.3.1. Tectonic setting

The DS is the terminal lake of the Jordan River system in the Dead Sea Transform (Fig. 29a). The DS is the deepest subaerial point on Earth (Neev and Hall, 1979), located in an extremely arid environment with annual precipitation of 50-70 mm. The DS has been created by eastern and western longitudinal boundary faults with vertical throws of many hundreds of meters. The depression is 150 km long and 15-17 km wide in its center. The Dead Sea basin is divided into two sub-basins (Fig. 29): The deepest point in the northern sub-basin is ~730 m b.s.l (maximum water depth of ~300 m). The southern basin is dry (with artificial evaporation ponds) and reaches a maximum elevation of about -405 m b.s.l. The Dead Sea level is dropping since the 1960s, at a mean rate of 1 m/year for the last decade, reaching -426.8 m b.s.l in late 2012.

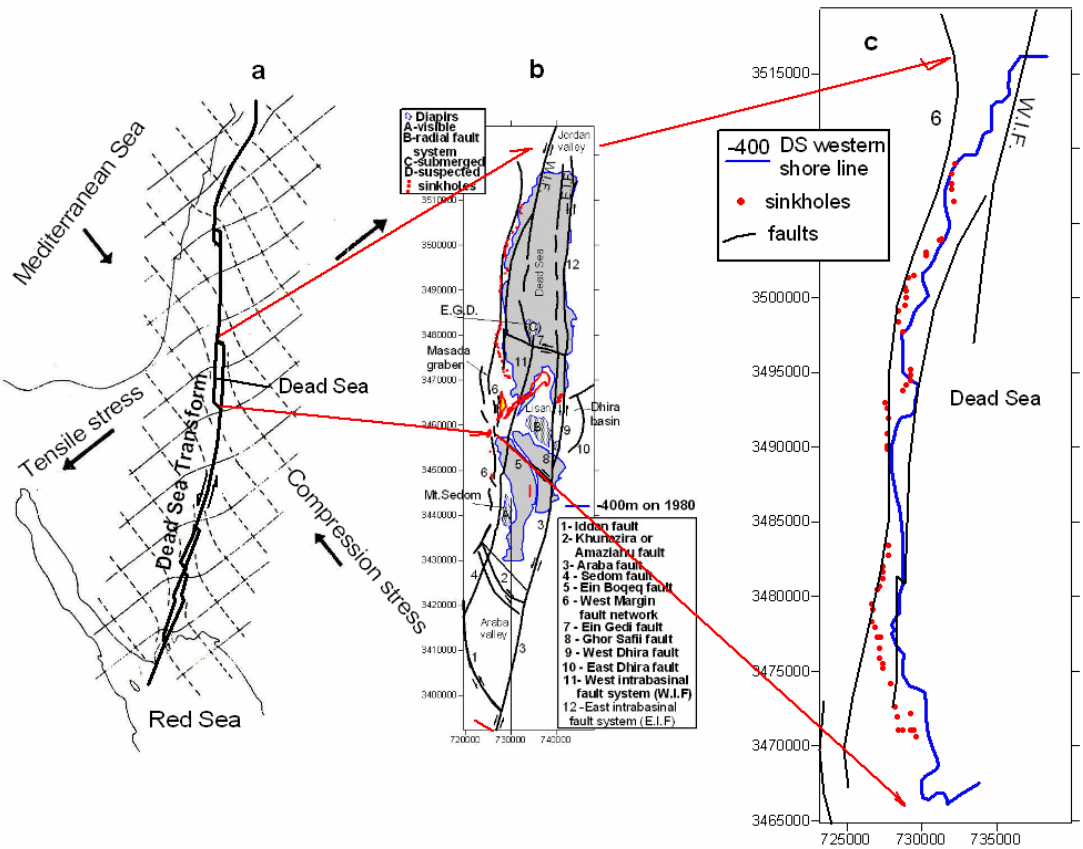

Figure 29. Dead Sea tectonic setting: (a) Pull-apart basin with stress acting in regional scale (Garfunkel, 1981); (b) Faults through the DS area (Ben-Avraham, 1997); (c) Western faults (gray lines), DS shoreline at -400 m lake level (blue) and sinkholes (red) in increased scale.

The DS is an actively subsiding N-S elongated basin formed along the Dead Sea-Jordan transform plate boundary (Niemi and Ben-Avraham, 1997). It is a classic example of a pull-apart basin (left stepping fault traces in a left-lateral, strike-slip fault system). The pull-apart is associated with NW-SE compression and NE-SW tensile stress (Fig. 29a) (Garfunkel and Ben-Avraham, 1996). Depth to the basement is estimated to be 6–8 and 12 km in the northern and southern basin respectively (Ben-Avraham and Lazar, 2006). Numerous faults have been detected throughout the DS area (Fig. 29b) mainly trending N-S and NW-SE (Al-Zoubi and ten Brink, 2001, Ben-Avraham, 1997; Shamir, 2006). The principal features of the DS structure based on surface geology, geophysical and borehole data are as follows: in the upper crustal levels longitudinal strike-slip and normal faults which extend along the basin margins are the most prominent elements controlling the basin structure. The latter faults express a small component of extension across the basin, whereas the pull-apart resulted from the much larger lateral movements along the basin. The basin is still tectonically active (Garfunkel and Ben-Avraham, 1996).

The NW-SE trending transverse faults divide the DS basin into several 20-30 km-long segments (Fig. 29b). The southern DS basin (shallower) is complicated by salt diapirism. The Lisan Peninsula dividing the northern and southern basins (Fig. 29b) reflects a very different tectonic regime controlled by an eastern segment of the strike-slip fault and a rising salt diapir.

The central part of the DS subsides along normal faults forming the graben area. The subsidence is conditioned by the pull-apart causing the W-E divergence of the marginal faults (Garfunkel, 1997).

The sinkhole arrangement along the western DS shoreline (Fig. 29c) is analyzed below.

3.2.3.2. DS sinkholes - Salt edge hypothesis

Visually, DS sinkholes develop along slightly tortuous lines that on aerial photography may look like a series of lineament segments. Numerous seismic refraction surveys have shown that sinkhole distribution in the DS area is controlled by a dissolution front developed along the edge of a salt layer (Ezersky, 2006). The spatial pattern of the sinkhole development along the salt edge was observed repeatedly (with small variations) in all studied sites in Israel and in the Ghor Al-Haditha area (Jordan). It enabled us to conclude that the salt edge is a major factor controlling sinkhole formation

(Legchenko et al., 2008a; Ezersky et al., 2013a). This hypothesis requires the existence of shallow salt layers in both sides of the DS.

3.2.3.3. Salt layer

Israel. A salt layer was indeed observed in boreholes along the western DS shore in Israel. Radiocarbon dating indicates that the salt age range is constrained between 10.2 and 10.8 ka. The salt layer was formed in the Pleistocene-Holocene transition when catastrophic regional aridity caused intensive evaporation of DS water (Yechieli et al., 1995; Stein et al., 2010). The salt is underlain by the 70-14 ka-old Lisan Formation, and is overlain by the Ze'elim Formation (9.9-2.0 ka). Numerous boreholes drilled in the western DS shore have shown a massive 6-30 m-thick salt layer with its top at a depth range of 20-50 m. Seismic refraction surveys carried out by Israeli geophysicists have permitted delineation of buried salt layers at Ein Gedi and 12 other sites of the Israeli DS shore (Ezersky et al., 2013b). Salt, as a rule, is sandwiched between clay layers below and above, thickening towards the center of the DS basin. The salt edge at the west of the DS is often in contact with sandy-gravel sediments. Hydrologically, the salt layers are enveloped by very saline groundwater undersaturated with respect to chloride (groundwater investigated in 19 boreholes contains 120 – 220 g/l chloride, reaching 53 – 98% of saturation). Therefore, although groundwater is very saline, it retains the potential for dissolving salt.

Jordan. Taqieddin et al. (2000) presumed an existing massive salt layer some 25-50 m deep in the Ghor Al-Haditha. This was supported by seismic refraction data (El-Isa et al., 1995; Abueladas and Al-Zoubi, 2004). A longitudinal wave velocity of 2900-3500 m/s was reported at a depth of 38-50 m. Recently, Bodet et al. (2010) revealed a high shear wave velocity unit (Vs > 1000 m/s) using a surface wave prospecting method. This unit is located at the depth range of 40-50 m. We suggest that the high velocity unit of Ghor Al-Haditha correlates with the Pleistocene-Holocene transition salt layers along the western DS shore (Yechieli et al., 1995). Similar geological formations along both Israeli and Jordanian (Ghor Al-Haditha) coasts (Bartov et al., 2006) support this suggestion. Under similar settings, there is no reason why salt would have formed along the western DS shore and not at the south and east. Salt was deposited at places of superficial coastal backwaters where the bed was sloping gently (Israeli shore and south-eastern and north-eastern parts of the DS in Jordan). At places where the shores were steep salt was either not deposited or deposited only along a narrow strip. Indeed, the central part of the Jordanian side of the northern DS basin, characterized by such steep shores, is devoid of sinkholes. The performed analysis shows that both stratigraphic setting and geophysical data suggest that a buried salt layer exists in the Ghor Al-Haditha area, where the slope is mild due to the Lisan Diapir.

3.2.3.4. Salt layer deposition and salt edge concepts.

Salt layer deposition and the "salt edge" concepts are explained on a W-E section presented in Fig. 30. A first phase of salt deposition (latest Pleistocene) may correspond to a period when DS water still covered the relatively flat surface topography of the shore (Fig. 30a). Following the second period, termed "catastrophic aridity" by Stein et al. (2010), salt was deposited from evaporated DS water, forming the salt layer (Fig. 30b). finally, around 10.0 ka ago salt layers were covered by fluvial and lacustrine sediments (Fig. 30c). Fig. 30 demonstrates that the salt edge may be constrained by vertical (or sub-vertical) up to 30 m-high fault walls articulating often in the uppermost part with thin salt featheredge (Fig. 30b). The salt layer, as well as feather-edge length and thickness, depend on the relationships between DS level and intermediate block elevation at the time of salt deposition (Fig. 30a left). The right part of the section shows the case where a salt layer was not formed (Fig. 30a). This section characterizes apparently the central part of the eastern DS shore. At gently sloping shores the salt feather-edge can be thin and long (Fig. 30b, left). However, the results have shown that the salt edge, or more exactly, the salt layer zone adjoining the edge is most susceptible for intensive dissolution and sinkhole formation (Legchenko et al., 2008a,b; Ezersky et al., 2010).

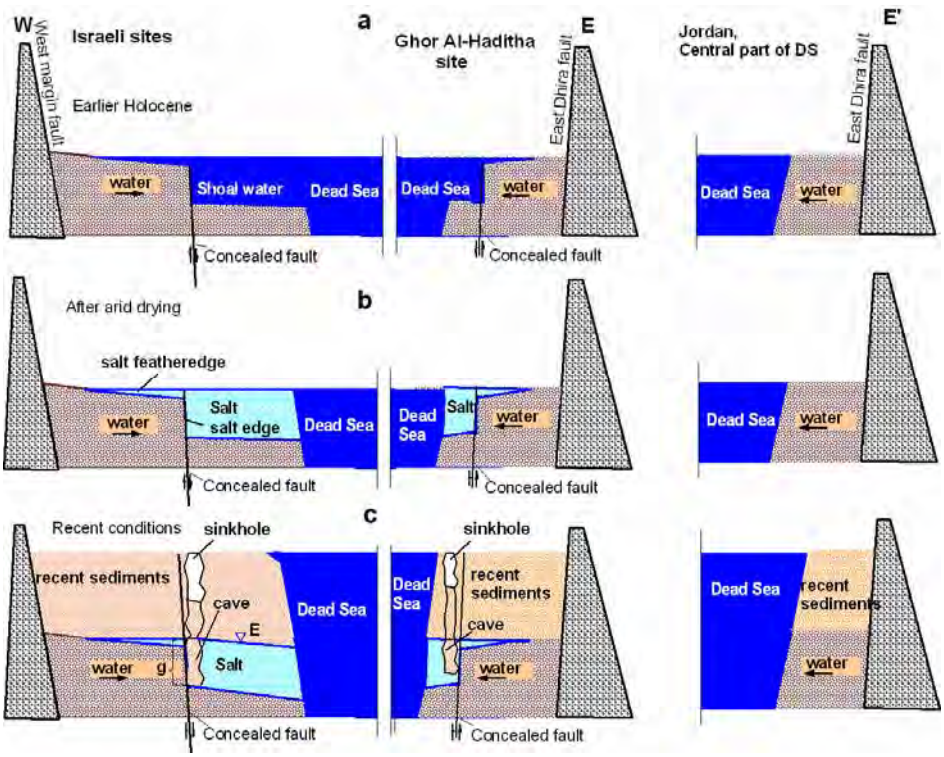

Figure 30. A cartoon showing hypothetic DS sinkholes configuration concept. The left part of the section (W-E) corresponds to gentle shores like the Israeli (western) ones and Ghor Al-Haditha (eastern), the right part of the section (E') corresponds to steeper shores like the central eastern shore: (a) latest Pleistocene setting, (b) after salt deposition following arid phase, and (c) recent conditions. g –thickness of the salt, E – salt top.

Hypothetically, the lakeward (towards the DS) edge of the karstified salt would be a geometrical line parallel to the salt edge. In fact, salt karstification occurs only where circulation of undersaturated water takes place. It was found experimentally, based on the distribution of shear wave velocities within the salt layer, that the dissolution of the salt layer is most intensive within 60-100 m lakeward from the salt edge (Ezersky et al., 2013a). An example of such Vs distribution within the salt unit at Mineral Beach area is shown in Fig. 31a (map). Fig. 31b illustrates the W-E geological section along line A-B with Vs variations lakeward from the salt edge. The belt along the salt edge with 750 m/s <Vs<1050 m/s is the hazardous zone where most sinkholes are formed. Fractures and faults within this belt promote groundwater circulation and accelerated sinkhole formation along these lineaments. The increase of shear wave velocity with distance from the salt edge (sinkhole area) to the DS shoreline is clearly seen in Figs. 31a and 31b. The authors associate this with a maximum salt karstification near the salt edge (within the dissolution front) and its graduate decrease lakeward (Frumkin et al., 2013).

A subsequent 80-120 m transition zone extends further in the DS direction, where karstification is spatially attenuated lakeward. It is a zone of expected forthcoming sinkholes, when the dissolution front will migrate towards the center of the basin. The flat area between this zone and the DS shoreline has a deeper layer of indurated salt sandwiched between clays, with less circulation of aggressive (capable of dissolving salt) water, so it is less hazardous.

Following the dissolution front salt edge concept, we suggest a general model of the salt layer deposited around the DS. This model (Fig. 32) suggests that there is a 10-30 m-thick salt belt around much of the DS shore, controlling the sinkhole hazard (Ezersky et al., 2013b). All known cases of collapses and accidents including the alarming catastrophe at pond 18 in Jordan (Closson, 2005) have occurred within this salt belt.

The model presented in Fig. 32 enables us to conclude that: (1) the dissolution front follows an ancient shoreline which existed at the stage of salt unit deposition (10.2 - 10.8 ka) - modern sinkholes are formed along this dissolution front; and (2) the buried salt layer extends from the modern Dead Sea shoreline landward, towards the dissolution front, permitting its investigation from the surface.

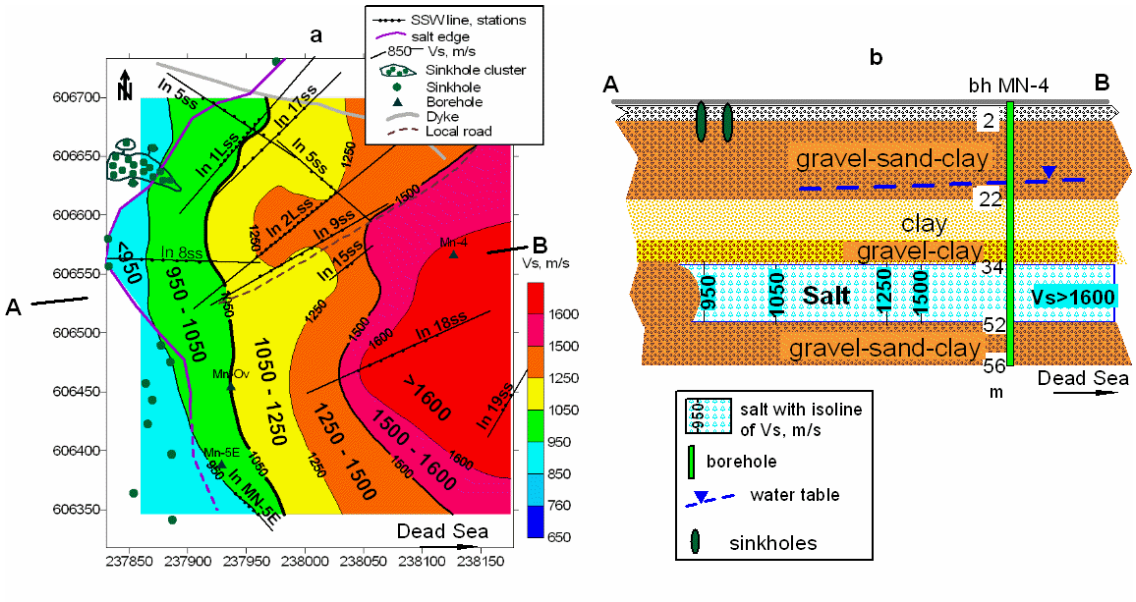

Figure 31. Shear wave velocity distribution within the salt layer in Mineral Beach area. (a) Vs map through the salt unit; (b) W-E lithological section A-B via borehole MN-4. (Ezersky et al., 2013a, permission of EAGE)

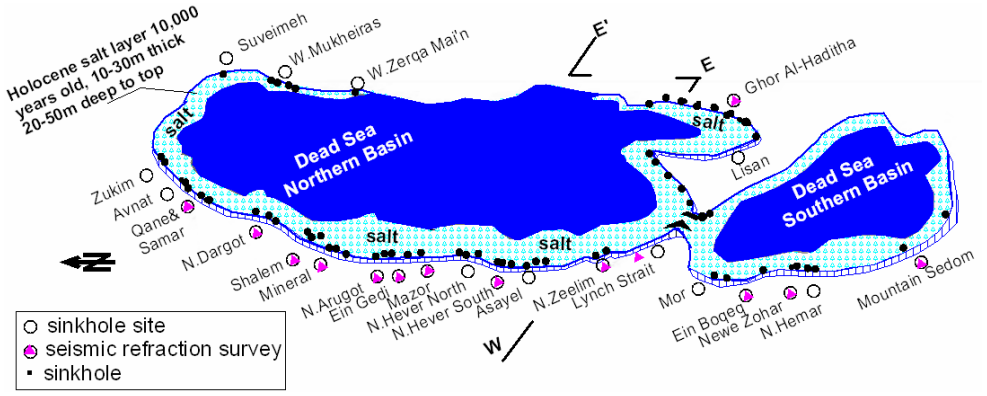

Figure 32. Hypothetic salt distribution around the Dead Sea at the elevation of -415 ÷ - 445 m where the salt layer was formed in latest Pleistocene (Ezersky et al., 2013b, permission of Springer). Sinkholes at the north-eastern shore and at Ghor Al-Haditha are given after Closson and Abu Karaki, (2009) and Frumkin et al. (2011)

3.2.3.5. Structural hypothesis.

We have analyzed the sinkhole distribution along the western DS shore in relation to the DS contour line at -400m (b.s.l.) and the main margin faults (Fig. 29c). From Fig. 29c one can see that, in general, the western major faults, DS shoreline and sinkholes are oriented roughly along the same N-S direction. From Fig. 29 it is also evident that the sinkholes deviate from faults to shoreline with an amplitude of hundreds of meters. Some segments of sinkhole clusters can be approximated by straight lines. More detailed comparisons have been presented in Fig. 33a for sinkholes developing through Mineral Beach area and its vicinities (Israel) and Fig. 33b for Ghor Al-Haditha (Jordan). Abelson et al. (2006) suggested parallelism of sinkholes and marginal faults through the Mineral Beach area (Fig. 33a). In addition, Closson and Abu Karaki (2009) compared sinkhole lineaments in the Ghor Al-Haditha with deep faults (Fig. 33b). However, recent sinkhole development along Mineral Beach area does not support this 'structural hypothesis': while prior to 2006 the Mineral Beach sinkhole line appeared to be parallel to lineaments and faults (Fig. 33a) today the sinkholes line extends eastward (Fig. 31d) along the salt edge, as delineated by a seismic refraction survey (Frumkin et al., 2011), deviating from the faults which propagate northward. Considering Fig. 33b one can see that also in Jordan, sinkhole arrangement 'along the main boundary faults' is only approximate. In fact, the sinkhole line diverges from the West Dhira fault in Ghor Al-Haditha by 18°, and the southern

sinkholes are 1-1.5 km away from the fault. Closson and Abu Karaki (2009) try to support their theory also by stress analysis (Fig. 33c).

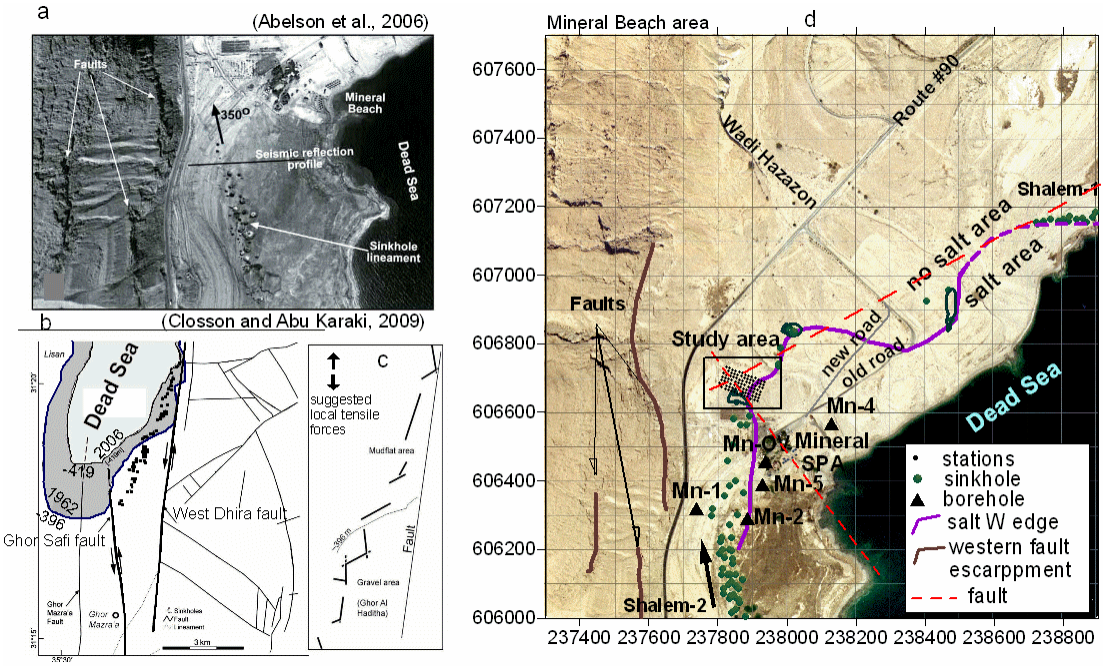

Figure 33. Sinkhole lineaments (a) in Mineral Beach (Abelson et al., 2006; Permission of AGU); (b) in Ghor Al-Haditha (Closson and Abu Karaki, 2009; Permission of Wiley & Sons); (c) tectonic interpretation of Ghor Al-Haditha sinkholes; (d) Recent spatial development of sinkholes in Mineral Beach. 3D seismic reflection layouts and concealed faults are shown in the study area.

However, attempts to link sinkholes with tensile stresses fail because sinkholes are located within the graben area in clastic sediments, which hardly keep or transfer stresses;

3.2.3.6. Combined model.

On one hand, the structural model is based on visible coupling of sinkholes and faults, existence of neotectonic faults in the close vicinity of sinkholes, and plausible scenarios of sinkhole formation via salt dissolution by under-saturated water reaching the salt via faults. Stated this way, the structural model ignores any connection of sinkholes with ancient or modern DS shores. On the other hand, the salt edge model based on geophysical studies substantiates sinkhole formation along a dissolution front in the salt zone close to the salt edge. In places, sinkholes propagate along this edge occupying the space between existing ones like in the Ein-Gedi – Arugot area (Ezersky et al., 2013b). In some places this zone gradually widens as in Mineral Beach (Frumkin et al., 2011) or advances to the DS direction like in the north of Ghor Al-Haditha (Frumkin et al., 2011; Ezersky et al., 2013b). The dissolution front model considers the salt edge as forming along the ancient DS shore and connects sinkholes with this shoreline.

To reconcile the two approaches we suggest a combined model of sinkhole formation comprising elements of both structural and salt edge models. Considering Fig. 30 one would suggest that in some places the walls of sediments constraining the salt edge were originally determined by active normal fault plains (Gardosh et al., 1990). In such segments, lacking large wadies (ephemeral streams), the salt edge may follow fault plains and, subsequently, sinkhole arrangement along the salt edge also follows faults. The 3-D seismic reflection (Fig. 21) shows that the salt layers can subside along these faults causing displacements of tens of meters. Within the dissolution front zone, faults and fractures may enhance the access of aggressive water into the salt, determining the spatial distribution of sinkholes of the salt edge zone.

Where large wadies flow into the DS, the shoreline is usually constrained by alluvial fans. Along these segments the present- and paleo-shoreline deviate from the fault lines, curving according to the fan topography. The salt edge, determined by the latest Pleistocene shoreline, curves accordingly,

establishing the spatial location of the modern sinkholes. The Mineral Beach study site supports the combined model: while the pre-2006 sinkhole line followed a NNW-trending salt edge pre-determined by a fault lineament, the recent sinkhole line develops eastward along the salt edge segment pre-determined by the Nahal (wadi) Hazazon alluvial fan (Fig. 33d). The dissolution front at the salt edge is karstified by undersaturated groundwater arriving from both deep and shallow sources.

The study of Stein et al. (2010) seems to support the **c**ombined model. These authors analyzed boreholes along the DS western shores (Fig. 34). Taking into account that the salt layer formed at approximately the same time by evaporation of DS water (Fig. 30) the upper surface level of the salt layer throughout the DS area should have been roughly similar, possibly with some initial dip. The relatively rapid deposition rate of salt would compensate for varying topography. Today, the salt layer top is found at different elevations varying in the range of 24 m (from -418 to -442 m). Moreover, boreholes drilled in the Ein Gedi site show that the difference in the salt top elevation near the salt edge (EG-7) and close to the DS shore (EG-17) amounts to 17 m per 350 m distance (i.e. 2.8^{o} lakeward inclination of the salt layer) (Ezersky et al., 2013b, Fig. 2). The level difference between boreholes may be due to normal faults moving horizontal blocks without inclination (Abelson et al., 2006). However, a TEM study carried out in the Nahal Hever South site with 50 m distance between sounding points supports the hypothesis of inclination rather than subsidence of blocks along normal faults (Ezersky et al., 2011, Fig. 11).

Based on these data one can suggest that the salt unit subsides with different rates along the boundary faults as shown in Fig. 30, whereas salt inclination is caused by tilting of the tectonic blocks (Garfunkel, 1997). Indeed, Garfunkel and Ben-Avraham (1996, p.155) note that "at any time large part of the basin subsides simultaneously, but the site of fastest subsidence seems to have shifted northward". At the same time, central parts of the DS subside more intensively (Garfunkel, 1981). The main reason for subsidence is the pull-apart origin causing widening of the basin (Garfunkel, 1981, 1997; Garfunkel and Ben-Avraham, 1996). We suggest that a greater subsidence rate would accommodate for a thicker salt layer ("*g*" in Fig. 30c). Post-depositional subsidence and basinward tilting would further depress the salt surface elevation ("*E*" in Fig. 30c). If our suggestion is right, then salt thickness (Fig. 30c) is a rough measure of subsidence rate. In addition, an anti-correlation would be expected between salt thickness and its elevation. Indeed, Fig. 34 demonstrates an anti-correlation

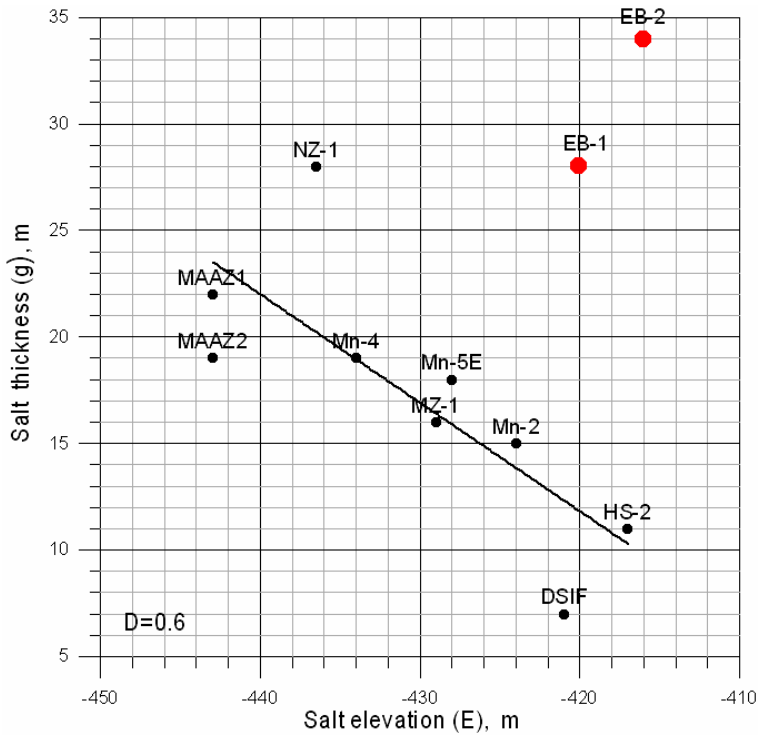

Figure 34. Anti-correlation between salt layer thickness and salt top elevation in boreholes along the western DS shore. Exceptions are boreholes in the shallow southern DS basin (EB-1, EB-2, NZ-1, see text).

between salt thickness (*g*) and salt top elevation (*E*) for 80% of the drilled boreholes. Exceptions are boreholes in the southern DS basin (EB-1, EB-2, NZ-1). This is explained by the shallow water depth

of the south basin which intermittently may become a lagoon, turning into a separate lake, and then a playa, a sequence which promotes rapid salt deposition. The relationships presented in Fig. 34 thus support our suggestion. The suggested model explains why sinkhole arrangement is roughly linear along the salt edge, sometimes also following faults. The dissolution front along the DS shoreline is a 60-100 m-wide strip adjoining the salt edge. Within this strip, individual sinkholes often grow, ultimately coalescing and becoming elongated dissolution troughs. Depending on local conditions, the dissolution front either stays along the salt edge, widens, or gradually migrates laterally towards the DS direction. Spatial W-E oscillations of the sinkhole trough along the salt edge (Fig. 29c) support the combined model for the origin of the sinkholes.

3.2.3.7. Conclusions on Section 3.2.3

Results of a geophysical study of sinkhole development sites in the Dead Sea coastal area in Israel and Jordan are presented. Relations between sinkhole lineaments, salt edge and faults have been studied using new imaging methodology. It is shown that sinkhole lineaments are arranged along the salt layer edge acting as a dynamic dissolution front. We suggest that superficial coastal basins where salt formed could be generated by sub-vertical displacements along faults. This reconciles the two major competing models of sinkhole formation: the structural model, considering control of faults, and the dissolution front model associating sinkhole formation with the salt edge. The combined model suggests that the salt layer edge follows a paleo-shoreline, ~10.5 ka old, constrained by faults and alluvial fans. The sinkholes develop along the dissolution front, controlled by these features. The buried salt layer extends landward, away from the modern Dead Sea shoreline, permitting its investigation from the surface.

3.2.4. Mapping of groundwater salinity (aggressiveness) using TEM method

(This issue is presented in details in the current report Ezersky and Levi, 2013; Levi et al., 2011, Ezersky et al. 2011 and has been prepared for publishing)

3.2.4.1. Introduction

Most researchers associate the sinkhole phenomenon with the formation of dissolution cavities within 10-30m thick salt layers located at depths of 25-50m with consequential gradual collapse of surface sediments. The continuous drop of the DS level at a rate of 1m/yr is generally proposed as the main triggering factor. The lowering water table induces the desaturation of shallow sediments overlying buried cavities. Both the timing and location of sinkholes suggest that the salt weakens as a result of increasing circulation of unsaturated (with respect to halite) water, thus intensifying the karstification process**.** The drop in the DS level allows the incursion of relatively fresh groundwater into the coastal aquifer (Yechieli et al., 2002). Indeed, when the DS level was of high salinity ground water was similar in composition to the DS water, with total dissolved solids (TDS) of 340g/l. DS water also has very high chloride (Cl^-) concentration (up to 224g/l), which constitutes 98% of the anions, with little sulfate and carbonate. Chloride concentration is therefore the main parameter used to characterize ground water (Yechieli, 2000). Migration of fresh or unsaturated (in relation to Cl^-) groundwater into the coastal area has caused different ecological changes via variation of the groundwater salinity causing dissolution of the buried salt layers. A similar effect can be caused by the planned Peace Conduit intended to transfer water from the Red Sea to the Dead Sea (Gavrieli et al., 2002). Thus, estimation of the groundwater salinity and its monitoring is of a high importance to the sinkhole problem.

Evaluation of water salinity is undeniably a worldwide problem, especially in coastal countries, because an intrusion of salt water from the sea into the mainland significantly deteriorating fresh water quality (Goes et al. 2009). Evaluation of water salinity is mainly based on the interpreting of bulk resistivity of aquifers measured by surface geoelectrical methods using either methods of direct current, e.g. the Vertical Electric Sounding (VES) (Kirsch 2006, Koefoed, 1979) or the Time Domain Electromagnetic (TDEM) also called Transient Electromagnetic (TEM) soundings (Fitterman and Stewart, 1986; Mills et al. 1988). Use of resistivity methods for estimation of water salinity is based on the dependence of the bulk resistivity (ρ_x) of the aquifers on resistivity of fluid filling its pores (ρ_w) and porosity (ϕ). This dependence is expressed by Archie's Law (Archie 1942) that we will

consider later. Yechieli et al. (2001, p.373) correlated bulk resistivity with groundwater chloride concentration in boreholes of the Dead Sea area. They have concluded that in cases of higher salinity, this correlation is a better indication that groundwater salinity is the main factor governing the TDEM resistivity, regardless of differences in the other factors such as lithology and porosity.

The TEM method is routinely used in Israel for locating the fresh-saline water interface in coastal areas of the Mediterranean, Red, and Dead Seas to delineate salt water intrusions into coastal areas (Goldman et al., 1991). Different classifications based on bulk resistivity of aquifers have been suggested to estimate water salinity in sandy-gravel aquifers (Kafri et al., 1997, Yechieli et al., 2001). Recently, TEM FAST methodology based on the use of corresponding portable equipment (Barsukov et al., 2007), has been applied in the sinkhole development areas along the DS shores for studying water salinity (Ezersky et al. 2011, Legchenko et al. 2009). A substantial feature of the geoelectrical structure of the subsurface throughout the DS coastal area is very high resistivity contrast between sandy gravel sediments (units and decades of Ωm) above and below the water table, (some tenth portion of Ωm) (Yechieli, 2000).

There are different possibilities for estimating groundwater salinity in the DS area using geoelectrical methods. They are based on: (a) qualitative characterization of the water salinity after Kafri et al. (1997), (b) combine use of TEM and other geophysical methods, for instance, Magnetic resonance sounding (MRS) (Legchenko et al., 2009) and (c) direct resistivity-salinity calibration (Kafri and Goldman, 2006, Yechieli et al., 2001).

(a) Qualitative estimation of the groundwater salinity is based on the finding of Kafri et al. (1997), who have established that bulk resistivity lower than $1\Omega m$ unambiguously defines the presence of DS brine in the pores of alluvial sediments without respect to any lithology. Respectively, pores of sediments with bulk resistivity of less than $1\Omega m$ are filled with the DS brine. Based on electrical resistivity measurements, Kafri et al. (1997) suggested the following classification for sediments located under water table in the DS coastal area: (1) very saline water (brine), with the resistivity of $\rho < 1\Omega m$ (eastern most zone nearest to the DS); (2) less saline (brackish) water, with the resistivity of $\rho_x > 3\Omega m$ (western most area from the DS); and (3) diluted brine, with the resistivity of $1\Omega m < \rho < 3\Omega m$ (intermediate zone between the two mentioned above).

(b) Use of the TEM-MRS combined methodology has allowed comparative estimation of the water resistivity in relation to lithology. TEM is known as an efficient tool for investigating electrically conductive targets like saline water, but it is sensitive to both the salinity of groundwater and the porosity of rocks. MRS, however, is sensitive primarily to groundwater volume but it also allows delineating lithological variations in water-saturated formations. MRS is much less sensitive to variations in groundwater salinity in comparison with TEM. It was shown that MRS enables us to resolve the fundamental uncertainty in TEM interpretation caused by the equivalence between groundwater resistivity and lithology (Legchenko et al., 2009).

(c) In the Dead Sea region, an empirical correlation between the groundwater resistivity ρ_w, and the chloride concentration (or total dissolution solid – TDS) was established by Yechieli (2000) and Kiro (2007). Authors found the relationship between water resistivity (conductivity) and water salinity for the sandy sediments based on laboratory measurements of the DS water samples diluted by the distilled water. Kafri and Goldman (2006) have found an empirical correlation between the bulk resistivity of the rock ρ_x and the chloride concentration. They also suggested the empirical Archie's law expression to connect ρ_x, ρ_w, and porosity ϕ for sandy sediments located under the water table (Kafri and Goldman, 2005).

Nevertheless, there are some aspects that require additional studying.

(1) The sinkhole development takes place through complex areas composed of two parts:
(a) areas (adjoined to the DS) including 5-30m thickness salt layer located at the depth of 25-50m from surface (Ezersky et al., 2010, 2013a; Frumkin et al., 2011); and
(b) areas composed of alluvial sediments located west to salt in Israel and east of that in Jordan. In accordance with our model sinkhole formation takes place at the boundary between both them, forming the salt dissolution front (Ezersky and Frumkin, 2013). It requires new approach to the mapping of aquifers using TEM resistivity method.

(2) The boreholes previously used for the calibration of TEM results in the Dead Sea region were mainly located several kilometers away from the shoreline (Yechieli et al., 2001). The range of

the resistivity-salinity relationships begins from $1\,\Omega m$ (Kafri and Goldman, 2006), whereas at the area of interest a bulk resistivity of sediments starts at $0.2\,\Omega m$. Therefore, more accurate calibration of TEM data is required for interpreting TEM resistivity in terms of groundwater salinity in the coastal area of the DS. Note also that salt dissolving in the sinkhole development area takes place at very low (ρ_x = 0.5-0.6 Ωm and even lower) bulk resistivities of groundwater enveloping the salt layer from above and from below (Ezersky et al. 2011, Yechieli et al. 2006). It means salt is dissolved by the DS brine. This phenomenon should be understood.

The main goal of the study is evaluation of the groundwater salinity based on surface measurements of the bulk resistivity to evaluate sinkhole hazardous zones.

Objectives of the study are, respectively:

- mapping of aquifers bringing groundwater to salt layers and evaluation of their salinity;
- generating relationships between groundwater salinity and resistivity based on resistivity-salinity calibration near boreholes;
- search the criteria on water aggressiveness with respect to buried salt layers.

The objectives of the study are resolved based on (a) mapping of sinkhole development areas using TEM method in its sounding mode; and (b) resistivity-salinity calibration near boreholes.

3.2.4.2. Hydrogeology

According to Yechieli et al. (2006), three main aquifers draining into the DS can be distinguished in the area to the west of the DS. Two of them, which extend far beyond the DS area, include the sandstone Kurnub aquifer of Lower Cretaceous age, and the limestone and dolomite Judean aquifer of Upper Cretaceous age. The aquifer formed by Quaternary alluvium is confined to the DS rift, bounded to the west by its marginal faults. Alternating clays and gravels within the alluvial sequence create several sub-aquifers with different heads and water compositions. The Quaternary aquifer derives most of its water through lateral flows across the rift faults from the Judea Group aquifer, which is recharged over the mountain terrain, some 20-50km to the west. Direct recharge to the aquifer over the alluvial segments is negligible because of the extreme aridity of the region (Yechieli et al., 2006).

3.2.4.3. Archie's Law

In sandy aquifers the resistivity of the subsurface, generally depends on several parameters, most important of which are salinity of the fluid in the pores and porosity. Quantitative interpretation of the results is based on *Archie's Law* (Archie 1942, Keller and Frischknecht 1966), which establishes that in saturated geologic materials with conductive water in the pores, bulk electrical resistivity depends on the porosity, and the resistivity of the pore fluid. In this case bulk resistivity is expressed as:

$$\rho_x = a\rho_w\phi^{-m} \qquad (6)$$

where ρ_w is the resistivity of the solution filling the pores, and ϕ is the porosity. Parameters a and m depend on the geometry of the pores. Writing (6) in the other form (ρ_w / ρ_w) = $a\phi^{-m}$ Archie's Law states that ρ_w / ρ_w ratio (named also *formation factor F*) is constant at constant porosity. Expression (6) can be further simplified if we accept a=0.81 and m=2 for sandy aquifers (Kafri and Goldman, 2005):

$$\rho_x = 0.81\rho_w\phi^{-2} \qquad (7)$$

Note that (7) does not relate to specifically DS coastal area. It follows from equations (6 and 7) that there is direct dependence connecting ρ_x measured by the TEM method with ρ_w. The latter is the function of the water salinity as measured by chloride concentration or total dissolved solids (TDS) (Keller and Frischknecht, 1966). This relationship allows interpretation of bulk resistivity in terms of salinity. It follows also from the above equations that it is impossible to use only TEM measurements for determining both the water resistivity and porosity (ϕ). Usually, parameters ρ_w and ϕ are not known, and one of them is assumed to be constant throughout the investigation area. When this assumption is not true, some additional information about the geological formation (for instance, from boreholes) is required for correct interpretation of TEM data. To resolve the problem, attempts are made to combine the geoelectrical methods with MRS (Legchenko et al., 2009) one and borehole logging (Yaramanci et al, 2002).

3.2.4.4. The TEM method

The Transient Electromagnetic (TEM) method (also referred to as the Time Domain Electromagnetic method) is sensitive specifically to bulk resistivity (conductivity) of the studied medium, especially in the range of low resistivity. The TEM method has been used for vertical sounding. A procedure involves laying a square loop in the vicinity of the borehole to be examined and performing sounding (McNeill, 1980a). In our study coincident loop configuration was used when the same loop serves both as transmitter (Tx) and as receiver (Rx) (Barsukov et al., 2007). Ideally 3D measurements should be performed. But the necessary technology is still under development, and both fieldwork and data processing are very expensive. In our case, dimensional multi-soundings (*quasi* 3D) served as a substitute for 3D measurements, and results must be interpreted with some caution.

In the coastal DS areas loop were used. Since 2005 we have used the TEM FAST 48HPC system with a single (coincident) Rx/Tx loop of 25 x 25m^2 and 50 x 50m^2 square (AEMR, Netherlands). Detailed description of the TEM equipment is given by Barsukov et al. (2007). Examples of practical use in the DS coastal area have been described by Ezersky et al. (2011). Two interpretational 1D inversion software packages are used. The IX1D software (Interpex, 2006) is considered to be the standard software for interpreting Geonics TEM data. The TEM-RESEARCHER was designed for interpreting TEMFAST data (TEM-RESEARCHER, 2005). Such a combination enables taking advantage of the IX1D software and ensuring that TEM FAST data are correctly inverted. Our experience shows that both software packages provide very similar results whether used for Geonics or TEMFAST data (Ezersky et al. 2011).

We will consider how selection of the multi-layered model affects result of inversion using TEM sounding carried out at the 11-10 TEM station in the NHS site in comparison with the HS-2 borehole in Fig. 35. We have inverted TEM data for 3 to 7 layered models. Results of inversion are presented in Figs. 35b to 35f, respectively).

One can see in Fig. 35 following regularities:

a) A depth to $1\,\Omega m$ interface (h_L) is very stable and it varies in range of $19.5 \pm 0.6m$;

b) Resistivity of the deepest part of the resistivity-depth function (at late time) is also stable ($\rho_{L2} = 0.3\,\Omega m$) for 4-7 layered models with RMS = 2.06-2.84% (Figs. 35c - 35f), whereas 3-layered (most rough) model in Fig. 35b (RMS=7.03%) shows $\rho_L = 0.55\,\Omega m$ at the same time range.

c) Salt layer with resistivity ρ_{L3} is seen well at 5-7 layered models in Figs. 35d - 35f (RMS = 2.84-2.06%). It is best fitted to the salt layer location (24-35m) at the 6-7-layered models (RMS = 2.06-2.08%)

d) We are interested in assessing resistivities of layers enveloping the salt layer. They are ρ_{L1} and ρ_{L2} in Figs. 35d and 35e and ρ_{L4} and ρ_{L2} in Fig. 35f. Resistivity of the layer underlying the salt is very stable $\rho_{L2} = 0.3\,\Omega m$. Resistivity of the layer overlying the salt from above is $\rho_{L1} = 0.3\,\Omega m$ (in

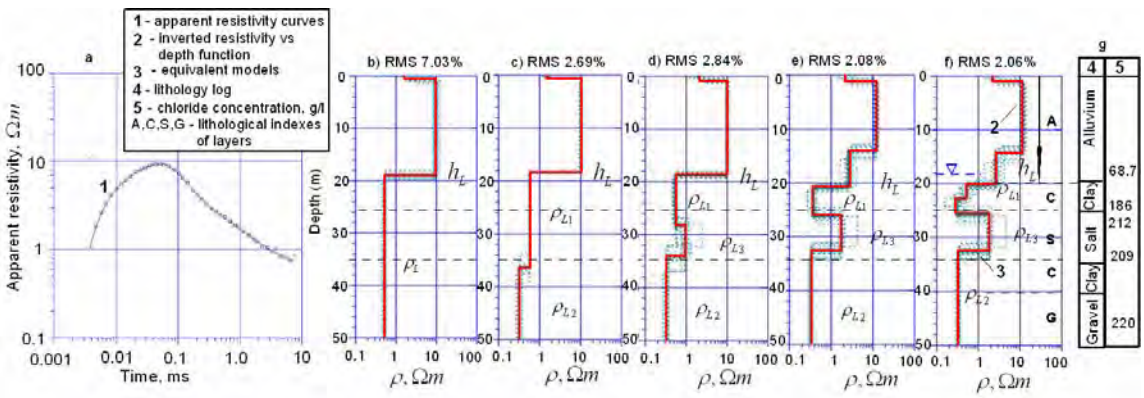

Figure 35. Resistivity vs. depth functions for different multilayered models at the 11-10 TEM station in the Nahal Hever Site. (a) transient curve; (b – f) – consequent increase of the number of layers from 3 to 7 ones, respectively; (g) lithological column (4) and chloride concentration (5); RMS – root mean square error.

Fig. 35d) and ρ_{L4} = 0.3 Ωm (in Fig. 35e). At the same time 4- and 5-layered models presented in Figs. 35c and 35d, respectively, show ρ_{L1} = 0.5 Ωm .
Thus, interpretation of the TEM soundings is generally stable in determination of a depth to 1 = 0.5 Ωm interface (h_L) and resistivities (ρ_L) under water table at late times. It, nevertheless, would insert a mistake at wrong interpretation of the intermediate layers.

3.2.4.5. The new approach of TEM mapping

Let us consider the typical 2D model of sinkhole development areas (Fig. 36). One can divide the model section by two parts. The right part of the section comprises the salt layer (with bulk resistivity ρ_x=1.5 Ωm) enveloped by very low resistivity sediments from above and from below overlain from above by high relatively resistivity (10 Ωm) layer. The red line in Fig. 36a is the interface separating as a rule alluvium above water table and below that. Because groundwater is DS brine bulk resistivity sharply drops at this interface from 2-20 Ωm to significantly less than 1 Ωm. Fig. 36c presents inverse resistivity section obtained at the TEM2 station. Left of salt alluvial sediments are located containing the DS brine filling pores. It results in low resistivity (0.5 Ωm) of second layer. The inverse resistivity section obtained at the TEM1 station is shown in Fig. 36b.
Knowing the salt edge location in-situ we can select model for inversion of TEM sounding data. If we will map area using TEM without knowledge salt layer border we can to reveal inverse resistivity section shown in Fig. 36d.

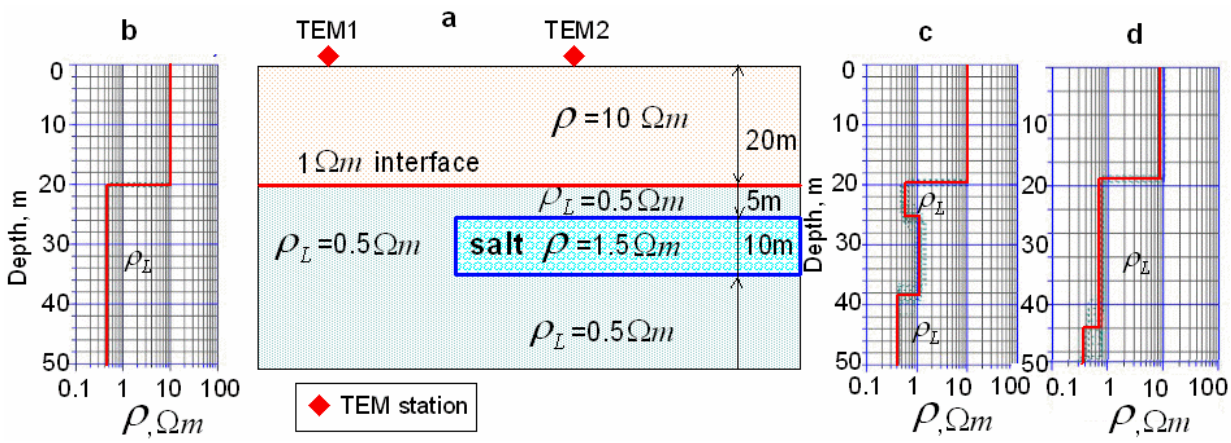

Figure 36. (a) Resistivity model of the subsurface comprising four layers; (b) inverse resistivity section measured at the TEM1 station; (c) and (d) four-layered and three-layered inverse resistivity sections measured at the TEM2 station.

The resistivity of aquifer (0.7-0.8 Ωm instead 0.5 Ωm) will result in no corrected resistivity (and consequently, salinity) of the aquifer. In addition, any no saturated water coming to the salt area and enveloping the unit will be very quickly saturated dissolving salt (Frumkin, 1994). Therefore the conclusion following from this example is that more exact resistivity mapping of aquifer can be performed away from the salt area, whereas mapping of salt area enables to reveal very important parameters of the salt layer (e.g. depth to salt top, salt layer thickness and its resistivity) to interpret salt layer conditions (Ezersky et al., 2011; Frumkin et al., 2011; Levi et al., 2011).
In accordance with mentioned above the new approach is based on the separate processing of the TEM data for salt and aquifer areas. It allows (a) accurate measurements of bulk resistivity of both salt and aquifer; and (b) avoiding 3D effects possible in the vicinity of salt. At first, the salt is delineated using seismic refraction method (Ezersky, 2006). It enables to separate the area into two sites of investigation: (1) “salt” area, where the measured resistivity is influenced by the salt porosity (estimated from the Archie’s law) (Frumkin et al., 2011) and (2) “no-salt” area, where the measured resistivity is influenced by the groundwater salinity (Levi et al., 2011). The evaluation of ground water salinity we will consider in continuation. The example of TEM mapping carried out through the Mineral Beach area is shown in Fig. 37. The salt layer edge (solid lilac line) has been determined using seismic refraction method (Ezersky, 2010).

Mapping the “no-salt area” (Fig. 37a) shows the high relatively (for the DS shore areas) resistivity of the clastic sediments (0.6-0.75 Ohm-m) along the salt edge. Such resistivity can characterize the saline groundwater with a chloride concentration of 60-100 g/l compare to 224 g/l at saturation.
The results of mapping of the "salt area" (Fig. 37b) characterize three zones based on their resistivity; the zones are in a good agreement with the distance from the Dead Sea shore:

1. Resistivity up to 0.5 Ohm-m: found far from the Dead Sea, near the salt edge. The zone is not regular and is associated with a salt karst. Sinkhole formation in these zones is the most probable.
2. Resistivity of 0.5-1 Ohm-m: intermediate zone with increased porosity.
3. Resistivity of more than 1 Ohm-m: found close to the shore, this is the background porosity. The map of the salt top surface shows deepest position in the central part of the area (-434 m) and it becomes shallower at the margins of the studied area (-424 m).

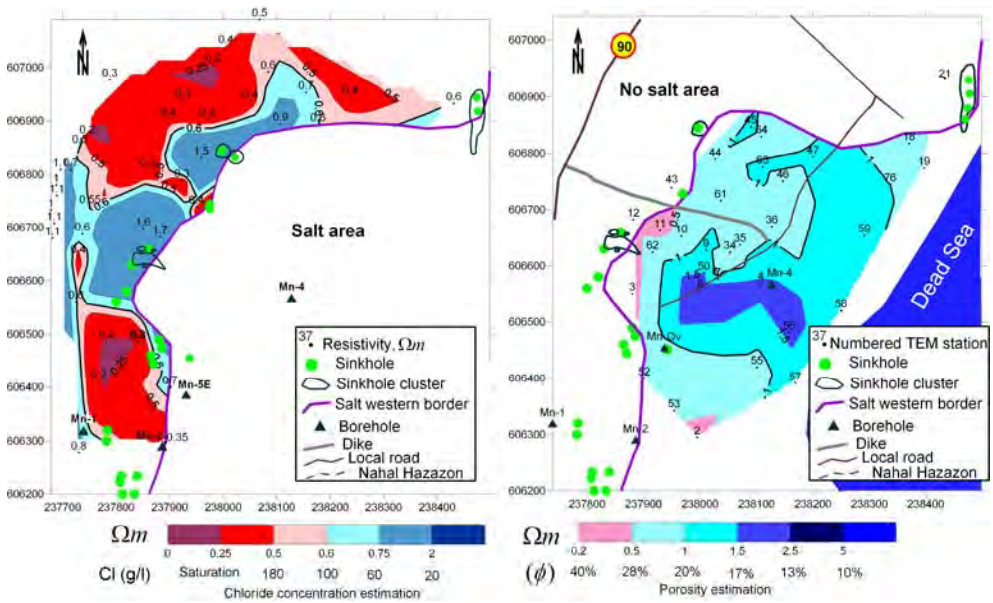

Figure 37. Two resistivity maps through the Mineral Beach area generated separately for aquifer (a) and salt layer (b) respectively, west and east of the salt layer border (purple line). Corresponding palettes connecting resistivity to chloride concentration and estimated porosity (%) are presented under maps. Red areas in the left map are zones of high chloride concentration whereas blue zones are zones of the unsaturated brine keeping potential to dissolve salt. The right map shows average resistivity and distribution of the salt layer through the Mineral Beach area.

3.2.4.6. Resistivity-salinity calibration near boreholes

We have compiled the relationships between water resistivity and chloride concentrations based on borehole measurements. Twenty eight observation boreholes have been drilled by the GSI along the DS and at the Evaporation ponds (EPs) coastal area (Yechieli et al., 2004). These boreholes are located in eight sites most of which are facing the sinkhole problem. Eighteen boreholes were studied previously. To correlate salinity and bulk resistivity we have added in framework of MERC project TEM soundings near 9 boreholes drilled in the high conductive sediments ($\rho_x < 1\,\Omega m$) where water salinity was determined by the Geological Survey of Israel (GSI) (Yechieli et al. 2004; Yechieli 2007). Location of all calibration boreholes is presented in Fig.38b and c.

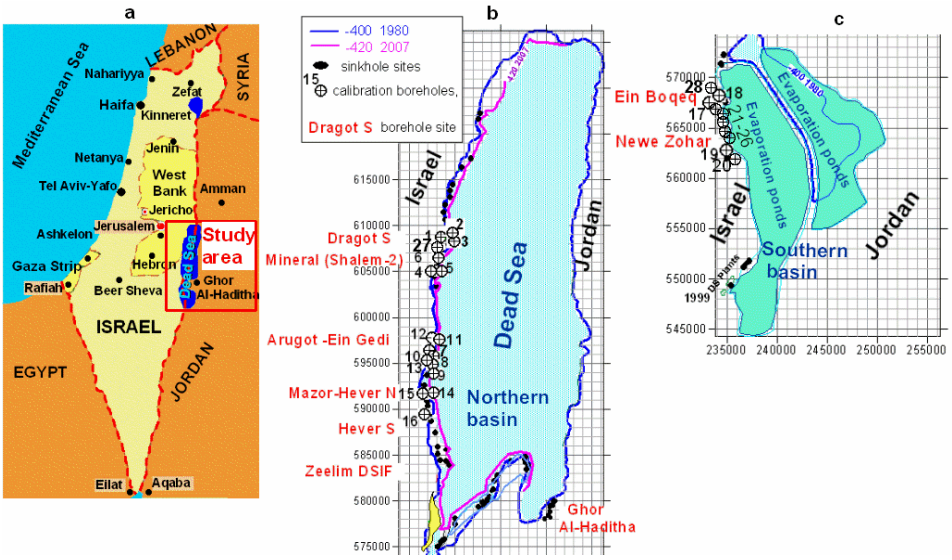

Figure 38. Location map of the study area (a); and calibration boreholes along the western DS shore: (b) northern basin and (c) southern one (Evaporation ponds). Black circles designate the calibration boreholes numbered as: 1 – Dr2, 2 – Dr3, 3 – Dr4, 4 – Mn1, 5 - Mn2, 6 – Mn4, 7 – EG6, 8 – EG7, 9 – EG11, 10 – EG13, 11 – EG17, 12 – EG18, 13 – EG19, 14 – Mz1, 15 – Mz2, 16 – HS2, 17 – EB1, 18-EB2, 19 – NZ1, 20-26 – NZ3-NZ9, 27 – Mn-5E, 28 – EB-3E

3.2.4.7. Water Resistivity – Salinity relationship

In the northern DS basin the chloride concentration at the saturated condition is 224g/l and in the southern EPs one – 259g/l. At the depth range corresponding to the salt layer (20-60m) the majority of these boreholes revealed groundwater salinity between 54% and 93% of chloride saturation. Only three of twenty eight boreholes (all of them located in the Ein-Gedi-Arugot area) have discovered groundwater with relatively low salinity 15-70 g/l of the chloride concentration (7-33% of the saturation).

Examples of TEM measurements performed near two boreholes are shown in Fig. 11f (Mn-5E) and Fig. 12f (EB-3E). The chloride concentration in the groundwater (mg/l) from closely (50m apart) located boreholes is presented in the left column of the geological sections. The inverted resistivity versus depth graphs derived from TEM measurements are shown with solid lines. A few equivalent solutions are presented by thin dashed lines. Temperature of the water is of $29 \pm 2^{o}C$.

Experimental relationships between ρ_x, ρ_w and C_{Cl} are presented in Fig. 39. We observe a generally good correlation between water resistivity ρ_w and the chloride concentration (blue crosses). Two segments of the correlation curve (1a and 1b in Fig. 39) could be distinguished. One segment corresponds to a high chloride concentration (87,700-220,000 mg/l) and another to a low concentration (<87,700mg/l). For these segments the chloride concentration (C_{Cl}) is correlated with the water resistivity by equation (based on data of Yechieli et al. (2004)):

$$C_{Cl}[mg/l] = \rho_w^{-1.229} \times 3018.6\ [\Omega m] \qquad for \quad C_{Cl} < 87{,}700[mg/l]$$
$$C_{Cl}[mg/l] = \rho_w^{-2.98} \times 23.35\ [\Omega m] \qquad for \quad 87{,}700 < C_{Cl} < 200{,}000\ [mg/l] \tag{8}$$

(Coefficients of correlation R^2 = 0.995 and R^2 = 0.96, respectively). Equation (8) allows estimation of the chloride concentration using the resistivity of groundwater ρ_w.

Equations (8) for low and high chloride concentration are equal at $\rho_w = 0.065\,\Omega m$ and chloride concentration C_{Cl} = 87,700mg/l. This point (curves 1a and 1b in Fig. 39) is accepted as the boundary between two branches of the equation (8).

3.2.4.8. Bulk Resistivity salinity relationships

Graphs (1a, 1b) are presented in Fig. 39 together with relationships between chloride concentration C_{Cl} and bulk resistivity ρ_x (based on TEM measurements) for different soils basically composed of clay and sand (curves 2 and 3-4, respectively).

- Brown triangles (2) characterize soil of clayey lithology (lime carbonate). This group comprises the boreholes Mn-1, Mn-2, Mn-4, Nz-1 – NZ-9, HS-2. The TEM derived bulk resistivity for clayey soils is of 0.2-0.4 Ωm.

$$C_{cl} = \rho_x^{-1.558} x 29234.11, \quad R^2 = 0.61 \qquad (9)$$

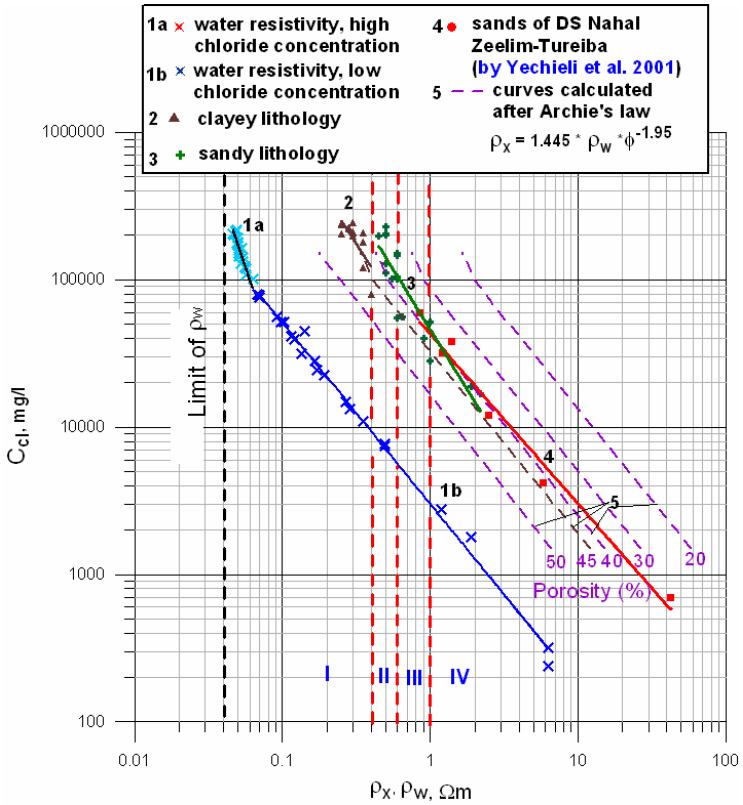

Figure 39. Various inter-relations between chloride concentration and resistivity: (1a, 1b) high and low, respectively, chloride concentration in pore water (fluid) vs. water resistivity ρ_w in boreholes (based on GSI data, Yechieli et al., 2004); (2) bulk resistivity ρ_x vs. chloride concentration in clayey soils (lime carbonates); (3) the same in sandy lithology, in saturated sediments; (4) calibration points by Yechieli et al. (2001); (5) dashed lines are calculated graphs based on Archie's law (see in continuation). Parameters of curves present porosity (in %).

- Green stars (3) correspond to sandy sediments in the relatively deep part of boreholes (at late time of transient), saturated by the DS brine with Cl concentration of 60,000-200,000 mg/l. These sediments have the resistivity of 0.5-2.0 Ωm.

$$C_{cl} = \rho_x^{-1.628} x 46167, \; R^2 = 0.83 \qquad (10)$$

These data have been aided by measurements of M. Goldman (4) obtained along DS (Nahal Zeelim) - Tureiba profile (Yechieli et al. 2001). However, inclination of the fit graph is slightly changed in accordance with 1a curve.

$$C_{cl} = \rho_x^{-1.121} x 39946, \; R^2 = 0.98 \qquad (11)$$

One can see that both lime carbonates and sandy materials saturated with the DS brine are characterized by very low bulk resistivity (< 1 Ωm). However, depending on the lithology the bulk resistivity of lime carbonates and sands may differ by two times (0.2-0.4 Ωm and 0.5-1.0 Ωm, respectively). Two relationships are presented in conventional mode in Fig. 40. First is the relation between bulk resistivity ρ_x and water resistivity ρ_w (Fig. 40a) and second is the dependence of

formation factor F = ρ_x/ρ_w on ρ_x is shown in Fig. 40b. The first graph allows fitting of ρ_x - ρ_w data to Archie's equation for porosity of sediments of 40% (Fig. 40a) that will be:

$$\rho_x = 1.445\rho_w * \phi^{-1.95} \qquad (12)$$

This expression differed from the similar equation (2) by Kafri and Goldman (2005) that estimates porosity of sandy - gravel sediments as 25-30% (Ezersky et al. 2011), whereas expected estimations of sand porosity are ϕ = 40 $\pm$0.02 (Stephens et al., 1998). .

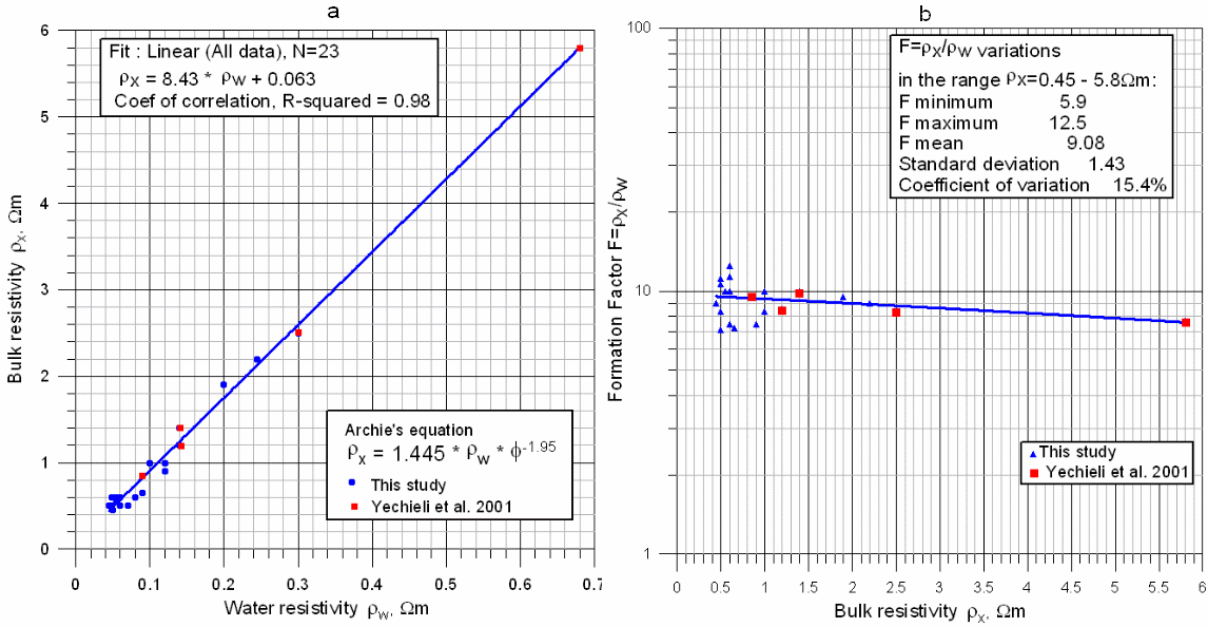

Figure 40. Relationships between (a) water resistivity ρ_w and bulk resistivity ρ_x; and (b) ρ_x and formation factor ρ_x/ρ_w for sandy lithology. Archie's equation shown in window in (a) is fitted to ρ_x - ρ_w data for porosity ϕ = 40%.

The second graph (Fig. 40b) shows the relation between ρ_x and formation factor F = ρ_x/ρ_w for sandy lithology that in the low resistivity range (0.45-5.8Ωm) is stable enough and equal to 8-10. Slight inclination of the graph in Fig. 40b was earlier noted by Keller and Frischknecht (1966, p.23). We have calculated curves porosity C_{Cl} versus ρ_x based on eq. (17) for different porosities of sandy sediments. Calculations are performed in the following order. At first, chloride concentration C_{Cl} is selected in a wide range of values. Then resistivity of water ρ_w is calculated from C_{Cl} using equations (13). Then bulk resistivity ρ_x is calculated using equation (17) for different porosity values. Calculated curves (lilac dashed lines) are presented in Fig. 39 for the porosity values of 20% to 60%. One can see that the graph calculated for ϕ = 40% well approximates experimental data. It seems that data for lime carbonates (2) are approximated by ϕ = 45-50% graph.

The results of calibration are summarized in Table 3. The left part of the Table 3 (columns 1 – 4) show the results of borehole measurements. At that groundwater resistivity ρ_w has been measured either in boreholes or calculated using equations (8). It has been found that in the DS coastal area the typical value of the bulk resistivity in lime carbonates varies between 0.2 and 0.35Ωm (generally, ρ_x < 0.4Ωm), whereas gravel and sandy sediments are characterized by a resistivity between 0.4 and 0.6Ωm (ρ_x > 0.4Ωm). Results of Yechieli et al. (2001), and Kafri and Goldman (2006) expand this range to 6.0 Ωm measured at distance of 3-5km from DS shoreline. At that, measured chloride concentration C_{ClM} is within a range of 101-204g/l (columns 2 and 4 in Table 3). The same follows from graphs (2) and (3) in Fig. 39. It allows distinguishing clayey and sandy sediments saturated with the DS brine based only on the resistivity values.

Table 3. Bulk resistivity of the DS aquifer near the calibration boreholes.

Borehole	Chloride concentration measured in borehole C_{ClM}, g/l	Ground-water resistivity in borehole ρ_w [1,2], Ωm	Bulk resistivity measured with TEM $\rho_x, \Omega m$,	Porosity estimated with TEM $\phi\%$	Formation factor $F=\rho_x/\rho_w$
1	2	3	4	5	7
Sandy soil					
Dr-2	105400	0.06 [1]	0.6	0.37	10
Dr-3 [3]	151800 [3]	0.048 [1]	0.6	0.35	12.5
Dr-4	200000	0.047 [1]	0.5	0.36	10.6
EB-2	230000	0.045 [1]	0.5	0.36	11.1
EG-11	198000	0.050 [2]	0.45	0.39	9
EG-18	101000	0.055 [2]	0.55	0.39	10
EG-17	204000	0.048 [1]	0.5	0.36	10.4
EG-19	147000	0.053 [1]	0.6	0.35	11.3
EG-19	16940	0.247 [1]	2.2	0.39	8.90
NZ-5	231800	0.046 [1]	0.45	0.37	9.8
YS-1	54800	0.095 [1]	0.6	0.47	6.31
T12	60000	0.089 [1]	0.85	0.38	9.6
T1	38000	0.129 [1]	1.4	0.36	10.8
T3	32000	0.148 [1]	1.2	0.41	8.1
T2	12000	0.327 [1]	2.5	0.43	7.64
T4	4200	0.765 [1]	5.8	0.43	7.6
Average	111680	0.141	1.21	0.39 ± 0.03	9.5 ± 1.5
Lime Carbonate					
Mn-1	120	0.055 [2]	0.3	0.52	5.45
Mn-2	205000	0.046 [2]	0.2	0.51	4.34
Mn-4	216000	0.05 [2]	0.25	0.51	5.0
HS-2	208000	0.047 [1]	0.3	0.47	6.4
NZ-3	211000	0.045 [2]	0.3	0.47	6.6
NZ-2	237000	0.049	0.25	0.53	5.1
NZ-3	224200	0.046	0.35	0.43	7.6
NZ-4	245500	0.049	0.25	0.50	5.1
NZ-7	228500	0.046	0.25	0.51	5.4
NZ-8	187800	0.049	0.25	0.53	5.1
NZ-9	209000	0.047	0.32	0.43	6.8
Average	208393	0.048	0.28	0.49 ± 0.04	5.7 ± 0.98

[1]) conductivity of groundwater is based on chloride concentration that was calculated using equation (13) for high concentrations,

[2]) conductivity of groundwater was measured just in borehole

[3]) Site names: Dr – Deragot; Mn – Mineral Beach (Shalem-2); EB – Ein Boqeq, HS – Nahal Hever south, EG – Ein Gedi – Arugot, NZ-Newe Zohar , T1-T12 data from (Nahal Zeelim) - Tureiba profile (Yechieli et al. 2001).

The groundwater resistivity varies between 0.04 and 0.06 Ωm with corresponding chloride concentration in the range of 54% to 93% from saturation. Columns 5 through 7 of the Table 3 present results of calculations using relationships obtained above. Porosity $\phi\%$ (column 5) has been calculated using the formula derived from Archie's equation (12). Note that porosity of 50% for lime

carbonates is supported by our laboratory tests and results reported by WBI (2006, unpublished report).

3.2.4.9. Constructing a salinity map based on bulk resistivity

Really, in-situ we do not know ρ_w and C_{Cl}. It is our target to evaluate these parameters measuring bulk resistivity ρ_x. Measuring bulk resistivity ρ_x we should determine resistivity ρ_w of fluid filling the pores. Such a problem would be resolved using relationships between water resistivity ρ_w and bulk resistivity ρ_x presented in Fig. 40. Relations between those parameters constitute formation factor F that is stable enough in the range of resistivities measured in the DS. As it was shown in Fig. 40b and in Table 3 formation factor of sandy-gravel sediments F = ρ_x / ρ_w = 9.5 $\pm$ 1.5, when ρ_x is ranged from 0.4 to 2.5 Ωm. In lime carbonates this one is 5.8.

We then determine the water resistivity by dividing of ρ_w = ρ_x /9.5 (sandy sediments) and divided by ρ_x /5.8 (lime carbonate) and calculate chloride concentration using equations (8). Let us consider the example mapping of sediments in the vicinity of the salt layer edge in the Mineral Beach area (see Fig. 33b for location) that was selected, as an example of a costal aquifer composed of sandy-gravel sediments. The geology of the site has been presented in the Section 3.1.3. We suggested a new approach based on the separate processing of the TEM data through salt and the aquifer. It allows avoiding 3D effects possible in the vicinity of the karstified salt. After locating the salt layer edge using seismic refraction method (Ezersky, 2006) we can separate the area into two sites of investigation (Fig. 41): (1) “salt” area, where the measured resistivity is influenced by the salt porosity (estimated from the Archie’s law) and (2) “no-salt” area, where the measured resistivity is influenced by the groundwater salinity. The methodology includes fast spacious mapping of the bulk resistivity in both vertical and horizontal directions through the area covering ~1 km^2 (Frumkin et al. 2011).

3.2.4.10. Evaluation of groundwater salinity and aggressivity using bulk resistivity

Evaluation of groundwater resistivity ρ_w using measured bulk resistivity ρ_x is the problem of great importance in predicting sinkhole hazard zones. Classifications available are directed to evaluating the water quality based on water resistivity. For instance, EU-directive of water quality (1998) (referenced by Kirsch, 2006) sets a lower limit ρ_w = 4 Ωm for electrical resistivity of drinking water. Classifications used in Israel (Kafri et al. 1997, Yechieli et al., 2001) consider bulk resistivity of ρ_x =1 Ωm as highest resistivity of DS brine. In accordance with our results presented in Fig. 39 bulk resistivity of 1 Ωm corresponds to a chloride concentration in groundwater C_{Cl} =40,000 mg/l and a water resistivity of ρ_w =0.12 Ωm.

If so much or less in needed to dissolve salt, one can understand comparing this value with maximum chloride concentration that can comprise DS water. We have mentioned above that maximum chloride concentration in the DS water is of 224 g/l in the northern basin and 259 g/l in the southern that (Total Dissolve Solid (TDS) is at 340 g/l and 380 g/l, respectively). It means that 40 g/l chloride constitutes 15% of saturation in the northern basin and 18% of that in the southern one. Thus, evaluating the sinkhole hazard we should operate with parameters of groundwater concentration relative to its maximum possible saturation with chloride. In other words, we have to use C_{Cl} / C_{ClMAX} ratio characterizing the degree of aggressivity of the DS water (where C_{Cl} is measured concentration and C_{ClMAX} is maximum one). Because there is no corresponding classification we suggest our version of groundwater aggressivity classification that presented in the Table 4.

Categories of aggressivity are based on C_{Cl} / C_{ClMAX} ratio. These ratios are added by absolute values of bulk resistivity ρ_x, water resistivity ρ_w and chloride concentration C_{Cl} (in g/l). One can see that groundwater with resistivity range ρ_x < 1.0 Ωm, classified by Kafri et al. (1997) as DS brine in the water quality evaluation, is aggressive with respect to salt dissolving.

Table 4. Groundwater aggressivity with respect to DS salt for sandy soil (ρ_x>0.4Ωm)

Water aggressivity	C_{Cl}, g/l	C_{Cl}/C_{Cl} max ~ (%*)	$\rho_w, \Omega m$	$\rho_x, \Omega m$	After Kafri et al., 1997
Very aggressive	< 40	< 18	> 0.12	> 1.0	diluted DS brine
Aggressive	40 - 95	18 - 40	0.063 – 0.12	0.6 - 1.0	DS brine
Averagely aggressive	95- 135	40 -60	0.055 – 0.063	0.50 - 0.60	DS brine
Slightly aggressive	135 - 200	60 – 90	0.045 - 0.055	0.4 - 0.5	DS brine
Non aggressive	> 200	> 90	<0.045	< 0.4	DS brine
Fresh water	< 0.5g/l	0.2	>4	>45	EU (1998)

*) C_{Cl} max =224 g/l in the northern DS basin and 259g/l – in the southern that. Because saturation rates are not differed significantly, the ratios C_{Cl}/C_{Cl} max are given approximately for both DS basins.

Such groundwater keeps the potential to dissolve up to 180g/l chloride (e.g., to 70-80% of its saturation rate). It is also importantly to notice that even sediments with very low resistivity ρ_x = 0.4-0.5Ωm are staying aggressive with respect to salt. It can explain why sinkhole formation was developed at very low resistivities of sediments (Ezersky et al., 2011).

The results of calibration presented in this paper allows for a new look at sinkhole hazard assessment. Let us consider water resistivity and aggressivity maps of study sites in a light of mentioned above criteria.

Mineral Beach (site II in Fig. 1). We can then generate the maps ρ_w (directly connected with C_{Cl}) throughout aquifer area based on bulk resistivity. These maps are presented in Fig. 41 separately for ρ_x (a) and ρ_w (b).

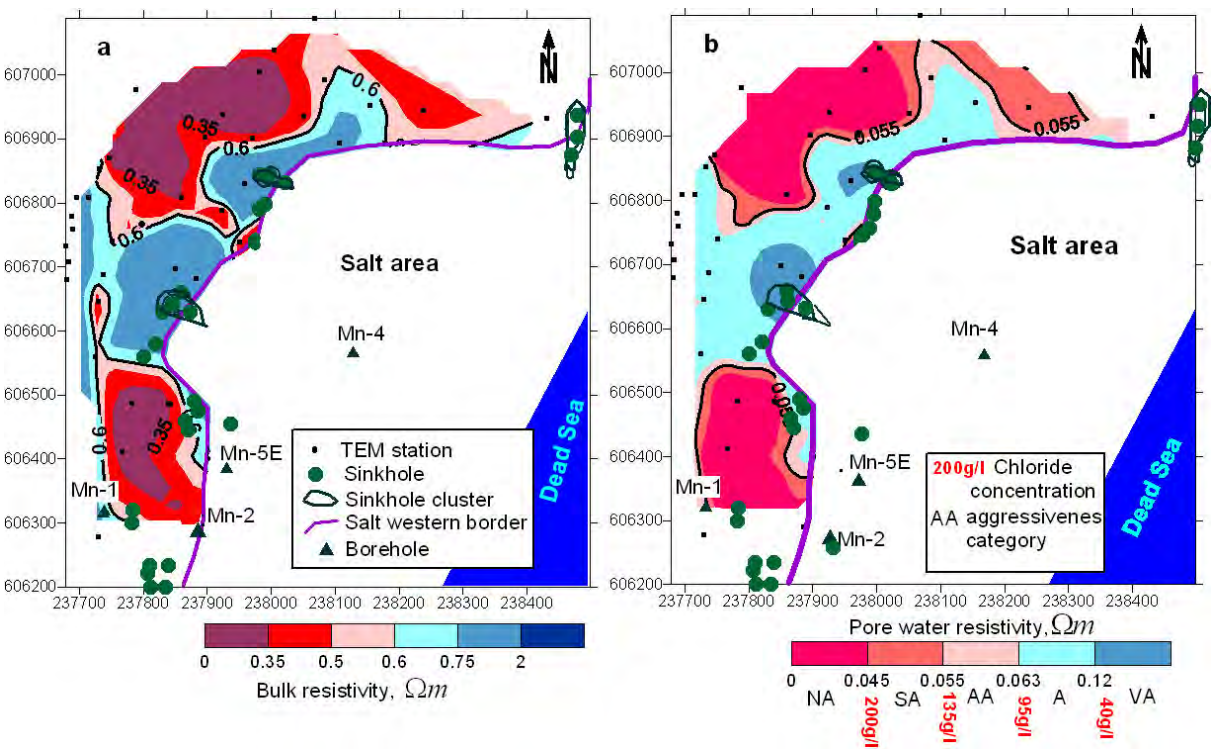

Figure 41. Evaluation of groundwater aggressivity through Mineral Beach area using resistivity distribution. (a) Bulk resistivity ρ_x map west to the salt layer and at its depth; and (b) map of the pore water resistivity calculated using formation ratio of $\rho_w = \rho_x / 9.5$ and chloride concentration calculated using equation (13). Denotations in Fig. 41b correspond to categories of groundwater aggressivity discussed in following section and in Table 4: VA – very aggressive groundwater, A – aggressive, AA – averagely aggressivity, SA – slightly aggressive, and NA – not aggressive.

The maps are similar. Zones of higher ρ_w (respectively, lower chloride concentration) on Fig. 41b correspond to zones of higher bulk resistivity in Fig. 41a. Moreover, zones of higher resistivities correlate with sinkhole formation line along the salt edge. There is borehole Mn-1 at the southern part of the map with chloride concentrations of 121 – 123 g/l. The borehole is located at the zones where calculated chloride concentration is between 95 and 135 g/l. It can be suggested that brackish groundwater came from closely located marginal fault west of the salt edge (central part of the map) and from Wadi Hazazon, characterized by high water recharge during floods. Note also based on Table 4 that the salt layer along its edge is in places in contact with highly aggressive groundwater. The great sinkholes are a result (Fig. 41b). But not only salinity of the groundwater is responsible for salt dissolving, but also the possibility of groundwater to approach the salt, dissolve it, and remove brine from the contact area (Reuter and Dietrich, 1993). Those are geological factors causing the difference in sinkhole formation at different sites. Examples from other studied sites show difference in the sinkhole hazard evaluation.

Nahal Ze'elim (site III in Fig. 1). Description of the site is given in the section 3.1.4. Location map of geophysical studies is shown in Fig. 7.

Salt map (Fig. 42b) shows gradual increase of the salt resistivity toward the DS (east direction). In accordance with Frumkin et al. (2011) increase in salt layer resistivity means decrease in its voidness and porosity. In this sense the map is conformed to that presented in Fig. 26b showing the shear wave (Vs) distribution through the Nahal Ze'elim area. Note low resistivity (0.5 – 1.0 Ωm) and low Vs (850 – 1050 m/s) zones near the salt layer edge characterizing the salt weakness caused by karstification process.

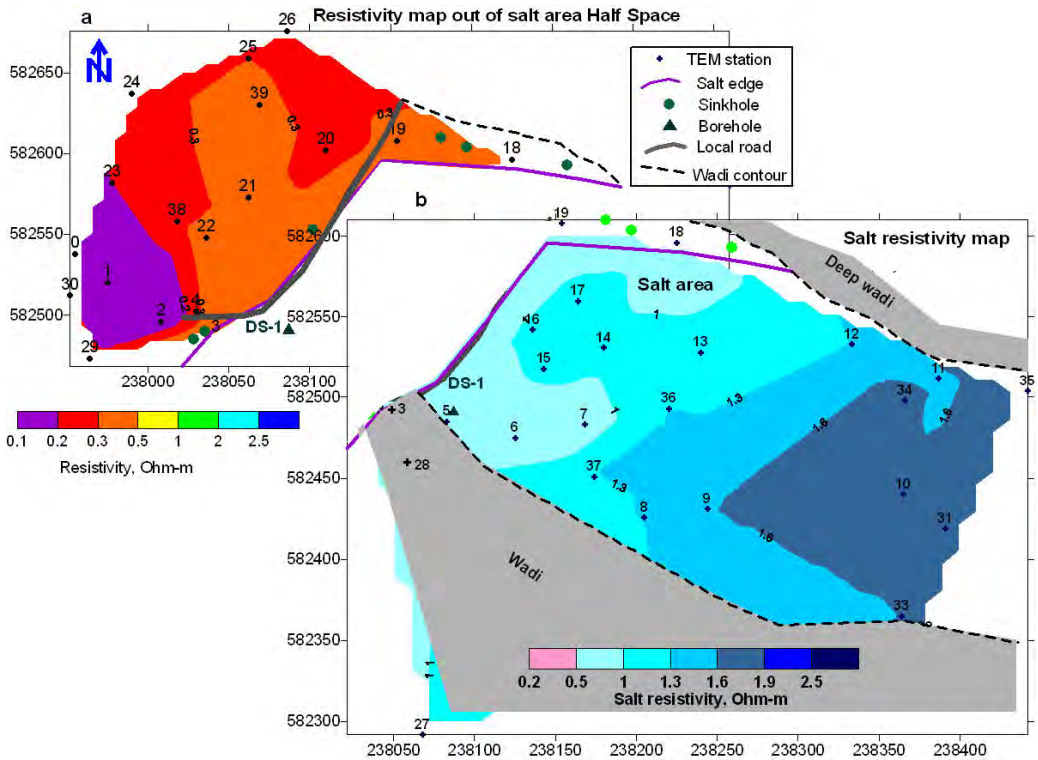

Figure 42. Bulk resistivity (ρ_x) maps generated for "out of salt area" (a) and "salt area" (b) in the Nahal Ze'elim site.

The resistivity map through the "out of salt" area (Fig. 42b) is built of resistivity $\rho_x < 0.5\,\Omega m$ that is significantly lower than that in the Mineral Beach area (Fig. 41a). Recalculating ρ_x to ρ_w using graphs in Fig. 39 we obtain the water resistivity ρ_w map presented in Fig. 43.

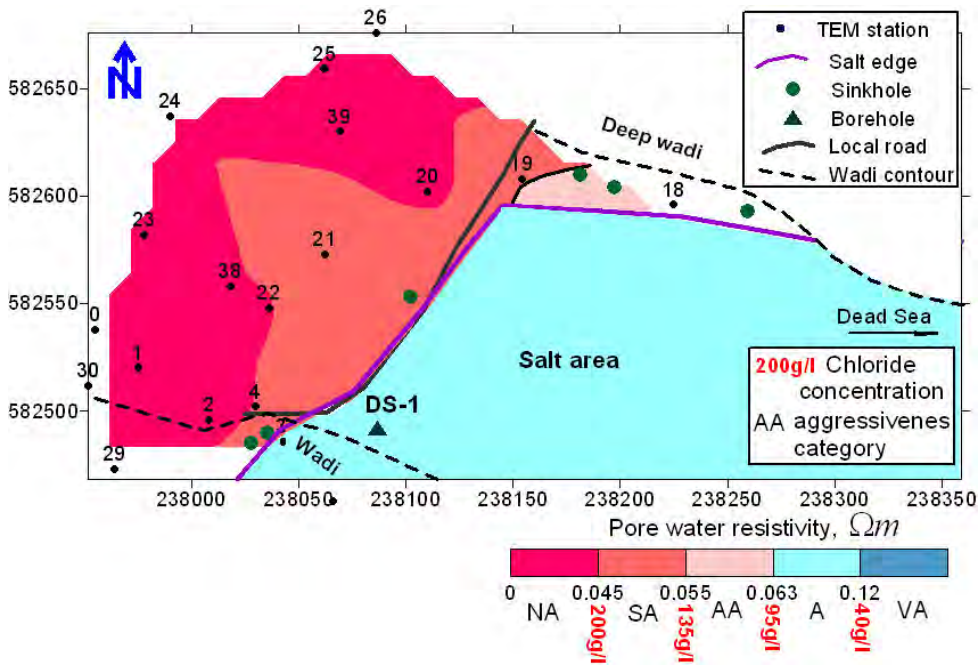

Figure 43. Pore water resistivity (ρ_w) map west to the salt layer in the Nahal Ze'elim area. Categories of groundwater aggressivity are in accordance to Table 4: VA – very aggressive groundwater, A – aggressive, AA – averagely aggressivity, SA – slightly aggressive, and NA – not aggressive.

One can conclude that sinkholes are formed in the area where pore water resistivity is ranged 0.045 – 0.055 Ωm. Such resistivity characterizes the pore water as "slightly aggressive" (Table 4 and Fig. 43). It is in rough agreement with timing of sinkhole appearance in this area. In spite the salt depth here is shallow (24m) first sinkholes have been appeared between 2004 and 2007 approximately (e.g. 5-6 years later than in Nahal Hever South area). At the same time Yechieli et al. (1995) extracted salt mixed with sand mass from borehole DS-1 (known in Israel as DSIF-1). Taking into account location of borehole some 40-50m east of salt edge we suggest salt dissolving here started for a long time before appearance of first sinkholes on surface. Perhaps, the late appearance of sinkholes is explained by local geological conditions.

Ghor Al-Haditha (site I in Fig. 1). Description of the site is given in the section 3.1.2. Location map of geophysical studies is shown in Figs. 44, 45.

At the Ghor Al-Haditha area, seismic refraction surveys carried out in the past were unable to delineate the salt layer. However, some conclusions on the resistivity structure and underground flows could be made based on the TEM and Magnetic Resonance Sounding (MRS) surveys (Akkawi, 2010; Al-Zoubi et al., 2012; Al-Zoubi et al., 2013b; Boucher et al., 2007; Boucher et al., 2012; Ezersky et al., 2012c). Totally twenty TEM soundings were carried out through the Ghor Al-Haditha area using the GEONICS PROTEM 47 D 20/30 Gate Model system (Akkawi, 2010, 3rd, 4th, and 5th Progress reports). The methodology of the TEM data processing and interpreting is presented in Ezersky et al. (2011). The purpose of this study is to infer information on the general feature of resistivity structure (distribution) in the shallow part of Ghor Al-Haditha from the interpretation of TEM (TDEM) data set. It enables to reveal signatures of salt unit and groundwater salinity in the vicinity of the salt. Results of the combined interpretation of TEM data based on the present study and reinterpreting of old data enable us to interpret the hydrogeological conditions of the Ghor Al-Haditha area.
The TEM W-E resistivity section (Fig. 44) shows hypothetic salt layer (confirmed also by seismic data of El-Isa et al., 1995) in relation to the saline water interface by 0.5 – 1.0 Ωm. We suggest that the eastern part of the salt layer is presently exposed to the fresh-brackish water contact. Two boreholes in Fig.44 are by Taqieddin et al. (2000).

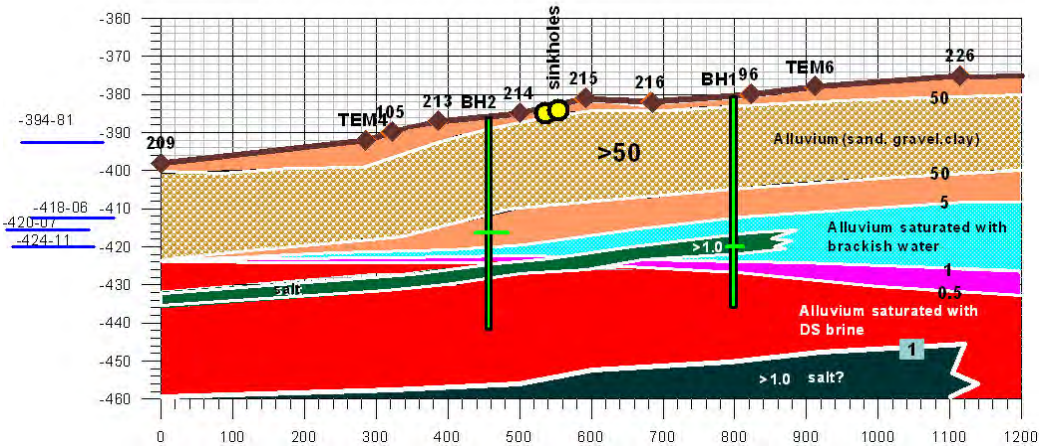

Figure 44. Hypothetic TEM W-E resistivity section through the Ghor Al-Haditha southern area (based on data of Akkawwi (2010) and Camerlynck (2007)) .

The TEM resistivity map generated for the north of the Ghor-Al-Haditha area is presented in Fig. 45. The map is based on TEM data carried out by both Akkawi (2010) and Camerlynck (Boucher et al. (2007).

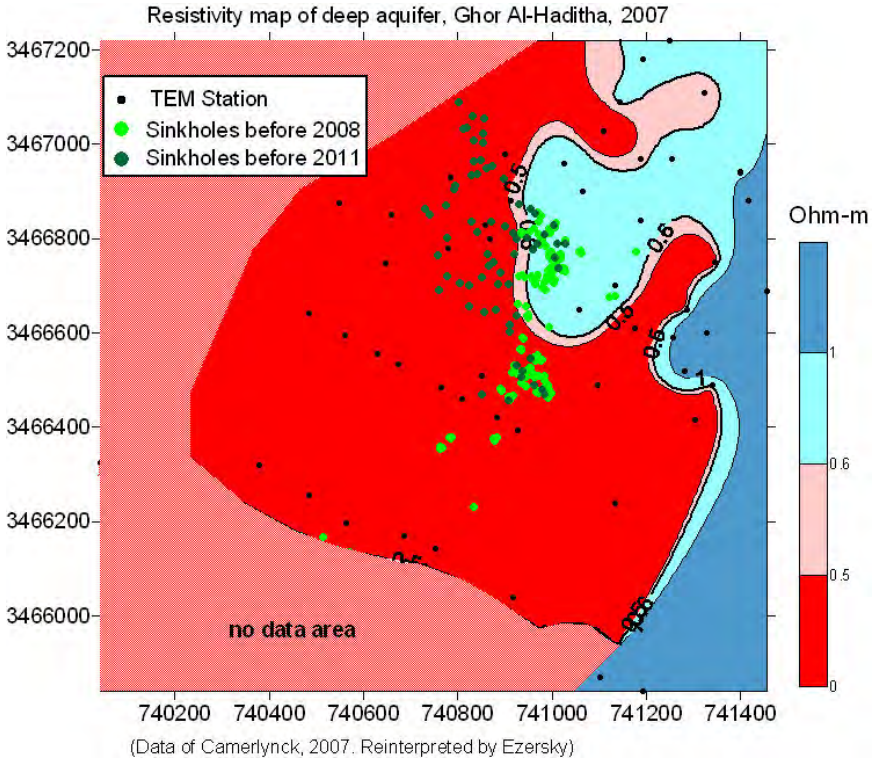

Figure 45. Resistivity map of the deep aquifer through the Ghor Al-Haditha area. Blue and dark blue zones shows water with resistivity of more than 0.6 Ωm and 1 Ωm, respectively, which contains 100g/l chloride and 60g/l one, respectively and keeps a high potential of salt dissolution (Ezersky and Legchenko, 2009).

The resistivity map shows that higher resistive sediments are located north, north-east to sinkholes. In accordance with the mentioned above (Section 3.2.4.9) pore water resistivity of alluvium is of 0.06 Ωm and 0.1 Ωm and contains 40-90 g/l chloride. Such water is aggressive with respect to salt (Table 4).

This is supported by other TEM and Magnetic Resonance Sounding (MRS) data (Fig. 46)

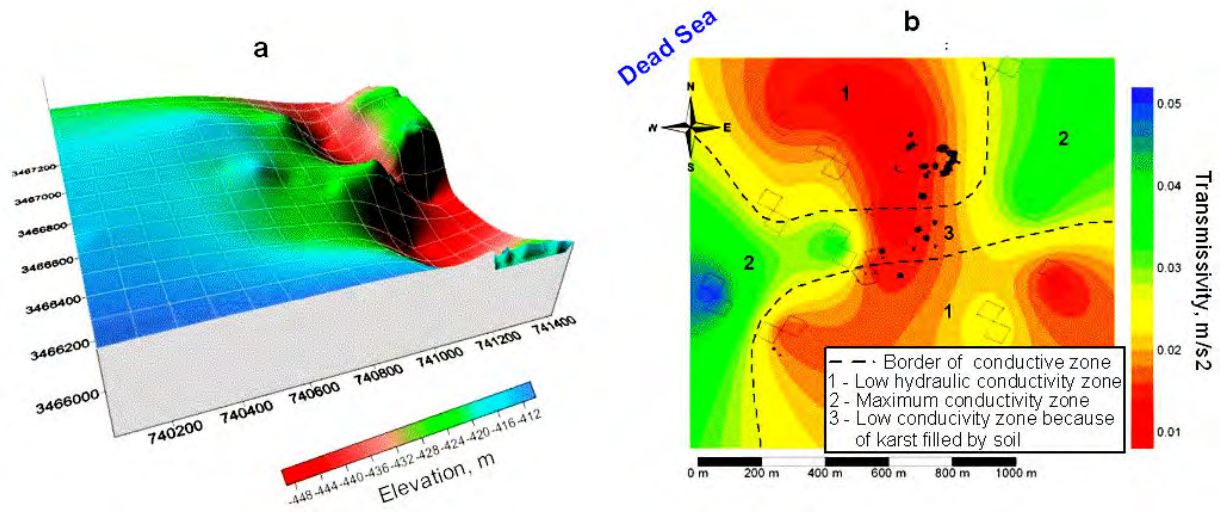

Figure 46. Interpreting of TEM and MRS results. (a) 0.5 Ωm interface in 3D presentation. The interface separating DS brine from below and less saline water from above is located at elevations of -420—424 meters. There is seen NS channel in this interface that would mean the unsaturated water in the eastern part of the Ghor Al-Haditha; (b) Transmissivity map through the Ghor Al-Haditha area showing the zone of the high transmissivity from northern-eastern part of the map (green area) that can be underground stream discharging to the DS direction (Boucher et al., 2012)

The surfer map (Fig. 46a) demonstrates the depression in the 0.5 Ωm interface that testifies that there is a channel of fresher water with resistivity more than 0.5 Ωm in the eastern part of section. The transmissivity map (Fig. 46b) shows the way of the groundwater stream toward DS (zone 2). The center of this channel (zone 3) has lower transmissivity as a result of surface collapse and sinkhole formation.

3.2.4.11. Conclusions on section 3.2.4.

The TEM method was updated for mapping of aquifers and salt layers through the areas of sinkhole formation. The TEM soundings were calibrated near 28 boreholes to reveal relationships between bulk resistivity (ρ_x), pore water resistivity (ρ_w) and chloride concentration (C_{Cl}) in the range of bulk resistivity < 1 Ωm characteristic for the DS coastal area. We suggested the classification of groundwater aggressiveness. It has allowed the generating of maps characterizing salinity of ground water and its aggressiveness with respect to salt layer. Such approach enables to delineate the sinkhole hazardous zone.

3.*2.5. Microgravity and Micromagnetic Methods*

(The method and results are presented in details Al-Zoubi et al. 2011a; Al-Zoubi et al. 2011b; Al-Zoubi et al 2012; Al-Zoubi et al. 2013; Eppelbaum, 2013a)

3.2.5.1. Background

Microgravity method. Microgravity has been recognized now as a powerful tool for analysis of geological inhomogeneities in subsurface caused by the density variations. Development of modern generation of field gravimetric equipment allows to register promptly and digitally microGal (10^{-8} m/s^2) anomalies that offer a new challenge in this direction. Correspondingly, an accuracy of gravity variometers (gradientometers) is also sharply increased.

Presence of the cavities and voids in the subsurface causes local negative gravity anomalies; salt layers also can be localized. That is why microgravity method was applied to the DS sinkhole problem.

Microgravity method in its 3D mode can detect concealed caverns regardless of shape or fill material, if there is sufficient density contrast. Moreover, temporal (4-D) changes in gravity at sinkhole sites suggest subsurface mass redistributions that may signal impending collapse. Sinkholes targets in the Dead Sea shores could be ranged by their density/geometrical characteristics in a several

groups. The performed model computations indicate that microgravity investigations might be successfully applied at least in 70-80% of sinkhole areas at the Dead Sea shores.

The applicability of microgravity has been confirmed worldwide for detecting karst caves in carbonate rocks. The density contrast in classic karst areas worldwide (remove) reaches 2.6 g/cm^3 for air-filled caves and 1.5-1.6 g/cm^3 for water-filled caves. However, it is not a case in the Dead Sea area, there are the sinkholes are developing in the young, unconsolidated, low-density sediments. The density contrast here is estimated to be 0.5-0.7 g/cm^3 or less. Distinct from the karst caves, the sinkholes on the Dead Sea shore are developing very rapidly. Further, the gravity effects of the concealed caverns are small distortion of the prominent Dead Sea gravity low (approximately -140 mGal). And these effects have to be found on the background of graben itself is large, with a horizontal gravity gradient of up to 10 mGal/km in an east-west direction.

Previous feasibility studies carried out during 1999 – 2003 in Israel have shown the reliability of the microgravity results in the coastal DS areas. Prominent studies of Rybakov et al. (2001) in the Nahal Hever South site (Israel) have detected large gravity anomaly by lateral size 50 x 80 m^2. Eppelbaum (2007a) presented a developed methodology of potential geophysical analysis for karst localization in complex conditions. Further collapse of the cavity during 5 years in the contour delineated by above survey (Ezersky et al., 2010) have shown that this anomaly was associated with the cluster of underground cavities by volume of 35,000m^3 (Eppelbaum et al., 2008). Another example is successful microgravity mapping and monitoring carried out along Route 90 over five years (Rybakov, 2003). The mapping has indicated that sinkhole sites are characterized by the negative residual gravity anomalies of – (0.055 - 0.08) mGal. These data indicate a subsurface mass deficiency below some of the areas where open sinkholes are observed, suggesting that additional sinkhole development can be expected. Evaluation of underground cavities volume carried out by Eppelbaum (in: Ezersky et al., 2013b) has shown that volume of underground voids would reach of 34,240m^3. These estimations are supported by karst volume evaluation (27,000m^3 $\pm$ 50%) carried out by Legchenko et al. (2008b) using Magnetic Resonance Sounding (MRS) method.

Microgravity can be an effective technique for monitoring the subsurface mass redistribution and prediction of collapse hazards. Successful testing of the microgravity in Israel made us to map Ghor Al-Haditha area by crew of BAU.

Magnetometry method. Micromagnetic technique is based on the assumption that nonmagnetic hollows existing in the low magnetic subsurface and foregoing to the ground collapse can be reliably delineated. Numerous measurements showed that the magnetic susceptibility of the shallow young sediments range from about 20-50*10^{-5} SI (Rybakov et al., 2005; Eppelbaum, 2013a). 3-D modeling suggested the hollows, with a volume like to volume of the open sinkholes, and located at the depth no more of a few diameters, caused to the dipole magnetic anomalies with the magnitude of a few nanoTesla. To study the method's feasibility the pilot magnetic surveys were carried out in the five sites of the Dead Sea area. The sites are located at the different geological conditions (alluvial fans, mud flats). The result of the micromagnetic survey shows that the sinkhole characterized by dipole pattern of magnetic anomaly. Therefore, we suppose that the magnetic method could be considered one of the efficient methods could be used to predict the sinkholes hazard (Rybakov et al., 2005).

Micromagnetic method was tested at the western shore of the DS area for subsurface void detection (Rybakov et al., 2005; Rybakov, 2006). The pilot micromagnetic surveys were carried out in the five sites of the area. There are observed magnetic anomalies that reflect: (a) open sinkhole and void beneath it (the soil fills the void partially); (b) open sinkhole only and void does not exist (the soil filled the void fully); and (c) void exists at depth but there is no expression of collapse on the surface. We suggested that the magnetic anomalies located out of the sinkhole cluster correspond to a subsurface mass deficiency, which will cause future ground collapse (Rybakov et al., 2005). A few months after this publication we documented a collapse at the predicted location. This is convincing proof-of concept for the application of micromagnetic surveying to predict subsurface voids that often become sinkholes (Rybakov et al., 2006).

3.2.5.2. Removing Regional Trends in microgravity complex environments: testing on 3D models and field investigations in the eastern Dead Sea coast (Jordan)

Microgravity. In spite Microgravity investigations are now recognized as a powerful tool for the localization of underground karsts, at the same time it is the geophysical method most affected by

corrections and reductions caused by different kinds of noise (disturbances). Analysis of most disturbances has been considered by Al-Zoubi et al. (2013a) and Eppelbaum (2013a). Numerous natural (geological), technical and environmental factors interfere with microgravity survey processing and interpretation. One of natural factors that cause the strongest disturbance in complex geological environments is the influence of regional trends. In the Dead Sea coastal areas the influence of regional trends can exceed residual gravity effects by some tenfold. The correct removal (elimination) of regional trends is not a trivial task (Tellford et al., 1990). Below we present two examples showing disturbing trend effects in detailed gravity investigations. Fig. 47 shows two cases of nonhorizontal gravity observations with the presence of an anomalous body. The distorting effect of a nonhorizontal observation line occurs when the target object differs from the host medium by a contrast density and produces an anomalous vertical gradient.

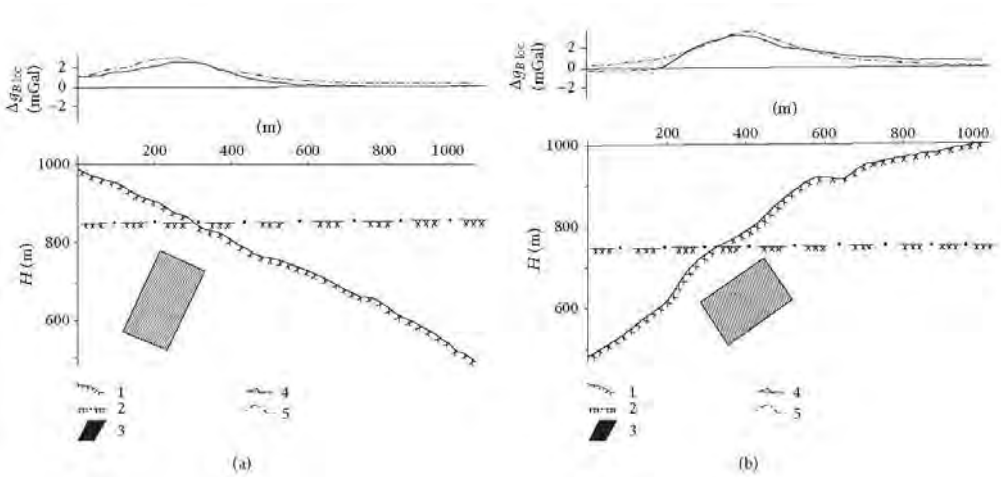

Figure 47. Negative effect of gravitational anomalies from a local anomalous body observed on inclined and horizontal profiles (after (Khesin et al. 1996), with modifications). (a) Smooth slope, (b) complicated slope. (1) Inclined profile; (2) horizontal profile; (3) anomalous body with a positive contrast density $\Delta\sigma$ = 1500 kg/m3; anomaly $\Delta g\ B$ from the same body after topographic mass attraction correction: (4) on an inclined profile, (5) on a horizontal profile.

Comparing the $\Delta g\ B$ anomalies from the local body observed on the inclined and horizontal relief indicates that the gravity effects in these situations are different (Fig. 47). Despite the fact that all the necessary corrections were applied to the observations on the inclined relief, the computed Bouguer anomaly is characterized by small negative values (minimum) in the downward direction of the relief, whereas the anomaly on the horizontal profile has no negative values (this kind of noise is named uneven terrain relief, Al-Zoubi, 2013a). Thus, applying all conventional corrections does not eliminate this trend because the observation point for the anomalous object was different (Khesin et al., 1996). Hence a special methodology is required for gravimetric quantitative anomaly interpretation in conditions of inclined relief (Eppelbaum, 2011). Sometimes even simple computing of the first and second derivatives of the gravity field $\Delta g\ x$ and $\Delta g\ xx$ (second and third derivatives of the gravity

potential, respectively) is enough to locate local bodies against a disturbing field background. One such example is presented in Fig.48 where the Bouguer gravity $\Delta g\ B$ is practically impossible to interpret, whereas the calculation of $\Delta g\ Bx$ was informative regarding the geometry of two closely occurring sinkholes.

Finally, the behavior of the graph $\Delta g\ Bxx$ clearly reflects the location of the vertical boundaries of two closely occurring objects with a small negative interval (surrounding medium) between them.

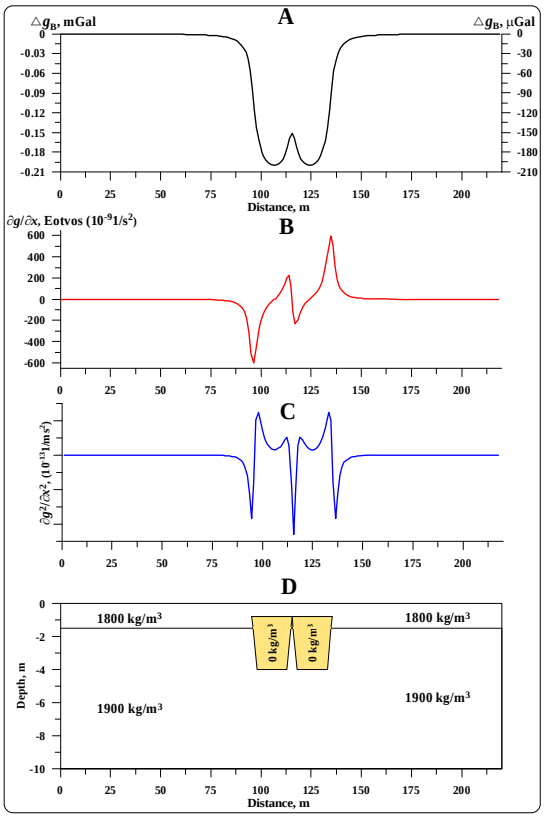

Figure 48. Computing of horizontal derivatives from models of two closely disposed caves. (a) Computed gravity curve, (b) Calculated first horizontal derivative of gravity field Δg_x, (c) Calculated second horizontal derivative of gravity field Δg_{xx}, (d) Physical-geological model

The area under study—Ghor Al-Haditha—is situated in the eastern coastal plain of the Dead Sea (Jordan) in conditions of very complex regional gravity pattern (Fig. 49). The satellite gravity data shown in this figure were obtained from the World Gravity DB as retraced from Geosat and ERS-1 altimetry (Sandwell et al., 2009). These observations were made with regular global 1-minute grids that can differentiate these data from previous odd surface and airborne gravity measurements.
This complex gravity field distribution in the vicinity of the area under study is caused mainly by the strong negative effect of the low density sedimentary associations and salt layers accumulated in the DST and also several other factors.

Many widely applied methods are unable to remove regional trends with sufficient accuracy. We tested number of transformation methods (including computing gravity field derivatives, self-adjusting and adaptive filtering, Fourier series, wavelet and other procedures) on a 3D model (complicated by randomly distributed noise), and field investigations carried out in Ghor Al-Haditha (the eastern side of the Dead Sea in Jordan). We show that the most effective methods for regional trend removal (at least for the theoretical and field cases here) are the *bi-linear saddle and local polynomial regressions*. Application of these methods made it possible to detect the anomalous gravity effect from buried targets in the theoretical model, and to extract the local gravity anomaly at the Ghor Al-Haditha site (Al-Zoubi et al., 2013a, Eppelbaum, 2013a). The local anomaly was utilized for 3D gravity modeling to construct a physical-geological model (PGM).

Magnetometry. The Dead Sea region is located between 31° and 32° north of the equator where the Earth's magnetic field is strongly inclined. For processing and interpretation of magnetic anomalies in conditions of oblique magnetization, rugged terrain relief and an unknown level of the total magnetic field the special interpretation methodologies were developed (Khesin et al., 1996; Eppelbaum, 2011).

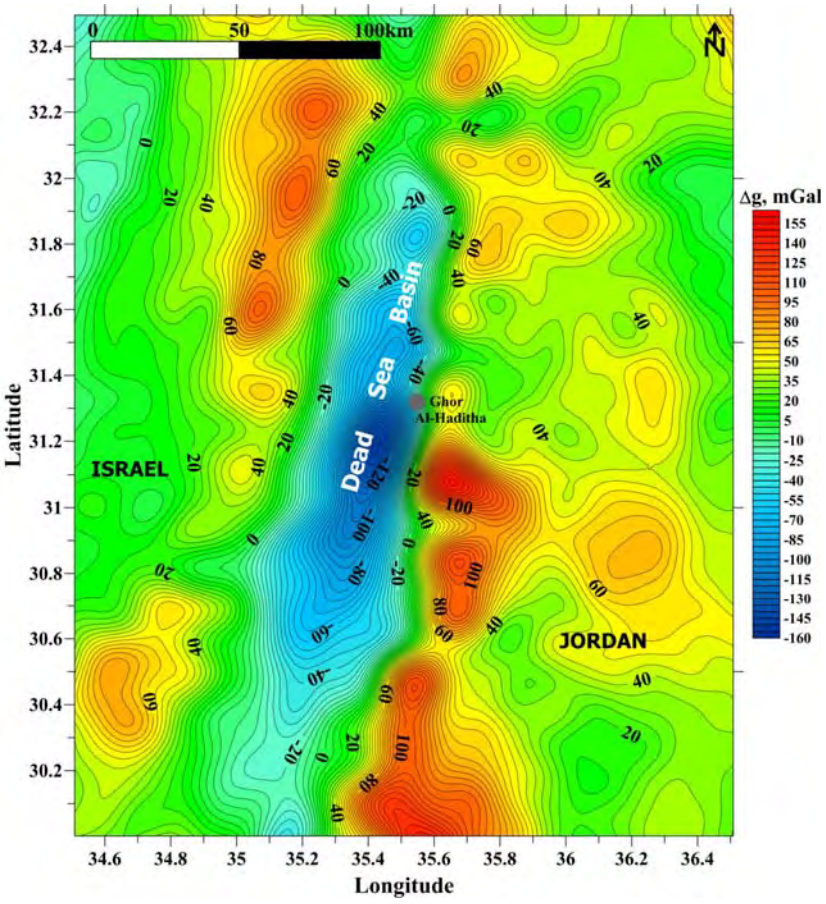

Figure 49. Areal map of the investigated site

These methodologies together with some recently developed approaches were successfully applied in Israel and the Dead Sea region for solving various applied and environmental problems (Eppelbaum, 2006, 2007a; 2007b, 2011). An example of inverse problem solution for the model of karst (I = 0) occurring in the magnetized medium (I = 500 mA/m) with oblique magnetization (45°) is presented in Fig.50. Simple analysis of magnetic curve displays that borehole drilled at the minimal amplitude of magnetic field will no discover the hidden object. Application of the developed methodology of inverse problem solution permits to determine the position of HCC center with high accuracy.

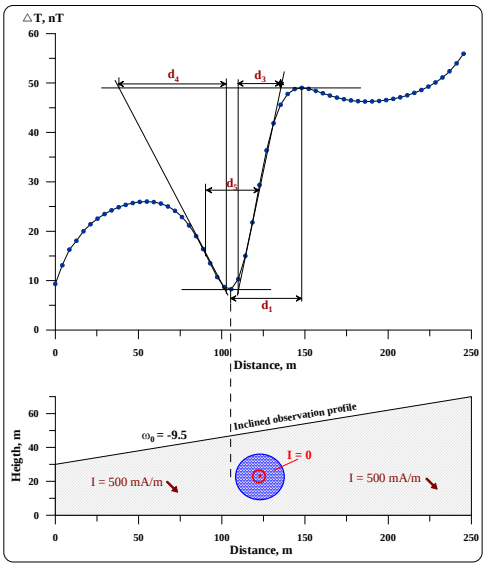

Figure 50. Model example of magnetic field quantitative analysis under complicated environments. Symbol ⊙ designates location of HCC center

Joint analysis of microgravity and magnetometry data. Wavelet methodology as whole has a significant impact on cardinal problems of geophysical signal processing such as: denoising of signals, enhancement of signals and distinguishing of signals with closely related characteristics (Alperovich et al., 2013; Eppelbaum et al., 2011, Grinsted et al., 2004; Kumar and Foufoula-Georgiou, 1997; Zheludev and Alperovich, 1999).

A new developed methodology is based on "recognition of images" or anomalies that should be induced by karst cavity located in subsurface on different geophysical fields measured on surface (like gravity, magnetic, electrical, etc). In other words, simulating cavities (differing in size, location depth, fill etc) located in subsurface (differing in layered structure, lithology, hydrogeological conditions etc) one can obtain different anomalies of spatial variations of magnetic, gravity, resistivity etc. parameters in the linear (graphs), 2D (sections and surfaces), and 3D (volume) modes. Each of these anomalies has some characteristic features which can be recognized by a method similar to “learning with teacher”.

A *three-phase approach* to the integrated Gravity–Magnetic (GM) localization of subsurface karsts has been developed (Eppelbaum et al., 2011, 2013a). The same approach could be used for following monitoring of karst dynamics.

- The *first phase* consists of computer modeling devoted to geophysical surveys characterizing karsts (*creation of images using modeling*). We consider here high-precision gravity and magnetic effects (combination of GPR and ERT will be considered in a separate publication).
- *The second phase* determines development of the signal processing approaches to analyzing of profiles or areal GM observations (*measurements of real GM fields*).
- Finally, at the *third phase* provides integration of these methods in order to create a new method of the combined interpretation of different geophysical data (*comparison of model images and measured ones to reveal these testifying karst cavities*).

In the base of our combine GM analysis we put modern developments in the wavelet technique of the signal and image processing.

Thus, development of the integrated methodology of geophysical field examination will enable to recognizing the karst terrains even by a small ratio of useful signal/noise in complex geological environments.

Description of the Applied Methodology. On the basis of review of numerous literature sources (e.g., Beck, 2003; Waltham et al., 2004; Fookes et al., 2005; Chalikakis, 2006; Eppelbaum, 2007a, b; Legchenko et al., 2008b, 2009; Ezersky et al., 2013b) and authors’ personal experience, 30 typical geological sections containing karst cavity were modeled. The same number of sections were also composed as non-containing karst cavity – altogether 60 working models were utilized. Figs. 51-52, 53 show gravity and magnetic curves computed (for these computations a GSFC software (Eppelbaum, 2007a, b; Eppelbaum et al., 2008) was used) from three typical geological sections containing karst cavity. It should be noted that anomalous gravity and magnetic effects from the karst

cavities (negative anomalies) were specially modeled as significantly small ones. Physical characteristics presented in the figures demonstrate not only density-magnetization properties but indicate that next stage of such analysis will include computing GPR and ERT images for the same sections.

Wavelet approach (WA) to recognition of karst terrains by the examination of geophysical method integration consists of advanced processing of each geophysical method and nonconventional integration of different geophysical methods between themselves. Modern developments in the wavelet theory and data mining will be utilized for the analysis of the integrated data. Wavelet approach will be applied for derivation of enhanced (e.g., coherence portraits) and combined images of geophysical fields observed in the areas ancient remain occurrence. The methodology based on the matching pursuit with wavelet packet dictionaries enables to extract desired signals even from strongly noised data.

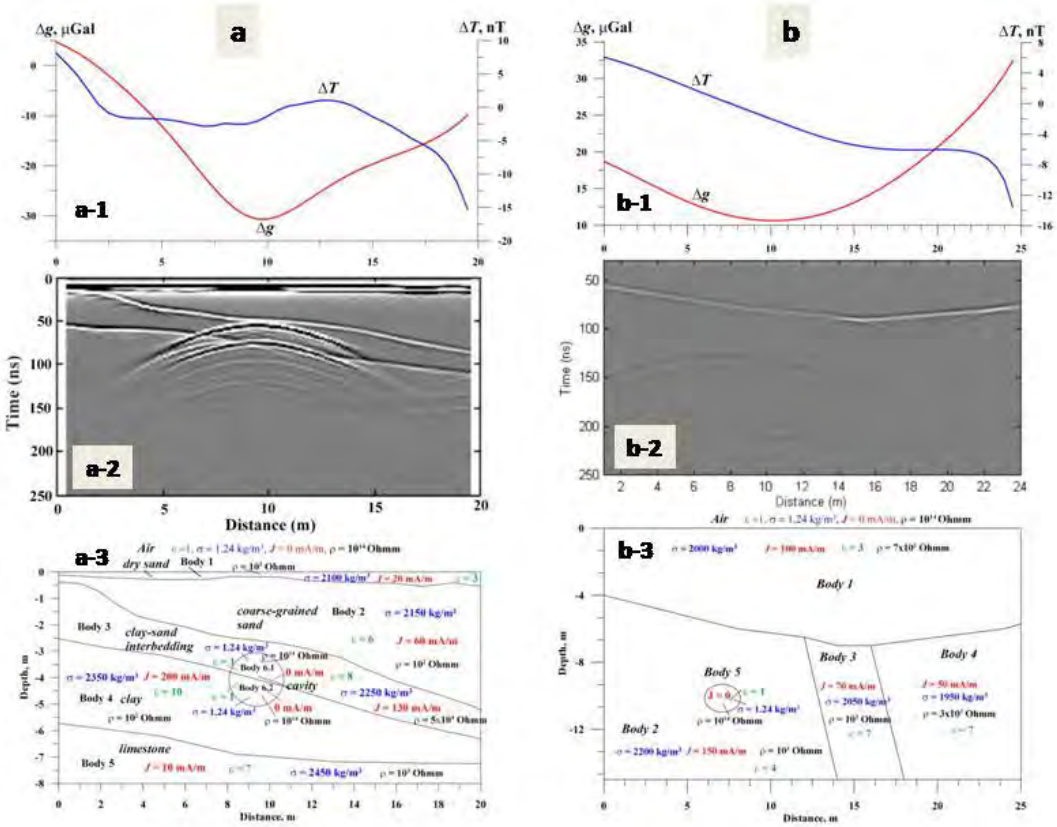

Figure 51-52. Examples of karst models and induced anomalies in different potential fields. (a-1) Magnetic and gravity anomalies along the geological section with karst shown in (a-3); (a-2) GPR anomaly along the same section (Model 1); (b-1 and b-2) similar anomalies along the section (b-3) (Model 19). Here σ is the density, J is the magnetization, ρ is the electric resistivity, and ε is the dielectric permittivity (last two parameters are intended for the further GPR and ERT modeling). Model 1

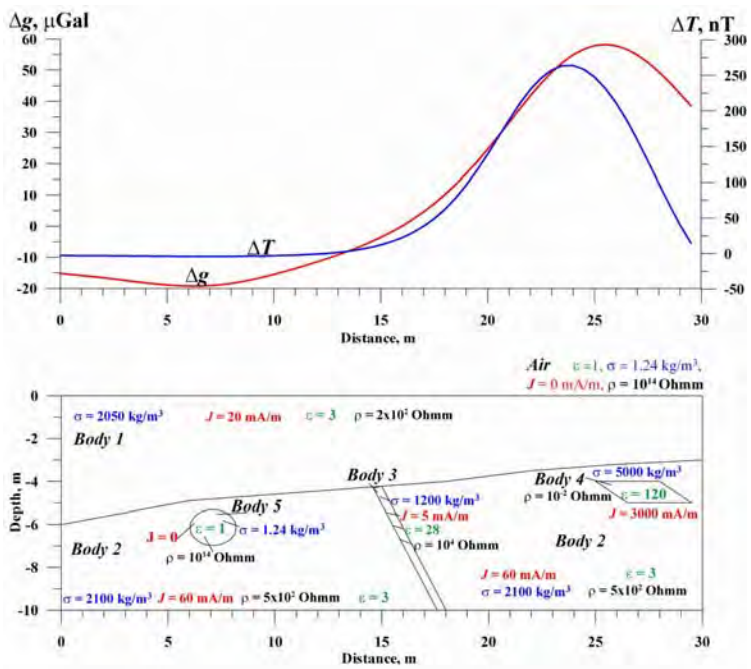

Figure 53. Third examples of 3D gravity-magnetic model (from above) for geological section with karst (from below). Here σ is the density, J is the magnetization, ρ is the electric resistivity, and ε is the dielectric permittivity (last two parameters are intended for the further GPR and ERT modeling). (Model 26)

Researchers usually met the problem of extraction of essential features from available data contaminated by a random noise and by a non-relevant background. If the essential structure of a signal consists of several sine waves then we may represent it via trigonometric basis (Fourier analysis). In this case one can compare the signal with a set of sinusoids and extract consistent ones. An indicator of presence a wave in a signal $f(t)$ is the Fourier coefficient

$$\int f(t) \sin wt \; dt \,. \tag{13}$$

Wavelet analysis provides a rich library of waveforms available and fast, computationally efficient procedures of representation of signals and of selection of relevant waveforms. The basic assumption justifying an application of wavelet analysis is that the essential structure of a signal analyzed consists of not a large number of various waveforms. The best way to reveal this structure is representation of the signal by a set of basic elements containing waveforms coherent to the signal. For structures of the signal coherent to the basis, large coefficients are attributed to a few basic waveforms, whereas we expect small coefficients for the noise and structures incoherent to all basic waveforms.

Wavelets are a family of functions ranging from functions of arbitrary smoothness to fractal ones. Wavelet procedure involves two aspects. The first one is a d*ecomposition*, i.e. breaking up a signal to obtain the wavelet coefficients and the 2nd one is a r*econstruction*, which consists of a reassembling the signal from coefficients

There are many modifications of the WA. Note, first of all, so-called *Continuous WA* in which signal *f(t)* is tested for presence of waveforms $\psi\left(\frac{t-b}{a}\right)$.

Here, *a* is scaling parameter (dilation), *b* determines location of the wavelet $\psi\left(\frac{t-b}{a}\right)$ in a signal $f(t)$. The integral

$$\left(W_\psi f\right)(b,a) = \int f(t)\,\psi\left(\frac{t-b}{a}\right) dt \tag{14}$$

is the Continuous Wavelet Transform.

When parameters a, b in $\psi\left(\frac{t-b}{a}\right)$ take some discrete values, we have the Discrete Wavelet Transform.
A simplified scheme of the Wavelet Decomposition Tree is shown in Fig. 54.

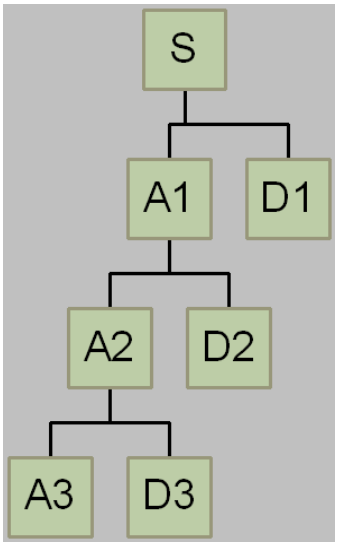

Figure 54. Block diagram of wavelet analysis. A_i = approximation, D_i = details

The signal is compared with the testing signal on each scale. It is estimated wavelet coefficients which enable to reconstruct the 1st approximation of the signal and details. On the next level, wavelet transform is applied to the approximation. Then, we can present A_1 as $A_2 + D_2$, etc. So, if S – Signal, A – Approximation, D – Details, then $S = A_1 + D_1 = A_2 + D_2 + D_1 = A_3 + D_3 + D_2 + D_1$.
Wavelet packet transform is applied to both low pass results (approximations) and high pass results (details) (Fig. 55).

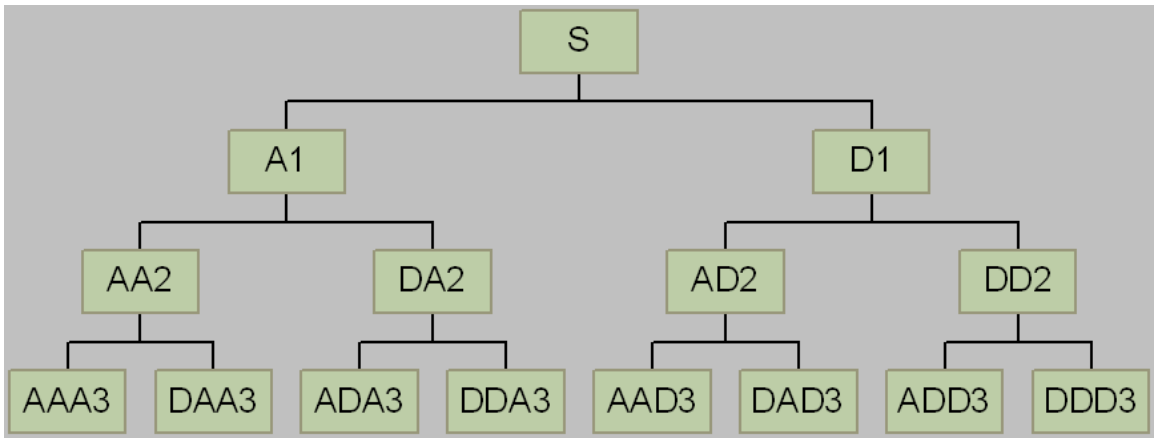

Figure 55. Wavelet packet tree

The recently developed technique of diffusion clustering combined with the abovementioned wavelet methods will be utilized in the project to integrate the data and to detect existing irregularities. The goal of the modern geophysical data examination is to detect the geophysical signatures of buried sinkholes at a noisy area via the analysis of some physical parameters with minimal number of false alarms and miss-detections.
The approach is based on the wavelet packet techniques applied as to the usual plots (or images) of gravity and magnetic fields versus coordinate. For example, as a result of the above operations we can embed the original combined gravity and magnetic data into 3-dimensional space where data related to the **K** (karst) subsurface are well separated from the **N** (non-karst) data. This 3D set of the data

representatives can be used as a reference set for the classification of newly arriving data (Alperovich et al., 2013a).
For analyzing the GM data, we used a technique based on the algorithm to characterize a GM image by a limited number of parameters. This set of parameters serves as a signature of the image and is to be utilized for discrimination of images containing karst cavity from the images non-containing karst. The constructed algorithm consists of the following main phases: (a) collection of the database, (b) characterization of GM images, (c) and dimensionality reduction. Then, each image is characterized by the histogram of the coherency directions. As a result of the previous steps we obtain two sets **K** and **N** of the signatures vectors for images from sections containing karst cavity and non-karst subsurface, respectively.

3.2.5.3. Data acquisition

Microgravity. Microgravity survey was performed by field crew of BAU leaded by Prof. Al-Zoubi. The Scintrex CG-5 AutoGrav gravity meter (Canada) with accuracy about of 0.007mGal was used for data acquisition (Fig 56a).
The coordinates and elevations of the stations were measured using Lieca 500 differential Global Position System (GPS) instruments (Fig. 56b) with an accuracy of a few millimeters. Elevations were measured to the top of instrument in real time. The geodetic survey also provided the detailed Digital Terrain Model (DTM) to calculate the complete Bouguer reduction (Hall, 1993).
The microgravity survey was carried out the entire Ghor Al-Haditha area, where total of 1228 microgravity stations were measured along parallel profile with approximately 20 m apart and 20 m distance between adjacent stations. The survey was carried out using CG-5 "Autograv" Gravity Meter from Scintrex, Canada (Fig.56c).

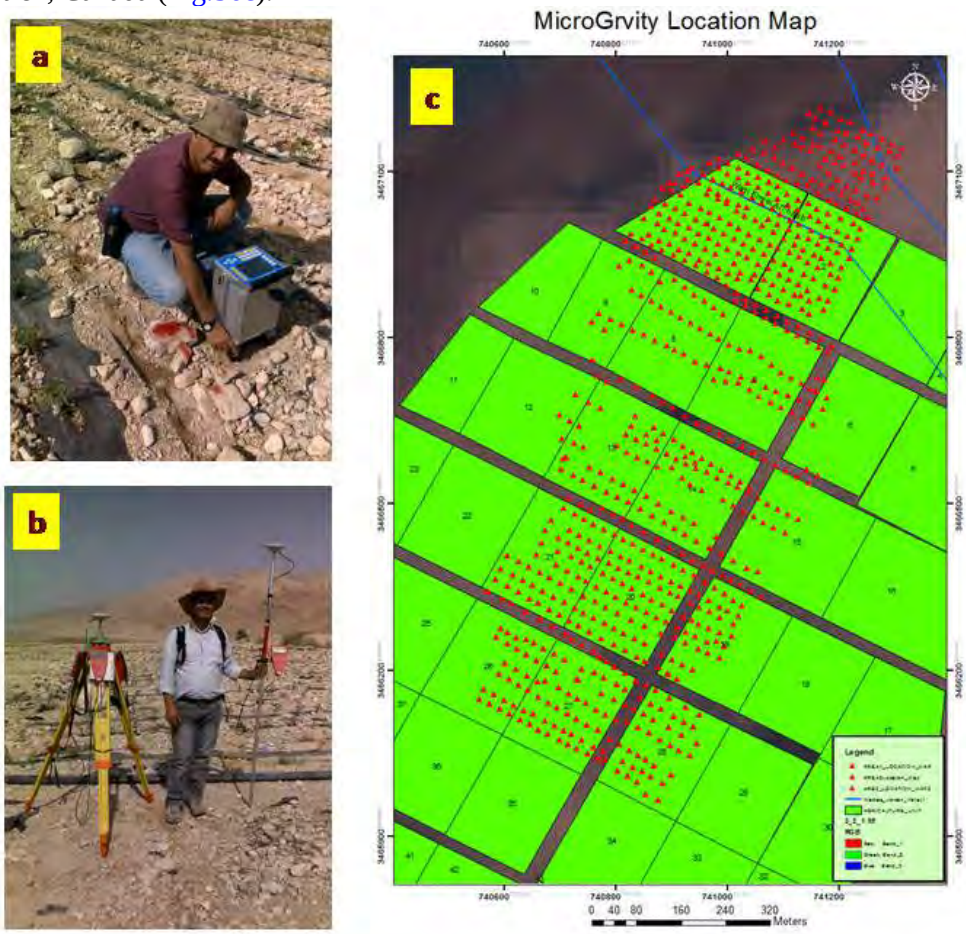

Figure 56. Microgravity surveying. (a) CG-5 "Autograv" Gravity Meter from Scintrex, Canada; (b) Lieca 500 differential Global Position System (GPS) instruments; (c) Location Map of microgravity measurement station through the sinkholes area (entire Ghor Al-Haditha area).

<u>*Magnetic Data acquisition.*</u> Field magnetic investigations have been carried out in the eastern Dead Sea coast (Jordan) (Abueladas et al., 2010) (Fig. 57a).

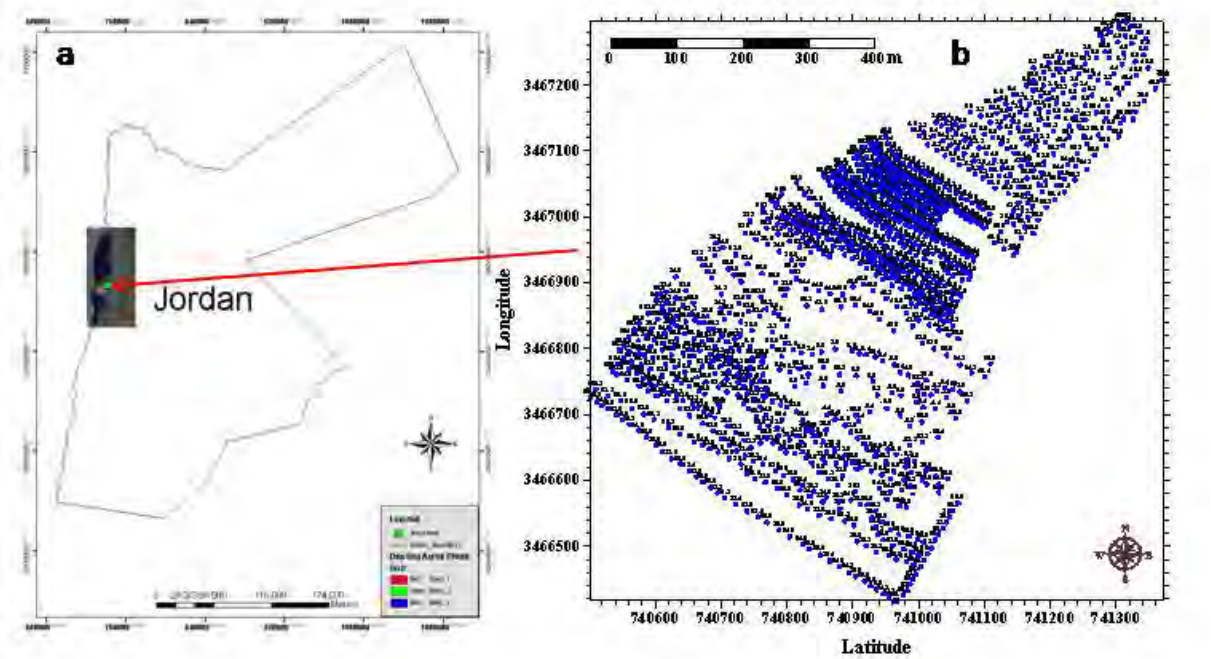

Figure 57. Location map of magnetic measurements. (a) Areal map of the magnetic observations at the eastern Dead Sea coast (Jordan), and (b) Location of magnetic field observation points(after Abueladas et al., 2010)

Two magnetic sensors were applied with a vertical distance of 1m at the levels of 2 and 1 m, respectively. Thus, both maps of the vertical magnetic gradient $\boldsymbol{T}_z$ and $\Delta\boldsymbol{T}$ maps could be compiled. Altogether 1122 points of irregularly displaced grid of the SW-NE (Abueladas et al., 2010) trend were observed (Fig. 57b). After removing the diurnal magnetic variations, a map of the total magnetic field (compiled for the top magnetic sensor) was constructed (Fig. 57b). For increasing the visibility, from the total magnetic field some averaged level of 44350 nT was removed.

3.2.5.4. Investigation of Physical Properties

To carry out modeling and interpreting of Microgravity and magnetometry determining of physical properties was carried out in the field and in the laboratory. Brief description is given in this Chapter.

Magnetic susceptibility Magnetic susceptibility determinations were performed by the use of Magnetic Susceptibility Meter SM-20. Altogether about 150 measurements of surface magnetization have been performed. Part of measurements obtained in the site Shalem-2 is presented in Table 5.

Table 5. Observed values of magnetic susceptibility in the area Shalem-2 (western Dead Sea coast)

Longi-tude	Lati-tude	Magn.*) 10^{-3} SI	Longi-tude	Lati-tude	Magn., 10^{-3} SI	Longi-tude	Lati-tude	Magn., 10^{-3} SI
238066	606666	-0.003	237836	606731	0	237960	606670	0.001
238009	606683	-0.003	237836	606733	-0.001	237965	606669	0.002
238002	606683	-0.002	237822	606675	0	238098	606718	0.001
237994	606683	-0.002	237834	606674	-0.001	238100	606707	0.001
237984	606687	-0.001	237838	606673	-0.001	238122	606718	0.001
237975	606692	-0.001	237849	606670	-0.001	238107	606718	0.001
237968	606693	-0.001	237858	606668	-0.076	238093	606718	0.001
237960	606693	0.01	237866	606665	0	238082	606718	0
237951	606697	0	237922	606704	0	238075	606718	0.001
237959	606700	-0.001	237876	606661	0	238069	606718	0.001
237933	606701	-0.003	237884	606656	0	238060	606718	0.001
237922	606704	0	237891	606656	0	238051	606718	0.003
237909	606706	0	237899	606650	0	238042	606718	0.004
237902	606726	-0.027	237908	606648	0	238035	606719	0.002
237886	606712	-0.003	237924	606647	0	238063	606726	0.003
237899	606708	0	237921	606646	0	238028	606719	0
237876	606714	-0.002	237949	606642	0	237929	606724	0

237846	606731	0	237987	606654	0.002	237909	606742	0
						237877	606754	0

*) Magnetisation

It is known that clear sample of salt gives a magnetization of 9.8 x 10^{-6}SI (Parasnis, 1997). Part of magnetic susceptibility determinations display low values (– 1÷3) x 10^{-6}SI (apparently there were weathered salt samples). Two values (–27 and 76) x 10^{-6}SI show some low-magnetic inclusions to the salt samples.

Density. Density determinations were carried out by the use of Electronic Densitometer MH-300Z (Table 6) with a high accuracy (10 kg/m^3= 0.01 g/cm^3).
Results are presented in details in Eppelbaum, (2013b).

As a whole, these measurements indicate that the salt density ranges in the interval from 1.910 and 2 g/cm^3. This indicates that the salt layers composing the upper part of geological section have low values of density that we need to take into account by subsequent 3D gravity field modeling.

Table 6. Values of salt specimen density withdrawn in three different sites of the western DS coast

Place	Density, kg/m^3	Weight of sample, kg
Ein Boqeq No. 1	1910± 10	0.182
Ein Boqeq No. 2	1930± 10	0.145
Ein Boqeq No. 3	1920± 10	0.192
Nanal South No. 1	1990± 10	0.154
Nanal South No. 2	1980± 10	0.167
Nanal South No. 3	2000± 10	0.162
Shalem-2 No. 1	1960± 10	0.148
Shalem-2 No. 2	1980 ±10	0.139
Shalem-2 No. 3	1985± 10	0.175

3.2.5.5. Results of magnetometry in the western DS coast (Site 2, Israel)

Site of Mineral Beach is located in the western coast of the Dead Sea (Fig. 58, See Fig. 1 for location).

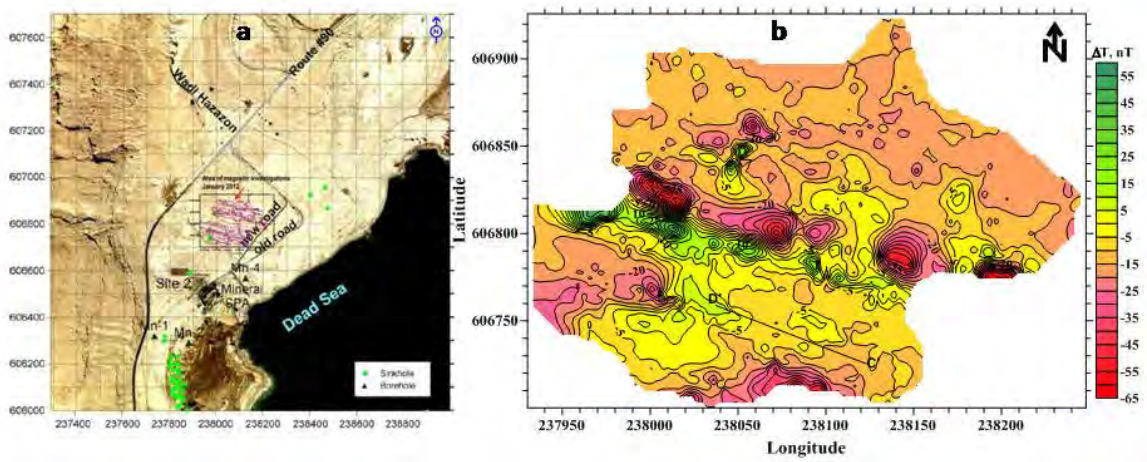

Figure 58. (a) Areal map of the investigated site with location of the observation pints in the center of this map (initial areal map after Frumkin et al., 2011); (b) Compiled map of the total magnetic field for the area Mineral Beach (Shalem-2)

Totally 2463 observation points were measured. From the total magnetic field some averaged level of 44530 nT was removed. The total magnetic field map is presented in Fig. 58b. As it follows from this map analysis, the magnetic pattern is composed by many anomalies of different origin. For instance, linear anomalous zone in the center of this map is caused by iron net. Magnetic properties of the upper part of the soil cover were measured by magnetic susceptibility meter (see Table 1).

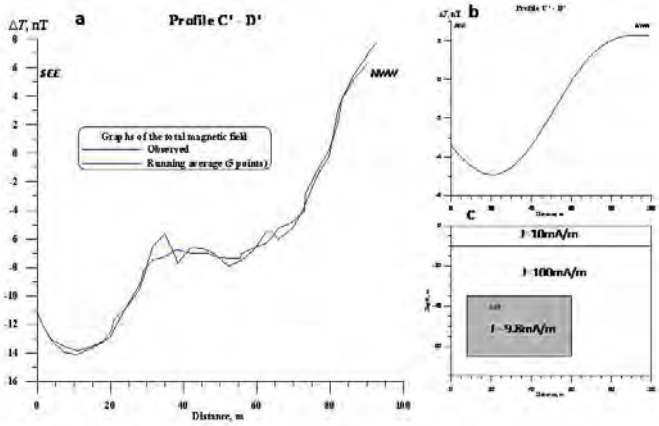

Figure 59. (a) Magnetic profile along the line C' – D'; (b) Part of the profile between 40 and 100 m distance; and (c) Preliminary Physical-Geological Model along the line C' – D'

With the aim to localize a border of salt layer (salt has a reverse magnetization of about 10 mA/m), a profile C' – D' was constructed (Fig. 59a). On the basis of some a priori data, a model profile was constructed along the same line (Fig. 59c). It should be noted that distribution of these graphs is similar, but amplitudes differ in three times (the observed curve is greatest). This fact may be explained by two main reasons:

(1) Depth of the salt layer is not 35-40 m, but significantly less (about 18-20 m),
(2) Magnetization of the surrounding rocks in two-three times more 100 mA/m.

<u>*Quantitate interpretation of magnetic anomalies produced by salt layers.*</u> A new solution The recently published results of performed investigations (Eppelbaum, 2013) indicate that for the analysis of magnetic anomalies produced by models of thin plates not very closely occurring to the earth surface the quantitative methods developed for the model of thick bed for complex environments (Fig. 60).

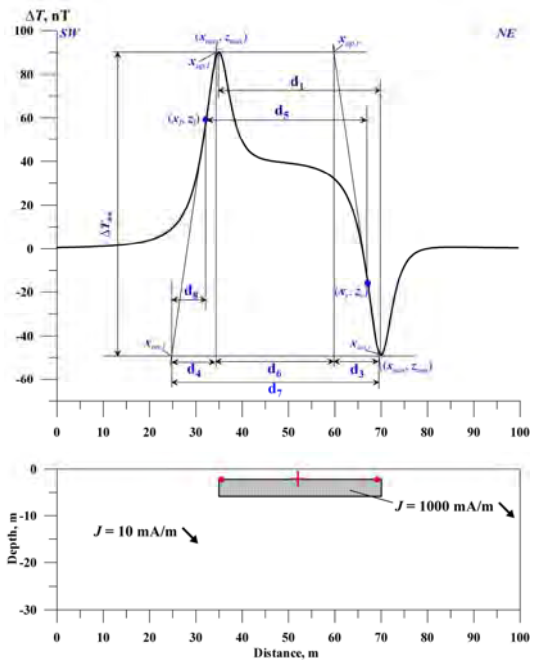

Figure 60. Example of quantitative analysis of magnetic field from the object occupying intermediate position between the model of thick bed and thin horizontal plate (after Eppelbaum, 2013)

Advanced analysis of the magnetic curve enables to obtain coordinates of angle points and middle of the upper edge of the anomalous body with a high accuracy. Note that geometrically this target (Fig. 59c) corresponds to a common Physical-Geological Model (*PGM*) of salt layers occurring in the Dead Sea coast (e.g. Ezersky et al., 2013). If we will substitute corresponding values of magnetization (salt magnetization ≈ -10 mA/m and host medium ≈50 mA/m), we will receive an anomaly from a salt body which could be successfully interpreted by the aforementioned methodology developed for a model of thick bed.

3.2.5.6. Results of magnetometry in the Ghor Al-Haditha (Site 1, Jordan)

The magnetic maps of the Ghor Al-Haditha are shown in Figs. 61a-c in progress. Taking into account that significant negative magnetic anomaly in the lower part essentially distorts the common normal level the initial magnetic map was reconstructed without several disturbing points caused obviously by the modern magnetic noise (Fig. 61a). The elliptical zone 3 of local anomalies is determined more clearly. A linear fault zone 6 of SE – NW trend is delineated, and the contact zone 7 (northern part) is revealed. In Figs. 61a – 61c a position of interpretation profile A – B is presented. Topographic map of the area is shown in Fig. 61b. Fig. 61c displays the map of the vertical gradient of magnetic field. We could propose that the magnetic anomalies compiled in this map, reflect mainly near-surface anomalies. The most part of these anomalies are associated with the elliptical zone 3 and linear gradient zone 4.
It is well known that various transformations play an important role in the potential geophysical field analysis (e.g., Blakely, 1995). It is especially significant when a superposition of anomalies of different order exists. Application of gradient operator (calculation of the gradient magnitude) allowed us to delineate some buried geological objects (Fig. 61d) (Al-Zoubi et al., 2011).

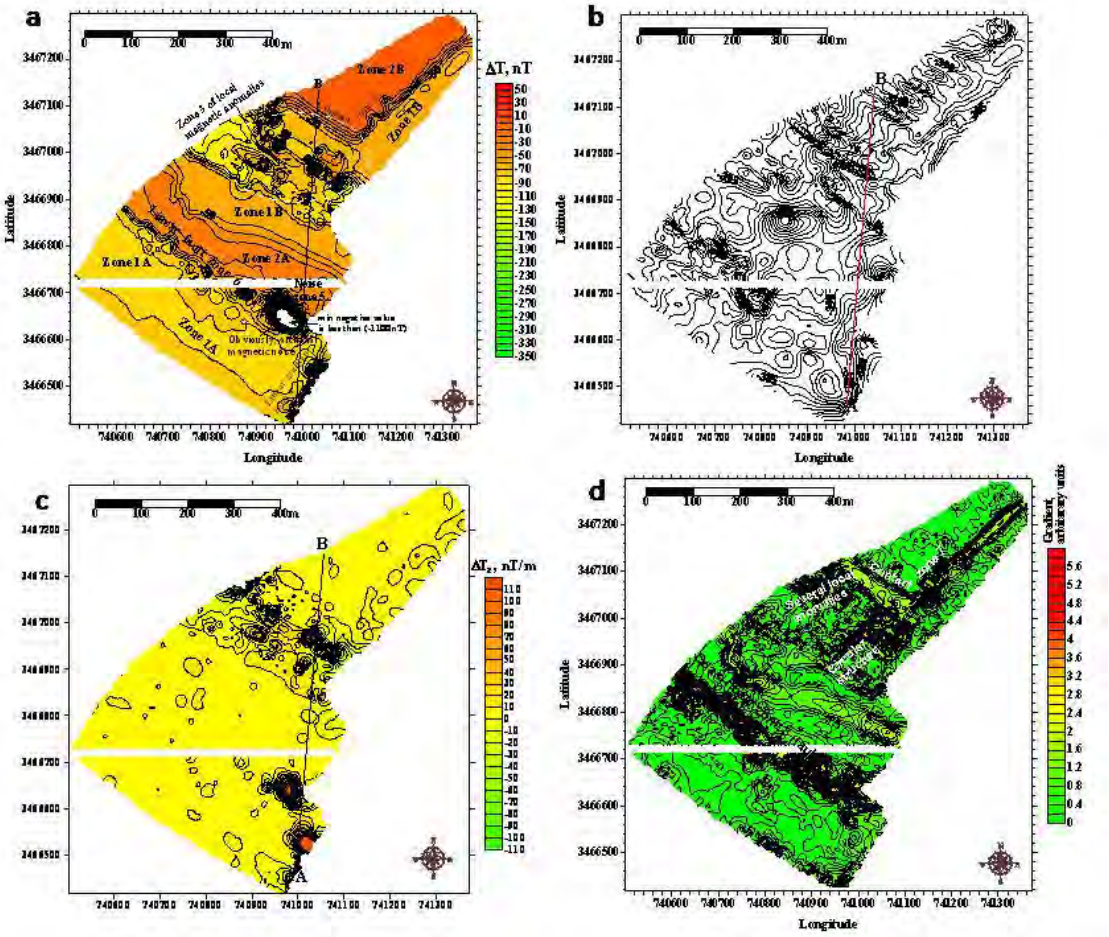

Figure 61(a) Total magnetic map for the area under study with some initial zonation (after removing several noise points); (b) Topographic map of the area under study; (c) Map of the vertical magnetic gradient for the area under study; (d) Total magnetic field map transformed by the use of gradient operator. Line A-B in Figs a-c shows the interpretation profile.

It is necessary to note that the linear fault zone 6 is clearly detected in the improved map of total magnetic field (Fig. 61a) and the total magnetic field map transformed by gradient operator (Fig. 61d) and partially – in the topographic map (Fig. 61b). Contact zone 7 has been distinctly expressed in all three above-mentioned maps. At the same time, application of gradient operator permitted to localize a quasi-circular structure in the upper part of the studied area at the longitudes 741000 – 741100. Figs. 61a and 61c illustrate sufficiently complex behavior of total magnetic field and vertical gradient of the magnetic field, respectively, along the interpretation profile A – B (Fig. 62a). Even simple visual analysis permits conclusion that we have here a superposition of magnetic anomalies of various orders. Analysis of ΔT and T_z comparison indicates to the complex character of the magnetic field in the studied area and possible presence of subsurface faults.

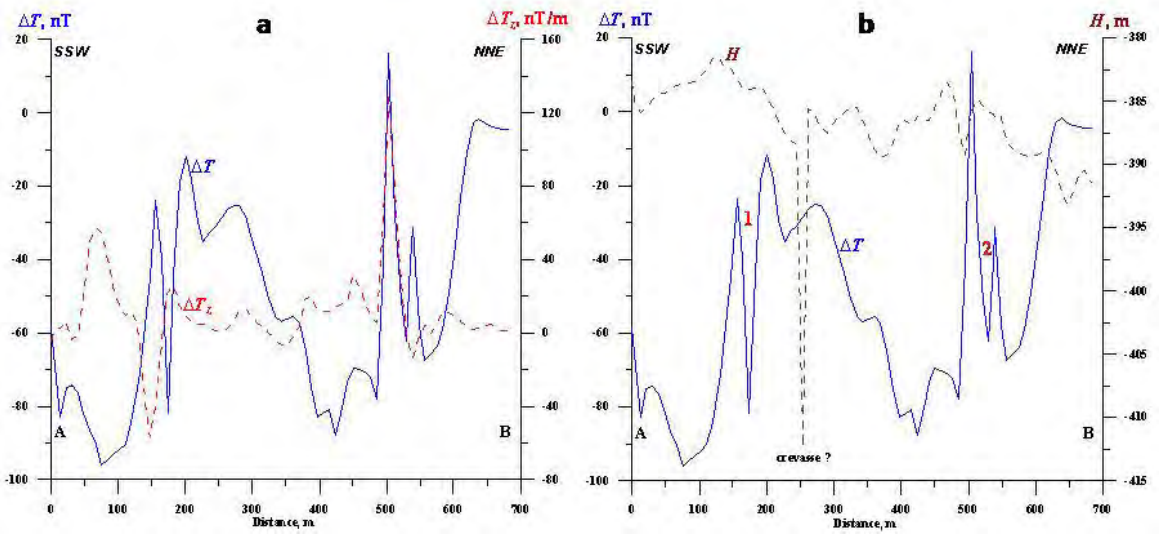

Figure 62. (a) Comparison of total magnetic field (ΔT) and vertical magnetic gradient (T_z) graphs along profile A – B; (b) Comparison of total magnetic field (ΔT) and surface topography (H) graphs along profile A – B

A first conclusion, which follows from the analysis of Fig. 62b, is that we have no any correlation between the magnetic field and topography. It is known indicator that the upper part of the geological section (rocks composing the terrain relief) or nonmagnetic ones or have very low magnetization (e.g., Khesin et al., 1996). Evidently, a local negative topography form at the 250 m may be a crevasse. Performed quantitative analysis of the local negative anomalies 1 and 2 (Fig. 62b) suggests that source of these anomalies (possibly, sinkholes or faults) occurs at the depth of 10-14 m (an interpreting model of the thin bed was utilized (e.g., Eppelbaum et al., 2001)).

3.2.5.7. Results of Microgravity in the Ghor Al-Haditha (Site 1, Jordan)

Microgravity data acquired through the Ghor Al-Haditha area (Al-Zoubi were processed using developed methodology presented in the Section 3.5.2.2. (Al-Zoubi et al. 2013; Eppelbaum, 2013a). Microgravity survey has been carried out at 528 observation points (Al-Zoubi et al., 2011, MERC Project) at the Ghor Haditha site (Jordan) (Fig. 63). All the necessary corrections were introduced by conventional way (e.g., Telford et al., 1993). From the absolute gravity values was deducted value of 979,413.9 mGal.

Fig. 63a and 63b show, respectively, the location of the total number of observed points and location of the observation points in the central area, respectively. The compiled Bouguer residual map (mainly, a kriging algorithm was applied) is presented in Fig. 64a. The horizontal Bouguer gravity gradient in this area (produced by a giant negative anomaly from the DST) consists of about 1 mGal/100 m or 100 Eotvos. Correct removing of this gradient, as it was shown in Eppelbaum et al. (2008), is not a simple problem.

As it was shown in Alexeyev et al. (1996), even in the case of the total Bouguer reduction computation effect of gravity field distortion along inclined terrain profile is not removed; thus a special correction scheme should be applied. It should be noted that the correction system is universal both with anomalous bodies with enhanced and negative densities.

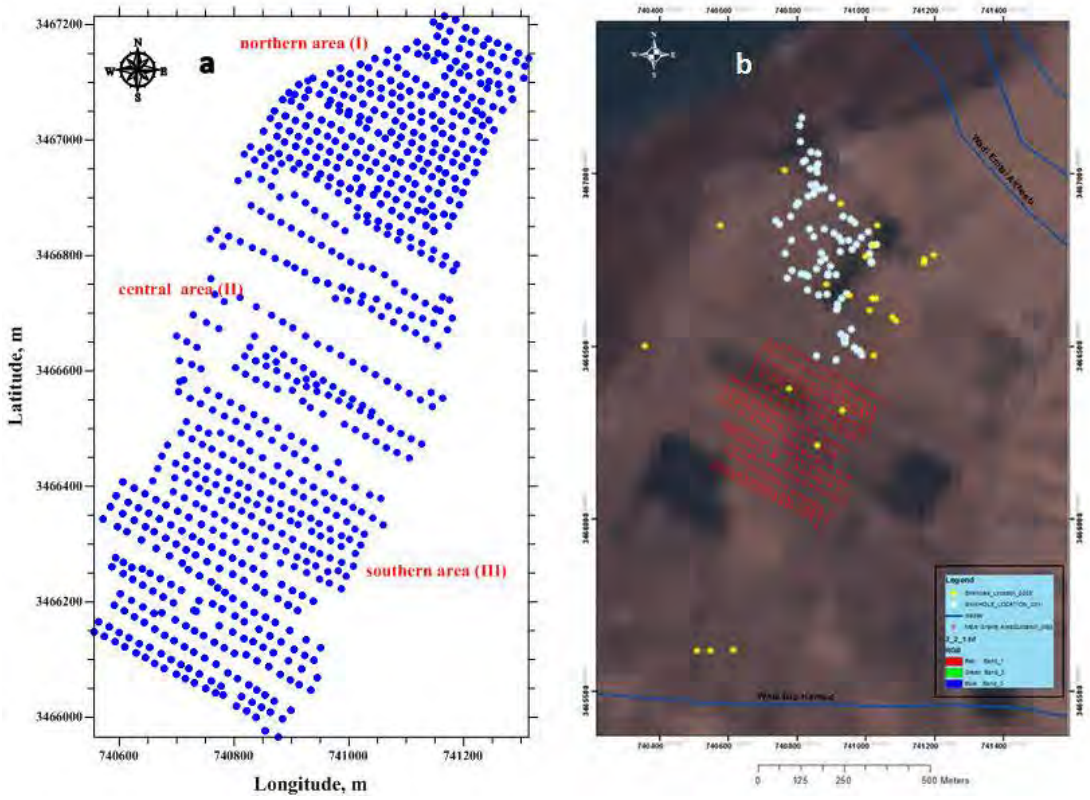

Figure 63. Microgravity location map in the Ghor Al-Haditha area. (a) Entire schema of measurement, (b) Ghor Al-Haditha survey area: red crosses – central area, yellow stars sinkholes location for the period of 2005 and white circles - sinkholes for the period of 2011 (Al-Zoubi et al., 2011, Al-Zoubi and Eppelbaum, 2012)

The area under study – Ghor Al-Haditha – is situated in the eastern coastal plain of the Dead Sea (Jordan) (Fig. 1, Site I) in conditions of very complex regional gravity pattern (Fig. 49).
The satellite gravity data shown in Fig. 49 were obtained from the World Gravity DB as re-tracked from Geosat and ERS-1 altimetry (Sandwell and Smith, 2009). These observations were made with regular global 1-minute grids that can differentiate these data from previous odd surface and airborne gravity measurements. This complex gravity field distribution in the vicinity of the area under study is caused mainly by the strong negative effect of the low density sedimentary associations and salt layers accumulated in the DST and also several other factors. The horizontal gravity gradient in this area (produced by a giant negative anomaly from the Dead Sea Transform) consists of about 1 mGal/100 m or 100 Eotvos. Correct removing of this gradient, as it was shown in Eppelbaum et al. (2008) is not a simple problem.

This section displays the results of gravity field analysis in all three areas (northern, central and southern) together (Fig. 63a). The process of consequential data analysis is presented in two panels (Fig. 64 and 65). Fig. 64a illustrates location of observed gravity points with their values. Even simple visual analysis indicates difficulties of the gravity field pattern due to strong variability of the gravity data. Bouguer gravity map of this area is presented in Fig. 64b. Fig. 64c shows simple planar surface approximation of negative regional gravity background (DST influence). The more complex approximation was singular and not acceptable for calculation. Residual Bouguer gravity map (after subtracting the regional negative trend) is shown in Fig. 64d. Note that the ring anomaly delineated earlier in the process of separate southern area is also shown but less clearly. This fact depicts that such complex gravity patterns as the total Ghor Al-Haditha area should by analyzed by separate parts. Fig. 64e displays the same residual gravity map (see Fig. 64d), but presented in a vector form.

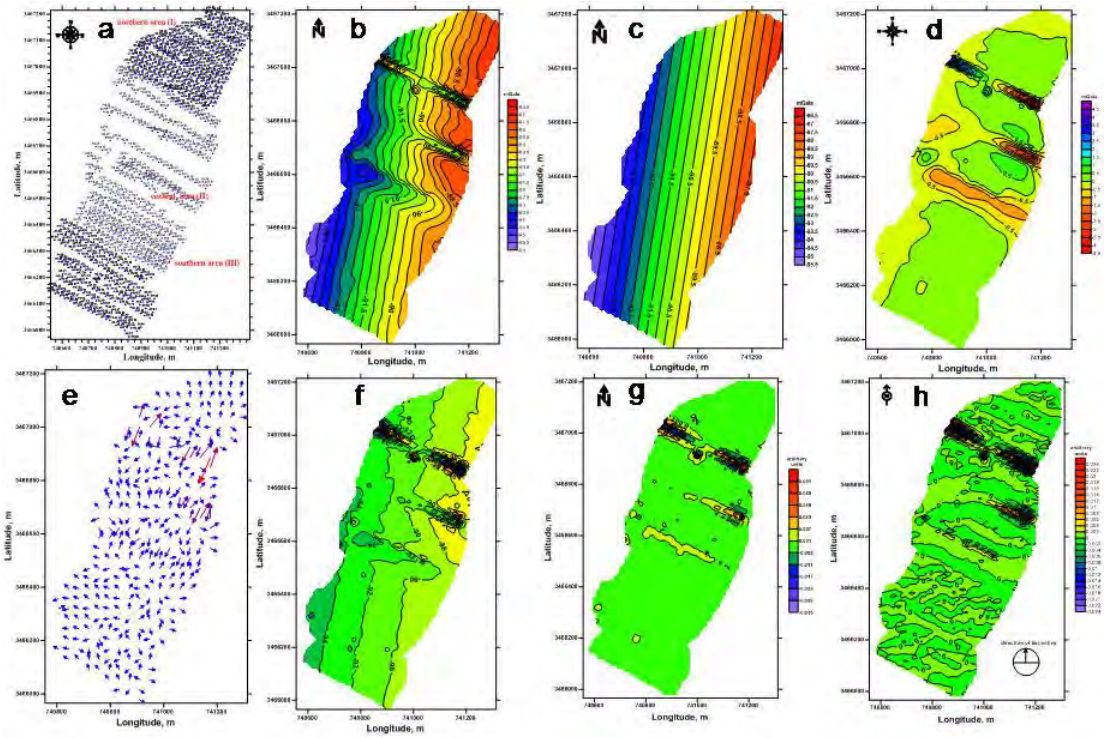

Figure 64. (a) Location of observation points in the total Ghor Al-Haditha area; (b) Bouguer gravity map for the total Ghor Al-Haditha area (isolines are given in mGals); (c) Simple planar surface approximation of regional gravity background for the total area of the Ghor Al-Haditha (isolines are given in mGals); (d) Residual gravity map after removing regional gradient caused by the DST for the total area of the Ghor Al-Haditha (isolines are given in mGals); (e) Residual gravity map after removing regional gradient caused by the DST for the total area of the Ghor Al-Haditha(see previous Figure) presented in a vector form (f) High-pass filtering of the Bouguer gravity map for total area of the Ghor Al-Haditha; (g) Laplasian operator applied to the Bouguer gravity map for total area of the Ghor Al-Haditha (h) Total map of the Ghor Al-Haditha area: Map of the second directional derivatives.

High-pass filtering map (Fig. 64f) and Laplasian operator map (Fig. 64g) do not provide any new information of the medium. Maps of the second vertical directional derivative (Fig. 64h), map of the gradient operator (Fig. 65a), and map of the tangential curvature (Fig. 65b) also do not display new geological information. Terrain aspect operator applied to the Bouguer gravity map shown more interesting results (Fig. 65c). On this pattern some circular anomalies possibly reflecting the buried sinkholes could be recognized. The final map in this section – statistical residual map (Fig. 65d) – was computed as difference between the gravity values in the data file and the interpolated gravity value on a gridded surface. We can see that in this case the intensive linear anomalies in the northern part of the map do not allow performing the correct statistical regularization.

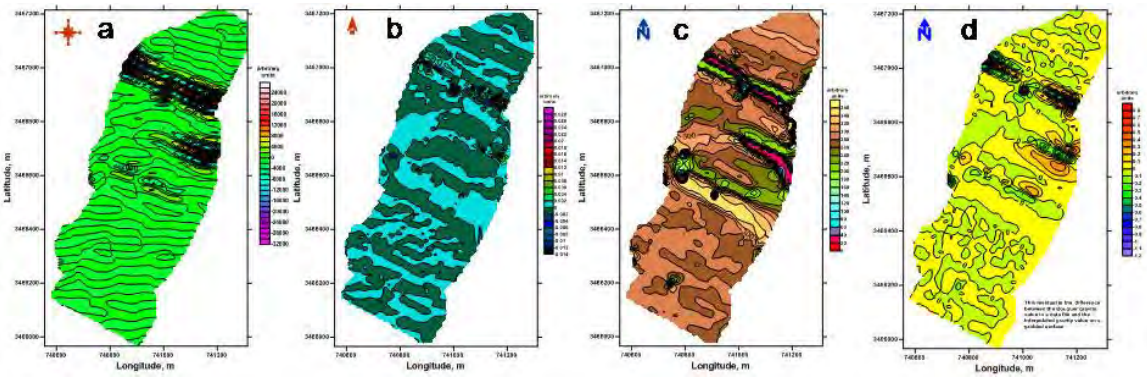

Figure 65. (a) Gradient operator applied to the total Bouguer gravity map of the Ghor Al-Haditha area; (b) Tangential curvature applied to the total Bouguer gravity map of the Ghor Al-Haditha area; (c) Terrain aspect operator applied to the total Bouguer gravity map of the Ghor Al-Haditha area (d) The statistical residual the total Bouguer gravity map of the Ghor Al-Haditha area

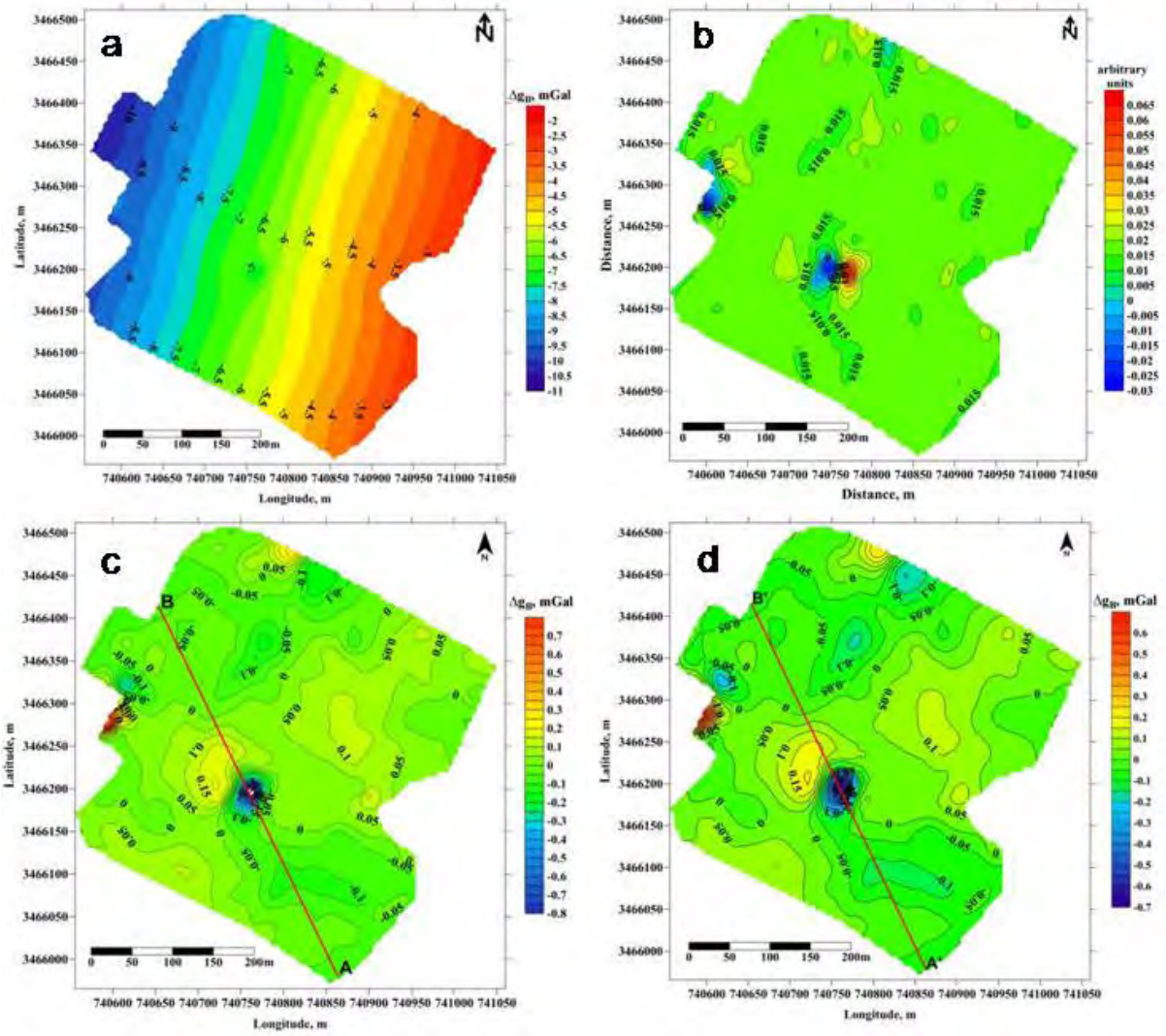

Figure 66. (a) Bouguer gravity map of the Ghor Al-Hadithaarea (Jordan); (b) Results of gradient sounding in the Ghor Al-Haditha area; (c) Residual gravity map of the Ghor Al-Hadithaarea after subtracting bi-linear saddle regression; (d) Residual gravity map of the Ghor Al-Hadithaarea after subtracting local polynomial

The observed gravity map (Fig. 66a) shows the strong influence of the negative gravity effect due to the DST (and possibly other geological factors). Computing the first and second derivatives, self-adjusting filtering, gradient directional filtering, Fourier series, principal component analysis, and other methods were less successful than the bilinear saddle and local polynomial regressions. Fig. 66b displays results of the gradient sounding. After regional trend removal two local anomalies were found: one complex in the center of the area and the other near the western border. Clearly, however, this type of analysis is only valid for target qualitative delineation.

A visual comparison of the residual maps (Figs. 66c and 66d, resp.) shows the great similarity between the two regression methods. A negative anomaly in the center of the map with amplitude of 0.6-0.7 mGal is very visible. An important advantage of the residual maps is that these maps can be used both for qualitative and quantitative analysis. The gravity profiles are constructed along the same line (A–B in Fig. 66c) and (A'–B' in Fig. 66d) demonstrate (Fig. 67) that there are some small differences, mainly in the amplitude value from the anomalous object with a negative density contrast. 3D modeling indicates that such a gravity anomaly may have been produced by a sinkhole with its upper edge occurring at a depth of 4m below the earth's surface (Fig. 68).

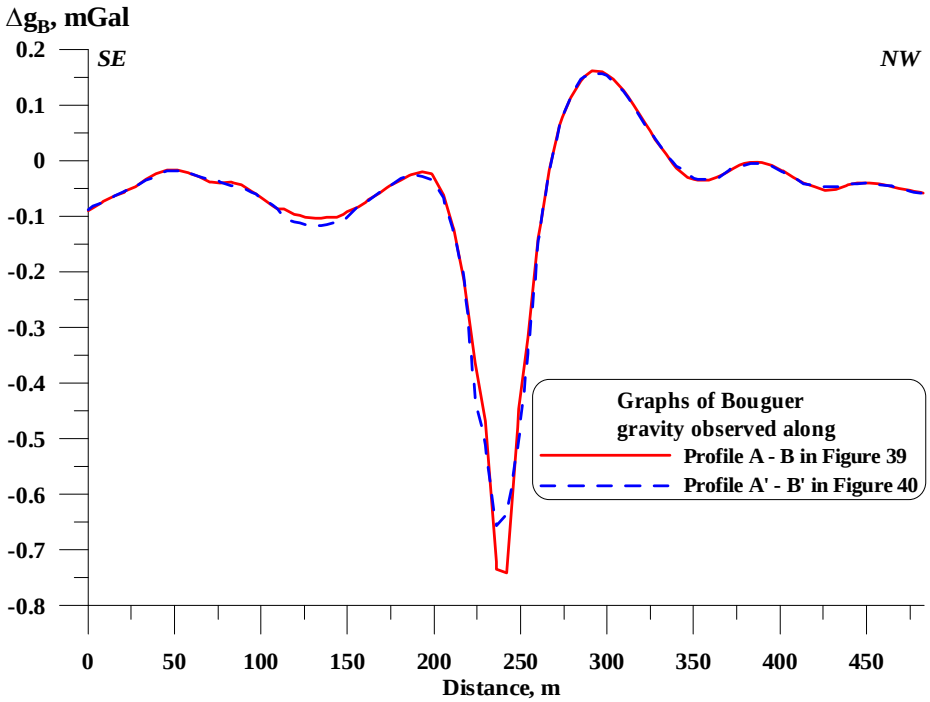

Figure 67. Comparison of gravity curves constructed along profile A – B for Fig. 64c (after subtracting the bi-linear saddle regression), and A' – B' for Fig. 64d after subtracting the local polynomial)

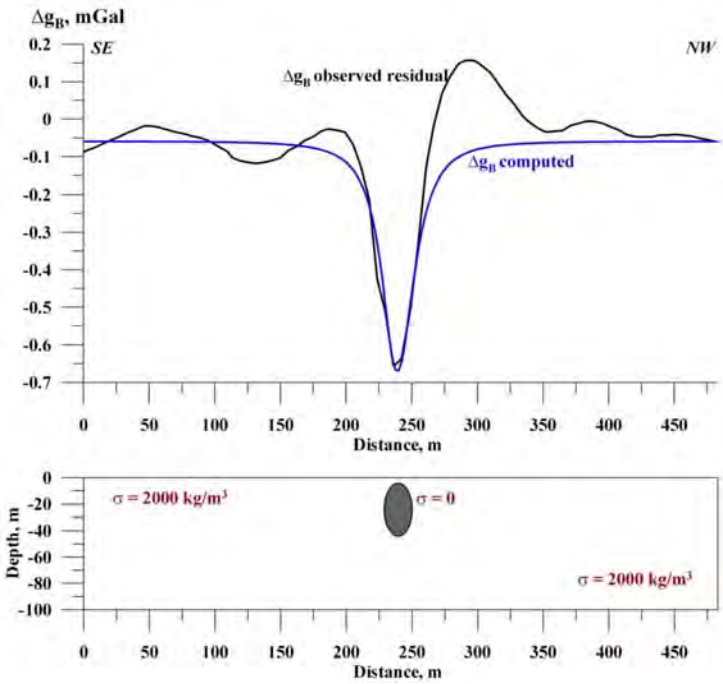

Figure 68. An initial physical-geological model along profile A' – B' developed on the basis of 3D gravity field modeling

The location of this sinkhole and its size are consistent with the available geological data (Al-Zoubi et al., 2012b). The disparity between the observed and computed $\Delta g\ B$ in the right part the profile may have been caused by the presence of an additional small underground cavity with an irregular shape.

3.2.5.8. Combined Modeling of Gravity and Magnetic Fields

Wavelet approach to recognition of karst terranes by the examination of geophysical method integration consists of advanced processing of each geophysical method and nonconventional integration of different geophysical methods between themselves. Modern developments in the wavelet theory and data mining are utilized for the analysis of the integrated data. Wavelet approach ia applied for derivation of enhanced (e.g., coherence portraits) and combined images of geophysical fields observed in the areas ancient remain occurrence. The methodology based on the matching pursuit with wavelet packet dictionaries enables to extract desired signals even from strongly noised data. The recently developed technique of diffusion clustering combined with the abovementioned wavelet methods is utilized in the project to integrate the data and to detect existing irregularities. The goal of the modern geophysical data examination is to detect the geophysical signatures of buried sinkholes at a noisy area via the analysis of some physical parameters with minimal number of false alarms and miss-detections. For analyzing the gravity, magnetic and GPR data (GM-GPR), we used a technique based on the algorithm to characterize a GM-GPR image by a limited number of parameters. This set of parameters serves as a signature of the image and is utilized for discrimination of images containing karst cavity from the images non-containing karst. The constructed algorithm consists of the following main phases: (a) development of the database, (b) characterization of GM-GPR images, (c) and dimensionality reduction. Then, each image is characterized by the histogram of the coherency directions. As a result of the previous steps we obtain two sets **K** (containing karst) and **N** (no containing) of the signatures vectors for images from sections containing karst cavity and non-karst subsurface, respectively.

3.5.2.9. Conclusions to section 3.2.5.

Microgravity surveys are now widely applied for subsurface investigation, especially for sinkholes (karst) phenomenon delineation. The Ghor Al-Haditha area situated in the eastern Dead Sea coast (Jordan) is a perspective object for microgravity (and other geophysical methods) application. However, microgravity observations more strongly than other methods are disturbed by very complex regional gravity pattern and complex topography in this area. After removing the Dead Sea Transform negative gravity effect by linear regressions, gravity anomalies more reliably and clearly were detected. Applications of numerous information, statistical, probabilistic and algebraic approaches at the gravity data sets were effectively applied. Quantitative analysis and 3D modeling were successfully applied to interpretation of several magnetic anomalies. Application in the site of the gravity and other geophysical method includes an employment of advanced combined coherency wavelet interpretation and diffusion maps.

3.2.6. Surface Geophysical Methods (In Israel and Jordan)

(The method and results are presented in details Akkawi et al., 2012; Al-Zoubi et al., 2012, Ezersky et al., 2013c; Frumkin et al., 2011; Levi et al., 2011)

3.2.6.1. General

Subsurface cavities and the processes that lead to the development of sinkholes cause changes in the subsurface (porosity, fracture density, water saturation, etc). These changes may be detected by geophysical methods such as gravity, seismic or electrical resistivity etc. (Ezersky et al., 2006). Therefore geophysical methods would facilitate sinkhole hazard assessment in the coastal areas of the DS in Jordan and Israel.

Surface geophysical methods are widely used for karst detection in most of carbonate karst regions of U.S.A. GPR and microgravity (Benson and Yuhr, 1993, Crawford at al., 1997, Thomas and Roth, 1997), geoelectrical methods (Zhou et al., 1999) etc. Comprehensive review of the geophysics use in the karst problem is given in Benson and Yuhr (1993).

Although methodologies for the detection of sinkholes and other karst features in carbonate rocks (generally limestone) have received much attention worldwide (Beck, 2003) these methodologies need to be adapted, or new methods developed, for the unique environment of evaporate deposits along the DS coast in Jordan and Israel. The main differences between the karst areas in carbonate rocks and the sites with unconsolidated sediments in the DS region is the rapid subsurface dissolution of the salt rock in response to changing environmental conditions. It allows observation for reliability of geophysical predictions in real time.

In addition favorable ground conditions for applying of geophysical instruments are available in the DS coastal area. For instance, seismic velocity of salt formation (of 2900-4000m/s) in the DS graben area is considerably higher than its surrounding rock environment (2100-2700m/s). It permits to map salt formation with a high reliability (Ezersky, 2006). Anomalous high resistivity of the sinkhole development sites was discovered in alluvial fans in Israel and Jordan (Ezersky, 2008, Al-Zoubi et al., 2007). It allows mapping of the sinkhole hazardous zones (Frumkin et al., 2008). Furthermore, it creates promising conditions for use of GPR technique for the detection of the subsurface signs of sinkhole hazard.

Jordanian geophysicists have shown high efficiency of surface geophysical methods to study different aspects of geological applications at conditions of the eastern coast of the DS (Al-Zoubi et al., 2007, Akkawi et al., 2006, Akkawi et al., 2008, Batayneh and Abueladas, 2002). At present geophysical methodology is in progress. New geophysical methods are developing and new objectives are resolving in framework of the Project M27-050 granted by MERC Program. Jordanian researchers develop different geophysical methodology to assess sinkhole hazard using surface geophysical methods such as Electric Resistivity Tomography (ERT), Ground Penetrating Radar (GPR), Electromagnetic Radiation (EMR), Microgravity and Magnetometery, Transient Electromagnetic (TEM). Part of results has been recently published (Frumkin et al., 2011, Ezersky et al., 2011, Abueladas et al., 2011).

Aims of this Section are present development of geophysical methodology of sinkhole hazard assessment and show some examples of its application in the Dead Sea coastal area of Jordan. TEM, Magnetometry and Microgravity results have been brought out to corresponding Sections (3.2.4 and 3.2.5). In this Section we will consider special investigations using Electrical Resistivity Tomography (ERT), Electromagnetic Radiation (EMR) and Ground Penetrating Radar (GPR) used for detection of buried voids (sinkholes) (Frumkin et al., 2011)

The complete schema of ERT, GPR and EMR measurements through the Ghor Al-Haditha area is presented in Fig. 69. The results were published in current reports of Jordanian researchers.

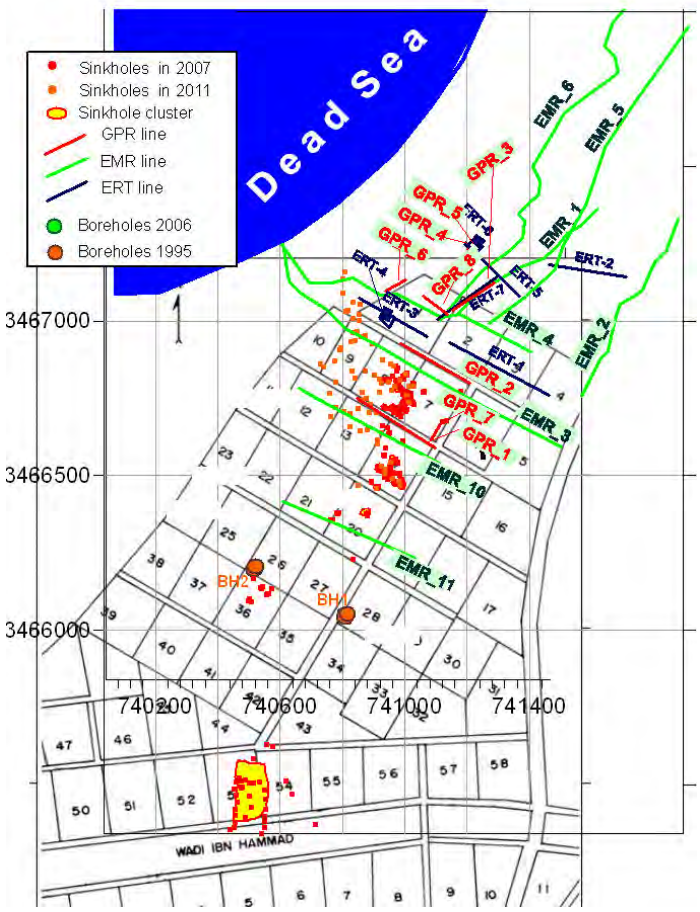

Figure 69. Location map of surface geophysical measurements in the Ghor Al-Haditha area

3.2.6.2. Electrical Resistivity Tomography (ERT)

General. 2D, 3D resistivity prospecting yields information about both the lateral and vertical distribution of resistivity through the geological section and can therefore be used in both qualitative and quantitative ways for the identification of structure and features at shallow depths. For this purpose the ERT method has been used (Lock and Barker, 1996). The subsurface resistivity distribution is determined by measurements performed on the ground surface. From these measurements, the distribution of a true resistivity of the subsurface is estimated. The geoelectrical method is adopted in geological engineering and hydrogeological applications, because of it high efficiency for detecting the presence of heterogeneities (cavities, ore bodies, etc.). This method could be also used for differentiation of such rock layers as clay, marl, sand, sandstone, limestone and water saturated soils and rocks. Quantitative interpretation of the results should be based on *modified Archie's Law* (Keller and Frischknecht, 1966), which establishes that in *partially* saturated soil with ionic pore water conductivity (*above water table*), bulk electrical resistivity depends on the porosity, pore volume occupied by the fluid and the resistivity of the fluid filling the pore space. In case of partially saturated medium bulk resistivity will be expressed:

$$\rho_x = a\rho_w S^{-n}\phi^{-m} \qquad (15)$$

where parameters ρ_x, ρ_w ϕ, a and m are as in (5), S=V_{el}/V_{Σ} is a fraction of the total pore volume filled with the same electrolyte (named also *degree of soil pore filling*); V_{el} is the volume of the electrolyte in pores; V_{Σ} is the total pore volume per unit volume of soil (that is by fact ϕ); n is an empirical parameter termed the *saturation exponent* (it usually has a value of approximately 2).

Expression (5) can be transformed taking into account that $V_{\Sigma} = \phi$. Then:

$$\rho_x = a\rho_w S^{-n}\phi^{-m} = a\rho_w (V_{el}/\phi)^{-n}\phi^{-m} = a\rho_w V_{el}^{-n}(\phi)^{m/n}$$

Accepting for the DS alluvium m= -2 (Kafri and Goldman, 2005) and n= -2 (Keller and Frischknecht, 1966) and m/n$\cong$1 we can rewrite (5):

$$\rho_x \cong a\rho_w V_{el}^{-2}\phi \qquad (16)$$

As it follows from the modified Archie's Law resistivity of the unsaturated sediments is determined by their porosity. The higher is porosity, the higher is resistivity. It will also depend on relative volume of electrolyte V_{el} (per volume unit) in pores and resistivity of fluid ρ_w.

Note the higher porosity of shallow sediments in sinkhole development sites is caused by the cavity presence at the depth (Maimon et al., 2005). Therefore the ERT method was firstly used in the Dead Sea sinkhole problem to detect subsurface high resistivity anomalies caused by the heighten porosity of the subsurface sediments (Ezersky, 2003, 2008, Al-Zoubi et al., 2007).

Equipment, data acquisition and processing.

The ERT studies in both Israel and Jordan were carried out using multichannel systems of the IRIS Instruments (Orleans, France). In Israel the measurements were carried out using an IRIS SYSCAL R2 resistivity meter with multi-electrode switching system comprised of 4 intelligent nodes 16 channels everyone. Entire system allows performing of automatic measurements using 64 electrodes. In Jordan the multi-electrode survey was conducted using Syscal-Pro Instrument with 48 electrodes.

We will consider 2D and 3D ERT techniques using results of measurements along line ERT-3 in Jordan as example (See Fig. 69 for location).

The 2-D electrical tomography survey used large number of electrodes connected to a seismic cable used as multi-electrodes cable. The measurements were read automatically by an electronic switching unit along the resistivity profile. Wenner–Schlumberger array was used that is a mixture between Wenner and Schlumberger arrays (Fig. 70a). This array allows the measuring of resistivity changes in the horizontal direction, as well as the detecting of lateral resistivity anomalies along the survey profiles (Pazdirek and Balha 1996). The array combines the advantages of the two different arrays. Some profiles were extended using a roll along technique (Dahlin 1996).

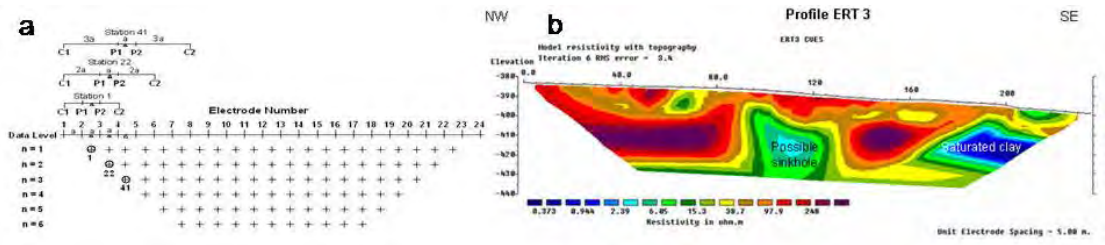

Figure 70. (a) The arrangement of electrode for a 2-D electrical survey and pseudo-section data pattern for the Wenner-Schlumberger arrays; (b) Model resistivity cross section along profile ERT 3.

Profile ERT-3 is about 235 m long and located farther to the west of the study area. The investigation depth that depends on the electrode array is of 60m. The low restive materials dominate at the resistivity section (Fig. 70b). The very low resistive layer less than 1 Ωm at the end of the profile (20m thickness layer at a depth of 10 m) represents clay saturated with the DS brine. The low resistivity zone (2.5-8 Ωm) located at the middle of the profile (about 10 m deep) may represent forthcoming developing sinkhole (Fig.70b).

Fig. 71 shows example of 3D multi-electrode imaging survey (ERT-4) that was carried out at the center of 2D ERT-3 line (see Fig. 69 for location). The Wenner-Schlumberger configuration was used for 3-D survey. The 48 multi electrodes cables were oriented in the X-direction, which is approximately east to west with a five meter spacing for X and Y directions (Fig. 71a).

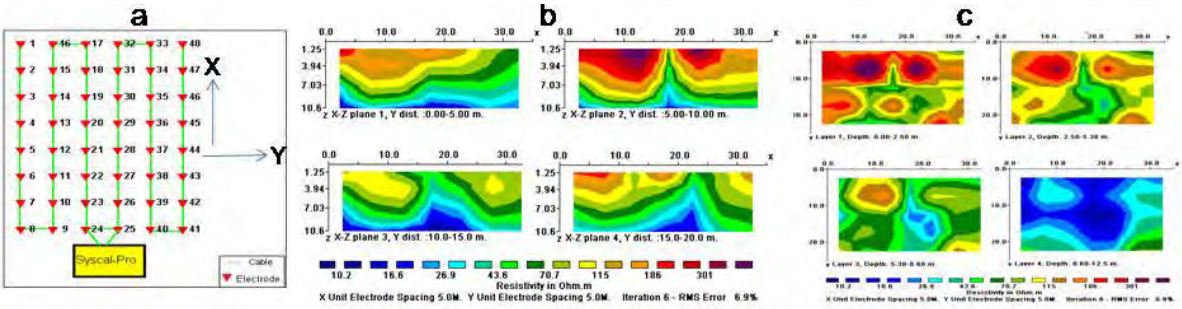

Figure 71. (a) 3D ERT study in Jordan. (a) The lay-outs of potential electrodes for the 3-D Wenner-Schlumberger electrical array; (b) Vertical X-Z inverse resistivity cross-sections along Y axis at distances = 0-5, 5-10, 10-15 and 15-20 m; (c) Horizontal X-Y inverse resistivity maps along Z axis at layer depths of 0-2.50m, 2.5-5.0m, 5.0-7.5m and 7.5–10m.

The outputs of the three dimensional modeling is a series vertical sections along one of horizontal axis and horizontal slices (resistivity maps) at different depths ranges across the areas of survey grid. In our case vertical resistivity cross-sections are presented by X-Z planes located along the Y-axis with distances of 5m (Fig. 71b). Horizontal slices are presented in Fig. 71c as resistivity maps of layers located at different depth intervals. Because of limited sizes of the resistivity array (here, 35m along X and 25m along Y directions) investigation depth is also limited by 10m (compare with 60m investigation depth along line ERT-3).
The Fig. 3Sc shows the resistivity changes for the slices with depth through X-Y horizontal plan from the surfaces to 10 m deep. Resistivity of the layers is decreased as the horizontal distance increased from the surface. The very low resistivity layer depth along this profile correlated the same depth along ERT3.

Real examples. Israeli and Jordanian researchers have used ERT studies to detect subsurface anomalies, cavities and formations and to anticipate imminent collapse Ghor Al-Haditha and Mineral Beach sites, following sinkhole development in these areas.

In Jordan. Here we present an example of two ERT sections along lines No. 1 and 2 carried out in the Ghor Al-Haditha area (Fig. 72a).

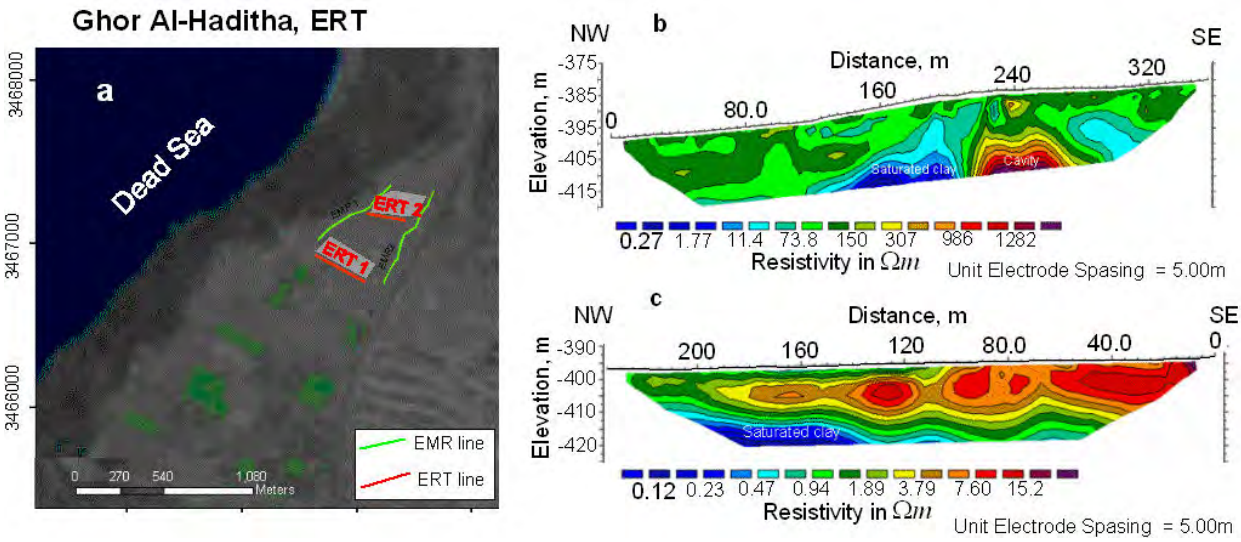

Figure 72. ERT results in Israel and Jordan. (a) ERT location map at the Mineral Beach area; (b1-b4) inverse resistivity sections along ERT lines; (c) location map of two ERT sections at the Ghor Al-Haditha area; (d1 and d2) inverse resistivity sections along respective ERT lines.

Wenner–Schlumberger array (a mixture between Wenner and Schlumberger arrays) allowing detecting of lateral resistivity changes was applied. The array combines the advantages of the two separated array modes. A characteristic feature of the section along line ERT 1 is a high resistivity anomaly of 2000 Ωm at 240 m distance and 10-15m depth. The anomaly contrasts with the low resistivity background of 15-100 Ωm (Fig. 72b). Conversely, ERT 2 section located some 400 m northward shows low resistivity values (1-50 Ωm) throughout the whole section (Fig. 72c). Similar background resistivity is typical for the DS area vadose zone. However, as mentioned above, sites of sinkhole development are characterized by higher resistivity values. Following the results in Shalem-2, we hypothesize that the anomaly detected by line ERT 1 is related to a gradually stoping cavity possibly indicating an imminent sinkhole.

<u>In Israel.</u> 5 ERT lines were surveyed at the Mineral Beach area (Site II in Fig. 1) during a period of active sinkhole development (2011-2012) over an area of 300×550 m2 (Fig. 73a).

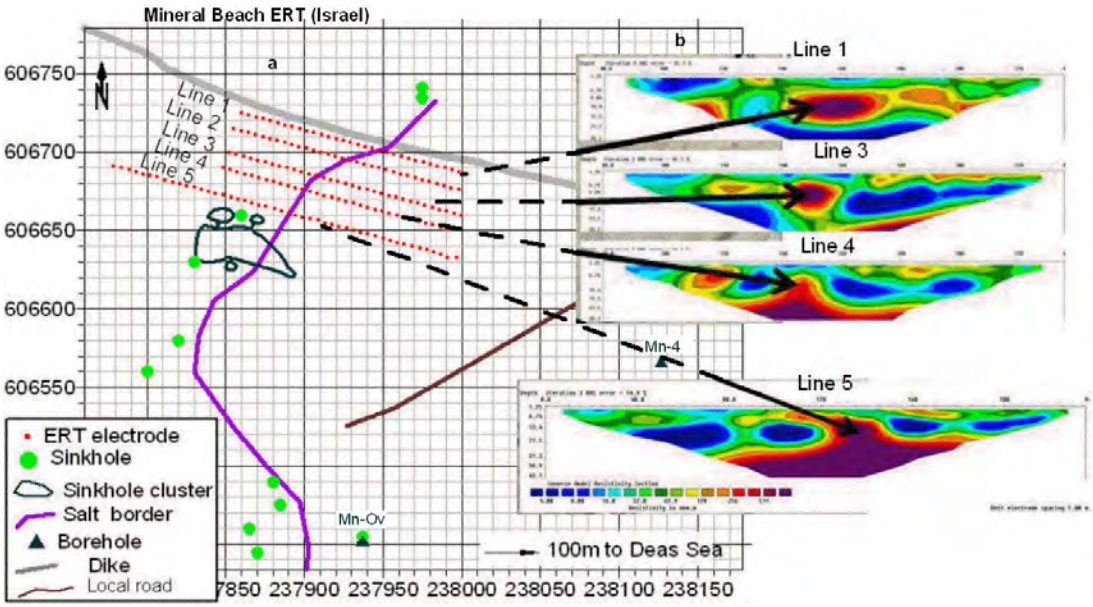

Figure 73. ERT results in Israel and Jordan. (a) ERT location map at the Mineral Beach area; (b1-b4) inverse resistivity sections along ERT lines; (c) location map of two ERT sections at the Ghor Al-Haditha area; (d1 and d2) inverse resistivity sections along respective ERT lines.

All ERT data have high noise level caused by high contact resistance of the electrodes with the dry Alluvium. Despite the noise, the 2D inversion sections (Figs. 73b Lines 1-4) show high resistivity anomaly (ρ_x>1000Ωm) at depth of ~13m and wide of 10-30m extended perpendicularly to all the lines. This anomaly match well with the salt edge delineated using seismic refraction method (Frumkin et al., 2011) and presented in Fig. 73a.

The spatial resistivity distribution is seen well on the resistivity maps constructed through the Mineral Beach area presented in Fig. 74. Such presentation is similar to quasi 3D ERT method described by Ezersky (2008). The method is based on extrapolation resistivities between separate lines and allows detection of heterogeneities with size more than separation between ERT lines.

One can see in Fig. 74b that there are high resistivity anomalies that presumably associated with decompaction of subsurface. Zones of higher resistivities are drawn towards the salt edge (shown in Fig. 73) by solid black line). Note that shallowest map is composed of resistivity values ranged mainly between 8 and 128Ωm. High resistivity anomaly (ρ_x > 260Ωm) appears on maps at 6.8 and deeper depths. Following the results in Mineral Beach, we hypothesize that the high resistivity anomalies detected by ERT lines are related to soils decompaction caused by gradual collapsing of soil into dissolution cavities at 40m deep. This process was considered by Frumkin et al. (2011). The decompaction gradually ascends with a time to surface resulting in sinkhole forming. Perhaps, there are cavities existing for a long time like that detected by borehole Mn-Ov (Fig. 73a).

The pre-existing sinkholes were suggested by Legchenko et al. (2008a). Abelson et al. (2013) reported heighten microseismic activity in vicinity of salt edge detected during monitoring in the Mineral Beach. Two above zones are conformed. Thus, we suggest that high resistivity of subsurface is caused by dissolution cavities within the salt layer along dissolution front. Falling of the soil and stones into these cavities causes microseismic events recorded by Abelson et al. (2013). He suggested also dissolution cavities within salt are formed 15 years before their appearance at surface.

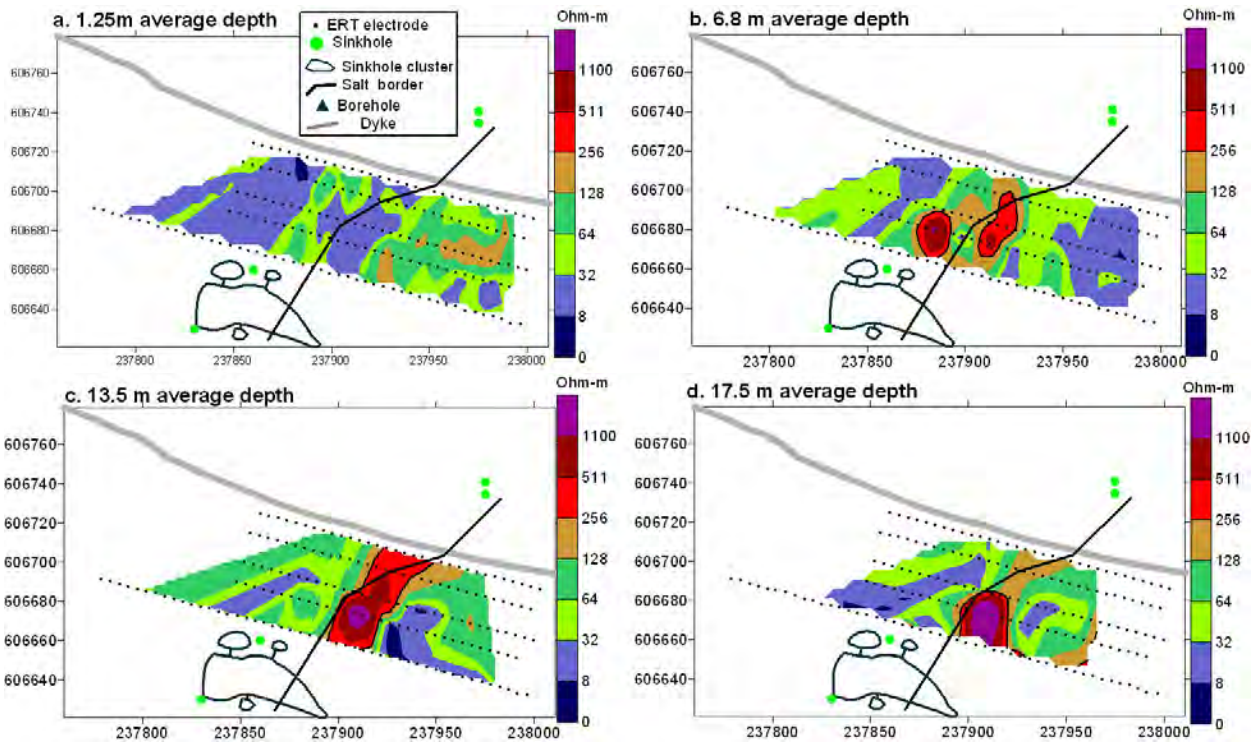

Figure 74. Inverse resistivity maps through the Mineral Beach area constructed for difference depths using 2D resistivity sections (quasi 3D survey after Ezersky, 2008). a-d – maps for different average depths denoted at maps.

3.2.6.3. Electro Magnetic Radiation (EMR) Method

The electromagnetic radiation (EMR) is the technique was used in this study to achieve the aim of this study. The principle of this method is the energy release from the fault and fractured activities. These are considered as zones of weakness of the groundwater discharge at the Dead Sea area.

The electromagnetic radiation (EMR) from rock and soil is known phenomena described in the literature (Cress et al., 1987; Gokhberg et al., 1982; Kennedy, 1968, Yoshino, 1991; Wang et al., 2007). The origin of the electromagnetic emission is not completely clear but it is studying in the laboratory (Cress et al., 1987, Wang et al., 2007) and in-situ (Akkawi et al., 2006, 2008, Gokhberg et al., 1982, Yoshino 1991). It was established that electromagnetic emission arises at the deformations of rocks and soil preceding to the earthquakes, collapse of surface etc. That is why the method is tested for prediction of the earthquakes and sinkhole collapse.

The development of the sinkholes tends to be influenced by underground mass mobilization; mass transportation cultivated by alluvium. Deformation of the soil, water flow causes the electromagnetic radiation (energy) that emanates in a wave like motion from features on the surface of the earth. This radiation is usually in a great many bands throughout most of the electromagnetic spectrum (Fakhry et al., 2004).

Kennedy (1968) has shown that microwave radiometers may be able to detect subsurface voids associated with karst development beneath relatively thick soil cover. To prove the potential of microwave surveys in locating and mapping subsurface voids, a mobile laboratory unit was used to obtain in situ data in the subsurface karst development area (Cool City, El Dorado County, California). The unit was equipped with passive microwave radiometers operating at 13.4-94 GHz (2.22cm-3.2mm wave length). The microwave survey showed significant radiometric "cold" anomalies associated with void-space development beneath several tens of feet of soil cover. Detection was positive in almost all cases, evidence of the strong probability that microwave systems may be used to detect and rapidly map karst systems from a remote platform. If such method will so successful it will greatly reduce surveying and construction costs in areas where caves and sinkholes have developed beneath obscuring soil cover.

The electromagnetic radiation (EMR) method depends on the measurement of natural pulsed low frequency. The electromagnetic radiation starts during crystal deformation superior to and at the same time of the nucleation phase of nanocracks. Where the more fractures are formed the more electromagnetic pulses are emitted. The emission and the radiation direction are normal with the fracture surfaces because of the polarization.

The EMR is used for identifying the underground active faults and fractured zone along the Dead Sea. These faults and joints are considered to be zones of weakness for the groundwater discharge along the shoreline. In the first experiments at the Dead Sea (Sweima-2) area (Akkawi et al., 2008) carried out by Jordanian researchers using the EMR high radiation energy was observed in some narrow of 5-10m zones, where many active faults and joints were found later. The main fractured zone of 15m long was detected along EMR line. We have suggested that likewise the buried sinkholes could be identified by using this method.

Equipment, data acquisition and processing. The EMR study was carried out in the Ghor Al-Haditha (only) using the Cerescope device intended for Fig. 75a. It is a scientific instrument for detection and registration of transient pulses of electromagnetic radiation (EMR), which produced by nanofractures, and by piezoelectric, turboelectric or pyroelectric effects (Bahat et al, 2005). Interpretation of the EMR-records is based (1) on empirical criterions and experience of researcher; (2) on analysis of detected EMR pulses (Akkawi et al., 2006, 2008): active faults are characterized by short (less than 10m) intensive pulses along the measurement line whereas sinkhole zones are significantly longer (15-20m and over) (Fig. 75b). Highly fractured zones (Fig. 75c) are characterized by long pulses (decades meters) of low intensity.

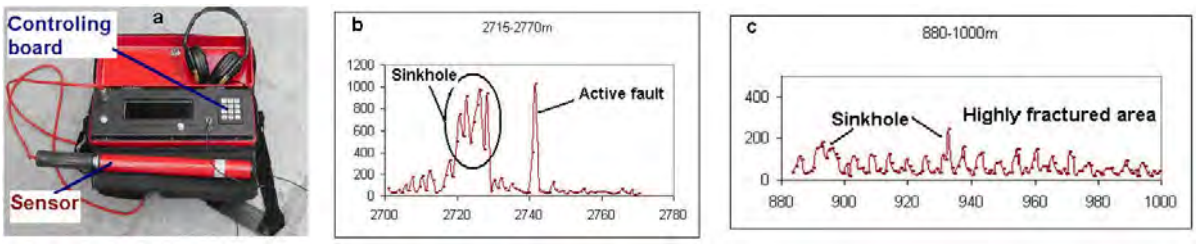

Figure 75. EMR data recording and interpreting. (a) CERESKOPE device; (b) empirically revealed examples of EMR-records for sinkholes and active faults and (c) for highly fractured areas (after Akkawi et al., 2008)

With these criterions we will then consider EMR-records obtained in the Ghor Al-Haditha area.

Line 1 (Fig. 76a) shows two main high EMR energies, the first one located at the southern part of the profile which represents a sinkhole. The second high energy peak at the northern part of the line

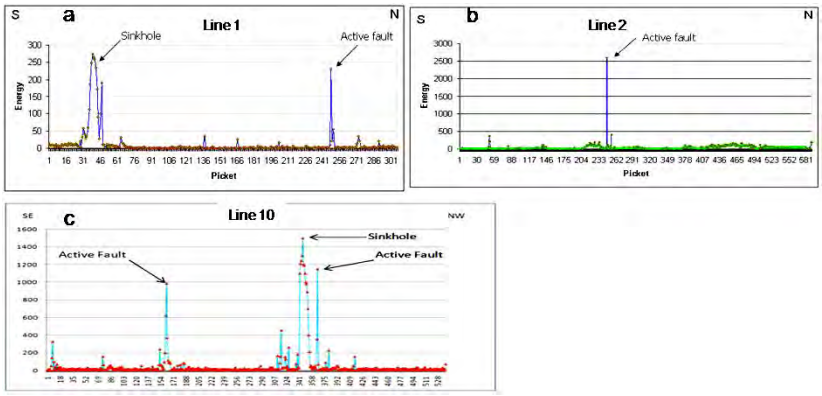

Figure 76. EMR record obtained in the Ghor Al-Haditha along line 1(see Fig. 69 for location).

represents active faults. At Line 2 (Fig. 76b) only one main high energy EMR pulse is appeared, which represents an active fault located at the middle of the profile. Finally, line 10 (Fig. 76c) located at the center of Ghor Al-Haditha area shows EMR record associated with sinkhole area. One can see in Fig. 69 that these sinkhole area is conformed to sinkhole group.

Note there are lines where EMR pulses are not correspond to sinkholes. It can be explained by high level of electromagnetic noises in the places of people activity. Thus, EMR method should be combined with other geophysical methods. The development of the EMR method it seems to be continued and its origin must be understood better.

3.2.6.4. Ground Penetrating Radar (GPR) Method

The GPR method is based on the transmission of electromagnetic waves into the underground and the receiving of reflected waves from objects or interfaces. A radar system comprises a signal generator, transmission and reception antennae and receiver. The system has an onboard computer that facilitates data processing both while acquiring data in the field and post-recording (Reynolds, 1997). As the antenna is moved on the top ground surface, the receiver signals are displayed as a function of their two-way travel time, i.e. the time taken from the instant of transmission to time of detection by the receiver, in the form of *radargram*. The advantages of GPR technique are that it can be used over hard surfaces such as road pavement and that it can give a vertical section through the deposits. In low-loss medium the reflection depth of an electromagnetic wave (S) is:

$$S = \frac{t * C}{2\sqrt{\varepsilon_r}}, \qquad (17)$$

where t is the two-way travel time, determined from the radargram, C is the speed of light in free space and ε_r is the relative dielectric constant, which is 1 for air and 81 for water. Thus, disadvantage is that this technique does not like humidity and salinity in the soil as this quickly reduces the depth to which the radio waves can penetrate.

GPR is a high-resolution method of imaging soil and structures that differ in their dielectric constant (ε_r), using electromagnetic waves (EM) in the frequency band of 10-1000 MHz It is a non-destructive and noninvasive method that detects electrical discontinuities in shallow subsurface. The GPR is extensively used for a variety of applications, in particular for the location of the shallow subsurface voids (at first decade meters). This task is very important in short-time prediction of surface collapse. Among all the high-resolution geophysical methods, GPR has been proven as the most suitable method for detection of shallow subsurface karstic cavities and sinkholes, in a wide range of soil and rock conditions (Benson et al, 1993, Beres et al, 2001, Casas et al., 1996, Mellett, 1995).

Through the DS area dielectric constant is varied in wide range from ε_r =3-6 (alluvial fans) to ε_r =25-45 (mud flats). Such wide range is determined by alternating of the soil salinity from very high at the mud flat sites (where sediments are saturated with the DS brine) to very low at the alluvial fan

sites (where sediments are strongly decompacted). However, sinkhole hazard is highest at the latter sites where dwellings and roads are located in both Israel and Jordan.
It can be said that there are favorable ground conditions for applying of geophysical instruments in the DS coastal area. Anomalous high resistivity of the sinkhole development sites was discovered in alluvial fans in Israel and Jordan (Ezersky, 2008, Al-Zoubi et al., 2007). It allows mapping of the sinkhole hazardous zones (Frumkin et al., 2007). Moreover, it creates promising conditions for use of GPR technique for the detection of the subsurface signs of sinkhole hazard. It has been shown that there should be observed some signs of the deep karst in the uppermost subsurface. They are heightened porosity, shear fractures and deformations of the layers (subsidence) predicted by the theoretical models. Usually the GPR images shaped like the hyperbolic anomalies are looking for. These anomalies are generated at reflection of electromagnetic waves from void surface. In the DS area voids and caverns of complicated forms arise as result of salt dissolution and collapse of the overlain soil into cavity. Collapse takes place in vicinity of the dissolved cavity. Then cavity begins gradual "floating" up to surface (stopping). Sinkhole forms when cavity reaches the surface. It is durable process that depends on the soil properties and size of cavity. During this period void can be detected by GPR method before surface collapse (Ezersky et al., 2006, Bataynh et al., 2002). There are also other predictors of the sinkhole hazard. Apart from voids and cavities they are buried (refilled) sinkholes, vertical and horizontal faults and fractures etc. disturbing the subsurface structure. These signs of sinkhole hazard are widely present in the sinkhole development areas in Israel and Jordan especially in the sinkhole strip arranged along the salt edge. One of such examples from Israeli side has been published in our joint paper (Frumkin et al. 2011). This example illustrates mentioned above signs of sinkhole hazard.

Interpreting of the GPR data is based on identification of the subsurface structural features that would be predictors of the sinkhole hazard. As it was predicted by the DS sinkhole formation models deformations of the subsurface layers can accept characteristic forms (voids, subsidence, vertical and horizontal fractures, buried sinkholes etc), which can be detected by the GPR technique (Frumkin et al., 2009). At that zone of sinkhole hazard can be localized within 150m width zone along the salt edge. This methodology has proved its high efficiency for sinkhole hazard assessment. Therefore there are very prominent GPR surveys carried in both countries (Arkin et al., 2002, Batayneh et al., 2002, Ezersky et al., 2006, Frumkin et al., 2009, Frumkin et al., 2011).

For geological applications, where often depth penetration tends to be more important than high resolution, antennas for frequencies of not more than 400-500 MHz are used.

Equipment and data processing and interpreting. In both areas continuous GPR profiles were surveyed using a SIR-20 system manufactured by GSSI (USA) came into operation using 400 MHz and 10 MHz frequency monostatic system antennas. Maximum depth penetration was greater than 15 m over most of the site for 10 MHz, 6-8m for 40-50 MHz antenna and 3 m for 400 MHz one. WINRAD A/VA 5 software was applied for post processing.

The survey in Jordan has been carried out using SIR-20 instrument (GSSI, USA). Two types of antenna 40MHz and 100MHz were used. Eight GPR profiles were conducted in the sinkholes area (Fig. 69).

GPR Line 1 runs from SE to NW with about 295m long (Fig. 77). The radar cross section along line 1 shows a main anomaly located at a shallow depth and extended for about 3 m may represent an subsidence associated to old buried sinkhole. GPR Line 7 runs from NE to SW with 64 m long (Fig. 77b). The two shallow half meter deep anomalies at distance 0.75 and 1.25 m represent two possible cavities.

Then we report on our GPR study carried out in the Mineral Beach site in framework of another Project. However it is given here for comparison to show the same origin of GPR anomalies (Frumkin et al., 2011). The study was aimed to detect hazardous locations along the dirt road connecting the Mineral SPA to Route #90. The dirt road runs perpendicular to the salt edge, crossing it at the south-western part of site

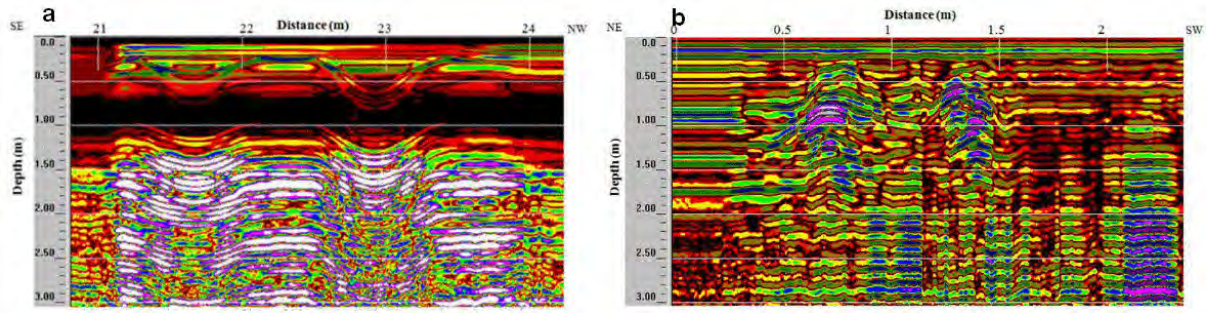

Figure 77. Examples of GPR anomalies recorded in the Ghor Al-Haditha area. (a) GPR Line 1. Subsidence associated to old buried sinkhole; (b) GPR Line 7. Two anomalies linked to subsurface voids.

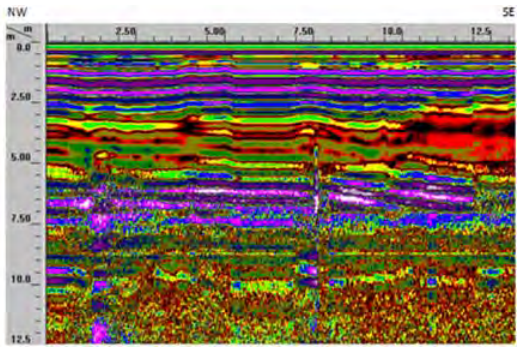

Figure 78. A GPR radar cross section along GPR MUD2 line carried out using 100 MHz antenna. The vertical anomaly located at 7.5 from the beginning of the profile and about 5 meter deep may represent subsurface fracture.

Five GPR lines were carried out at Mineral Beach site along the dirt road where sinkhole hazard was suspected. Antennae 400 MHz were used. On November 2008 the dirt road surface topography along line 1 was smooth, with a slight slope 0.2 m high at the western part. Three anomalies can be distinguished in the radargram acquired along line 1 on November 2008 (Fig. 79 lower 2D section).

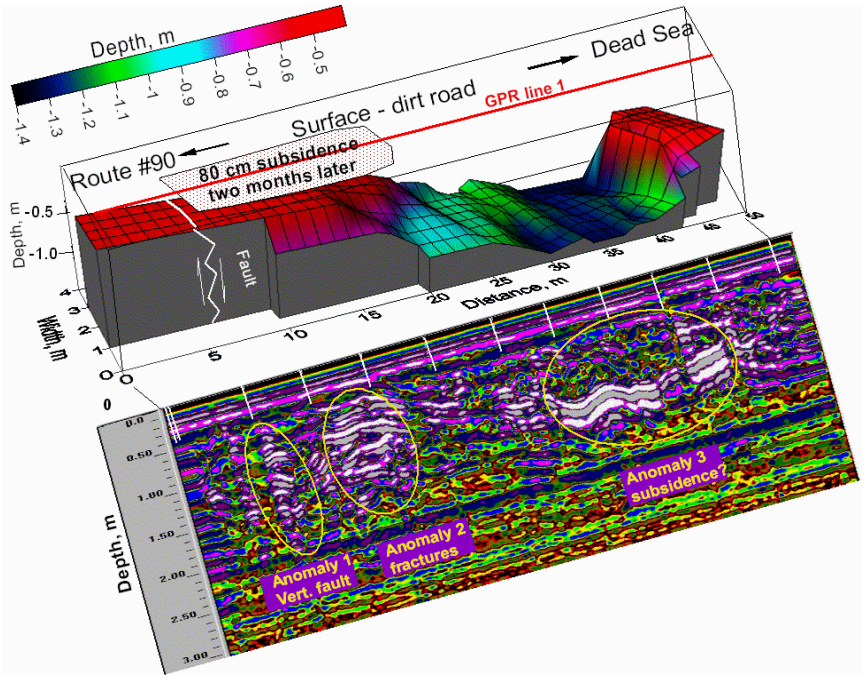

Figure 79. 3D presentation of the anomalous surface detected by the GPR scanning in the Mineral Beach sinkhole forming area: schema of measurements and 3D surface of reflector (upper figure) and GPR 2D section (lower one).

The western-most anomaly no. 1 corresponds to a vertical structure, apparently a fault or fracture. Anomaly 2 reveals a disturbed medium interpreted as fractures and voids filled with air. Finally, anomaly 3 is a strong reflector whose pores can be filled with air or water. Anomalies 2 and 3 reveal an inclined and sagged layer. No signs of sinkholes were seen on the surface. The shape of anomalous reflector is shown in the 3D presentation (upper figure) generated with the profiles acquired along 5 lines. Two weeks later a sharp scarp formed at the place of anomaly 1. One month later vertical shift 0.8-1.0m in height was developed and a new collapse sinkhole was formed. The surface has then subsided at the location of anomaly 2. A sinkhole 5 m in diameter and 2 m deep formed above anomaly 2, and concentric fractures 5-10 mm wide were seen at the surface above anomaly 3. Finally, on 21 December 2010, a new 3m deep sinkhole was observed above anomaly 3. At present 3 sinkholes has been formed above the anomaly no.3 along the dirt road. Thus, the GPR anomaly reflecting the complicate structure of the site predicted formation of new sinkhole site located close (some 50m) to the salt edge. Subsurface anomalies were successfully detected by GPR, providing precursory signs of catastrophic collapse.

3.2.6.5. Conclusions on Section 3.2.6.

Three methods considered in this Section are used for detection of signs of forthcoming sinkholes through the dangerous areas.

1. ERT method is working well at the resistive subsurface (alluvial fans) and fails to give deep image at the mud flats.
2. EMR method allows detection of buried sinkholes, faults and fractures with different energy level and spatial extent. Disadvantage is high sensitivity to ambient noise.
3. GPR method is most reliable and allowing interpretation of results in real time. That is why, GPR was used by Jordanian researchers for safe data acquisition during fieldwork at the sinkhole dangerous areas. Disadvantage of the method is its sensitivity to soil resistivity. In the low resistive subsurface (e.g. high salinity and water saturation of soil) penetration of electromagnetic waves strongly decreases. Method is used in the areas of alluvial fans.

3.2.7. Laboratory and In-situ testing of DS soil

(The method and results are presented in details in Report M6/M27-050 by Ezersky, 2013; Ezersky and Livne, 2013)

3.2.7.1. General

The study of the sinkhole hazard problem requires knowledge of the soil geotechnical and geophysical properties. There are only few publications devoted to this problem. However, these properties are a very important issue of the geotechnical modelling and calculations of the sinkhole site stability.
Arkin and Gilat (2000) selected three types of sinkholes: (1) gravel holes occur in alluvial fans, (2) mud holes develop in the mud flats between fans, and (3) a combination of both types that are formed at the front of young alluvial fans where they overlap mud flats. Fig. 80 shows main sinkhole types formed in alluvial fans of Ein Gedi (a) and Ein Boqeq (b) and in the DS mud (c).

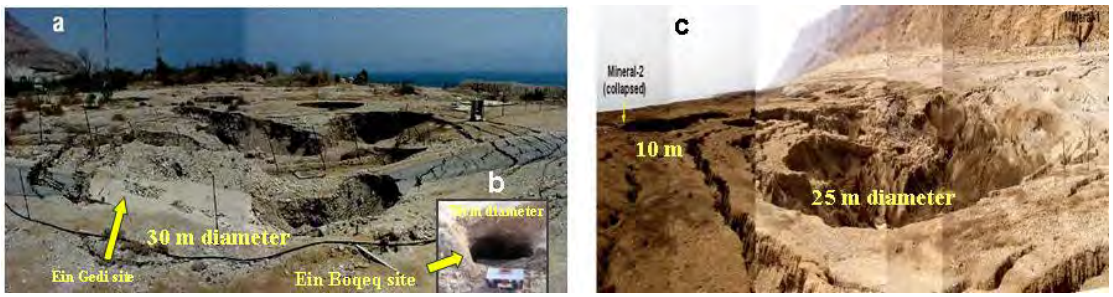

Figure 80. Two types of sinkholes (a, b) in sandy-gravel sediments of Ein Gedi and Ein Boqeq, respectively; and (c) in a DS mud (lime carbonates) of Mineral Beach site

In this study that is a part of the MERC Project M27-050 we have carried out a small volume of joint measurements of the geotechnical and geophysical properties of the DS shore soils, derived inter-

relationships and reviewed literature available (Ezersky, 2013). The study is based on interrelations available between geophysical (elastic, electrical etc) properties and geotechnical ones. The propagation of elastic waves through geomaterials provides information about critical properties of engineering materials (saturation, state of stress, stiffness, diagenesis and even soil type) and spatial distribution of these properties (e.g. layers, anomalies, inclusions, water table etc) (Stokoe et al., 1994; Santamarina et al., 2001). The development of geophysical application is based on evaluation of near-surface geotechnical materials on two directions: (1) soil dynamics specifically, for designing dynamically loaded foundations where small-strain shear stiffness $G_{\max}$ and G_o (*hereafter, dynamic shear modul*us) is the key soil properties responsible for its strength; and (2) geotechnical earthquake engineering for site response analysis. In latter case, measurements in the small-strain and nonlinear-strain ranges are required. This requirement necessitated the combined use of field dynamic (small-strain) and laboratory dynamic and static (small-to-large-strain) measurements. Resistivity also provides useful information on fluid properties (Ezersky and Levi, 2013; Frumkin et al., 2011; Legchenko et al. 2009, Schon, 1996).

Different authors suggest the existing of a relationship between dynamic and geotechnical properties for cohesive (Blake and Gilbert, 1997; Schultheiss, 1985) and cohesionless (Cha and Cho, 2007) soils. If such correlation exists the Vs values measured in the field would be used for evaluation in-situ strength. We will return to the analysis of this issue in continuation. The Standard Penetration Test (SPT) and other borehole soundings (CPT, DSPT) methods are widely used for studying of the geotechnical soil properties (DIN 4094 – 2, 1980; Lutenegger, 2008; Rogers J. D., 2006). In particularity, Terzaghi et al. (1997) suggests that there is correlation between SPT N_{60} and unconfined undrained shear strength. Recently a lot of researchers link SPT N-blow parameter with shear wave velocities Vs of different soils (DeJong, 2007; Hasancebi and Ulusay, 2007; Jinan, Z., 1987).

This study is aimed to reveal geotechnical and geophysical properties of the mentioned above soils and inter-relationships between geophysical parameters (Vs, ρ_x) and geotechnical ones (porosity, strength etc) for the use at the calculations of earth stability in the sinkhole development areas along the DS shores.

The objectives of the study are as following:

(1) To investigate geotechnical and geophysical properties of soils in-situ (boreholes, surface methods);
(2) To study the laboratory properties of soils (physical properties, undrained shear strength s_u, unconfined uniaxial strength q_u
(3) To search inter-relationships between the laboratory and in-situ properties and between geotechnical and geophysical parameters

The complete Table of properties of the DS main soil types is presented in (Ezersky, 2013). The geotechnical soil properties correlate with geophysical ones in both the laboratory and field conditions. Results obtained in this study show the perspective of further investigations. Nevertheless, this data would be used for an approximate estimation of soil properties in the modelling, calculations of stability etc.

3.2.7.2. Methods

We have used the following methods: (1) boreholes were studied using Standard Penetration Test (SPT) and seismic downhole (DH) survey. Transient Electromagnetic (TEM) soundings were carried out near every borehole. Samples of undisturbed structure were selected from borehole of clayey lithology and other samples were obtained from sampling spoons. (2) The laboratory testing included determining of density, water content, Atterberg limits and USGS classification.

Clayey samples (lime carbonates) of undisturbed structure were studied additionally.

- Shear wave velocity Vs was measured by a *bender element* in order to (a) estimate this parameter in consolidated brine saturated specimens; (b) compare those with in-situ values and, finally (c) to reveal relationships between Vs and strength s_u. For this, unconfined compressive strength q_u of those samples was measured after testing by bender element.

- Unconsolidated undrained (UU) triaxial compression tests were carried out on naturally wet unconsolidated samples to define undrained shear strength s_u and compare that with strength of consolidated water saturated soil (CU tests).

3.2.7.3. Boreholes

Two types of lithology were studied in-situ and laboratory conditions to reveal geotechnical and geophysical properties of these soils. Two boreholes MN-5E and EB-3E, of clayey and sandy-gravel, respectively lithology, were drilled in the Mineral Beach (Site II in Fig. 1) and Ein Boqeq (Site IV in Fig. 1) sites by jointly Geophysical Institute of Israel (GII), Geological Survey of Israel (GSI) and Ben-Gurion University of the Negev (BGU). Description of boreholes and results of their testing are presented in the Section 3.1.6. and in Figs. 11 (Mn-5E) and 12 (EB-3E).

SPT results. N_{SPT} in lime carbonate sediments (Fig. 11d) is ranged from 5 to 25 blows (per 30 cm) that allows classifying of clayey sediments as firm to stiff consistency. N_{SPT} in sandy-gravel sediments (Fig. 12d) varies from 16 to 50 blows that characterize these sediments as from medium to dense ones.

Vane test results. Results of borehole testing using vane test were calculated in the geotechnical laboratory of the Ben Gurion University (Livne 2012).

Table 7. Results of undrained shear strength calculation using field vane test

	depth (m)	Peak resistance (lbf*ft)	Residual resistance (lbf*ft)	Peak resistance (N*m)	Residual resistance (N*m)	Peak shear strength S_{up} (kPa)	Residual shear strength S_{ur} (kPa)
1	3.1	35	15	47.45	20.34	202.42	86.75
2	10.3	5	0	6.78	0	28.92	0

Two shear strength values are presented in Table 2. The first one is s_{up} - peak value measured at the moment of start of rotation, and the second one s_{ur} is resistance at stable rotation of vane instrument.

Shear wave velocity. Vs in lime carbonates varies in limits of 120 – 250 m/s (Fig. 11e), whereas sandy-gravel sediments (Fig. 12e) are characterized by Vs = 300 – 630 m/s.

TEM bulk resistivity ρ_x in lime carbonates varies from 0.2 – 0.3 Ωm whereas in sandy gravel sediments it is 0.3-0.5 Ωm (Figs 11f and 12f, respectively). The high resistivity unit of ~1 Ωm is clearly seen in both graphs. This unit is a salt layer that generally has TEM resistivity of 0.8 – 2 Ωm .

Correlations between SPT and Vs. Two SPT parameters were calculated: N_{SPT} (uncorrected values) and $N_{SPT\ 60}$ corrected for different corrections (Terzaghi et al. 1996).

Two inter-relationships were looked for: Vs versus N_{SPT} (red graphs in Figs. 81a and 81b) and Vs versus $N_{SPT\ 60}$ (blue graphs in the same figures). Analysis of both graphs shows that there is not significant difference between two above correlations that can be written as following:

(a) for clayey sediments of Mn-5E borehole

$$V_S = N_{SPT}^{0.261} x107.20 \ (R^2=0.82), \quad V_S = N_{SPT\,60}^{0.238} x113.86 \ (R^2=0.81) \qquad (18)$$

(b) for sandy-gravel sediments of EB-3E borehole

$$V_S = N_{SPT}^{0.347} x151.75 \ (R^2=0.61), \quad V_S = N_{SPT\,60}^{0.281} x177.82 \ (R^2=0.41) \qquad (19)$$

One can see comparing expressions (18) and (19) that coefficient of correlation for lime carbonates is significantly higher (R^2=0.82 for N_{SPT} and R^2=0.81 for $N_{SPT\ 60}$) than that for sandy-gravel sediments (R^2=0.61 for N_{SPT} and R^2=0.41 for $N_{SPT\ 60}$).

At the same time coefficients of correlation for both N_{SPT} and $N_{SPT\ 60}$ are equal in clayey sediments (R^2=0.81 - 0.82) and are significantly different in sandy-gravel ones so that R^2=0.61 for N_{SPT} is higher than R^2=0.41 for $N_{SPT\ 60}$. Noted above regularities are confirmed at comparison of different relationships derived by different researches for similar lithology. Clayey sediments are characterized by closer relationships (Fig. 81a), whereas sandy-gravel sediments show essentially different correlations.

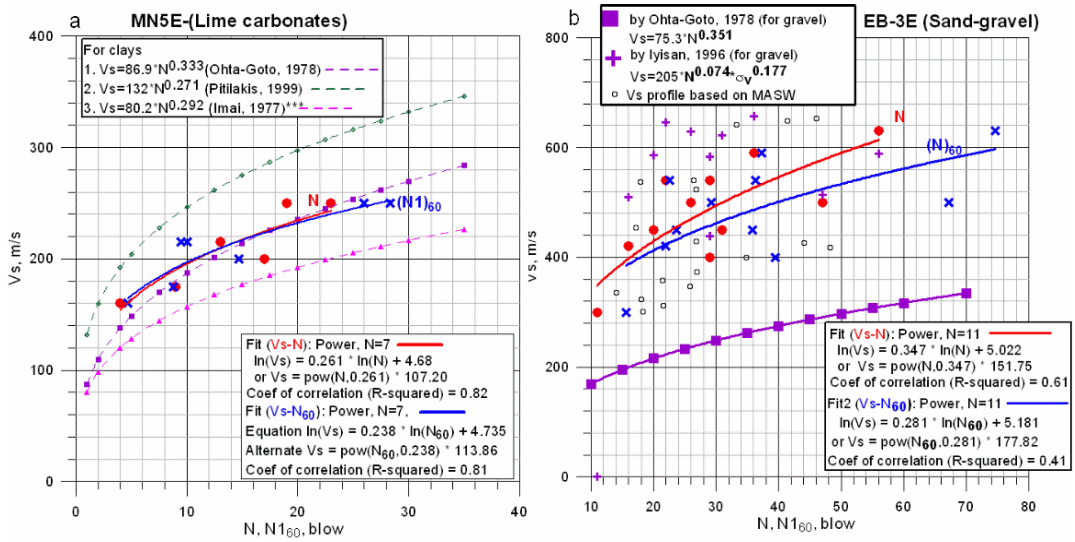

*Figure 81. SPT versus Vs inter-relationships obtained in 2 boreholes: (a) Mn-5E, and (b) EB-3E. Relationships of other authors obtained in similar soils are presented for comparison (*** is referenced by Sykora 1987).*

3.2.7.4. Laboratory study

Sandy-gravel soil

Sandy gravel sediments from borehole EB-3E (Ein Boqeq) were tested in the BGU geotechnical laboratory by Livne (2012) in accordance with the methodology suggested by Frydman et al. (2008). These sediments are classified as SW, SM, SP coarse clastic gravels and sands (after USCS). The water content is of 15-25%. The sands consists of carbonate particles with total unit weight γ_t varying from 16.6 to 23 kN/m^3 and fines. The pore fluid is the DS brine with density of $\rho_f = 1240 kg/m^3$.

Lime carbonates

<u>*Atterberg limits*</u>. The soil used in this research study was lime carbonate. Its properties are presented in the Table 8.

Table 8. Summary of test results obtained in the BITL Ltd (Haifa) at temperature of T=60°C

Amount of fines (-200#)	Plasticity index,	Plastic Limit,	Liquid Limit,	Water content,	Depth of specimen,	Borehole No
%	PI (I_p)	PL (w_p)	LL (w_l)	%	m	
98.4	15	24	39	40.5	2.8-2.9	MN-5
98.9	9	23	32	31.0	2.7–2.8	MN-5
98.8	18	26	44	48.0	2.6-2.7	MN-5
93.7	8	23	31	44.9	2.3-2.4	MN-5

In accordance to the plasticity chart, the saturated lime carbonates relate to CL (clay) after the Unified Soil Classification System (USCS). It should expose medium to high dry strength, medium toughness at plastic limits, and no to very slow reaction to shaking test (Terzaghi et al., 1996)

Void ratio and porosity. Void ratio and porosity determining are presented in Table 9. Pore space parameters were determined for completely unloaded conditions and for specimens subjected to consolidation in the consolidation pressure range 50 – 500 kPa.

Table 9. Void ratio and porosity of lime carbonate

	ρ_{wet}	ρ_{dry}	e	ϕ	ρ_{wet}	ρ_{dry}	e	ϕ
	No confining pressure				Confining pressure 50 – 500 kPa			
1	1783	1427	0.821	0.45	1806	1301	1.02	0.50
2	1783	1393	0.867	0.46	1878	1416	0.86	0.46
3	1803	1380	0.884	0.47	1878	1416	0.86	0.46
4	1787	1272	1.07	0.52	1896	1446	0.82	0.45
5	1806	1378	0.91	0.48	1889	1456	0.785	0.44
6	1700	1149	1.29	0.56	1900	1495	0.57	0.425
7	1628	1085	1.53	0.60	1920	1534	0.69	0.41
8	1725	1191	1.31	0.57				
9	1770	1356	1.03	0.51				
Average	1753.9	1292.3	1.079	0.513	1881	1452	0.8007	0.451
Standard	58.912	123.27	0.2454	0.0541	36.088	100.35	0.1421	0.0307
W%	0.03359	0.09538	0.22743	0.10535	0.01919	0.06911	0.17752	0.06806

Analysis of the table shows that void ratio of unloaded specimens varies in the range of 0.82 – 1.53 at average value $e_{av} = 1.079 \pm 0.25$, porosity of unloaded specimens varies in the range of 0.45 – 0.60 at average value $\phi_{av} = 0.51 \pm 0.05$. The loading of specimens leads to slight decrease of both parameters. Void ratio of loaded specimens varies in the range of 0.57 – 1.02 at average value $e_{av} = 0.80 \pm 0.14$, the porosity of loaded specimens varies in the range of 0.41 – 0.50 at average value $\phi_{av} = 0.45 \pm 0.03$.

The Bender Element test.

Examples of typical oscillograms obtained in the Bender element tests are presented in Fig. 82 that shows signal measured at 150 kPa confining pressure (a) and the signal recorded at 380 kPa confining pressure (b). One can see that with the increase of confining, the pressure signal is improved and the velocity Vs increases too.

Results of five Vs measurements carried out at different confining pressures using Bender Element are presented in Table 10. Other parameters also are shown during these tests as geometry of specimens, wet and dry density, dynamic shear moduli, UCS parameters $\mathbf{q}_u$ and undrained shear strength $\mathbf{s}_u$.

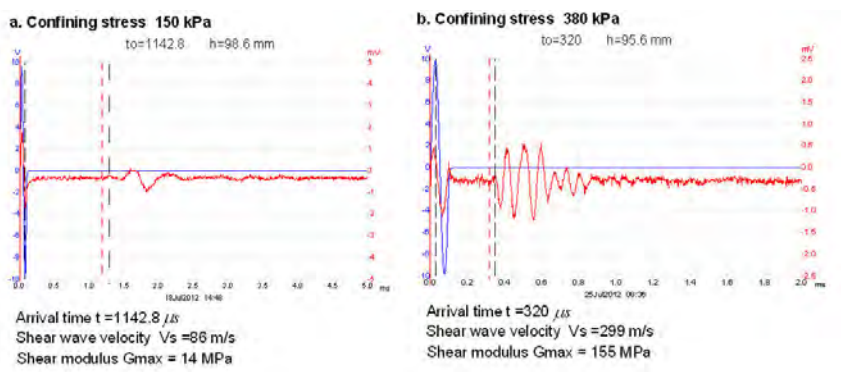

Figure 82. Examples of oscillograms obtained in the Bender element tests: (a) at confining pressure of 150 kPa; (b) at confining pressure of 380 kPa. The vertical red dashed line is the arrival time of the signal, the vertical black dashed line is the time of the first phase of signal.

It follows from Table 10 that Vs varies in the range of 86 m/s to 350 m/s increasing with the increase of the confining pressure.

Table 10. Results of Bender Element tests*

Spec. No	Confining Pressure, kPa	Height, mm	Wet Density, kg/m^3	Dry Density kg/m^3	Vs, m/s	G, MPa	Vp m/s	ρ_x, Ωm	q_u,** kPa	s_u,*** kPa
1	50	102.1	1806	1301	119.1	26	1771	1.87	53.2	26.6
2	150	98.6	1878	1416	86	14				
3	270	97.6	1896	1446	132	33	1980	0.59	98	49
4	380	95.6	1900	1185	299	170				
5	500	94.6	1920	1259	350	235	1780	1.28	243.5	121.8

Comments: *) Tests were carried out after water saturation and consolidation
**) Unconfined Compression Strength (preliminary consolidated specimens to 50-500kPa)
***) Undrained shear strength at zero confining pressure

UCS tests.

Three specimens were subjected to the Unconfined Compression Strength testing to reveal possible correlation between Vs and the Undrained shear strength. Results of the UCS testing are presented in the Table 10 as unconfined compressive strength q_u [kPa] and undrained shear strength s_u [kPa]. Results of the three UCS tests are presented in the Table 10. Results show that range of q_u is between 53.3 and 243.2 kPa at a confining pressure varying from 50 kPa to 500 kPa. Undrained shear strength varies, respectively, between 118 kPa to 122 kPa.

Unconsolidated-Undrained (UU) triaxial compression test results.

The testing was carried out on naturally wet lime carbonate specimens to compare strength parameters of these specimens with results of Frydman et al. (2008) tests on saturated consolidated specimens. This test should demonstrate difference in strength conditions in the saturated soil of mud flats and strength conditions during drying of soil at drop in the DS level. Calculations of strength parameters resulted in friction angle $\varphi = 2.43^o$, and cohesion C=18.7 kPa.

Correlations between geotechnical and geophysical parameters.

Lime carbonates tested by the Binder element show correlations between measured geophysical parameters (Vp, Vs and ρ_x) and confining pressure during consolidation. These correlations are clearly seen in Fig. 84a. Increase of the confining pressure results in the increase of all the geophysical parameters. It can be connected with the porosity decrease in the soil specimens. The mentioned regularity is confirmed by relationships presented in Fig. 84b between porosity and all the measured parameters. Note that Vs was measured after saturation and consolidation at confining pressure during Bender test, whereas Vp, ρ and s_u were measured after unloading of samples.

One can see that the increase in porosity leads to decrease of Vp (1900 to 1750 m/s), Vs (350 to 50 m/s) and the resistivity (1.0 to 0.5 Ωm). Lower graph (in b) shows increase of porosity resulted by pressure decrease.

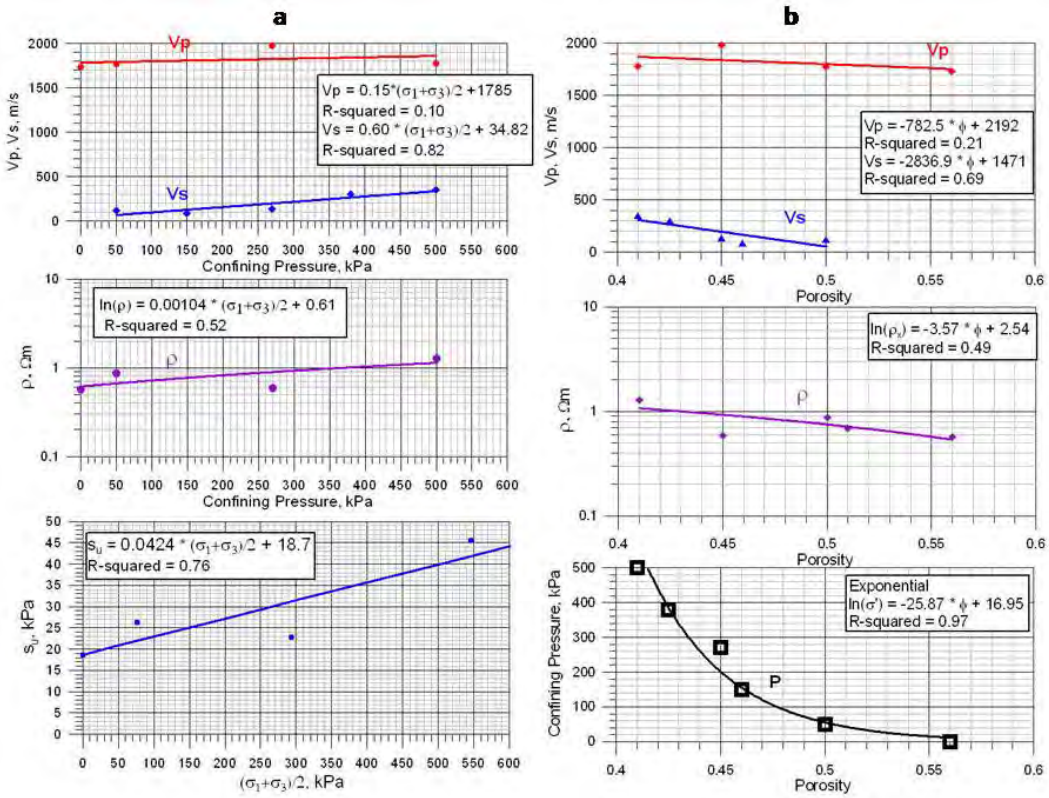

Figure 84. Variation of geophysical parameters versus (a) confining pressure and (b) porosity. From above to below: Compression (Vp) and S-wave (Vs) velocities, specific resistivity (ρ), undrained shear strength (s_u) of saturated consolidated samples tested at UCS conditions, confining pressure (P).

3.2.7.5. Interpretation and Discussion

Lime carbonates.

As follows from Modified plasticity card [Terzaghy et al., 1996] undisturbed specimens extracted from the borehole MN-5E are classified after USCS as CL (Goretski, 2012; Livne, 2012). They consist of 94-99% fines (< 0.074mm), have water content ranged from 40 to 48% with Liquid limit LL = 31 - 44 and Plasticity index PI = 8 – 18. It is a very fine material that was considered in the past as DS clay or mud (Arkin and Gilat, 2000). Respectively the areas of such soil were named mud flats. These areas when brine saturated are characterized by miry consistence like marshland. The earth surface subsides under foots. The upper soil layer when dried seems to be dense, but under this layer soil remains miry. There were cases when at such sites the wheel of a 4x4 vehicle momentarily felled through such soil and the vehicle could be took out only by a power tractor.

In spite of the similarity to clay this soil is not composed of clay minerals. The DS "clays" (lime carbonate) composed of clay-sized soil (particles smaller than 2 μm) from the DS area is not made up of clay minerals. It is carbonate soil named by Frydman et al. (2008) *lime carbonate* that composed predominantly of calcite and not clay minerals, whereas other Israeli clays are comprised largely of montmorillonite (spectite) clay minerals. The DS data lie consistently above those of other Israeli clays, and correspond to average effective strength parameters (Frydman et al., 2008): C'=0kPa and φ'=34°.

Undrained shear strength of unsaturated lime carbonate

Frydman et al. (2008) reports undrained triaxial strength (CU test) on brine saturated consolidated samples (dry unit weight ranging from 7 – 15 kN/m^3) with friction angle of φ=34° and effective cohesion of zero (Curve 1 in Fig. 85). Unconfined undrained (UU) testing of naturally wet lime carbonates show C=18.7kPa and φ=2.43^o (curve 2 in Fig. 85).

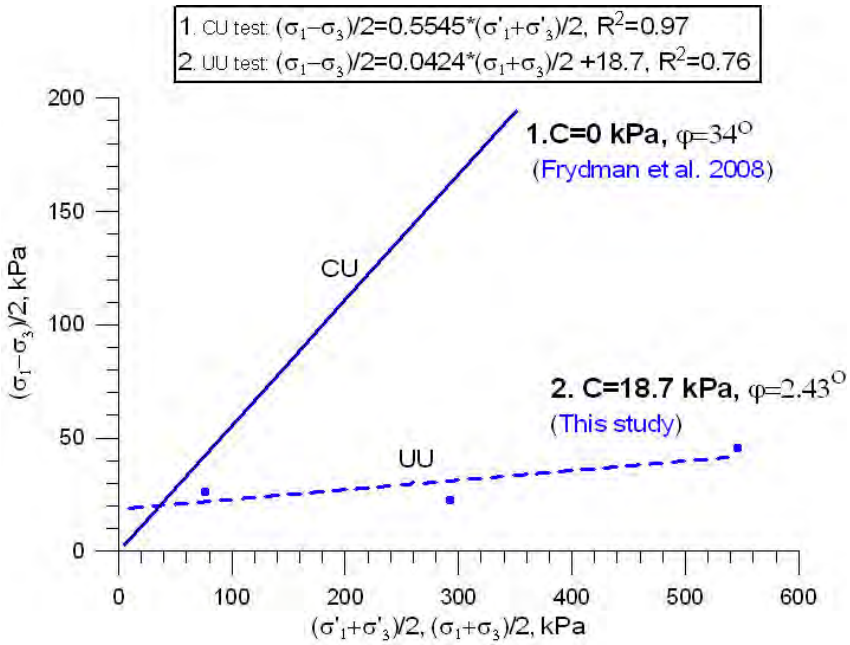

Figure 85. Undrained shear strength in triaxial tests on undisturbed lime carbonates: (1) consolidated undrained (CU) tests on brine saturated samples (Frydman et al., 2008) and (2) unconsolidated undrained (UU) tests on naturally wet samples (this study)

The effect of the cohesion increase with the decrease in clay saturation was discussed by Frydman et al. (2000) with a reference to the studies of Tuffour (1984), investigated the shear strength of unsaturated, compacted Israeli clays. It was found that failure envelopes for all the soils could be reasonably defined, regardless of degree of saturation, with an angle of internal friction of approximately $\varphi = 26^o$, similar to that obtained for the saturated clays. The cohesion value was found to be a function of the degree of the saturation (Tuffour, 1984). The increase in the cohesion with decreasing saturation can be related to the suction in the soil (after Terzaghi et al. (1996) it is an *"apparent cohesion"* caused by the surface tension in the moist grains).

On the other hand, a very low (almost zero) value of the friction angle $\varphi = 2.5^o$ is characteristic for UU tests. Our tests characterize natural mud that was not consolidated and water saturated. It is our goal to check the properties of DS mud in such conditions. The soil shows very low vane strength in-situ conditions (peak shear strength of 28 kPa at 10m depth and 0 kPa, residual one). The Drilling crew was not able to extract undisturbed sample from this depth because of very high fluidity of soil.

Our results obtained on undisturbed lime carbonates show that natural desaturated soil has a strength parameter that can be significantly different than those collected from sites where engineering structures are designed. It is important at the performing of modeling of the sinkhole forming. The properties obtained in these experiments reflect, evidently, local soil characteristics in sinkhole sites. However, we consider these results as very preliminary. Additional investigations should be carried out in future.

Comparison of Vs measured in borehole and in the Bender Element (BE) tests.

Let us at first compare the laboratory and in-situ Vs values (Fig. 86). Consolidated and water saturated lime carbonates in the laboratory and field conditions are characterized by low Vs values of 100 – 250 m/s. In the field conditions naturally moist soil has velocity of 160 - 215 m/s.

In order to compare Vs measured in borehole and by BE we have recalculated confining pressure of the BE test to depth.

The depth of soil specimens was calculated from consolidation pressure in presumption that:

(1) Consolidation pressure is equal to the stress σ_H at the depth H;

(2) At the depth range between 0 – 23m and water table at the depth of 18m we can neglect by the pore pressure and accept σ_H as:

$\sigma_H = (\sigma_1 + \sigma_3)/2 = (\sigma_1 + \sigma_1 K_o)/2$, where K_o=1- sinφ is the coefficient of earth pressure (horizontal-to-vertical stress ratio) (Terzaghi et al., 1996, Section 16.5, p.104) and φ - is the friction angle that is 2.4^o above water table and 34° under that.

(3) Then H = σ_H / γ where γ is unit weight of soil that is 17.5 kN/ m^3 above water table and 18.8 kN/ m^3 under that.

The calculated depth versus consolidation pressure graph is presented in Fig. 86 (curve 1).

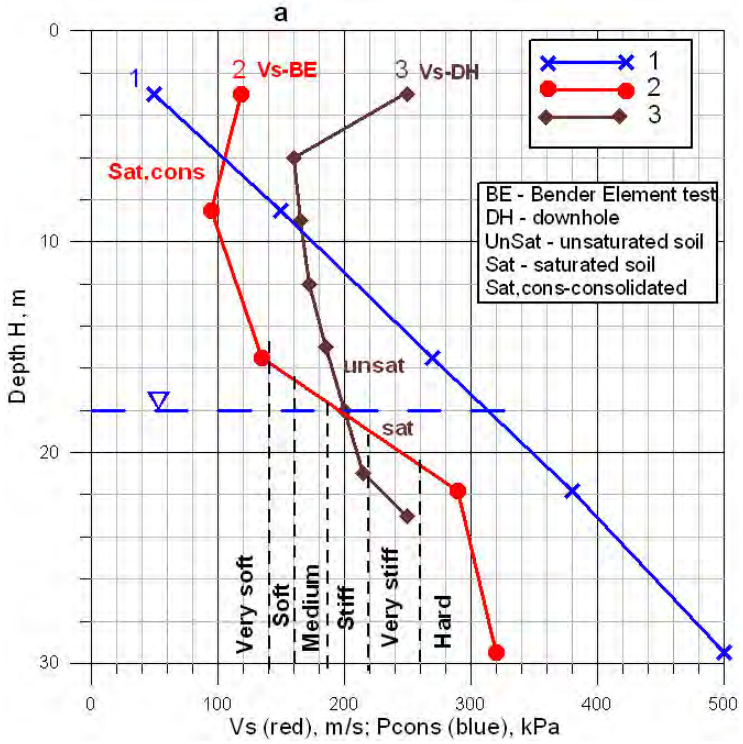

Figure 86. Variation of different parameters with calculated depth. Curve 1 - Depth of soil specimens versus consolidation pressure; Curve 2 - Vs versus calculated depth graph derived from BE test of undisturbed saturated and consolidated lime carbonate specimens; Curve 3 – Vs versus depth from downhole data in the MN-5E borehole

Depth velocity graph from BE test on saturated consolidated specimens is presented in Fig. 86 (curve 2, red). Downhole (DH) Vs graph is presented in Fig. 86 by curve 3 (brown). One can see that difference Vs between DH and BE test velocities in upper unsaturated part of the subsurface is of 50% and gradually converged in the deep saturated soils.

Generally this phenomenon is known. Anderson and Woods (1975) note that invariably, when field and laboratory Vs values are compared, values of Vs_{lab} range from slightly less to considerably less than the in-situ values, Vs_{field}. Stokoe and Santamarina (2000) suggest number of factors that can affect (Vs_{lab} / Vs_{field}) ratio. Particularly, based on testing of 47 specimens they concluded that *the loss in the stiffness in laboratory samples results from irrecoverable damage at interparticle contacts.* On the other hand a number of researchers (Schneider et al., 1999; Szczepański, 2008) resume that in-situ measurement of low-amplitude shear moduli from seismic piezocones, seismic flat dilatometers, SASW, and cross-hole tests were found to be in good agreement with laboratory values using the resonant column or Bender element.

In our tests undisturbed specimens of a good quality were used and other reasons would be responsible for difference in measured Vs values. Remind that Vs values in the laboratory BE tests were obtained on water saturated samples, whereas downhole measurements were carried out in the desaturated DS mud. It means that difference in the saturation state would be responsible for difference in measured Vs values.

Theoretically, Dvorkin (2008) suggests explanation based on following presumed relationship between Vs values in dry and saturated soils:

$$V_s = V_{sDry}\sqrt{\frac{\rho_{bDry}}{\rho_b}} = (1-\phi)^2 V_{sS}\sqrt{\frac{(1-\phi)\rho_b}{(1-\phi)\rho_s + \phi\rho_f}} \qquad (20)$$

Where ρ_{bDry} and ρ_b are the bulk densities of dry and wet sediments, respectively; and ρ_s and ρ_f are the densities of the solid and fluid phases, respectively. Values V_{sS} as well as V_{pS} can be calculated from the elastic moduli and density of the appropriate mineral mix as the square root of the modulus divided by the density. Using (20) we can estimate $V_{sDry}/V_s = \sqrt{\rho_b/\rho_{bDry}}$ using data of laboratory testing (Table 1) as $\sqrt{1858/1321}$ = $\sqrt{1.40}$ =1.18. This theoretical evaluation is less than experimental ratio that is of 1.5 folds. This discrepancy can be explained by the experimental study of Sharma and Bukkapatham (2008) who have shown that at increase of soil (sand) saturation from 80 to 100% G_{max} can decrease by 2.5 fold (respectively, Vs should decrease as $\sqrt{2.5}$ =1.6 fold). It means Vs values measured by Bender Element are in good accordance with field data. The difference in Vs measured by BE and downhole is explained by different humidity conditions but not by method of measurements.

Su versus Vs inter-relationships. Lime carbonates demonstrates the correlation between undrained shear strength *Su* and *Vs* (4 in Fig. 87).

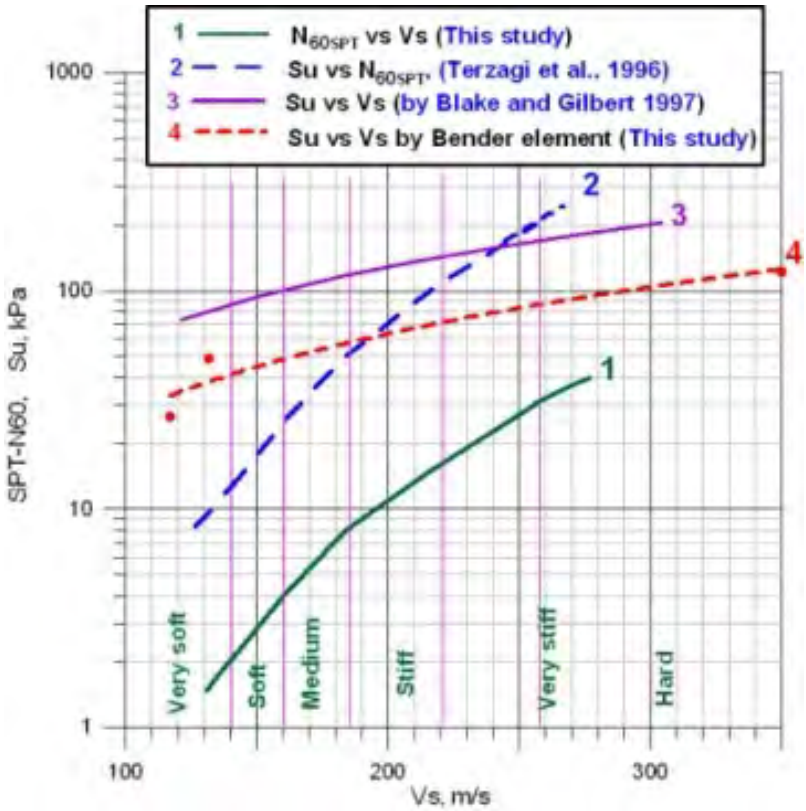

Figure 87. Inter-relationships between Vs and undrained shear strength. 1-NSPT vs Vs from borehole data (this study; 2-Su derived from SPT based on Terzaghi et al. (1996); 3-Clay by Blake and Gilbert (1997), 4-lime carbonate (Bender element, this study)

Similar relationships have been revealed in laboratory by Blake and Gilbert (1997) (3 in Fig. 87) and suggested by Terzaghi et al. (1996) based on SPT testing (1 and 2 in Fig. 87) are presented for comparison. The SPT data from Terzaghi classification was recalculated to the Vs versus SPT N (curve 1, green in Fig. 87) using relationships obtained from SPT tests (see eqs. in Fig. 81). Line 2 in Fig. 87 reflects hypothesis of Terzaghi et al. (1996) suggested that under many conditions of practical

importance, the undrained shearing strength of clay is approximately equal to one-half the unconfined compressive strength *qu* of undisturbed samples. This hypothesis is illustrated by dashed curve 2 in Fig. 87 generated from Table 12.2 (Terzaghi et al., 1996). Curve 3 (lilac solid line in Fig. 9) characterizes relationship s_u versus Vs calculated from Blake and Gilbert (1997) for red clays of Schultheiss (1985). The algorithm considers hydrostatic stress conditions for normally consolidated clays. Finally, red dashed curve (4 in Fig. 87) presents results of the BE test of DS lime carbonate and their *su* derived from UCS tests. The curve 4 (UCS conditions) is similar by shape to curve 3 (calculated for hydrostatic stress conditions) and crosses the hypothetic curve 2. Difference in the Su level would be result of zero cohesion of the saturated lime carbonate.

Concluding the discussion note that carbonate soils of the western DS area are typical also (with some reserves) for its eastern (Jordanian) shores where both coarse sandy gravel sediments (Taqieddin et al. 2000) and mud flats composed of lime carbonates (Khlaifata et al. 2010) are met. This feature allows considering of saturated lime carbonate as cohesionless soil like very fine sands. In unsaturated conditions cohesion should be taken into consideration. Lime carbonates demonstrate one more peculiarity, e.g. very low cation exchange capacity (CEC) (Khlaifata et al. 2010) that allows use of TEM resistivity method for determining of porosity of both sands and DS mud as suggested by Kafri and Goldman (2005) (See Table 3 in the Section 3.2.4).
Sandy-gravel sediments, for comparison, are characterized by heighten Vs values of 300 – 650 m/s, that apparently could be caused by increased the soil stiffness reported by Mahasneh (2004). Properties of sandy-gravel sediments were mainly studied by Livne (2012) and are presented in the Appendix 1.

3.2.7.6. Conclusions on Section 3.2.7.

This study compiles (1) results of DS soils testing founded in literature and (2) our own borehole and laboratory testing enabling to understand particularities of DS soil geotechnical and geophysical properties necessary for modelling, calculations of stability and geophysical measurements. Two types of lithology were studied in-situ and laboratory conditions to reveal geotechnical and geophysical properties of these soils. Two boreholes MN-5E and EB-3E, of clayey and sandy-gravel, respectively lithology, were drilled in the Mineral Beach and Ein Boqeq sites. We have revealed following features of the DS soil properties (Ezersky, 2013; Ezersky and Livne, 2013). Sandy-gravel sediments are presented by coarse sands, which are characterized by Vs = 300 – 650 m/s. Such increased shear wave values can be caused by increased the DS soil stiffness described in the literature. Brine saturated lime carbonates (DS mud) are characterized by low Vs values of 120 – 250 m/s.
In addition to the borehole testing clayey sediments (lime carbonates) were studied in the laboratory conditions using Bender Element (BE) and uniaxial and three axial strength for unconsolidated undrained (UU) conditions. Frydman et al. 2008 reported cohesion of 0 kPa and friction angle 34° obtained in consolidated undrained (CU) conditions, e.g. lime carbonates do not exhibit cohesion when saturated in the DS brine. It is explained by mineralogical composition of the Dead Sea material, composed predominantly of calcite and not clay minerals, whereas other Israeli clays are comprised largely of montmorillonite (spectite) clay minerals. This feature allows considering of saturated lime carbonate as cohesionless soil like fine sands. On the other hand our tests have shown that unsaturated (or naturally moist) lime carbonates have a low friction angle of ~2° and cohesion of 18 kPa caused by apparent cohesion or suction effect (Terzaghi et al., 1996). After Khlaifata et al. (2010) lime carbonates demonstrate also very low cation exchange capacity (CEC) that allows use of TEM resistivity method for determining of porosity of both sands and DS mud as suggested by Kafri and Goldman (2005) (Ezersky and Levi, 2013). Note also that significant difference of Vs in sands and lime carbonates allows mapping of different lithology along DS coastal areas. Geotechnical properties of soils have been determined in laboratory conditions (Ezersky, 2013)

3.2.8. Laboratory and in-situ testing of DS salt.

(The method and results are presented in details in Report 5/M27-050/2012 by Ezersky and Eppelbaum, 2013; 3 papers are submitted and are under review).

3.2.8.1. General

Increasing construction and sinkhole hazards, have underlined the need for intensive investigation of mechanical parameters of both soil and salt in field and laboratory conditions (Al-Homoud et al., 1999; Frydman et al., 2008; Hatzor and Heyman, 1997; Mansour et al., 2009; Mahasneh, 2004; Weisbrod et al., 2012). Taking into account expensive drilling, performing in-situ tests, and extraction of undisturbed soil and salt samples in the complicated conditions of the DS, attention has been directed to alternative investigation schemes such as geophysical methods (Ezersky, 2006; Ezersky et al., 2013a; Ezersky and Eppelbaum 2013, Frumkin et al., 2011; Frydman et al., 2008, Legchenko et al., 2008a,b).

The mechanism of DS sinkhole formation accepted by most researchers links this phenomena with karstification of the buried salt layers by under-saturated groundwater (Abelson et al., 2006; Ezersky et al., 2010, 2013b; Frumkin et al., 2011; Legchenko et al., 2008a, b; Shalev et al., 2006; Yechieli et al., 2006). Respectively, interest in the salt properties such as porosity and permeability is of first priority.
This study is intended to investigate Dead Sea (DS) salt porosity permeability inter-relations and their relationship to geophysical parameters such as Compression waves velocities (Vp), Shear waves ones (Vs), geo-electrical resistances (R) and specific resistivity (ρ_x) in laboratory and field conditions to estimate real salt properties in the sinkhole development sites. Sites for respective investigations are shown in Fig.1. We have studied salt samples extracted mainly from two boreholes drilled in the Mineral Beach (Mn-5E) and Ein Boqeq (EB-3E). In addition, some specimens were used from Nahal Arugot, Mazor, Newe Zohar and other sites.
In the laboratory geophysical parameters were measured using ultrasonic pulse method and resistance meter (Ezersky and Eppelbaum, 2013). In situ conditions these parameters were measured using, borehole and surface geophysical methods. Uultrasonic and electrical investigations of salt uncased walls carried out for a first time within two boreholes MN-5E and EB-3E (Ezersky and Eppelbaum, 2013). From surface salt layers were studied using, respectively, the Multichannel Analysis of Surface Waves (MASW) method (Ezersky et al., 2013a), and the Transient Electromagnetic (TEM) method (Ezersky et al., 2011; Frumkin et al., 2011). Additionally, we have used results of the Magnetic resonance Sounding (MRS) method (Legchenko et al., 2007; 2009) to characterize salt hydraulic conductivity in-situ conditions.

The salt of the coastal Dead Sea area is revealed in 10.2 -10.8 ka (10,200-10,800 years old) (Yechieli et al., 1995; Stein et al., 2010). The halite layer was deposited during the Earlier Holocene owing to the development of extremely arid conditions in the shrinking phase between the Lisan Lake and the present Dead Sea. The salt was formed within the Dead Sea area and its boundary extends west of the existing pool. Salt unit is located below groundwater table at a depth range of 20-50 meters from surface and has a thickness of 6-30 meters. Salt layers are very conductive hydraulically and water-saturated with the DS brine of very high salinity with total dissolved solids [TDS] of 340g/l.

3.2.8.2. In situ salt properties

Our field studies were based on seismic refraction, surface wave prospecting using MASW technique and Transient Electromagnetic (TEM) methods.

Seismic P-wave refraction method has shown that in-situ salt velocities Vp are ranged between 2900 and 4200 m/s (Ezersky 2006, Ezersky et al., 2010, Frumkin et al., 2011)
Seismic S-wave refraction and MASW methods evaluate shear wave velocities (Vs) varying between limits of 750m/s to more than 1600 m/s (Ezersky et al., 2012a; 2013a),

TEM method enabled us to estimate salt bulk resistivity (ρ_x) varying mainly from 0.8 to 2.5 Ωm (Ezersky et al., 2011; Frumkin et al., 2011; Levi et al., 2011).

3.2.8.3. Salt specimens.

In the borehole MN-5E (Fig. 11b), the salt layer (located at the depth of 22m) is overlain and underlain by DS clay (lime carbonate), whereas in the EB-3E borehole (Fig. 12b), the salt layer (26.3m deep) is enveloped from above and from below by sandy gravel sediments. In borehole MN-5E, the clay content in the salt layer does not exceed 3%, as well as in borehole EB-3E, it is not more than 2%. Boreholes crossed the different kinds of salt (Fig. 88). Mineral Beach layers are composed of

gray coarse "crystalline transparent salt" (CTS) (Fig. 88, upper photo), whereas the Ein Boqeq area is composed of fine crystalline "white massive salt" (WMS) (lower column in Fig. 88). Salt types are denoted similarly to Weisbrod et al. (2012).

Figure 88. Salt columns from boreholes: gray coarse crystalline transparent salt (CTS) from MN-5E (upper) and fine crystalline white massive salt (WMS) from EB-3 borehole.

Numerous boreholes have shown that the CTS salt is distributed throughout the whole coastal area of the northern DS basin and partially so in the southern one (Yechieli et al. 2004). The WMS salt is located in the Ein Boqeq site and along the DS dyke (Frydman et al. 2008). Thus, we suggest that salt specimens used in the laboratory conditions, as well as salt layers investigated in in-situ conditions are representative for the entire DS coastal area, taking into account that salt is of the same age and both formed in past and is at present in a similar condition.
Examples of salt specimens for testing are shown in Fig. 89. All cores consisted of natural salt rocks composed of halite crystals. In accordance with the above salt classification, salt samples from borehole EB-3E were identified as WMS salt (Fig. 89a, e), and samples from other boreholes as CTS one (Fig. 89b-d). Note homogeneous samples from Ein Boqeq (a) and heterogeneous samples (b-d). Two samples no. MN5-24.1 and EB3-5 comprise the clay filled fracture (d, e). The quantitative evaluation of the impurities and clay within the salt samples was performed at Tel Aviv University by Eppelbaum (2013) using an electronic densitometer MH-300Z (Taiwan). This study has shown a small content of clay and calcite (1-1.4% by weight) in salt samples.

Scanning Electron Microscope (SEM) photographs were performed at the Geological Survey of Israel (GSI) using model FEI Quanta 450 (USA) to study the salt structure. CTS samples are composed of 2-3 cm halite crystals.

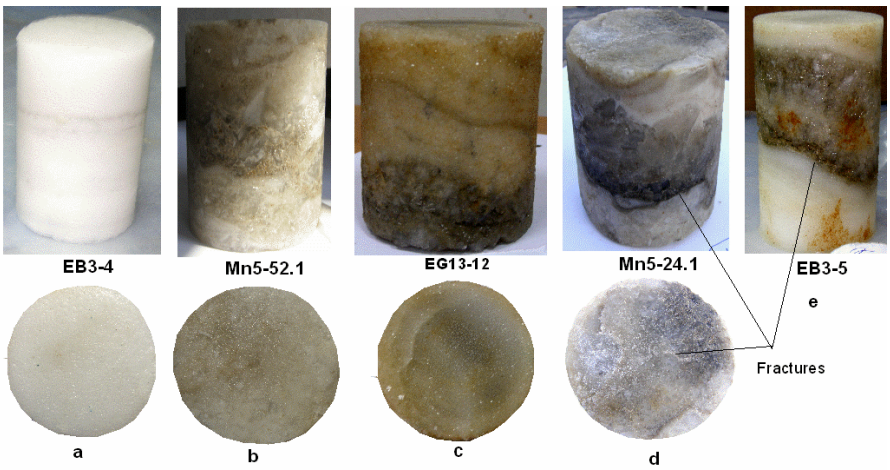

Figure 89. Typical salt specimens classified as "white massive salt" (WMS) (a, e) and "crystalline transparent salt" CTM (b-d) (after Weisbrod et al., 2012). Presented here are samples from borehole EB-3E nos. 4 and 5 (Ein Boqeq), MN-5E nos. 52.1 and 24.1 (Mineral Beach), and from borehole EG-13 no.12 (Ein Gedi). Two samples are crossed by the clay filled fracture (d, e)

On SEM photographs presented by secondary electron image (ETD), one can see micro fractures and pores developing along them (Fig. 90a). These pores are increased 6 folds in Fig. 90b. Fine crystals of

WMS salt are not visible by the naked eye. SEM photographs (Fig. 90c) show that WMS cores are composed of microscopic halite crystals by size 1.5-3 mm. Dissolution pores within the crystals are clearly seen in the photograph (Fig. 90d). Another feature of this photograph is fractures partially healed by the halite as shown by Welton (1984, p.182). Thus, fractures and dissolution pores are present in both samples and crystals.

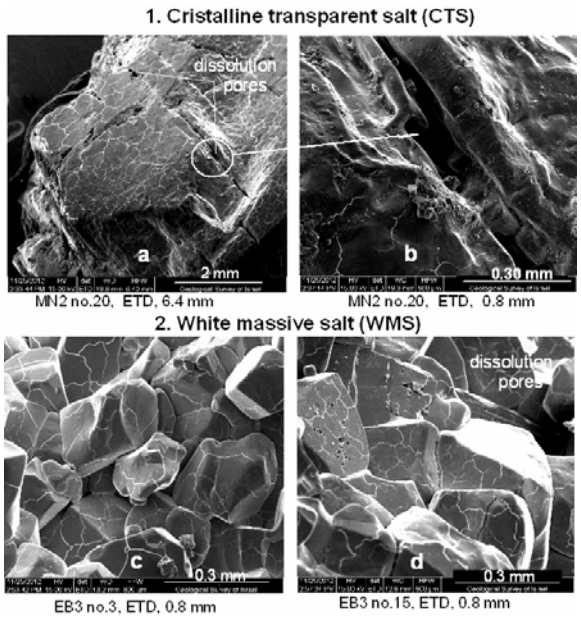

Figure 90. SEM photographs of salt samples of (a) CTS and (b) WMF types. The results are presented by secondary electron image (ETD), which displays surface texture, morphology, and surface roughness. (a) Salt sample no.20 from borehole MN2. Dissolution pores develop along the fractures; (b) the same scan increased by 3 folds: dissolution pore is shown by arrow; (c) and (d) SEM photographs of the WMF salt samples from EB3 borehole: halite crystals 0.15-0.3 mm size are seen in (c) and dissolution voids within similar crystals are seen in (d), white lines are subgrains boundaries.

3.2.8.4. Methods

3.2.8.4.1. Laboratory test methods

The porosity and permeability measurements of the Dead Sea salt specimens were performed in the Building and Infrastructure Testing Lab, Ltd. (Haifa) (Goretsky, 2012). A number of tests were performed at the Standards Institute of Israel (SII, Tel Aviv). Ultrasonic and resistivity measurements were performed in part at the same laboratories, as well as at the Geophysical Institute of Israel (GII, Lod). Salt porosity measurements have been performed in accordance with ASTM D 2937. Generally, the method includes determination of the dry and wet density, moisture content, and calculation of void ratio and porosity. Complete description of test methods and methodology of testing are presented in Ezersky and Goretsky (2013). Here we give brief description of the testing and main results.

The testing was performed by two stages: (1) At first stages time of weight stabilization during sample drying in the oven at temperature 60° C was determined (See explanation in continuation). This experiment was performed in the Geotechnical Laboratory of the SII.

(2) The second stage, porosity and permeability of salt cores, their mutual relationships, were determined. Samples were weighted and averaged geometric parameters (height and diameter) were measured. Square of transverse section and sample volume were calculated.

(a) Temporal measurements while drying salt samples have shown that complete evaporation of intergranular water from salt samples (~99%) is reached after 30 days of drying at 60° C. Temporal variations of the density for 3 salt samples are shown in Fig. 91.

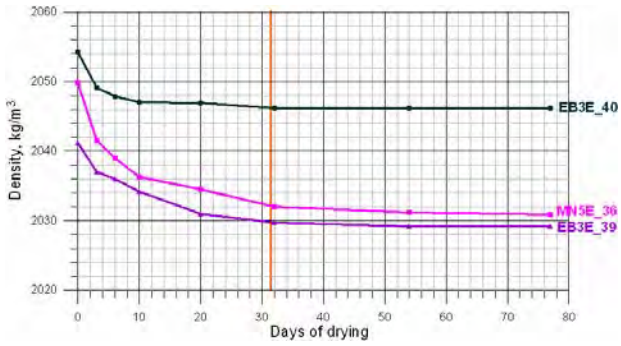

Figure 91. Temporal variations of the salt sample densities. It can be seen that the weight of the sample is stable after 30 days when 99% of intergranular water is evaporated from the sample

(b) Porosity measurements. A total of 33 samples of DS salt were tested for density and porosity determination. Samples were saturated and a number of their parameters were determined:

(c). *Permeability measurements.*

Laboratory hydraulic conductivity tests were performed according to ASTM D-5084 on 23 samples. The testing was performed on 20 samples at a hydraulic head of 5.0m and effective cell pressure of 20 kPa. We applied the constant head method (A) using the Flexible Wall Permeameter. Permeability *k* is calculated using expression of Hubert (Schon, 2004) based on Darcy`s equation.

(d) Ultrasonic measurements

Ultrasonic method intended for laboratory measurements of the pulse velocities of compression waves (Vp) and shear waves (Vs) in rocks and the determination of ultrasonic elastic constants of an isotropic rock, or one exhibiting slight anisotropy. The velocity measurement procedure was carried out in accordance with the ASTM (D 2845-05, 2005). The primary advantages of ultrasonic testing are that it yields compression and shear wave velocities, and ultrasonic values for the elastic constants of intact homogeneous isotropic rock specimens (Cannaday, 1964, Savich et al., 1969). Likewise, measured wave velocities may not agree with seismic velocities, but offer good approximation. Savich et al. (1969) explain it by the heterogeneity of rock mass comprising fractures, weakness zones, etc., causing, so named, anomaly dispersion of elastic wave velocities. The latter is determined as dependence of the elastic velocities on frequency range of waves used for the rock investigation. Such dependence permits studying the scale effect characteristic for rock masses and is reflected in a decrease of velocity with respect to volume of rock involved in measuring its elastic properties (Palmstrom, 1996).

For laboratory measurements we used SonicViewer SX Model 5251C (OYO Corporation, Japan) digital device based on XP operational system with two coupled piezoelectric transducers: 200 kHz P-wave sensors (model-5223) and 100 kHz S-wave ones (model-5224). The SonicViewer is intended for highly accurate measuring the travel time of the ultrasonic wave propagating through a bore core and rock specimen to determine its P-wave and S-wave velocities. The advantage of the SonicViewer is its visual registration of the arrival times on screen and reading the travel times by operator. The device is used with a reference aluminum sample 60 mm diameter and 80 mm long.

Another device, the S-70 (Terentiev, 1993) is the compact field ultrasonic meter (hereafter, US-meter) with oscilloscopic registration of signal (Institute of the Physics of Earth, Russian Academy, Moscow). The US meter comprises a generator of rectangular pulses (400*V* output) and a unit for reception of elastic waves passed via a studied medium. The quartz generator of time marks provides highly accurate arrival time readings of not less than 0.1-0.2 μs . The US-meter is intended, mainly for ultrasonic measurements in boreholes using special multi-channel sonde. However, at slight signals of SonicViewer we used this oscilloscope for sample measurements. For this, joint calibration of both devices was carried out to determine delay time in every system. Photographic registration of the signal is carried out using a digital camera mounted on a special tube. Examples of laboratory and field records obtained using both systems are shown in Fig. 92.

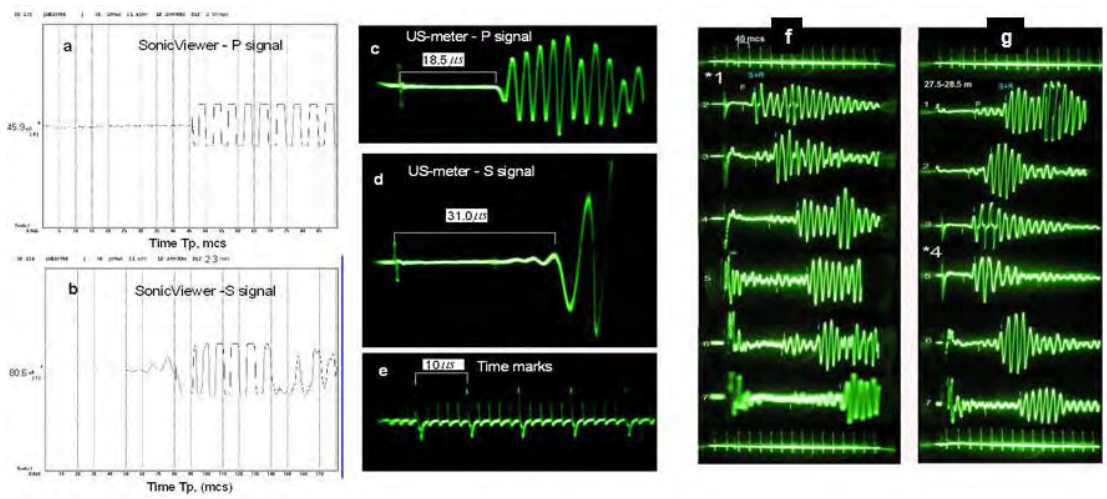

Figure 92. Ultrasonic records obtained on salt specimens with SonicViewer (a, b) and S-70 US-meter (c, d); (c) time marks (there is 2 μs between minor marks). Ultrasonic records are obtained with P-wave OYO 200 KHz transducers (a, c); shear wave records (b and d) were obtained with S-wave OYO 100 KHz transducers (c) Time marks (there is 2 μs between main marks). (f, g) Oscillograms obtained during ultrasonic logging in the borehole EB-3E from 27.5m depth. (f) Transmitter is 1st transducer, 2-7 transducers are receivers (direct shot); (g) transmitter is fourth transducer, ones 1-3 and 5-7 are receivers (split shot). P and S+R arrivals are marked by yellow and blue, respectively. Digits denote numbers of transducers.

P-wave records (Figs.92a and 92c) are characterized by sharp arrivals on both the Sonic Viewer (a) and the US-meter (c). Shear-wave records are identified in accordance with Rao and Lakshmi (2003) as a sharp arrival on a background of forerunner P-wave light oscillations (Fig. 92d).

(e) Resistivity measurements

Salt samples were investigated using the resistivity method at 25° C after saturation in the DS brine and in air after thorough drying. Bulk Resistivity of salt samples was measured using 2 electrode configurations without a guard ring (ASTM G187 – 05, Duba et al. 1978) with both electrode disks made of brass. In the brine-saturated conditions the electrodes were placed at the ends of samples. A cellulose sponge soaked with brine solution was used to hold the core sample between the electrodes in dry conditions. This enables the core sample to make full contact with the current source. To avoid surface current the side surface of cores after drying was isolated by hydroscopic paper.

Nilsson 400 electrical resistance meter (Nilsson Model 400) was used. The Mode1 400 Soil Resistance Meter is a 4 terminal, null balancing ohmmeter that measures resistance from 0.01 ohm to 1.1 $M\Omega$. The Model 400 can be used as a 4, 3, or 2-pin device for soil resistance measurements, or it can be used with a soil box or a single probe.

3.2.8.4.2. In-Situ (borehole) test methods

One of the main goals for drilling was to obtain compared properties of salt in boreholes and in the laboratory and to study their inter-relations. The following objectives were formulated for these studies: (1) To collect samples of salt and to test those in the laboratory; (2) To carry out ultrasonic profiling in boreholes to measure distribution of velocities of compression (Vp) and shear (Vs) waves with depth, and compare those with similar parameters of salt samples selected from the same depth. Note both modes of measurement are principally carried out at the same ultrasonic range of frequencies (100-200 kHz); (3) The same with respect to resistivity; (4) Estimate variation of geophysical parameters in dependence on measured volume (scale effect); (5) To calibrate results of geophysical measurements performed from the surface with those in borehole (for instance, refraction and TEM with downhole and resistivity measurements in boreholes

We planned to reach an understanding of the effect of salt porosity and permeability (determining the degree of salt dissolving) to geophysical parameters (velocities and resistivity). As result of these studies, we have obtained instruments for facilitating an estimation of these parameters, in-situ, using geophysical methods. Different geophysical measurements were carried out in boreholes just after

their drilling: (a) Ultrasonic logging and (b) Resistivity logging. (See Ezersky and Eppelbaum 2013 for the detailed description of methods)

(a) Ultrasonic logging

In the ultrasonic logging (USL) the elastic waves are spreading from a high frequency (10-100 kHz) transmitter to receivers along the borehole wall under investigation (Beck, 1981). Savich et al. (1969) suggested "dotty" (detailed) ultrasonic logging enabling to measure elastic velocities within 0.1 – 0.2 m along the borehole wall. Since the sonde is held against the side of the wall, the results are unaffected by the "adjacent beds" effect (as it is in seismic refractions) because of the wave's direct path. Wave penetration into the rock is approximately 0.1-0.2m in accordance with the wave length. The schema of the dotted ultrasonic logging is shown in Fig. 93 (a,b).

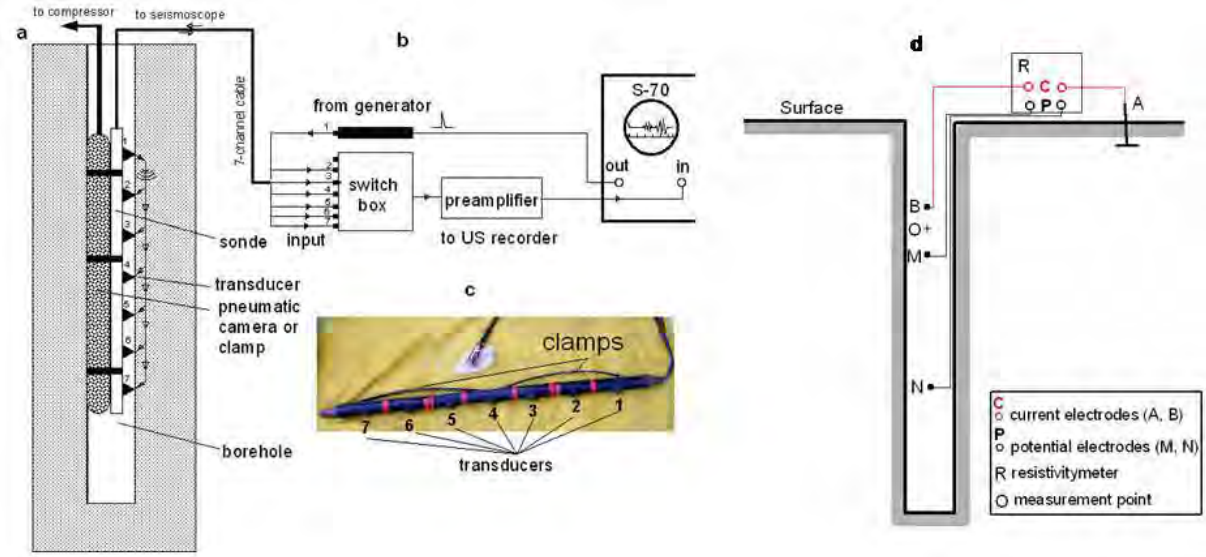

Figure 93. Borehole measurements. (a-b) Ultrasonic logging lay-outs: (a) 7-transducer sonde within borehole; (b) communication schema; (c) sonde photography; (d) Schema of measurements by method of apparent resistivity using a potential sonde.

In our investigation, a 7-transducer sonde, with 0.2m separation between sensors (Fig. 93c), was placed into the borehole (Fig. 93a) and clamped onto the wall by means of metallic clamps. Every transducer (100 kHz frequency) can act both as transmitter and as receiver when connected to a generator or oscilloscope, respectively. Switching is carried out with a switch-box (Fig. 93b). Elastic wave spreading along the borehole wall of from transmitter consequently arrives at the receiving sensors where it is converted, gained and visualized on the oscilloscope's electronic tube of the US meter S-70 (Fig. 93b). In general, compression wave velocity Vp, shear wave velocity Vs, and Rayleigh wave (R) velocity V_{SR}, are calculated based on corresponding measured arrival times. S-wave and R-wave form the interferential wave propagating along the borehole wall with a velocity depending on the relation between wavelength and the borehole diameter (Knopoff, 1952). The smaller the diameter of borehole the stronger S-wave velocity predominates and V_{SR} reduces to Vs. The greater of the borehole diameter, the closer the velocity approaches the V_R value. Identification of wave mode at the records is carried out by an interpreter. The following equation is used to calculate Vs/V_R ratio (Knopoff, 1952):

$$\left(\frac{Vp}{Vs}\right)^2 = \frac{16 - 24(Vr/Vs)^2 + 8(Vr/Vs)^4 - (Vr/Vs)^6}{16[1-(Vr/Vs)^2]} \qquad (21)$$

The interval velocities are integrated to give a velocity-depth profile, which is useful for good interpretation of the deep subsurface structure. This logging is used in engineering geophysics and tunneling to investigate a geological section with high resolution (Ezersky et al., 1991, 1993). Examples of field records are presented in Fig. 92f and 92g. Note that compression wave velocities Vp are consistent to the same velocity measured in samples, whereas V_{SR} measured in borehole can be 0.8744 to 0.9553of Vs.

(b) Measurements by the method of Apparent Resistivity

The method is based on differentiation of rocks around a borehole in accordance with their specific electrical resistivity (Hmelevskoi, 1979). A 3-electrode potential sonde was used (Fig. 93d). In the potential sonde, separation between potential electrodes MN extends separation between current electrode B and M. Electrode current A is earthed at the surface. Resistivity relates to point O named the "measurement point". Apparent resistivity is calculated using the expression:

$$\rho_a = k_a * (\Delta U / I) \qquad (22)$$

Where

$$k_a = \frac{4\pi * BM * BN}{MN} \qquad (23)$$

The larger the BM-to-borehole diameter ratio is, the apparent resistivity-to-true resistivity ratio becomes closer to 1. In our survey MN = 0.8, BM = 0.4m; borehole diameter was 9.6 cm; respectively, the above ratio was of ~4. The Syscal R2 (IRIS, Orlean, France) digital device was used as a resistivity meter (R in Fig. 93d) to generate current and to measure potentials between MN electrodes.

3.2.8.5. Results of the laboratory studies

(a) Range of measured laboratory parameters for the DS salt

Results of the laboratory testing shows that statistically WMS samples are characterized by higher values of wet and dry densities than these of CTS ones. Geophysical parameters Vp, Vs, and ρ_x are also higher in the WMS (wet and dry) samples. At the same time, porosity ϕ and hydraulic conductivity (coefficient of permeability) K of WMS samples are statistically lower than those of CTS salt. Taking into account results of the tests presented in Frydman et al (2008), we can determine porosity range of the salt samples from 3.5% to some higher than 20%, whereas Hydraulic conductivity (K) ranged 10^{-9}-10^{-5} m/s (or permeability
k = $2.2*10^{-16}$ to $2.2*10^{-12}$ m^2).

b) Permeability-porosity inter-relations.

The relationships are shown in Fig. 94. The results of our experiments on samples of WMF and CTS salt (Fig. 94a) are designated by red solid circles. The *K* of damaged samples is shown by black squares. For comparison, data from experiments of Frydman et al. (2008) carried out only on WMS samples are shown by green rhombs. Porosity – conductivity relationships are well fit by the power equation:

$$K = \phi^{3.684} * 0.0015 \qquad (24)$$

where K is in [m/s]. Regression equations for permeability (*k*) – porosity (ϕ) for DS salt (this study) will be written:

$$\ln(k) = 4.165 * \ln(\phi) - 20.865 \qquad (25)$$

where *k* is in [m^2].

Ezersky and Eppelbaum (2013) analyzing published results of numerous laboratory testing of salt samples carried out by different researchers at different conditions (effective pressure, fluid varying from gases to brines, size of grain etc.) have shown that (1) there is a porosity-permeability range similar to all data presenting the DS salt and (2) permeability-porosity relations are very similar when dynamic viscosity is taken to account (Fig. 94b). Note higher permeability of fractured samples at the same porosity.

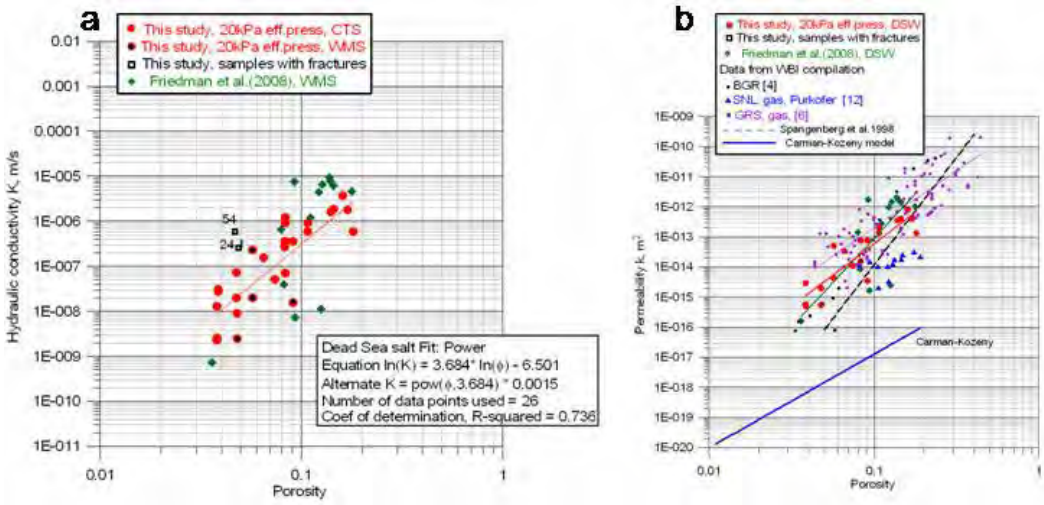

Figure 94. Hydraulic conductivity (coefficient of permeability) K versus porosity ϕ relationship obtained (a) For undamaged WMS and CTS salt samples in our tests. The K of damaged samples is shown by black squares. Data from experiments of Frydman et al. (2008) carried out on WMS samples are shown by green rhombs; (b) DS salt and different published data. Permeability was calculated for fluids with different viscosity (Ezersky and Eppelbaum, 2013). Kozeny-Carman model for experimental data on WIPP salt is shown

(c) Porosity and permeability versus velocity relationships

Relationships between porosity (permeability) and ultrasonic wave velocities Vp and Vs were derived for salt samples in wet and dry state. Velocity versus porosity graphs for brine saturated salt specimens is shown in Fig. 95a.

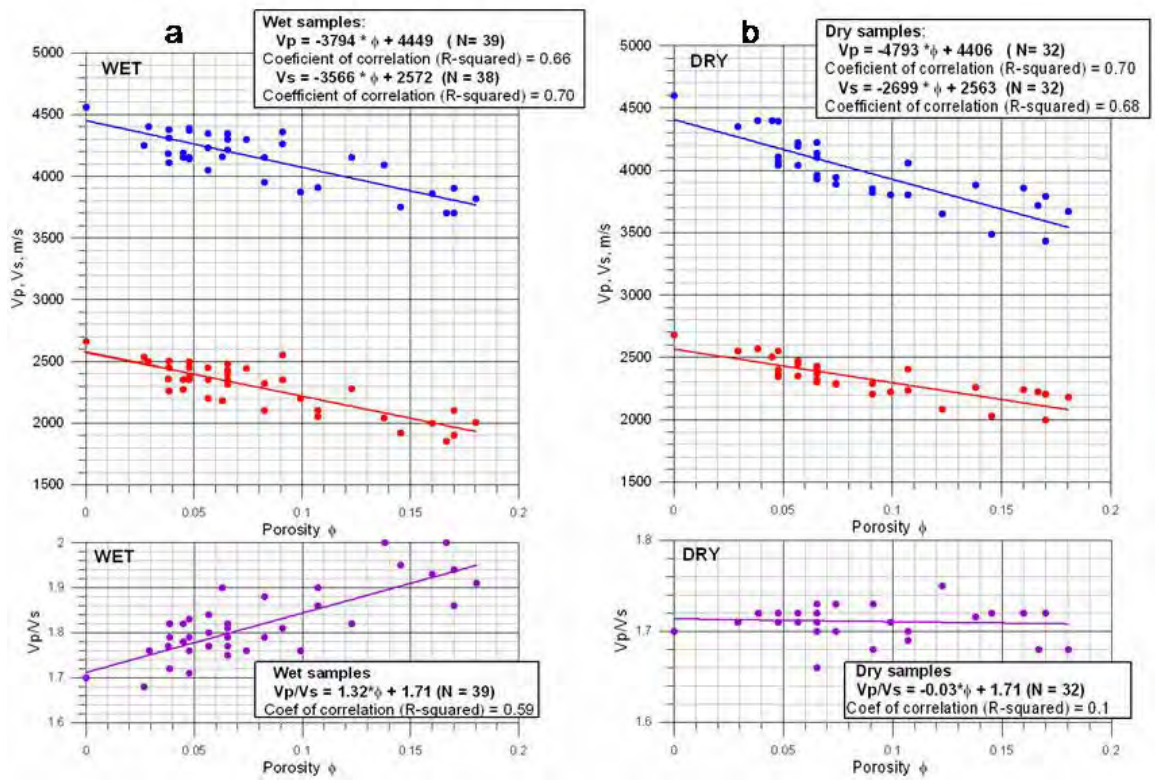

Figure 95. Variations of US velocities versus porosity in saturated with DS brine (a) and dried (b) salt samples. Blue curve is Vp, red - Vs and lilac curve - Vp/Vs

Inter-relationships for saturated salt samples are:

$$Vp = -3794 * \phi + 4449 \text{ (at } \phi < 20\%) \quad (26)$$
$$Vs = -3566 * \phi + 2572 \text{ (at } \phi < 20\%) \quad (27)$$

Similar relationships for dried (over 30 days) salt samples graphs are shown in Fig. 95b.

$$Vp = -4793 * \phi + 4406 \text{ (at } \phi < 20\%) \quad (28)$$
$$Vs = -2699 * \phi + 2563 \text{ (at } \phi < 20\%) \quad (29)$$

In both cases Vp and Vs linearly decreases with porosity increase. Vp/Vs ratio increases for wet salt and does not vary for dried one, staying at 1.68-1.72. Coefficients of correlation vary mostly between 0.66 and 0.70. The closest correlation (0.70) has been obtained for shear wave velocities in wet samples. No correlation has been detected for Vp/Vs ratio in dry salt samples. Relationships between ultrasonic velocities and hydraulic conductivity in brine saturated salt samples are shown in Fig. 95.

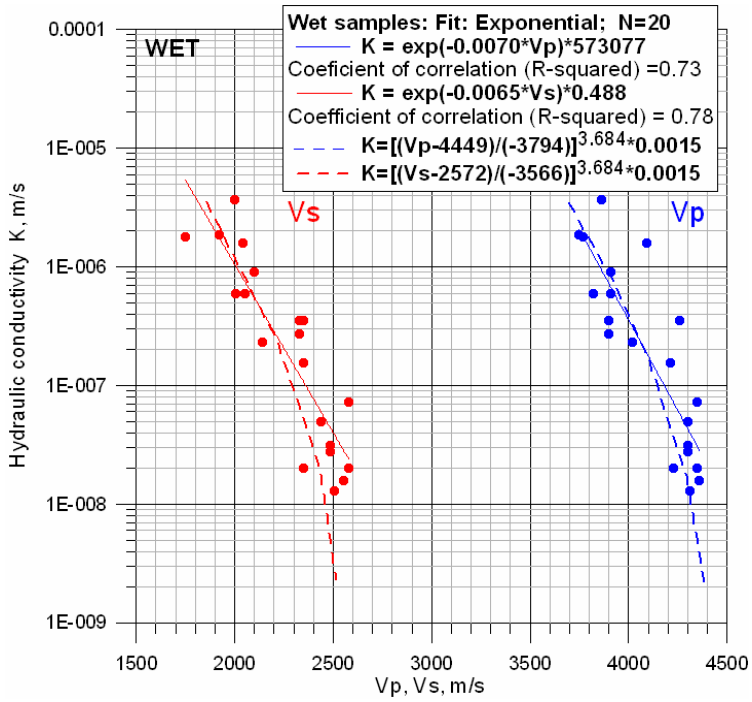

Figure 95. Hydraulic conductive K versus velocity Vp and Vs (red) graphs obtained for salt specimens saturated with the DS brine. Points are well approached by the exponential functions (thin solid lines). Dashed lines are curves revealed from Porosity – Velocity and Porosity – Hydraulic conductivity relations

Experimental points are described by exponential equations:

$$K = e^{-0.0070*Vp} * 573077 \quad (30)$$
$$K = e^{-0.0065*Vs} * 0.488 \quad (31)$$

(Correlation R-squared coefficient = 0.73 and 0.78, respectively). Dashed lines are curves revealed by combination of equations (24) and (26) for Vp and (24) and (27) for Vs. No correlation between velocities and permeability values has been revealed for dried salt samples (Correlation R-squared coefficient is of 0.20-0.21).

(d) Porosity and permeability versus resistivity relationships

Similar inter-relationships have been derived for bulk resistivity of saturated salt samples versus porosity (Fig. 96a) and versus permeability (Fig.96b).
Experimental points are fitted by power equations:

$$\rho_x = 0.080 * \phi^{-1.977} \quad (32)$$
$$K = 5.832 * 10^{-6} * \rho_x^{-1.558} \quad (33)$$

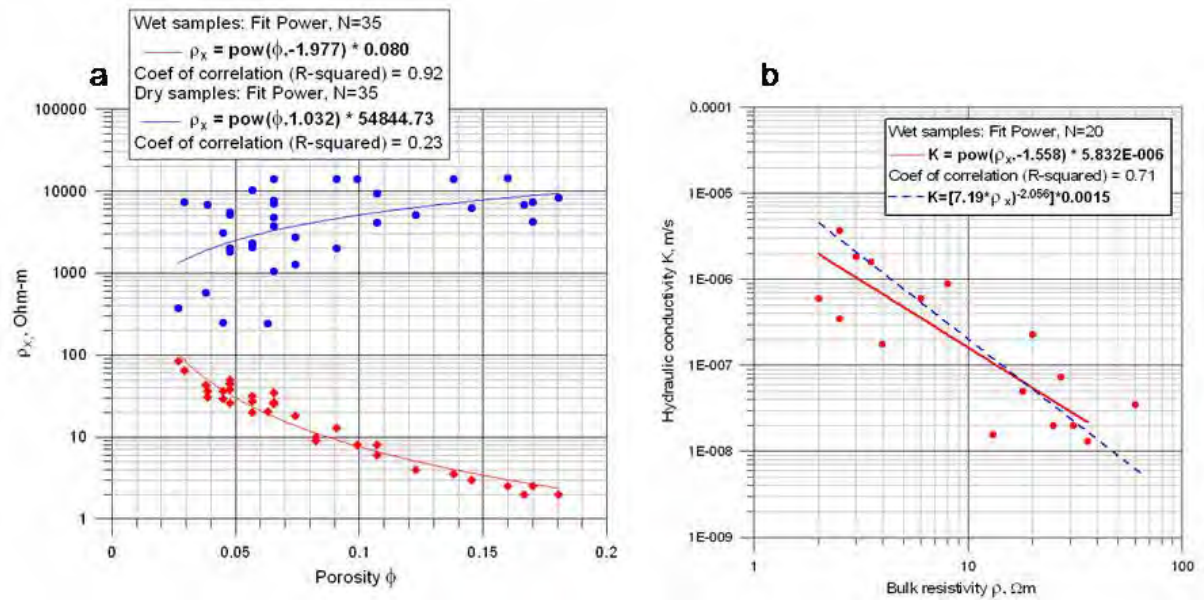

Figure 96. (a) Resistivity-porosity relationships for wet and dry samples of DS salt; (b) Resistivity - Hydraulic conductivity relationships revealed for wet salt samples

Equation (32) is analogue of Archie's Law (1) where $\rho_w = 0.04\ \Omega m$ (Kafri and Goldman, 2005), a = 3.47, and m = 1.793. The dashed line in Fig. 96b is the fit derived by combining equations (24) and (32). It is very close to (33) derived by direct correlation of experimental data.

3.2.8.6. Results of the borehole study

Ultrasonic and resistivity logging

The ultrasonic and resistivity logs (Vp, Vs and ρ_a versus depth graphs) are shown in Figs. 97a and 97b, respectively. Taking into account the more complicated origin of S-wave velocities, we compare Vp and ρ_a measured within boreholes, whereas Vs graph has been calculated from Vp using the inter-relation derived from ultrasonic measurements on salt samples: $V_s = 0.945V_p - 1626.2$ (R^2 = 0.78).Both velocities and resistivity show a trend increase with depth (thin dashed black lines). Vp and Vs velocities measured in salt samples are shown in Fig. 97a by red circles and green rhombs, respectively. Similarly, resistivity values are shown in Fig. 97b by lilac squares. One can see from comparison data that both velocity and resistivity values obtained on salt samples are higher than those measured in the borehole. The difference is more in upper part of the salt layer. Both velocity of salt samples and ultrasonic logs converges with a depth. Resistivity data show similar regularities.

The porosity logs (Fig. 97c) are calculated on the base of velocity and resistivity samples and Vp log using expressions (26, 27, and 32). Permeability logs (Fig. 97d) are based on equations (30, 31 and 33). It is logical to limit the range of calculated values by the range of data tested in the laboratory. Thick dashed black lines in Figs. 97c and 97d show upper limit of the reliable porosity and permeability values. One can see that porosity and permeability values measured in situ are statistically 2 times higher than the same parameters measured in samples under laboratory conditions.

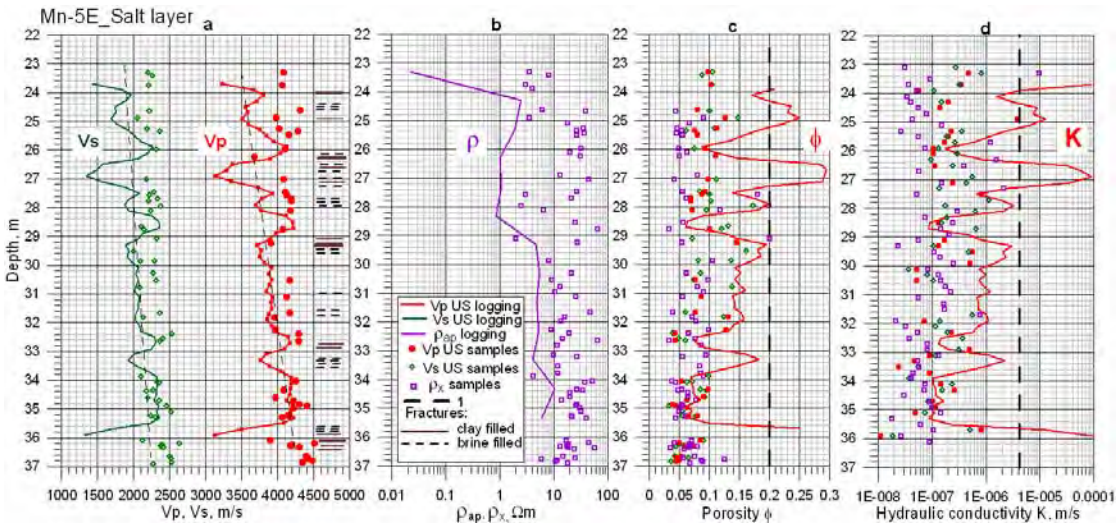

Figure 97. Combined interpretation of data acquired in the borehole Mn-5E. (a) Velocity versus depth graph (ultrasonic logging and velocities measured on salt samples); (b) resistivity versus depth graph (resistivity logging in borehole and resistivity measured on salt samples); (c) Calculated porosity versus depth graphs (calculated from all data using equations (26, 27, and 32); (d) Calculated permeability versus depth graphs (calculated from all data using equations (30, 31 and 33); 1 – correlation range. limited by range of laboratory tests

3.2.8.7. Discussion

Dead Sea salt porosity, permeability and their relationships are generally consistent to data of Frydman et al. (2008) for white (WMS) DS salt, as well as other published experimental data (WBI compilation, for instance). It is interesting that different salts from different sites and depths tested with different fluids from brine to gases show very similar permeability – porosity inter-relations especially when dynamic viscosity of fluid has been taken into account (salt subjected to the high 3-axial loading is not a case) (Ezersky and Eppelbaum, 2013).

Elastic parameters and electrical resistivities obtained in our laboratory tests are also, generally consistent with data described worldwide, as well as their inter-relations with porosity and permeability. In particularity, velocity (Vp, Vs) – porosity (ϕ) relationships obtained for dried (dry) salt are consistent to data by Popp and Kern (1998) obtained on artificial salt samples (Fig. 98a). Note: Vp in saturated salt (black line in Fig. 98a) expose higher values than those in dry samples (blue line in Fig. 98a). Shear wave (Vs) velocities expose reverse pattern: Vs in saturated samples (red line) are lower than those in dry ones (lilac line). Such behavior is explained by Dvorkin (2008), suggested that Vs not being depending on water fill, depends however on dry-to-wet densities ratio. This Ratio is slightly less than 1 and, respectively, Vs saturated is slightly less than Vs of dry salt.

In Fig. 98b: ρ_x versus ϕ relationship obtained for DS salt is compared with that obtained by Spangenberg et al. (1998) for artificially saturated salt samples. It is seen that resistivity level measured in artificial salt are lower, especially in the high porosity part. Perhaps, it is associated with salt preparation in the study by Spangenberg et al. (1998) when low porous samples were carried out at a pressure of 180 MPa, whereas samples with a porosity of more than that were produced from loose packs without axial pressure. In these tests, resistivity was measured using 4-electrode arrangement whereas our experiments were carried out using 2-electrode resistance measurements

Our study has shown good inter-relationships in salt samples that can be compared with results of borehole measurements. It at first relates to ultrasonic measurements and borehole logging giving the same parameters measured in the same frequency range of tens to hundreds of kHz. Resistivity logging gives the apparent resistivities, which are very close to true values because of the high ratio of BM separation to borehole diameter. However, could results of measurements be used for evaluation of in-situ porosity and permeability? This question can be answered after investigation of similar relationships in situ conditions.

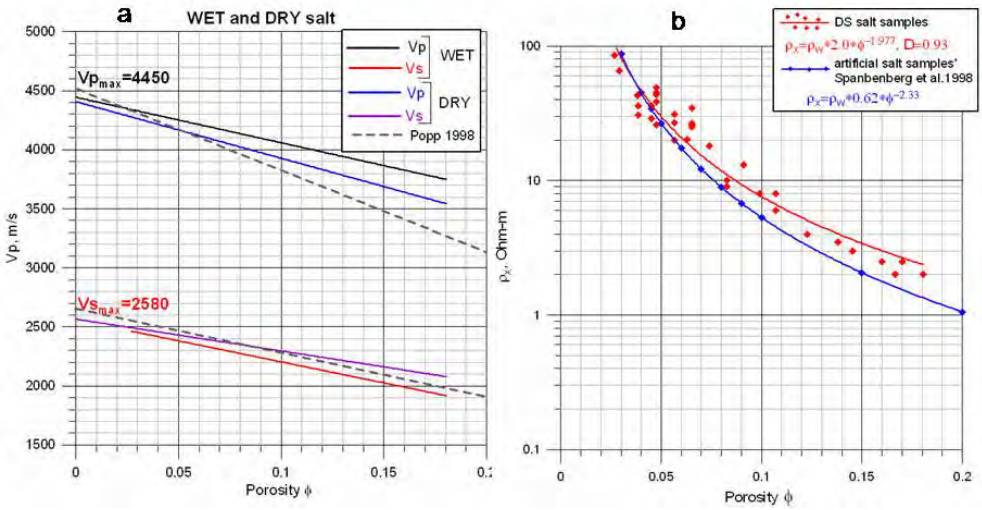

Figure 98. (a) Velocity porosity relationships obtained for the DS salt saturated (wet) and dried (dry) salt samples. Dashed gray line is similar to graphs for dry artificial salt samples (Popp and Kern 1998). (b) Resistivity porosity relationships for DS salt samples and Archie's law based on this relationship. Similar graph for artificial samples is shown for comparison (Spangenberg et al., 1998).

It is known that properties of rocks in-situ significantly differed of those in laboratory conditions (Hendron 1968). The salt rock is even more complex material, whose in-situ behavior after Baar (1977) cannot be predicted from most laboratory tests on cores because in the laboratory the same salt (that is plastic in situ) exhibit elastic behavior under most testing conditions used to determine the mechanical behavior of samples or models simulating the underground structures. Indeed, during the laboratory testing of DS salt samples we have measured following geophysical parameters: Vp = 3700 – 4450 m/s, Vs = 1900 – 2500 m/s and ρ_x = 2 – 100 Ωm). On the other hand, our field studies have shown that in-situ salt velocities Vp are ranged 2900-4200 m/s (Ezersky, 2006), Vs varies in limits of 750m/s to more than 1600 m/s (Ezersky et al., 2013a) and bulk resistivity is of 0.8 to 2.5 Ωm (Frumkin et al. 2011). These values are considerably less than analogous parameters measured in the salt samples. The same conclusion has been made from a comparison of salt sample properties and borehole logging obtained in the present study. Such differences are usually explained by presence of fractures and pores in-situ rock masses as against intact rock samples (Palmstrom 1996, Beniawsky 1974). It is especially so in actuality for the DS salt that is located at very shallow subsurface, which is subjected to deformations (Abelson et al. 2006) and comprises both fractures and voids, especially, in karstification zones (Eppelbaum et al. 2008, Ezersky et al., 2013b, Legchenko et al. 2008b). In the next Section we will suggest in situ evaluations of salt pore space properties using geophysical methods. In-situ velocity (Vs) – hydraulic conductivity (K) inter-relations as well as resistivity ρ_x – porosity ϕ ones will be presented in the next Section.

3.2.9. In-situ Shear Wave Velocity – Resistivity versus Hydraulic Conductivity Inter-relationships in the Dead Sea Salt Layers

3.2.9.1. General

In a previous Section we have found correlative relationships of porosity and permeability with velocities (resistivities) for DS salt samples saturated with brine. However, there is the problem of extrapolating laboratory-based relationships to in-situ conditions. Comparison of ultrasonic velocities (Vp, Vs) measured in laboratory with data from ultrasonic logging in boreholes has shown that in-situ salt is characterized by lower velocities than salt samples selected from the same depth. Moreover, seismic S-wave refraction and MASW methods show Vs in salt layers considerably lower than those in samples. Indeed, in-situ salt velocities Vs vary within limits of 750m/s to more than 1650 m/s (Ezersky et al., 2013a), while laboratory testing of the DS salt specimens have shown Vs = 1900 - 2500 m/s and

hydraulic conductivity (K) varying in range between 10^{-5} - 10^{-9} m/s. Taking into account that there are relationships Vs – K in salt samples one can expect corresponding relationships in a scale of in-situ measurements (lower frequency and longer wavelength).
Ezersky et al. (2013a) suggested the methodology to map buried salt layers using the Multichannel Analysis of Surface Waves (MASW) method. The methodology allows constructing of Vs maps through salt layers. Similar methodology based on mapping salt layer resistivity using Transient Electromagnetic (TEM) method was suggested by Ezersky et al. (2011), and Frumkin et al. (2011).
Hydraulic conductivity of salt karstification was suggested by Legchenko et al. (2008a) using Magnetic Resonance Sounding (MRS) method.
In this Section the problem of salt permeability-porosity determination using surface geophysical methods is considered. In spite in the Section **3.2.8**. correlative relationships of porosity and permeability with velocities and resistivity for DS salt samples saturated with brine were found, there is the problem of extrapolating laboratory-based relationships to in-situ conditions. Therefore the main goal of this part is to check relationships between salt hydraulic conductivity (K) and shear wave velocities (Vs) and resistivity (ρ_x) measured in salt layers in-situ conditions and connect it with those parameters measured in the salt specimens in the laboratory conditions.

3.2.9.2. Main Methods

MASW method was presented in details in Section 3.2.2.3 and TEM method was described in the Section 3.2.4.4. Here we present briefly MRS method.
Magnetic Resonance Sounding (MRS) Method
MRS is a selective method specifically sensitive to groundwater (Legchenko and Valla, 2002; Legchenko et al., 2004). For performing MRS measurements, the hydrogen protons of groundwater molecules are energized by a pulse of alternating current generated in the surface loop. Measured magnetic resonance signal is sent back by the protons after the excitation current is cut off. One sounding consists of measuring the MRS signal for different values of the current in the loop. Two main parameters are derived from MRS measurements (Lachassagne et al., 2005): (a) the MRS water content (w), which is closely related to the amplitude of the MRS signal; (b) the MRS relaxation time T_1. Assuming a horizontal stratification, inversion of sounding data estimates the water content $w(z)$ and the relaxation time $T_1(z)$ as a function of depth (z) (Legchenko and Shushakov, 1998). Combinations of the MRS water content and relaxation time allows for estimating rock hydraulic conductivity, with C_p being an empirical constant that can be calibrated to similar hydrogeological parameter using the pumping test.

$$K_{MRS} = C_p w T_1^2, \qquad (4)$$

These MRS parameters can be linked more-or-less to the following hydrogeological parameters that are core parameters in the field or applied hydrogeology (Lachassagne et al., 2005):

- *Porosity* (ϕ; dimensionless); hydrogeological parameter "water content" appears to be related to this hydrogeological parameter;
- *Permeability* (or Darcy's permeability), which describes the ability of a fluid to flow through a medium under the influence of a hydraulic head gradient. It is expressed quantitatively by the intrinsic permeability (dimensions: L^2) and, for water in standard conditions by the coefficient of *hydraulic conductivity K* (L/T);
- *Transmissivity T* (L^2/T), which is equal to the coefficient of conductivity of an aquifer, multiplied by its thickness (measured perpendicularly to the flow direction, most frequently along the Z axis).

MRS is an efficient tool for characterizing aquifers, but also for locating water-filled voids in the subsurface (Vouillamoz et al., 2003; Boucher et al., 2006). Legchenko et al. (2006) have shown using both numerical modeling and field measurements that MRS could be applied to the investigation of the weathered part of hard-rock aquifers when the product of the free water content multiplied by the thickness of the aquifer is > 0.2. This is a case in the northern DS coastal areas, where 10-30m thick

salt layers comprise (after laboratory tests) more than 3.8% porosity with the water content w > 2.3% (e.g. minimum 10m salt with a 2.3% water content and over) (Ezersky and Eppelbaum, 2013).

Data acquisition. All MRS measurements at the Nahal Hever South site were carried out using NUMIS^{plus} MRS System developed by IRIS Instruments (France). In the Dead Sea area, interpretation of MRS data requires knowledge of the subsurface electrical conductivity. For that reason, each MRS measurement was accompanied by TEM measurements.

Scale factor. In conclusion we have to note that hydraulic conductivity is a scale-dependent parameter. MRS results averaged over a large area are determined by the loop size. Similarly the pumping tests also provide results averaged over a large volume. That enables to calibrate MRS hydraulic conductivity to the hydrogeological that. Moreover, to reach a depth of 25-70m, MASW profiles should be also 120-150m long. Thus, both MRS and MASW methods used for generation of correlative inter-relations between Vs and K give results in the same scale of ~ 100m.

3.2.9.3. Results

To generate correlative relationships Vs - K we have used results of MRS, MASW, and TEM methods jointly carried out on 2005-2007 in-situ conditions of the Nahal Hever South (NHS) site (Sinkhole site 8 in Fig. 1). The subsurface of the NHS test site (clastic sediments and salt layers) are representative for the DS coastal areas. The MRS measurements were carried out earlier at NHS by Legchenko et al. (2007, 2008a, 2008b). Vs sections were extracted from the long seismic refraction field records (record length of 1-2s) obtained during the same period using the MASW technique. Only a few of MASW measurements were performed in the NHS area during 2012 at distance from sinkhole sites where no surface signs of sinkholes was observed (Fig. 1). The methodology of Vs measurements in the salt layer was suggested by Ezersky et al. (2013a). We used also a methodology for determining salt parameters utilizing TEM soundings (Ezersky et al., 2011).

Fifteen MRS soundings were performed on the site during 2005, and twenty three 100x100m^2 MRS soundings were carried during 2007. The location of MRS stations is depicted in Fig. 99 (Legchenko et al., 2007; Legchenko et al., 2009).

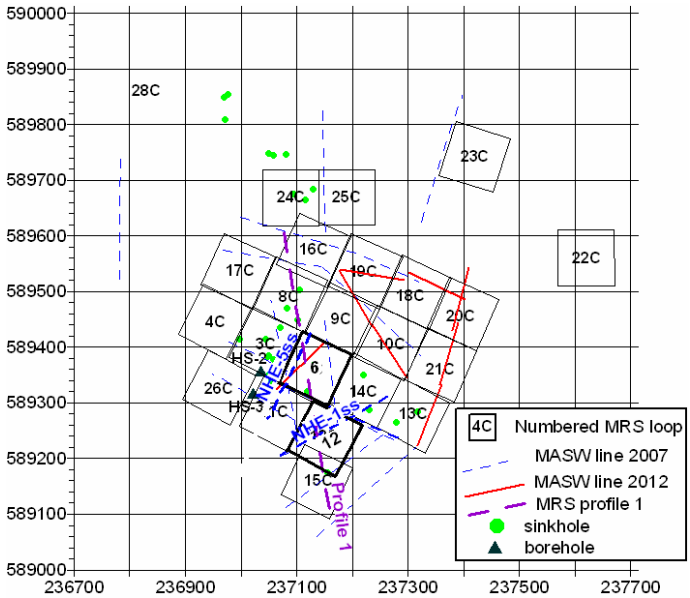

Figure 99. MRS and MASW location map in the Nahal Hever South (NHS) site

13 MASW lines, 235m long (10Hz vertical geophones with a 5m separation), were shot through the NHS area during 2007 (Ezersky et al., 2008). During 2012, 10 MASW additional lines, 120m long (2.5 Hz geophones 5m separation), were carried out.

TEM soundings accompanying the MRS ones were carried out at every MRS stations by loops 25x25 m^2, 50x50 m^2, and 100x100 m^2 simultaneously with MRS soundings (Legchenko et al., 2009). The system of MRS and TEM loops covered by MASW lines have enabled us to search correlation between MRS hydraulic conductivity (K) on one hand, and shear-wave velocity (Vs) on the other hand. The measurements were carried out at the same place and in the same scale (approximately 100

m^2). Such scale corresponds to that of conventional pumping tests performed in the hydrogeological investigations.
We generated 2 distribution maps of measured parameters within salt layer through the NHS area (Fig. 100).

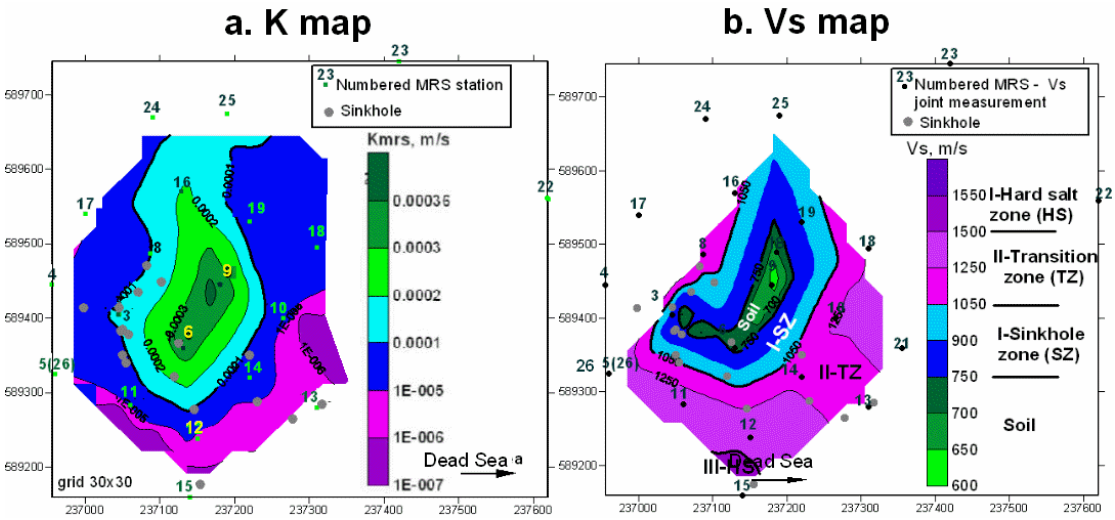

Figure 100. Maps of hydraulic conductivity K_{MRS} (a), and shear wave velocity Vs (b) within salt layer through the NHS area

One can see from K_{MRS} map (Fig. 100a) maximum hydraulic conductivity is characteristic for the center of the area where karstified salt is located (Legchenko et al., 2008a). This map is conformed to map published by Legchenko et al. (2009). Parameter K in the salt layer decreases to the NHS area margins. The Velocity (Vs) map (Fig. 100b) shows a low velocity zone in the center of the salt area, velocity increases toward Dead Sea. Such a velocity distribution shows that permeability (and consequently, voidness) of salt layer decreases in the direction of the Dead Sea and margins of the area. Similar distribution of the salt velocity is characteristic for all studied sites using the MASW technique (Ezersky et al., 2013). Thus both maps testify to the decrease of salt permeability towards the DS and the area's western and southern margins. At the same time, all these maps display a trend of salt permeability increase toward the northern margins of the NHS area. Since a great deal of studies were carried out during 2005-2007, we can state that during following years intensive sinkhole development took place in the northern direction, exactly confirming the correctness of geophysical predictions. Note that the inverse relationships between Vs and K in the saturated salt samples were obtained in our laboratory testing (Ezersky and Eppelbaum, 2013). Thus, we can use maps presented in Fig. 100 for generating relationships K versus Vs. The inter-relationship of K versus Vs is presented in Fig. 101 (red circles).

One can see that the red circles are located in the velocity range of Vs = 1600-600 m/s, corresponding to the permeability range of 10^{-6} - $4*10^{-3}$ m/s. Accepting Vs = 750m/s as a lower limit of the porous salt Vs (Romero and Rix, 2001), we can conclude that K = $2*10^{-4}$ m/s is an upper value of hydraulic conductivity in the field conditions. The lower hydraulic conductivity limit of red circles is caused by the threshold of the MRS method that is 10^{-6} m/s for conditions at NHS (Legchenko et al., 2007). Respectively, Vs = 1600 m/s is an upper limit of Vs corresponding to this conductivity value. We present the similar relationship obtained for salt samples in the laboratory conditions (blue circles in Fig. 101). First of all, one can see that K - Vs graph is located at the range of high Vs values (1900-2600 m/s). Respectively, hydraulic conductivity values are disposed at the range of lower values (10^{-5} - 10^{-9} m/s). The lowest ultrasonic velocity of Vs = 1900 m/s is a threshold of the shear-wave velocity testified by attenuation of ultrasonic waves, whereas the upper Vs limit is caused by low porosity and permeability characterizing the properties of halite (Vs = 2600m/s for a clean Polyhalite matrix).

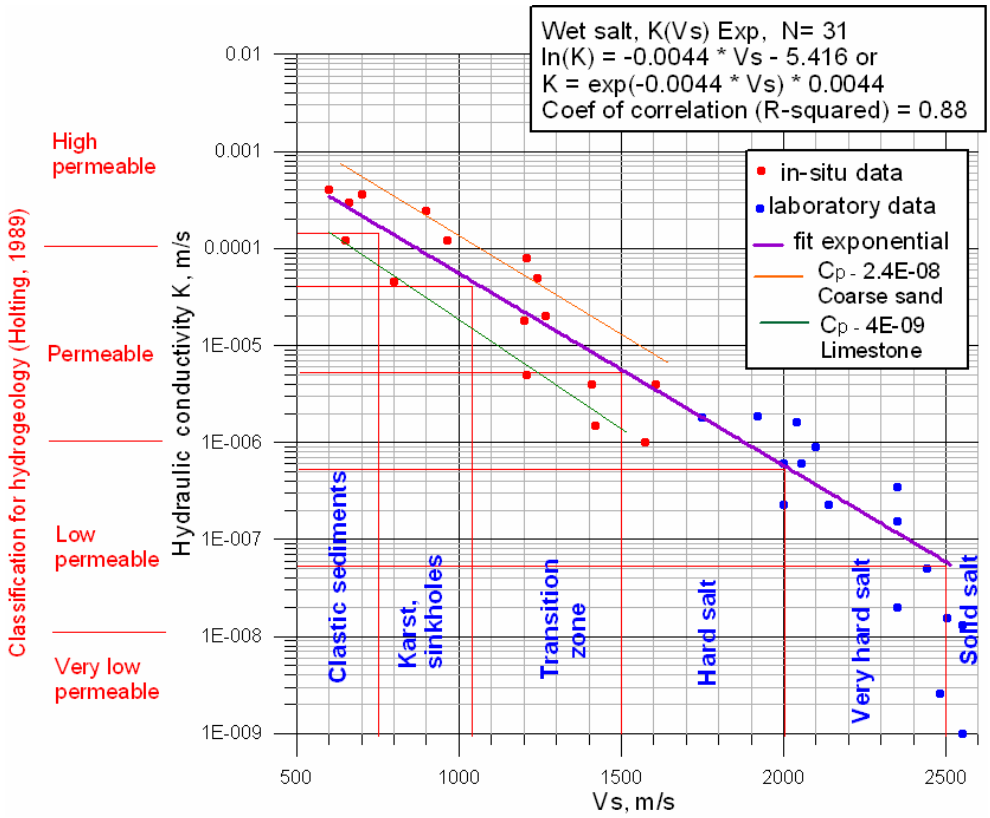

Figure 101. Relationship Vs - K based on calibration of elastic shear wave velocities to Hydraulic conductivity in different scales of measurements. Blue circles are pair laboratory ultrasonic and permeability measurements performed on brine-saturated salt samples. Red circles are in-situ K_{MRS} and Vs_{MASW} measurements in the water saturated salt layer using a 100x100m^2 loop and a 120m long line, respectively. Alternative graphs for different Cp are given by Nielsen et al. (2011). A classification of hydraulic conductivity used in hydrogeology (Holting, 1989) is presented the left of the graphs.

All experimental points are well-fit the exponential function:

$$\ln(K) = -0.0044 * V_s - 5.416 \qquad (7)$$

with a correlation coefficient (R-squared) of 0.88.

We have mapped sinkhole sites based on Vs values (Ezersky et al., 2013). Let us consider an example distribution of Vs and corresponding hydraulic conductivity K values in salt layer through the Mineral Beach area (Fig. 102). Both maps show an increase of shear wave velocity from the salt edge towards the DS. The Vs map (Fig. 102a) shows an increase of Vs from 760 m/s near the salt edge (blue zone) up to 1650 m/s and more near the DS. In terms of permeability, it corresponds to a decrease of K from slightly more than 10^{-4} m/s near the salt edge to slightly more than 10^{-7} near the DS.

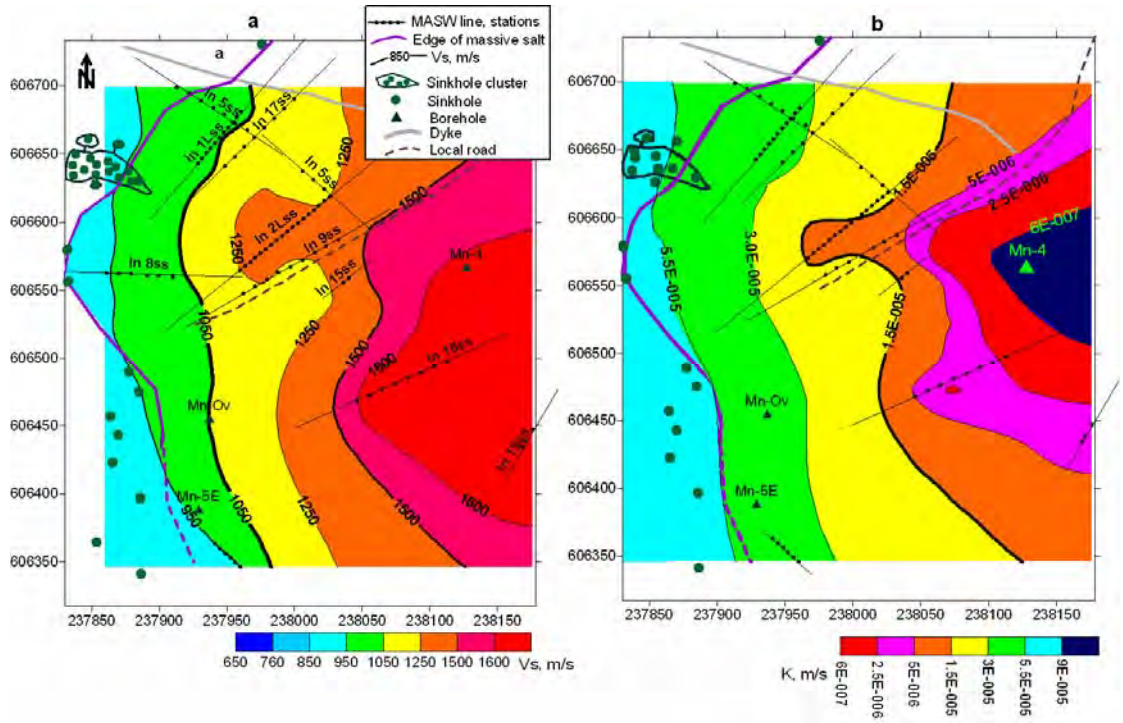

Figure 102. Distribution of the permeability within salt layer through the Mineral Beach area based on Vs (a). ((a) With permission of EEGS, (Ezersky et al., 2013a)

Similar map has been constructed for the Nahal Ze'elim area (Ezersky and Legchenko, 2014, accepted for publishing in the Springer press).

Note also that similar relationships have been generated for ρ_x - K parameters (Ezersky and Eppelbaum, 2013).

3.2.9.4. Discussion

Inter-relationship Vs – K presented in Fig. 101 consists of two different components: K values dispersed at large values of Vs are measured by the direct laboratory testing, whereas velocity has been measured by ultrasonic pulse method. K values disposed at low shear-wave velocities are based on K measured by the MRS method (e.g., K_{MRS}) and converted to the pumping-based parameter (K_{pump}) by use of an optimal calibration coefficient of C_p = 7E-9. At that, the Vs have been derived from MASW measurements. Thus, two parts of the graph in Fig. 101 are based on measurements of different mutually matched scales: salt sample – ultrasound (volume of 0.00036m^3) and salt layer – MASW and MRS measurements (100x100x10 = 10^5 m^3). As mentioned above, hydraulic conductivity of geological formations is a scale-dependent parameter. Results obtained in a different scale can be different. An example of two aquifers of different types is presented in Fig. 103. In an aquifer with a single porosity (type A) presented in Fig. 103a, the water is located in similar pores and hydraulic conductivity of this aquifer is closely related to the pore size. In this case, information about the aquifer derived from MRS measurements is also related to hydraulic conductivity even if investigated samples are of a different volume. In an aquifer with a double porosity (type B), as shown in Fig. 103b, most of the water is located in large pores, but hydraulic conductivity mostly depends on small pores. In this case, if the volume of investigated sample is small (laboratory measurements), and the result of hydraulic conductivity estimation depends on whether the selected sample represents small or large pores. A large-scale method like the MRS will provide us with information mostly related to large pores, as they contain a larger quantity of water than small pores do. Obviously, the hydraulic conductivity estimation is much less accurate in this case. In practice, different types of porosity are usually mixed, and the measured magnetic resonance signal is often composed of a sum of signals decaying with different relaxation times and thus, contains information about different pores.

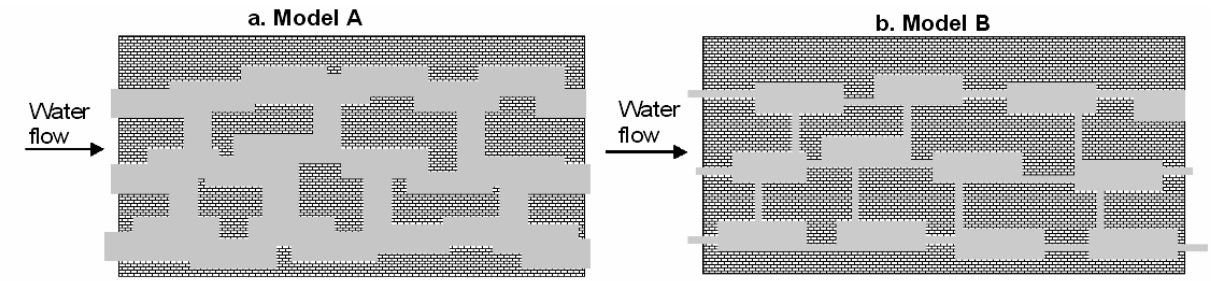

Figure 103. Hydraulic conductivity of aquifers: Type A – single porosity; Type B – double porosity.

The same can be said relatively to Vs versus porosity relationship. That is why expressing Vs versus hydraulic conductivity K is not possible analytically and correlative inter-relations are worth looking for. Exponential graph in Fig. 101 well fits both groups of experimental points for both laboratory and in-situ measurements. We have also shown in Fig. 101 graphs calculated with Cp = $4*10^{-9}$ for limestone (green line) and one calculated with Cp = $2.4*10^{-8}$ for coarse sand (orange line). The experimental points can be seen arranged between those graphs.
Suggesting the same origin of relationships between Vs and K (e.g., that those are determined by voidness) we can conclude that the graph in Fig. 101 describe an entire range of Vs and corresponding values of K, which can characterize hydraulic conductivity of salt irrespective of the measurement scale. Note only that this relationship should be verified by a pumping test within salt layer. Accepting this relationship in Fig. 101 as a first approach one could doubt that the DS salt has high enough permeability in comparison with laboratory measurements. However, some tests have shown that such high hydraulic conductivities are very reliable for the DS conditions. Yechieli et al. (1995) extracted the salt sample from borehole DS-1 in the Nahal Ze'elim site. The sample looked like sand and its laboratory test for hydraulic conductivity showed K=10^{-5} m/s (compare it with laboratory points in Figs. 101 and 102. The author concluded that unconsolidated nature of the salt could be results of some factors prevented its cementation and diagenesis. High hydraulic conductivity K = 10^{-3} m/s has been suggested by W. Wittke in the southern DS area based on testing of salt samples (unpublished data, 2006). Our Vs mapping in the Nahal Ze'elim site has shown that high permeability K = 10^{-3} - 10^{-5} is a local phenomena associated with the location of borehole DS-1 close (some 40-50m east) to salt edge (see Fig. 99 for location). With increasing distance from the salt edge towards the DS, Vs increases and permeability decreases. However, K is keeping at 10^{-6} m/s that is characterized as between permeable to low-permeable that was supported by pumping tests. These data show that salt hydraulic conductivity decreases towards to DS staying, nevertheless permeable to low-permeable (in terms of Holting (1989) classification shown in Fig. 102) as linked to the DS. Based on above data we can suggest classification system of DS salt based on shear-wave velocities (Vs) measured in-situ conditions. Table 11 suggests classification of salt with respect to its geophysical properties and permeability (Hydraulic conductivity value).

Table 11. Classifications of salt conditions based on Vs and ρ_x

Classification by salt conditions	Karstified salt	Transition zone (salt)	Hard salt	Very hard salt	Solid salt
Classification by sinkhole hazard	sinkhole hazardous	forthcoming sinkholes	no sinkholes	no sinkholes	no sinkholes
Classification by permeability*	HPerm-to-Perm	Perm	Perm-to-LPerm	LPerm	LPerm-to-VLPerm
Hydraulic Conductivity, m/s	$1.1*10^{-4}$ - $4*10^{-5}$	$4*10^{-5}$ - $5*10^{-6}$	$5*10^{-6}$ - $5*10^{-7}$	$5*10^{-7}$ - $5*10^{-8}$	$5*10^{-8}$ - $1*10^{-9}$
Porosity	>30%	30% - 17%	17% - 10%	10% - 6%	< 6%
Velocity Vs, m/s	760-1050	1050 - 1500	1500-1950	1950-2450	2450 – 2600
Velocity Vp, m/s	2500-2800	2800 - 3300	3300-3800	3800-4300	4300 - 4450
ρ_x, Ωm	0.4 – 0.7	0.7 – 2.0	2.0 – 7.0	7.0 – 21	21 – 100

*) HPerm- High permeability; Perm – permeability; LPerm – low permeability; VLPerm – very low permeability

In accordance with Table 11, K values presented in Fig. 102 relate the DS salt to the high permeable unit near the salt edge to permeable-to-low permeable unit near the DS that corresponds to determinations by geologists. The following study should check out these inter-relationships by direct pumping tests to implement this methodology for the DS Work (Israel) and the Arab Potash Company (Jordan).

3.2.10. Implementation of the MASW method at the Dead Sea Dam 5/8 (Southern Basin)

3.2.10.1. General

We have implemented the MASW method at the Dam 5/8 of southern DS basin. The problem of salt shear wave velocity (Vs) arises when Site Response should be calculated using H/V Method (Zaslavsky et al., 2009). Our experience has shown that at salt location more than 30 meters seismic S-wave refraction method fails to reach the salt layer using most of S-wave seismic sources available in Israel. In these cases Vp/Vs ratio is used to reveal approximate Vs values using Vp ones (Ezersky, 2003). Note the Vp/Vs Ratio is different for rocks and salt and depends on many factors such as lithology, porosity, water content, isotropy etc. (Tatham and McCormack, 1991, p.p 47-49). Our study shows that Vp/Vs can vary in specimens from 1.7 to 2.1 and over. That is why in-situ measurements of Vs are very important for evaluation of salt properties. One MASW line was shot in accordance with MERC permission and in agreement with Dead Sea Works Ltd.

3.2.10.2. Geological context

Dyke 5/8 is the northern border of evaporation ponds. Interpreting of drilling data was carried out prior to the building of the dyke testifies that the area is covered with young sediments of halite interbedded with soft clay to silt sized limestone (previously described as clay or marl) (Bruner et al., 2003). Recently, these sediments are named as lime carbonates and have properties described in the Section 3.2.7. These sediments show signs of recent active tectonic faulting and salt diapirism. In the southern part of the Dead Sea Basin the uppermost part of the sequence is dominated by some 60-80 m of salt layers alternating with some lime mud deposited over the last 15,000 years. These sediments belong to the Ze'elim Formation. The sequence below to a depth of hundreds of meters consists of lime mud, clay and possibly some sand and gravel of the Lisan and Samra Fms. The area is intersected by salt diapirs of different dimensions and depth below surface and is disturbed by complex fault systems and hallokinesis (Shalev et al., 2005).

3.2.10.3. Geophysical measurements layouts

MASW study was carried out on the lower ledge of the Dam (dyke (Fig. 104).

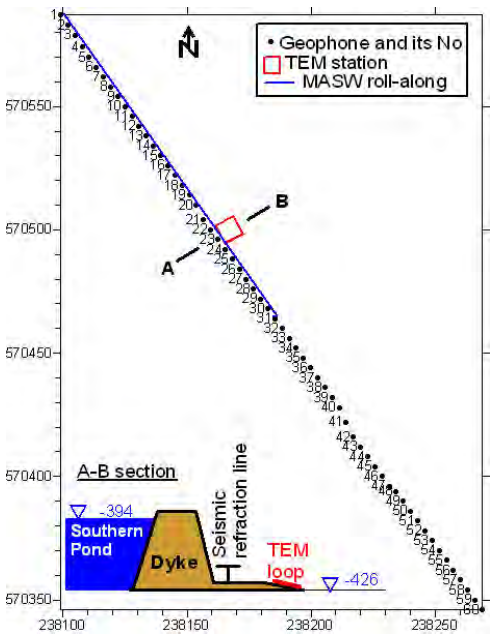

Figure 104. Geophysical study layouts along the Dam 5/8

Seismic Refraction line of 295 m long was shot using the General Reciprocal (GRM) Method (Palmer, 1986). Sixty 10 Hz vertical geophones were separated by 5m. The Digipulse seismic source operated at 5 points: at the ends of line, at its center and at distance of 150m from both ends of line (offsets).

The MASW study was carried out using 2.5 Hz vertical geophones (Gisco, Minneapolis, U.S.A) purchased for the project. One line comprises of 31 geophones with 5m separation providing line length of 150m. The MASW measurement was shot using roll-along technique with offset of 10m from behind of line (technique is similar to seismic reflection data acquisition). The line was shifted by 10m forward with simultaneous shift of the source. One TEM sounding 25x25 m^2 loop was carried out using TEM FAST 48HPC system at the middle of seismic refraction line (Fig. 104).

3.2.10.4. Results

Constraints

As we have mentioned in the Section 3.2.2.4 in *linearized inversion* methods, constraints are applied to the solution in order to reduce the degree of non-uniqueness (Cercato, 2009). The dispersion equation depends mainly on Vs and thickness value in the layers. An appropriate choice of these parameters (the initial model) is considered as a fundamental issue for the successful application of inversion (Socco and Strobia, 2004, Renalier et al. 2010). Let us consider data acquired on the DS Dam 5/8 Fig. 105. The sStarting model was constrained by existing external geological and geophysical data (see below).

The seismic refraction section (Fig. 105a) allows distinguishing of 3 layers. Uppermost one with Vp=900-1000m/s undoubtedly characterizes the clastic sediments down to 5-7m deep.

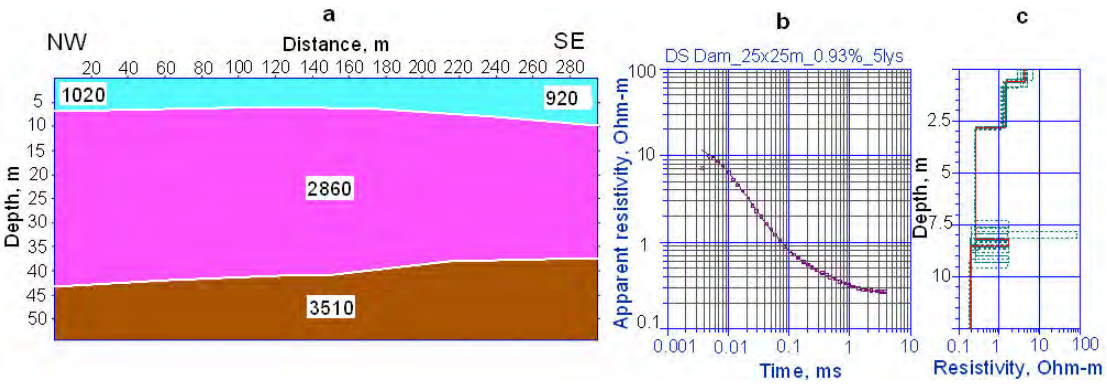

Figure 105. Constraints for MASW inversion. (a) Seismic refraction P-wave velocity depth section; (b) TEM signal, (c) TEM inverse resistivity depth graph (red line). Green dotted graphs are equivalent solutions.

The third layer at a depth of 40-43 m is salt characterized by Vp=3510 m/s. Finally, intermediate layer with Vp = 2860-2900 m/s is not clastic sediments and it can be considered as uppermost salt layer (may be some layers) interbedded with clastic sediments saturated with DS brine. Such interpretation is supported by TEM data presented in Figs 105b,c. Fig. 105b shows the transient signal of good quality till 4 ms. Inverted resistivity – depth graph in Fig. 105c shows that there is badly resolved thin high resistivity layer that can be salt. Unfortunately this layer is located at a border of resolution of MASW method evaluated as 6m.

Inversion results. An example of data processing from the DS Dam 5/8 is shown in Fig. 106

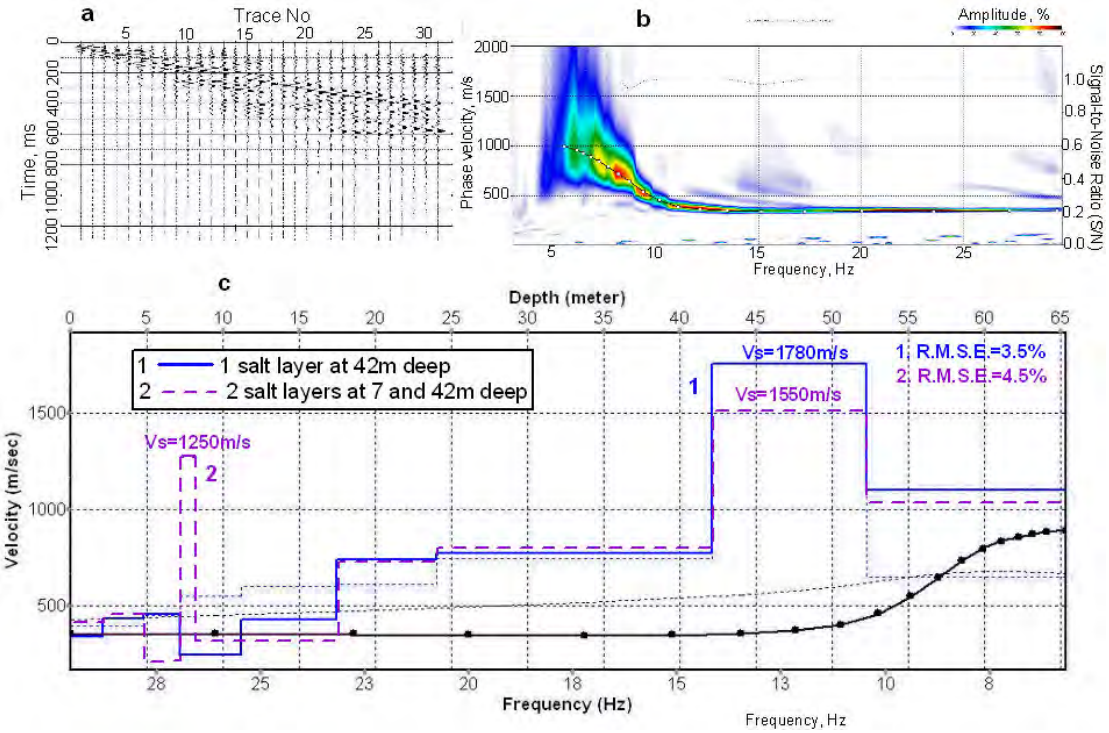

Figure 106. Results of Surface Waves inversion. (a) Field records 2s length; (b) Dispersion image with extracted dispersion curve; (c) Two inversion Vs versus depth graphs for one and two salt layers models (See Section 3.2.2.4 for explanation)

Results of the processing of data acquired at the Dam 5/8.

The seismic signal (Fig. 106a) is comprised of 4 stacks. The signal-to-noise (S/N) ratio is high (0.9-1.0) (dotted line in Fig. 106b). The dispersion image and the extracted dispersion curve are also depicted in Fig. 106b. Only the fundamental mode is clearly seen in the dispersion image, higher modes being absent or obscured in this case. In Fig. 106c, the same dispersion image is combined with the theoretical dispersion curve (black points) fitted using a forward modelling for the 9-layered model shown in Fig. 106c. The model to invert comprises 7 low Vs velocity layers above an eighth high-velocity one (salt) and a ninth low-velocity layer for considering the existing geological information.

Then we applied the least-squares inversion to investigate variations of the salt Vs at different parameterization and start models. Inversion was carried out at fixed Vp value of 3500m/s. Solution converges after 20-25 iterations. Results of the data inversion are summarized in Fig. 106c For optimum 9-layered model (starting Vs = 1500m/s) inverted Vs value is of 1780 m/s at R.M.S.E. = 3.5%. Varying of the initial velocity model slightly changes salt layer velocity in framework of $\pm 5\%$ (from 1690 to 1860m/s model comprising one salt layer). Inserting to model 2 salt layers (Fig. 106c dashed lilac line) results in varying the misfit error in the realm of 8% (1550 – 1840m/s).

Resolution. The resolution of the uppermost layer is limited by $\lambda_{\min}$=12 m ($V_{ph\,\min}$ = 354 m/s, $f_{\max}$=29.6Hz in this case). Thus, Vs in a layer shallower than H_1 = 6.0 m thick is unreliable in accordance with the half-wavelength criterion (e.g. Rix and Leipsky 1991). The maximum wavelength $\lambda_{\max}$=160m ($V_{ph\,\max}$ = 893 m/s, $f_{\min}$ = 5.6 Hz), defining a maximum penetration depth of 80m.

3.2.10.5. Conclusion on Section 3.2.10

The method of salt mapping from the surface using MASW technique has been tested on the Dam 5/8 bordering southern evaporation ponds to keep DS level at elevation of -394m (some 30m higher than it is in the northern DS basin. MASW method allows the characterizing Vs of the consolidated salt layer located at a depth of 42-45 m that was not possible earlier using conventional seismic S-wave refraction method.

3.2.11. Discussion and conclusions on Section 3.2.

The main aim of this study is to find an optimal way of integrating several geophysical methods in order to provide a basic sinkhole susceptibility assessment. An additional benefit is a better understanding of sinkhole formation above salt deposits. Indeed, the integration of several methods at studied sites allowed the prediction of sinkhole formation before it actually occurred.

General model: salt distribution and sinkhole location. In spite of the various DS sinkhole formation models, most researchers agree that sinkhole development is connected with the drop of the Dead Sea level, either because of aggressive water incursion into the coastal area (Yechieli et al., 2002, 2006), or because of artesian flow via faults and conduits (Abelson et al., 2006, Shalev et al., 2006), or because of collapse of surface sediments into pre-existing dissolution cavities due to decreasing buoyant support (Legchenko et al., 2008a). A combination of these non-exclusive models, which often enhance one another is a probable situation..

Moreover, our recent studies (Ezersky and Frumkin, 2013, Ezersky et al., 2013a,b; Frumkin et al., 2011) based on new imaging methodology (Keydar et al., 2012; Keydar et al., 2013) have suggested improved model presented in Sections 3.2.3. It was shown that sinkhole lineaments are arranged along the salt layer edge acting as a dynamic dissolution front. We suggest that superficial coastal basins where salt formed could be generated by sub-vertical displacements along faults. This reconciles the two major competing models of sinkhole formation: the structural model, considering control of faults, and the dissolution front model associating sinkhole formation with the salt edge. The combined model suggests that the salt layer edge follows a paleo-shoreline, ~10.5 ka old, constrained by faults and alluvial fans. The sinkholes develop along the dissolution front, is controlled by these features. The buried salt layer extends landward, away from the modern Dead Sea shoreline, permitting its investigation from the surface.

As result, we can map buried salt layers by shear wave velocity (Vs) using MASW technique (Ezersky et al., 2013a) and to distinguish zones of different mechanical properties or permeability within the salt layer (Ezersky and Eppelbaum, 2013)

Application of geophysical methods to the DS sinkhole problem is based upon the model formulated in our earlier works (Bruner et al., 2003; Ezersky, 2003; Ezersky et al., 2010). The present study, following previous ones, shows that the dissolution process occurs preferentially where the salt and clay lake sediments interfingering with alluvial and colluvial gravel and sand (Frumkin et al., 2011). Further towards the lake, the salt layer is sandwiched within thick fine-grained lake deposits, commonly clay, acting as hydraulic protective layers above and below the salt. It is supported by results of the salt layer mapping stated that Vs values vary from 760 m/s at the salt edge and rising to 1500 m/s and more with the distance from the salt edge towards the Dead Sea (Ezersky et al., 2013a). We suggest based on borehole data that such variations in Vs are caused by a change of salt voidness.

The circulation of under-saturated water with respect to chloride causes salt dissolution. This water circulation is more intensive near the salt edge and attenuates with distance from it. Correspondingly, karstification (voidness) of salt is active near the layer edge and gradually decreases towards the Dead Sea. The decrease of salt karstification towards the Dead Sea is caused also by thickening of clay layers above and below salt (blocking the water circulation) with approaching to the DS shoreline.

Considered process fits the sinkhole formation along the salt edge (Ezersky et al. 2010; Frumkin et al. 2011; Legchenko et al. 2008) and is supported by the salt dissolution model proposed by Shalev et al. (2006).

Following the dissolution front salt edge concept, we suggest a general model of the salt layer deposited around the DS. This model (Ezersky et al., 2010; Ezersky et al., 2013b; Ezersky and Frumkin 2013) suggests that there is a 10-30 m-thick salt belt around much of the DS shore, controlling the sinkhole hazard. All known cases of collapses and accidents including the alarming catastrophe at pond 18 in Jordan (Closson, 2005) have occurred within this salt belt. The dissolution belt along the salt edge is wide at the western side, and in the northern and southern parts of the Jordanian side of the DS. It can become narrow and even completely disappear in the central part of the Jordanian side. As a result of the heterogeneous dissolution, the seismic properties in salt should strongly vary along (e.g., parallel to DS shoreline) and gradually change (increase) perpendicular to shoreline (i.e., towards the DS direction).

Model of sinkhole formation. Frumkin et al. (2011) have considered model of sinkhole formation when karst has been formed. In the case presented here, the head of the overlying aquifer has diminished dramatically during the last decades due to the fall of Dead Sea levels, causing increased artesian flow

and rapid dissolution. Salt dissolution may take place a short or long period before any signs are evident on the surface (Fig. 107a). At that after hydrogeological and geophysical evidences salt edge during a long time is located

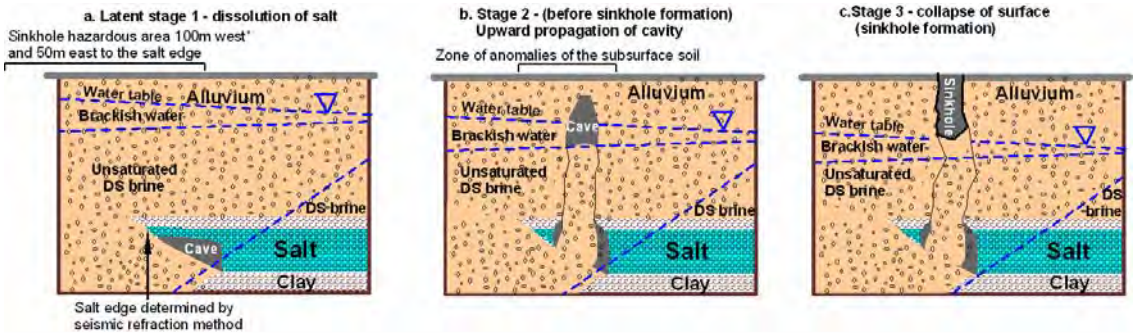

Figure 107. Gradual sinkhole formation at the salt edge: (a) latent stage; (b) upward propagation of cavity (stoping); (c) sinkhole formation. Comment in (a) (*) in spite there is not salt west to salt edge salt would be dissolved earlier. Therefore dissolution cavities can exist in this zone testifying the sinkhole hazard. It is confirmed by statistics of sinkhole formation.

within high mineralized Dead Sea brine that is, nevertheless, unsaturated with respect to chloride (Ezersky et al., 2010; Legchenko et al., 2009; Yechieli et al., 2006, 2007). This water is aggressive with respect to salt and it keeps potential to the salt dissolving (see Ezersky and Levi, 2013 and Section 3.2.4 of the present report). Instability of the salt cavity ceiling causes upward stoping through the mechanically-weak sediments situated between the cavity and the surface (Fig. 107b). Ford and Williams (2007, p. 385) report cases in different geological settings, where the stoping process propagated through >1000 m of cover rocks. This intermediate stage continues until the surface collapses and a sinkhole forms (Fig. 107c).

Extrapolating the ongoing retreat of the Dead Sea, the water-table will fall progressively below the salt layer, leaving it within the vadose zone. This situation will favor the karstification process by downward vadose flow from ephemeral streams (e.g. Frumkin, 1995).

Role and potential of geophysical methods in the sinkhole problem. Considering the above-mentioned processes, we have resolved number of important aspects by means of surface geophysics:

1. Distribution of the salt layer, and particularly its edge (Seismic P-wave refraction method);
2. Zones of increased porosity and their lateral distribution throughout the salt area (Seismic S-wave refraction method and MASW methods). We suggested also the methodology of salt hydraulic conductivity evaluation;
3. Changes in the properties and structure of shallow sediments, overlying cavities. These disturbances include increased porosity and various types of ductile and brittle deformation structures (Yang and Drumm, 2002; Maimon et al., 2005). Porous and fractured zones in the subsurface detected by geophysical methods (TEM, ERT, GPR etc.) may allow anticipating imminent sinkholes before the collapse reaches the surface, allowing for timely warning.
4. Evaluation of DS water salinity and aggressiveness (TEM);

Especial place in the Project was devoted to potential methods. Microgravity and Magnetometery surveys are now widely applied for subsurface investigation, especially for sinkholes (karst) phenomenon delineation. The Ghor Al-Haditha area situated in the eastern Dead Sea coast (Jordan) is a perspective object for microgravity (and other geophysical methods) application. However, microgravity observations more strongly than other methods are disturbed by very complex regional gravity pattern and complex topography in this area. After removing the Dead Sea Transform negative gravity effect by linear regressions, gravity anomalies more reliably and clearly were detected (Al-Zoubi et al., 2013a, Eppelbaum, 2013). Applications of numerous information, statistical, probabilistic and algebraic approaches at the gravity data sets were effectively applied. Quantitative analysis and 3D modeling were successfully applied to interpretation of several magnetic anomalies. Application in the site of the gravity and other geophysical method includes an employment of advanced combined coherency wavelet interpretation and diffusion maps.

Surface geophysical methods tested at the Ghor Al-Haditha area (Akkawi et al., Al-Zoubi et al., 2013b; Frumkin et al., 2011) allowed following conclusions. GPR method is most

reliable and allowing interpretation of results in real time. Disadvantage of the method is its sensitivity to soil resistivity. In the low resistive subsurface (e.g. high salinity and water saturation of soil) penetration of electromagnetic waves strongly decreases. Method is used in the areas of alluvial fans. EMR method allows detection of buried sinkholes, faults and fractures with different energy level and spatial extent. Note there are lines where EMR pulses are not correspond to sinkholes. It can be explained by high level of electromagnetic noises in the places of people activity. Thus, EMR method should be combined with other geophysical methods. The development of the EMR method it seems to be continued and its origin must be understood better. ERT method is working well at the resistive subsurface (alluvial fans) and fails to give deep image at the mud flats.

Soil property testing. Finally, this study compiles (1) results of DS soils testing founded in literature and (2) our own borehole and laboratory testing enabling to understand particularities of DS soil geotechnical and geophysical properties necessary for modelling, calculations of stability and geophysical measurements. Two types of lithology were studied in-situ and laboratory conditions to reveal geotechnical and geophysical properties of these soils (Ezersky, 2013; Ezersky and Livne, 2013). Sandy-gravel sediments are presented by coarse sands, which are characterized by Vs = 300 – 650 m/s. Such increased shear wave values can be caused by increased the DS soil stiffness described in the literature. Brine saturated lime carbonates (DS mud) are characterized by low Vs values of 120 – 250 m/s. In addition to borehole testing clayey sediments (lime carbonates) were studied in the laboratory conditions using Bender Element (BE) and uniaxial and three axial strength for unconsolidated undrained (UU) conditions. Frydman et al. 2008 reported cohesion of 0 kPa and friction angle 34° obtained in consolidated undrained (CU) conditions, e.g. lime carbonates do not exhibit cohesion when saturated in the DS brine. It is explained by mineralogical composition of the Dead Sea material, composed predominantly of calcite and not clay minerals, whereas other Israeli clays are comprised largely of montmorillonite (spectite) clay minerals. This feature allows considering of saturated lime carbonate as cohesionless soil like fine sands. On the other hand our tests have shown that unsaturated (or naturally moist) lime carbonates have a low friction angle of $\sim 2^o$ and cohesion of 18 kPa caused by apparent cohesion or suction effect (Terzaghi et al., 1996). After Khlaifata et al. (2010) lime carbonates demonstrate also very low cation exchange capacity (CEC) that allows use of TEM resistivity method for determining of porosity of both sands and DS mud as suggested by Kafri and Goldman (2005) (Ezersky and Levi, 2013). Note also that significant difference of Vs in sands and lime carbonates allows mapping of different lithology along DS coastal areas. Geotechnical properties of soils have been determined in laboratory conditions (Ezersky, 2013)

References

Abelson M., Aksinenko T., Pinsky V., and Yechieli Y. 2013. Geological indications for fiasibility microseismic experiment at Mineral Beach, Dead sea: monitoring concealed collapses long before sinkhole occurence. Annual GSI meeting, 28-30 May, 2013, Ako, Israel.

Abelson, M., Baer, G., Shtivelman, V., Wachs, D., Raz. E., Crouvi, O., Kurzon, I., Yechieli, Y., 2003. Collapse-sinkholes and radar interferometry reveal neotectonics concealed within the Dead Sea basin. Geophysical Research Letters 30 (10), 1545, doi:10.1029/2003GL017103.

Abelson, M., Yechieli, Y., Crouvi, O., Baer, G., Wacks, D., Bein, A., Shtivelman, V., 2006. Evolution of the Dead Sea sinkholes. In Enzel, Y., Agnon, A., Stein, M. (Eds), Geological Society of America, Geological Society America Special Paper, 401, pp. 241-253. DOI: 10.1130/2006.2401.(16)

Abueladas, A., and Al-Zoubi, A., 2004. The application of a combined geophysical survey (GPR and seismic refraction) for mapping sinkholes in Ghor Al-Haditha Area, Jordan: in EOS Transactions: AGUnion, **85**, No. 47, Fall Meeting Supplement, Abstract GP11A-0825.

Abueladas, A-R., Al-Zoubi, A., Akkawi, E. and Al-Ruzouq, R., 2010. New Geophysical Approach to Prediction of Sinkhole Hazard related to the drop of the Dead Sea level and human activity. Report of presentation at the MERC-2011 Meeting at Cyprus.

Abueladas A-R., and Eppelbaum L., 2011. Sinkhole hazard assessment Part X. Magnetic field processing and analysis. Report MERC 10/M27-050, January 2011, 15pp.

Akkawi E., 2010. Electrical Time Domain Method. Progress report for the sinkholes at the southern part of the Dead Sea. BAU, October, 2010, 17pp

Akawwi E, Al-Zoubi A, Abueadas A, Eppelbaum L, Ezersky M, Levi E, Legchenko A, and Boucher M. 2012. Mechanism of Sinkhole Formation in the Ghor Al-Haditha Based on Geophysical Data. Geophysical Research Abstracts Vol. 14, EGU2012-2244, EGU General Assembly 2012

Akkawi E., Kakish M., Al-Zoubi A., 2006. Using Electromagnetic Radiation (EMR) method to locate the active faults and non-0pened subsurface sinkholes along the eastern shores of the Dead Sea, Jordan. Proc of the 2nd WSEAS International Conference on Engineering Mechanics, Structures and Engineering Geology: 85-88.

Akkawi E., Kakish, M., Al-Zoubi, A., 2008. Investigation the active faults, sinkholes at the eastern shores of the Dead sea by using electromagnetic readiation. Proc. of the 2nd WSEAS International Conference on Engineering Mechanics, structures and Engineering Geology (EMESEG'08). Heraklion, Crete Island, Greece, July 22-24, 2008.

Alexeyev, V.V., Khesin, B.E. and Eppelbaum, L.V., 1996. Geophysical fields observed at different heights: A common interpretation technique. *Proceed. of the Meeting of Soc. of Explor. Geophys*., Jakarta, 104-108.

Al-Homoud, A.S., Makinson, C., Tal, A.B., Penman, J.G., 1999. In situ geotechnical experimentation and stability evaluation of an instrumented 180 m 9 70 m 9 12.5 m fill dike constructed on laminated soft ground. Environ. Geol. 39 (2), 177–196

Alperovich, L., Averbuch, A., Eppelbaum, L. and Zheludev, V., 2013. Delineation of karst terranes in complex environments: Application of modern developments in the wavelet theory and data mining. *Trans. of the 9th EUG Meet.*, Geophysical Research Abstracts, Vol. **15**, EGU2013-11063, Vienna, Austria, 2 pp.

Al-Zoubi, A., Abueladas, A-R., Camerlynck, C., Al-Ruzouq, R, Al-Rawashdeh,S., Ezersky, M., and Ali, W. 2007. Use of 2D multi electrodes resistivity imagining for sinkholes hazard assessment along the eastern part of the Dead Sea, Jordan., American Journal of Environmental Sciences 3(4), 229-233

Al-Zoubi A., Eppelbaum L., Abueladas A., Ezersky M., Akkawi E. 2011a. Preliminary magnetic data analysis in the eastern Dead Sea shore for identification of subsurface inhomogeneties and sinkholes EAGE-*ES 17 th Meeting*, 12-14 September 2011., Lechester, UK., P30, 4pp.

Al-Zoubi, A., Abueladas A.-R., Eppelbaum, L. 2011b. Current Report. Preliminary results of the Microgravity Mapping through the Ghor Al-Haditha Area, Jordan.

Al-Zoubi A, Akkawi E, Abueladas A, Eppelbaum L, Keydar S, Medvedev B, Levi E, and , and M. Ezersky. 2012a. Integrated Geophysical Tools for Sinkholes Study along the Dead Sea shoreline. Geophysical Research Abstracts Vol. 14, EGU2012-1980, EGU General Assembly, 2012

Al-Zoubi A, Abueladas A, Akkawi E, Eppelbaum L, Levi E, and Ezersky M. 2012b. Use of Microgravity survey in the Dead Sea areas affected by the sinkholes hazard. Geophysical Research Abstracts, Vol. 14, EGU2012-1982, EGU General Assembly 2012

Al-Zoubi A, Abueladas A, Akkawi E. 2012c. MERC sinkholes project. Progress Report.

Al-Zoubi A., Akkawi E., Abueladas A. 2013. Sinkhole hazard assessment **Part XI**. Electromagnetic Radiation Method (EMR) for sinkhole detection. Report MERC 11/M27-050, April 2013, 9pp.

Al-Zoubi, A., ten Brink, U.S., 2001. Salt diapir in the Dead Sea and their relationship to Quaternary Extensional Tectonics. *Marine and Petroleum Geology*, 18**,** pp. 779-797

Al-Zoubi A., L. Eppelbaum*, A. Abueladas, M. Ezersky and E. Akkawi 2013a. Removing regional trends in microgravity in complex environments: Testing on 3D model and field investigations in the eastern Dead Sea coast (Jordan). International Journal of Geophysics. Special Issue. Vol. 2013. Article ID341797, 13pp. http://dx.doi.org/10.155/2013/341797

Al-Zoubi A., Ezersky M.G., Akkawi E., Abueladas A-R., Levi, E., 2013b. Sinkhole hazard assessment. **Part XII**. Surface Geophysical Methods in the sinkhole problem. Report MERC 12/M27-050, January 2011, 15pp.

Archie, G.E., 1942. Electrical resistivity as an aid in determining some reservoir characteristics. Transactions of American Institute of mining Engineers, 146, 54-62.

Arkin,Y. & Gilat,A., 2000. Dead Sea sinkholes- an ever-developing hazard. *Environm. Geol*. 39, 7: 711-722

Arkin, Y., Gilat, A. & Kofman, L., 2000. Developing Dead Sea sinkholes revealed by ground penetrating radar. GSI Current Res., 12, 25-30.

Bahat, D., Rabinovitch A., Frid, V., 2005. Tensile Fracturing in Rocks –ectonofractographic and Electromagnetic Radiation Methods. *Springer Berlin Heidelberg*. 569pp.

Banab, K. K., and Motazedian, D., 2010, On the Efficiency of the Multi-Channel Analysis of Surface Wave Method for Shallow and Semi-Deep Loose Soil Layers: International Journal of Geophysics, **2010**, Article ID 403016, 13 pp., doi:10.1155/2010/403016

Barsukov, P., Fainberg, E., and Khabensky, E. 2007. Shallow investigations by TEM-FAST technique: Methodology and examples. In Electromagnetic sounding of the Earth's interior, (Ed. Spichak, V)., Methods in Geochemistry and Geophysics, V. 40., Elsevier, vol. 10

Baar, C.A., 1977. Applied salt-rock mechanics 1. In-situ behavior of salt rocks. Elsevier, Amsterdam-Oxford-New-York, 294pp

Bartov, Y., Agnon, A., Enzel, Y., Stein, M., 2006. Late Quaternary faulting and subsidence in the central Dead Sea basin. Israel Journal of Earth Sciences, 55 (1), 18-31

Batayneh, A.T., Abueladas, A.A. and Moumani, K.A., 2002. Use of ground penetrating radar for assessment of potential sinkhole conditions: an example from Ghor al Haditha area, Jordan. Environmental Geology, V. 41, pp. 977-983.

Beck, A.E., 1981. Physical Principles of Exploration Methods, Macmillan Press Ltd., London.

Beck, B.F., 2003. *Sinkholes and the Engineering and Environmental Impacts of Karst*, Geotechnical Special Publication **122**, American Soc. of Civil Engineers, RestonVA.

Begin, B., Ehrlich, A., Nathan, Y., 1974. Lake Lisan the Pleistocene precursor of the Dead Sea. Geological Survey of Israel, Bulletin 63, 30p.

Ben-Avraham, Z., 1997. Geophysical framework of the Dead Sea: structure and tectonics, In: Niemi, T.M., Ben-Avraham, Z., Gat, J. (Eds.) The Dead Sea: the lake and its setting. Oxford University Press, Oxford, pp. 22-35.

Ben-Avraham, Z., Lazar, M., 2006. The structure and development of the DS basin: recent studies. In New Frontiers in Dead Sea. in Enzel, Y., Agnon, A., Stein, M. (Eds): Paleo-environmental Research, Geological Society America Special Paper, 401, pp.13.

Beniawsky, Z.T., 1974. Geomechanical classification of rock masses and its application in tunneling, 3rd Congress of the ISRM, Denver, USA, Proceedings, Vol. II., Part A, 27-32.

Benson R.C. and Yuhr, L., 1993. Spatial sampling consideration and their applications to characterizing fractured rock and karst systems. Applied Karst Geology, Beck (ed). Balkema, Rotterdam: 99-113.

Beres M., Luetscher M. and Olivier R. (2001). Integration of ground penetrating radar and microgravimetric methods to map shallow caves. *Journal of Applied Geophysics*, Vol. 46, Issue 4, pp. 249-262.

Bernabé, Y., Mok, U., and Evans, B., 2003, Permeability-porosity relationship in rocks subjected to various evolution processes: Pure and Applied Geophysics, **160**, 937-960

Biot, M.A., 1956a. Theory of propagation of elastic waves in fluid saturated porous solid. I. Low-frequency range. J.Acoust.Soc.Am., 28, pp. 168-178.

Biot, M.A., 1956. Theory of propagation of elastic waves in fluid saturated porous solid. II. Higher-frequency range. J.Acoust.Soc.Am., 28, pp. 179-191

Blake W.D. and .Gilbert R.B. 1997 Investigation of Possible Relationship between Undrained Shear Strength and Shear Wave Velocity for Normally Consolidated Clays. Offshore Technology Conference, 5 May-8 May 1997, Houston, Texas

Blakely, R.J. 1995. *Potential Theory in Gravity and Magnetic Applications*. Cambridge Univ. Press.

Bodet, L., Galibert, P. Y., Dhemaied, A., Camerlynck, C., Al-Zoubi, A., 2010. Surface-wave profiling for sinkhole hazard assessment along the eastern Dead Sea shoreline (Ghor Al-Haditha, Jordan). 72nd EAGE Conference & Exhibition incorporating SPE EUROPEC 2010, Barcelona, Spain, 14-17 June 2010. M027

Boucher, M., J.-F. Girard, A. Legchenko, J.-M. Baltassat, N. Dörfliger, and K. Chalikakis, 2006, Using magnetic resonance soundings to locate a water-filled karst conduit: J. Hydrology, **330**, 413– 421.

Boucher, M., Camerlinck, C., Legchenko, A., and Ezersky, M., 2007. Preliminary results of the MRS and TEM studies after development of sinkholes through Ghor Al-Haditha area, Technical Notes, Jordan, IRD-Paris6University-GII

Bruner I., Charach, J., and Medvedev, B. 2003. High resolution seismic reflection survey along dike 5/8, Dead Sea Works. Ecolog Report No. 320/336/03.

Cannaday, F.X., 1964. Modulus of elasticity of a rock determined by four different methods. Report of investigations U.S. Bureau of mines, 6533.Ca

Casto, D.W., Luke, B., Calderon-Matias, C., and Kaufmann, R., 2009, Interpreting Surface-wave data for a site with shallow bedrock: Journal Environmental and Engineering geophysics, **14**, No. 3, 115–127

Cha, M., and Cho, G.-C, 2007. Shear strength estimation of sandy soils using shear wave velocity. Geotechnical Testing Journal, 30 (6), 484-495

Chalikakis, M.K., 2006. Application de methodes geophysiques pour la reconnaissance et la protection de ressources en eau dans les milieux karstiques. PhD Thesis, Univ. Paris 6.

Cercato, M., 2009, Addressing non-uniqueness in linearized multichannel surface wave inversion: Geophysical Prospecting, **57**, No. 1, 27-47, doi: 10.1111/j.1365-2478.2007.00719.x

Closson, D., 2005. Structural control of sinkholes and subsidence hazards along the Jordanian Dead Sea coast. Environmental Geology, 47, 290-301

Closson D., and Abu Karaki N., 2009. Salt karst and tectonics: sinkholes development along tension cracks between parallel strike-slip faults, Dead Sea, Jordan. Earth surface processes and landforms 34, 1408-1421.

Crawford, N.C., Lewis, M.A., Winter, S.A. and Webster, J.A., 1999. Microgravity techniques for subsurface investigations of sinkhole collapses and for detection of groundwater flow paths through karst aquifers. *Hydrogeology and engineering geology of sinkholes and karst*, Beck,B., Pettit, A., and Herring J.G,Balkema, Rotterdam: 203-218.

Cress, G.O., Brady, B.T., and Rowell, G.A., 1987. Source of electromagnetic radiation from fracture of rock samples in laboratory. Geophysical Res. Lett, 14, 331-334.

Dahlin T. 1996. 2D resistivity surveying for environmental and engineering applications, First Break, 14(7), 275-283.

Dejong J. T., 2007. Site characterization – Guidelines for estimating Vs based on in-situ tests. Stage I. Interin Report. http://dap3.dot.ca.gov/shaketable/references/Vs30_correlations_ US. Davis.pdf

Domenico, S.N., 1977. Elastic properties of unconsolidated porous sand reservoirs. Geophysics, 42 (7), pp.1339 – 1368.

Dvorkin, J., 2008, Yet another Vs equation: Geophysics, **73**, No. 2, E35-E39 10.1190/ 1.2820604

Duba A., Piwinskii A.J., Santor M., and Weed H.C., 1978. Geophys. J.Astr.Soc. 53, pp. 583-597.

El-Isa, Z., Rimawi, O., Jarrar, G., Abu-Karaki, N., Taqieddin, S., Atalah, M., Abderahman, N., and Al Saed, A., 1995, Assessment of the hazard of subsidence and sinkholes in Ghor Al-Haditha area. Report submitted to Jordan Valley Authority: University of Jordan, Amman, 141pp.

Eppelbaum, L.V., 2006. Methodology of 3-D combined modeling of magnetic and gravity fields in the Eastern Mediterranean. *Proceed. of the 3rd EUG Meeting*, Vol. **8**, 02057, 4 pp.

Eppelbaum, L.V., 2007a. Revealing of subterranean karst using modern analysis of potential and quasi-potential fields. *Proceed. of the 2007 SAGEEP Conference*, **20**, Denver, USA, 797-810.

Eppelbaum, L.V., 2007b. Localization of Ring Structures in Earth's Environments. *Jour. of the Archaeological Soc. of the Slovakian Acad. of Sci., Spec. Issue: Arch. Prosp.*, **XLI**, 145-148.

Eppelbaum, L.V., 2008. Remote operated vehicle geophysical survey using magnetic and VLF methods: proposed schemes for data processing and interpretation. *Collections of Selected Papers of the 2008 SAGEEP Conference*, **21**, Philadelphia, USA, 938-963.

Eppelbaum, L.V., Ezersky, M.G., Al-Zoubi, A.S., Goldshmidt, V.I. and Legchenko, A., 2008. Study of the factors affecting the karst volume assessment in the Dead Sea sinkhole problem using microgravity field analysis and 3D modeling. *Advances in GeoSciences*, **19**,97-115.

Eppelbaum, L.V., 2011. Study of magnetic anomalies over archaeological targets in urban conditions. *Physics and Chemistry of the Earth*, doi: 10.1016/j.pce.2011.02.005.

Eppelbaum, L.V., Alperovich, L., Zheludev, V. and Pechersky, A., 2011. Application of informational and wavelet approaches for integrated processing of geophysical data in complex environments. *Proceed. of the 2011 SAGEEP Conference*, Charleston, South Carolina, USA, **24**, 37 pp.

Eppelbaum, L.V., 2013a. Interpretation of magnetic anomalies due to archaeological and environmental targets classified as "quasi thick bed bodies" in complex physical-geological environments. Proceed. of the 2013 SAGEEP Conference, Denver, Colorado, USA, 26, No. 1, 1-10.

Eppelbaum L. 2013b. Sinkhole Hazard Assessment. **Part IX**. Measurements of Density of Salt Samples using densitometer. TAU separate report: MERC 9/M27-050, April 2013, 8pp.

Eppelbaum L., Al-Zoubi A., Abueladas A-R., Ezersky M.G., 2013. Sinkhole Hazard Assessment. **Part VIII**. Analysis of potential fields in the Dead Sea Sinkhole problem. TAU Final Report: MERC 8/M27-050, June, 2013. 89 pp.

Ezersky, M., 2003. The seismic refraction study at the Northern Dam of the Pool 5, Dead Sea. GII Report No.263/305/03

Ezersky, M., 2006. The seismic velocities of Dead Sea salt applied to the sinkhole problem. Journal of Applied Geophysics, 58, 45– 58.

Ezersky, M., Bruner, I., Keydar, S. and Trachtman, P. and Rybakov, 2006. Integrated study of the sinkhole development site using geophysical methods at the Dead Sea western shore. *Near Surface Geophysics, 4, 5: 335-343*

Ezersky, M, 2008. Geoelectric structure of the Ein Gedi sinkhole occurrence site at the Dead Sea shore in Israel. Journal of Applied Geophysics, 64, 56-69 (doi: 10.1016/j/jappgeo. 12.003)

Ezersky, M., 2009. Improvement of seismic refraction method for mapping of the buried salt layers along the Dead Sea shoreline (Ein Boqeq site). Study No. 032-17-28, Report MNI-ES-21-2009, GII No. 211/486/09

Ezersky, M., 2010. Improvement of seismic refraction method for mapping of the buried salt layers along the Dead Sea shoreline (Mineral Beach site). Study No. 012-17-29, Report MNI-ES-1-2010, GII No. 211/538/10

Ezersky, M., and Legchenko, A. 2008. Sinkhole Hazards. Sinkhole Hazards. **Part I**. Mapping of the salt in sinkhole hazardous sites along western Dead Sea shore using Seismic Refraction method. NATO Programme Science for Peace, Project SfP 981128. Report No.232/361/08. GII-IRD.

Ezersky, M., and Legchenko, A., 2009. TEM resistivity - salinity calibration in the brine saturated sediments along the Dead Sea coast of Israel. 15th EAGE Meeting, 3-7 September 2009, Dublin, Ireland, P03

Ezersky M., and Legchenko A., 2014. Mapping of salt weakness and permeability using MASW method in the Dead Sea sinkhole problem. Proceedings of VII IAEG Congress, Torino 2014, Springer, 6pp.. (In press)

Ezersky, M., Legchenko, A., Camerlynck, C., Al-Zoubi, A., Eppelbaum, L. and Keydar, S., 2010. The Dead Sea sinkhole hazards – new findings based on the multidisciplinary geophysical study. *Zeitschrift für Geomorphologie*, **54**, Suppl. 2, 54-89.

Ezersky, M., Legchenko, A., Al-Zoubi, A., E. Akkawi., Chalikakis, K, 2011. TEM study of the geoelectrical structure and groundwater salinity at the Nahal Hever sinkhole site, Dead Sea shore, Israel. Journal of Applied Geophysics, 75, 99-112, doi: 10.1016/j.jappgeo.2011.06.011

Ezersky M, Bodet L, Al-Zoubi A, Camerlynck C, Dhemaied A, Galibert P-Y, and Keydar S. 2012a. Seismic surface-wave prospecting methods for sinkhole hazard assessment along the Dead Sea shoreline Geophysical Research Abstracts Vol. 14, EGU2012-3959, EGU General Assembly 2012

Ezersky M., Keydar S., Al-Zoubi A., Medvedev B., Eppelbaum L.. 2012b. Relations between Dead Sea sinkholes and faults. EAGE Near Surface Geosciences, 3-5 September 2012, Paris, France, P18, 4pp

Ezersky, M, Al-Zoubi, A, Eppelbaum, L, Keydar, S, Akkawi, E, Medvedev, B, Levi, E, and Legchenko, A., 2012c. Mechanism of sinkhole formation along the Dead Sea shores –geophysical evidences. Geophysical Research Abstracts, Vol. 14, EGU2012-1450, 2012, EGU General Assembly 2012

Ezersky, M.G. 2013. Sinkhole Hazard Assessment. **Part VI**. Geotechnical and geophysical properties of soils in the Dead Sea sinkhole problem. MERC_6/M27-050

Ezersky M, and Livne E. 2013. Geotechnical and geophysical properties of soils in the Dead Sea sinkhole problem, EAGE Annual Meeting of Near Surface Geoscience, 9-12 September, 2013, Bohum Mo P 13

Ezersky, M. and Eppelbaum 2013. Sinkhole Hazard Assessment. **Part V**. Dead Sea salt porosity and permeability and their inter-relations with geophysical parameters. MERC_5/M27-050.

Ezersky M., and Levi E., 2013. Sinkhole Hazard Assessment. **Part VII**. TEM method for groundwater salinity and salt parameters study. Report MERC_7/M27-050 (In preparation)

Ezersky M., and Frumkin 2013. Faults – dissolution front relations and the DS sinkholes problem. *Geomorphology*, 201, 35-44. DOI: 10.1016/j.geomorph.2013.06.002,

Ezersky M., L. Bodet, A. Al-Zoubi, C. Camerlynck, A. Dhemaied, P-Y. Galibert and S. Keydar. 2013a. Seismic surface-wave prospecting methods for sinkhole hazard assessment along the Dead Sea shoreline. Journal of Environmental and Engineering Geophysics, 18, (4), pp. 233-253. DOI: 10.2113/JEEG18.4.233.

Ezersky, M.G., Eppelbaum, L.V., Al-Zoubi, A., Keydar S., Abueladas, A-R., Akkawi E., and Medvedev, B. 2013b. Geophysical prediction and following development sinkholes in two Dead Sea areas, Israel and Jordan. *Journal of Environmental Earth Sciences*, doi: 10.1007/s12665-013-2233-2 (in press)

Ezersky, M.G., Ilyin, M.M., Yakovlev, B.P., Kolichko, A.V., 1991. Specifics of rock mass unloading during construction of the Rogun hydropower station with the use of geophysical data. *7th Congress on ISRM, September, 1991, Aahen. A.A.Balkema/Rotterdam/Boston*., 1099-1104.

Ezersky, M.G., Rudyak, M.S., Zhdanov, V.V., 1993. Forecast and monitoring of stability of the tunnel Zhinvali Project on basis of geophysical data. *International Symposium on Assessment and Prevention of Failure Phenomena in Rock Engineering, Istambul, Turkey, April*, 1993, 485-492

Ezersky M., and Legchenko A., 2014. Mapping of salt consolidation and permeability using MASW method in the Dead Sea sinkhole problem. Proceedings of VII IAEG Congress, Torino 2014, Springer, 6pp. (In press)

EU, 1998. Richtinie 98/83/EG des rates der Europaischen Gemeinschaften vom brauch. Amtsblatt der Europaischen Gemeinschaften, 5.12.98, pp. 32-55

Fakhry, A.A., LaMoreaux, P.E., and Hughes T.H., 2004. Field methods for geologists and hydrogeologists. Springer.

Fitterman D. V., and Stewart M.T., 1986. Transient electromagnetic soundings for groundwater. Geophysics, 51, 995-1005.

Fookes, P.G., Lee, E.M., Milligan, G. (Eds.), 2005. *Geomorphology for Engineers*, Whittles Publisher, Dunbeath, UK.

Ford, D.C. and Williams, P.W., 2007. Karst Hydrogeology and Geomorphology. Wiley, Chichester, 562 pp.

Frydman, S., Charrash, J., and Goretsky, I., 2008. Geotechnical properties of evaporate soils on the Dead Sea area. Engineering Geology, 101, pp. 236-244. doi:10.1016/j.enggeo.2008.06.003

Frumkin, A., 1994. Hydrology and denudation rates of halite karst. Journal of Hydrology, 162, 171–189.

Frumkin, A. and Raz, E., 2001. Collapse and subsidence associated with salt karstification along the Dead Sea. Carbonates and Evaporites, 16(2), 117-130.

Frumkin, A., Ezersky, M., Al-Zoubi, A., Akkawi, E., Abueladas, A.-R. 2011. The Dead Sea hazard: geophysical assessment of salt dissolution and collapse. *Geomorphology* (2011), v.134, 102-117 doi: 10.1016/j.geomorph.2011.04.023

Frumkin A., Kofman L., and Ezersky M., 2009. Improvement of the reliability of subsurface void detection, including sinkhole development, at the Dead Sea shore area by means of Ground Penetration Radar (GPR). Hebrew University - TECHNION Research and Development Foundation LTD - Geophysical Institute of Israel, Report No.MNI-ES-36-2008.

Gardosh, M., Reshes, Z., Garfunkel, Z., 1990. Holocene tectonic deformation along the western margins of the Dead Sea. Tectonophysics**,** 180**,** 123-137

Gavrieli, I., Lensky, N., Gazit-Yaari, N., Oren, A., 2002. The impact of the proposed "Peace Conduit" on the Dead Sea. Evaluation of current knowledge on Dead Sea – Seawater mixing. GSI Report GSI/23/2002.

Gavrieli, I. I. Gavrieli, A. Bein and A. Oren, 2005. The expected impact of the “Peace conduit” project (the Red Sea–Dead Sea pipeline) on the Dead Sea, Mitigation and Adaptation Strategies for Global Change, 10 3–21.

Garfunkel, Z., 1981. Internal structure of the Dead Sea leaky transform (rift) in relation to plate kinematics. Tectonophysics, 80, 81-108

Garfunkel, Z., 1997. The history and formation of the Dead Sea basin, In: Niemi, T.M., Ben-Avraham, Z., Gat, J., The Dead Sea: the lake and its setting. Oxford University Press, Oxford, pp. 36-55

Garfunkel, Z., and Ben-Avraham, Z., 1996, The structure of the Dead Sea basin: Tectonophysics, **266**, No. 1-4, 155-176.

Goes B.J.M., Oude Essink G.H.P., Vernes R.W. and Sergi F. 2009. Estimating the depth of fresh and brackish groundwater in a predominantly saline region using geophysical and hydrological methods, Zeeland, the Netherlands. Near Surface Geophysics, 2009, 401-412

Gokhberg, M.B., Morgounov, V.A., Yoshino, T., and Tomizava, I., 1982. Experimental measurement of electromagnetic emission possibly related to earthquake in Japan. Journal of Geophysical Research, 87, 7824-7827.

Goldman., M., Gilad, D., Ronen, A. and Melloul, A., 1991. Mapping of sea water intrusion into the coastal aquifer of Israel by the time domain electromagnetic method. *Geoexploration*, 28, 153-174.

Grinsted, A., Moore, J.C. and Jevrejeva, S., 2004. Application of the cross wavelet transform and wavelet coherence to geophysical time series. *Nonlinear Processes in Geophysics*, 11, 561–566, SRef-ID: 1607-7946/npg/2004-11-561.

Hatzor, Y.H., Heyman, E.P., 1997. Dilation of anisotropic rock salt: evidence from Mount Sedom diapir. Journ. Geophys. Res., 102, No.B7, pp. 14853-14868.

Hendron A.J. 1968. Mechanical properties of rock. In Rock mechanics in Engineering practice, Stagg K.G. and Zienkiewich O.C. (Eds), John Willey & Sons, London, 21-53

Hmelevskoi B.K. 1979. Brief course of exploration geophysics. Moscow University Press, 288pp

Interpex Ltd., 2006, IX1D v.3 inversion software, accessed June 6, 2006 at http://www.interpex.com/SoftwareIndex.htm .

Holting B. 1989. Hydrogeologie, 3rd ed., Ferdinand Enke, Stutgart

Iyisan R. 1996. Correlation between shear wave velocity and in-situ penetration test results. Digest, 371-374

Kafri, U., Goldman, M. and Lang, B., 1997. Detection of subsurface brines, freshwater bodies and the interface configuration in-between by the time domain electromagnetic method in the Dead Sea Rift, Israel. Environmental Geology, 31 (1/2), 42-49

Kafri, U., Goldman, M., 2005. The use of the time domain electromagnetic method to delineate saline groundwater in granular and carbonate aquifers and evaluate their porosity. Journal of Applied Jeophysics, 57, 167-178.

Kafri, U. and Goldman, M., 2006. Are the lower subaquiffers off the Mediterranean coastal aquifer off Israel blocked to sea water intrusion? Results off a TDEM (Time domain electromagnetic) study. Israel Journal of Earth Sciences, 55, 2, 55-68.

Keller, G.V. and Frischknecht, F.C., 1966. Electrical Methods in Geophysical Prospecting, Pergamon Press, Oxford.

Kennedy, J.M.. 1968. A microwave radiometric study of buried karst topography. Bulletin of the Geological Society of America, doi. 10.1130/0016-7606(1968)79(735:AMRSOB]2.0.CO;2 v.79, no.6., 735-742

Keydar, S., 2004. Homeomorphic imaging using path integrals. 66th EAGE Conference & Exhibition – Paris, France, 7-10 June 2004.

Keydar, S. and Mikenberg, M. 2010. Prestack Time Migration using the Kirchhoff Sum along a new approximation of the reflection travel time curve. 72nd EAGE Conference and Exhibition incorporating EUROPEC 2010, Barcelona, Spain, 14-17 June, 2010, P401

Keydar, S., and Shtivelman, V., 2005. Imaging zero-offset sections using multipath summation. First Break, 23, 21-24.

Keydar, S., Pelman, D., and Ezersky, M., 2010. Application of seismic diffraction imaging for detecting near-surface inhomogeneities in the Dead Sea area", Journal of Applied Geophysics, 71, (2-3), 47-52.

Keydar S., Bodet L., Camerlynck C., Dhemaied A., Galibert P-Y., Ezersky M., Dror O., Akkawi E., and Al-Zoubi A. 2011. A new approach for shallow subsurface imaging and its application to the Dead Sea sinkhole problem. 73rd EAGE Conference and Exhibition, Vienna, Austria, April, 2011. A401, 4pp

Keydar, S., Medvedev, B., Ezersky, M., and Sobolevsky, L. 2012a. Imaging shallow subsurface of Dead Sea area by Common Shot Point stacking and diffraction method using weighted multipath summation *Journal of Civil Engineering and Science (JCES).* **1,** (2): 75-79. http://www.ij-ces.org/Issue.aspx?Abstr=false

Keydar S, Medvedev B, Al-Zoubi A, and Ezersky M. 2012b Another look of imaging of shallow subsurface: Real examples from the Dead Sea sinkhole development areas. Geophysical Research Abstracts, Vol. 14, EGU2012-1432, EGU General Assembly 2012

Keydar S., Medvedev B., Al-Zoubi A., Ezersky M., and Akkawi E., 2013a. 3D Imaging of Dead Sea Area Using Weighted Multipath Summation: A Case Study. International Journal of Geophysics, Special Issue. Vol. 2013, Article ID 692452, 7 pp. http://dx.doi.org/10.155/2013/692452

Keydar S., Ezersky M., Al-Zoubi A., Medvedev B., Abueladas A-R., Akkawi E. 2013b. 3D imaging of shallow subsurface at Dead Sea area (Case study). 75th EAGE Conference & Exhibition incorporating SPE EUROPEC 2013, London, UK, 10-13 June 2013. Tu-P05-03.

Keydar, S., Gelchinsky, B. and Berkovitch, A., 1996. Common shot-point stacking and imaging method. Journal of Seismic Exploration, 5.

Keydar, S., Pelman, D., and Ezersky, M. 2010 Application of seismic diffraction imaging for detecting near-surface inhomogeneities in the Dead Sea area. Journal of Applied Geophysics, 71.

Khlaifata A., Al-Khashmanb O., Qutoba H., and Oil W. 2010. Physical and chemical characterization of Dead Sea mud Materials characterization 61, 564-568

Khesin, B.E., Alexeyev, V.V. and Eppelbaum, L.V., 1996. Interpretation of Geophysical Fields in Complicated Environments. Kluwer Academic Publishers, *Ser.: Modern Approaches in Geophysics*, Boston - Dordrecht - London, 368 pp.

Kiro, Y., 2007. The effect of the Dead Sea level drop on the groundwater system in the alluvial aquifer in its vicinity. GSI Report No. GSI/05/2007.

Kirsch R. 2006. Groundwater quality – salt water intrusions. In Groundwater geophysics. R.Kirsch Ed. Springer, Berlin., 423-438

Knopoff L., 1952. On Rayleigh wave velocities. BullSeism.Soc.Amer., 42 (4), 307-308

Koefoed O. 1979. Geosounding principles, 1, Elsevier, Balkema, 270pp

Kumar, P. and Foufoula-Georgiou, E., 1997. Wavelet analysis for geophysical applications. *Review of Geophysics*, **35**, No. 4, 385-412.

Landa, E. and Keydar, S., 1998. Seismic monitoring of diffraction images for detection of local heterogeneities in the shallow subsurface. Geophysics, 63.

Landa, E., Fomel, S., and Moser, T. J., 2006. Path-integral seismic imaging. Geophysical Prospecting, 54, 491-506.

Lachassagne, P., Baltassat, J.-M., Legchenko, A. and de Gramont, H.M. 2005. The links between MRS parameters and the hydrogeological parameters. Near Surface Geophysics, 3, (4), 259-265.

Legchenko A., Baltassat J-M., Bobachev A., Martin C., Robin H., and Vouillamoz J-M., 2004. Magnetic resonance sounding applied to aquifer characterization. *Journal of Ground Water, vol. 42, Number 3, May-June 2004, pp. 363-373.*

Legchenko A., M. Ezersky, C. Camerlynck, and A. Al-Zoubi., 2007. MRS study of the evolution of aquifer in sinkhole hazardous area (Dead Sea coast). 13th EAGE Near Surface Meeting & Exhibition 2007, Istambul, Turkey, 3-5 Sep 2007, *B29*

Legchenko, A., Ezersky, M., Boucher, M., Camerlynck, C., and Al-Zoubi, A., 2008a, Pre-existing caverns in salt formations could be a major cause of sinkhole hazards along the coast of the Dead Sea: Geophysical Research Letters, **35**, L19404, doi:10.1029/2008GL035510

Legchenko, A., Ezersky, M., Camerlynck, C., Al-Zoubi, A., Chalikakis, K., Girard J-F., 2008b. Locating water-filled karst caverns and estimating their volume using magnetic resonance soundings. Geophysics 73(5), 51-61, doi: 10.1190/1.2958007

Legchenko, A., Ezersky, M., Kamerlynck, C., Al-Zoubi, A., and Chalikakis, K., 2009. Joint use of TEM and MRS method in complex geological setting. Comptes Rendus (C.R.) Geosciences, 341, 908-917. DOI. 10.1016/j.crte.2009.07.013

Legchenko A.V., and Shushakov O.A. 1998. Inversion of surface NMR data. *Geophysics*, 63 (1), 75-84.

Legchenko A., and Valla P. 2002. A review of the basic principles for proton magnetic resonance sounding measurements. *Journal of Applied Geophysics*, 50, 3-19.

Levi E., Ezersky M., Al-Zoubi A., Eppelbaum L., 2011. Study of the salt layer environments using TEM method in the Dead Sea sinkhole problem. EAGE-*ES 17 th Meeting*, 12-14 September 2011, Lechester, UK., P29, 4pp

Livne E. 2012. Evaluation of the Liquefaction Potential along the Dead-Sea Western Shores - Regional Screening and Geotechnical Analysis of Two Boreholes. Sc.M. Thesis. Ben Gurion University of the Negev, 118pp.

Loke, M.H., 1999. Electrical imaging surveys for environmental and engineering studies, *A practical guide to 2D and 3D surveys.* Malaysia.

Loke, M.H. and Barker, R.D., 1996. Rapid least-squares inversion of apparent resistivity pseudo-sections by a quasi-Newton method, *Geophysical Prospecting*, 44:131-152.

Maimon, O., Lyakhovsky, V., Agnon, A., Abelson, M., 2005. Stability of cavities and formation of sinkholes along the Dead Sea coast. Geological Survey of Israel Report GSI/19/05, Jerusalem. . 65 pp (in Hebrew).

Mahasneh BZ (2004) Dead Sea water as a soil improvement agent. Electron Journ. of Geotech Eng 9

Mansour, Z., Taha M.R., Chik Z., 2009. Engineering behavior of the Lisan Marl as a dyke foundation material: Dead Sea, Jordan. Bull Eng Geol Environ (2009) 68:97–106 DOI 10.1007/s10064-008-0177-7

McNeill, J.,1980a. Electromagnetic terrain conductivity measurement at Low induction numbers. *Technical Note TN-6*, Geonics Limited, Canada

Medvedev B, Keydar S, Al-Zoubi A, Abueladas A, and Ezersky M. 2012. 3D reflection on the edge of a sinkhole: Evidence from the western Dead Sea shore. Geophysical Research Abstracts, Vol. 14, EGU2012-3473-1, EGU General Assembly 2012

Mills T., Hoekstra P., Blohm M., and Evans L., 1988. Time domain electromagnetic soundings for mapping sea water intrusion in Monterey County, CA, Ground Water, 26, 771-782.

Neev, D., and Hall, J.D. 1979. Geophysical investigations in the Dead Sea. Sedimentary Geolology 23, 209-238

Nelson P.H. 1994. Permeability-porosity relationships in sedimentary rocks. The Log Analist, 35 (3), 38-63.

Nielsen M.R., Hagensen T.F., Chalikakis K., Legchenko A., 2011. Comparison of transmissivities from MRS and pumping tests in Denmark. *Near Surface Geophysics*, **9**, 211-223 doi:10.3997/1873-0604.2010071

Niemi, T., Ben-Avraham, Z., 1997. Active tectonics in the Dead Sea Basin. The Dead Sea: the lake and its setting. Oxford University Press, Oxford, pp. 73-81

Nilsson Model 400. Solid state. 4-Pin soil resistance meter. Instruction manual. Nilsson Electrical Laboratory. Inc., Jersey, U.S.A.) http://qcqa.com/docs/doc_2644.pdf

Ohta Y. and Goto N. 1978. Empirical shear wave velocity equations in terms of characteristic soil indexes. Earth Eng. And Struc. Dynamics, 6: 167-187

O'Neill, A., Kampbell, T., and Matsuoka, T., 2008, Lateral resolution and lithological interpretation of surface wave profiling: The Leading Edge**, 27**, 1550-1563

Palmer, D., 1986, Refraction seismics. The lateral resolution of structure and seismic velocity: Geophysical Press Ltd., London-Amsterdam, 269 pp.

Palmstrom, A., 1996. Characterizing rock masses by the RMi for use in practical rock engineering. Part 1. The development of the rock mass index (RMi). Journal of Tunneling and Underground Space Technology, Vol. 11, No 2, 175-188.

Parasnis, D.S., 1997. *Principles of Applied Geophysics*. Chapman & Hall, London.

Park C.B., Miller, R.D., and Xia, J., 1999. Estimation of near-surface shear wave velocity by inversion of Rayleigh waves. Geophysics, 64, 691–700

Pazdirek, O. and Blaha, V., 1996. Examples of resistivity imaging using ME-100 resistivity field acquisition system. EAGE 58th Conference and Technical Exhibition Extended Abstracts, Amsterdam.

Popp, T. and Kern, H., 1998. Ultrasonic wave velocities, gas permeability and porosity in natural and granular rock salt. Physics and Chemistry of the Earth. v. 23, No. 3., pp.373-378.

Raymer, L.L., Hunt, E.R., and Gardner, J. U. S., 1980. An improved sonic transit time-to-porosity transform: Transactions of the Society of professional well log analysts. 21st Annual Logging Symposium, Paper P.

Rao M. V. M. S and Lakshmi K. J. P., 2003. Shear-wave propagation in rocks and other lossy media: An experimental study. Current science, 85 (8), pp. 1221-1225.

Reuter,F. and Dietrich, S., 1993. Sinkholes in carbonate, sulphate, and chloride karst regions: Principles and problems of engineering geological investigations and predictions, with comments for the construction and mining industries. *Applied Karst Geology*, Beck (ed.). Balkema, Rotterdam, 3-25.

Reynolds, J.M., 1997. An introduction to applied and environmental geophysics. Jon Wiley & Sons, New York.

Renalier, F., Jongmans, D., Savvaidis, A., Wathelet, M., Endrun, B., and Cornou, C., 2010, Influence of parameterization on inversion of surface wave dispersion curves and definition of an inversion strategy for sites with a strong *Vs* contrast. Geophysics, **75**, B197, doi:10.1190/1.3506556.

Roedder, E., Bassett, R.L., 1981. Problem in determination of the water content of rock-salt samples and its significance in nuclear-waste storage sitting. Geology, 9, pp. 525-530.

Romero, S., Rix, G.J., 2001, Regional Variations in Near Surface Shear Wave Velocity in the Greater Memphis Area., Engineering Geology, 62, 137-158, USA.

Rybakov, M., Goldshmidt, V., Fleischer, L. and Rotstein, Y., 2001. Cave detection and 4-d monitoring: a microgravity case history near the Dead Sea. *The Leading Edge,***20**, No. 8, 896-900.

Rybakov, M., 2003. Microgravity survey along the Ein Gedi bypass. GII *Report No. 860/240/02*.

Rybakov, M., Rotstein, Y., Shirman, B. and Al-Zoubi, A., 2005. Cave Cave detection near the Dead Sea – a micromagnetic feasibility study. *The Leading Edge*, No. 6, 585-590.

Rybakov, M., Millegan, P., and Shirman, B., 2006. Predictive environmental geophysics in Israel – an update. The Leading Edge, 25,(4): p.426.

Salameh E. and Abu Naseir T., 1999. The Quantitative and Qualitative Impacts of the Rehabilitation of the Municipal Water Supply Network on the Groundwater Resources in Amman Area, Jordan. Journal of Hydrogeology and Environment, 18, 189-197.

Salameh E. and El-Naser H., 1999. Does the Actual Drop in Dead Sea Level Reflect the Development of Water Sources Within its Drainage Basin? Acta Hydrochemica et Hydrobiologica, 27, 5-11.

Salganik, R. L., 1979. Effective conductivity of a body with a large number of cracks taking into account their capacitance and the action of mechanical loads, Journal of engineering physics, 36, (6), 704-709

Santamarina, J. C., Klein, K. A., and Fam, M. A., 2001, *Soils and Waves*, JohnWiley & Sons, Chichester, UK, 488 pp.

Salameh E. and El-Naser H., 2000. The Interface Configuration of the Fresh / Dead Sea Water – Theory and Measurements. Acta Hydrochemica et Hydrobiologica, 28, 6, 323-328.

Savich A.I., Koptev, V.I., Nikitin, B.N., and Yaschenko, Z.G., 1969. Seismic-acoustic methods for study of the rock masses. (Epinatieva A.M. ed.)"Nedra", Moscow, 239pp. (In Russian)

Sandwell, D.T., and Smith, W. H. F., 2009. Global marine gravity from retraced Geosat and ERS-1 altimetry: ridge segmentation versus spreading rate, *Journal of Geophysical Research B*, **114**, No. 1, Article ID B01411.

Schleicher J and Costa J, Migration velocity analysis by double path-integral migration, *Geophysics*, 77 (5), 2012

Schon, J.H., 2004. Physical properties of rocks. In: Fundamentals and Principles of Petrophysics. Helbig, K. and Treitel, S. (Eds), Seismic exploration V.18. Elsevier, Amsterdam.

Shalev, E., Lyakhovsky, V., and Yechieli, Y., 2006, Salt dissolution and sinkhole formation along the Dead Sea shore: Journal of Geophysical Research, **111**, B03102, doi:10.1029/2005JB004038.

Shalev, E., Yechieli, Y., Bein, A. and Halamish, N., 2005b. Prohibiting groundwater flux into the Dead Sea evaporation ponds - hydrogeological alternatives. Israel Geol. Surv. Report, TR-GSI/11/2005, (In Hebrew)

Shamir, G., 2006. The active structure of the Dead Sea depression, Geological Society of America Special Paper 401-02, pp. 15-32

Shtivelman, V., and Keydar, S., 2005. Imaging shallow subsurface inhomogeneities 3D multipath diffraction summation. First Break, 23, 39-42.

Shtivelman, V., Keydar, S., and Mikenberg, M. 2009 Imaging near surface heterogeneties using weighted multipath summation. Near Surface Geophysics, 7.

Silaeva, O.I. and Shamina, O. G., 1958. The distribution elastic pulses in celindrical specimens. USSR Academy of sciences (Izvestiya), Geophysics series, 32-43, (English ed. 1, (1), 1958, 17-24)

Socco, L.V., and Strobia, C., 2004, Surface-wave method for near-surface characterization: a tutorial: Near Surface Geophysics**, 2**, 165-185

Socco, L.V., Foti, S., and Boiero, D., 2010, Surface-wave analysis for building near-surface velocity models — Established approaches and new perspectives: Geophysics, **75A**, No. 5, 83-102.

Spangenberg, E., Spangenberg, U., Heindorf, C., 1998. An experimental study of transport properties of porous rock salt. Physics and Chemistry of the Earth, 23, (3), pp. 367-371.

Stephens,D.B., Hsu, K.S., Prieksat, M.A., Ankeny, M.D., Blanford, N., Roth, T.L., Kelsey, J.A., and Whitworth, J.R., 1998. A comparison of estimated and calculated effective porosity, Hydrogeology Journal, 6, 156-165.

Stein, M., Torfstein, A., Gavrieli, I., Yechieli, Y., 2010. Abrupt aridities and salt deposition in the post-glacial Dead Sea and its north Atlantic connection. Quaternary Science Reviews 29, 567-575.

Stokoe, K.H., Wright, S.G., Bay, J., and Roesset, J.M., 1994,.Characterization of geotechnical sites by SASW method: In: Geophysical Characterization of Sites (ISSMFE TC#10) Woods, R.D., (ed.), 15–25. Oxford and IBH Publishers.

Taqieddin, S.A., Abderahman, N.S. and Atallah, M., 2000. Sinkhole hazards along the eastern Dead Sea shoreline area, Jordan: a geological and geotechnical consideration. Environmental geology, 39, No.11:1237-1253.

Tatham, R. H., and McCormack, M.D., 1991. Multicomponent seismology in petroleum exploration. 1. Petroleum Prospecting. Neitzel E.B., and Winterstein, D.F. Eds. Society of Exploration Geophysics, Tulsa, U.S.A., 91pp.

Telford, W.M., Geldart, L.P. and Sheriff, R.E., 1990. *Applied Geophysics*. Cambridge Univ. Press, Cambridge, UK

TEM-RESEARCHER, 2005. Manual v. 7. www.AEMR.net

Terentiev, V.A. 1993. Compact field impulsive ultrasonic meter S-70. USSR Academy of Sciences (Izvestiya), Physics of Earth series, 11, 54-57.

Terzaghi K., and Peck R.B., Mesri G., 1996. Soil Mechanics in Engineering Practice. 3rd edition John Wiley and Sons, New York

Thomas,B. & Roth,M.J.S., 1997. Site characterization for sinkholes in Pensylvania and New Jersey. *Engineering geology and hydrogeology of karst terrains*, Beck & Stephenson (eds),Balkema, Rotterdam: 281-286.

Vouillamoz J-M., Legchenko A., Albouy Y., Bakalowicz M., Baltassat J-M., and Al-Fares W, 2003, - Localization of saturated karst aquifer with magnetic resonance sounding and resistivity imagery, *Journal of Ground Water, vol 41, Number 5, September-October 2003, pp. 578-587.*

Waltham, T., Bell, F.G. and Culshow, M.G., 2004. *Sinkholes and Subsidence: Karst and Cavernous Rocks in Engineering and Construction*. Springer.

Wang, E. Zaho, E., Experimental mstudy on electromagnetic emission character of rock and soil in process of uniaxial compressing loading. Journal of Liaoning Technical University

WBI compilation: Salt permeability versus porosity Palette, by Wittke, W. http://www.wbionline.de/

WBI 2006. Unpublished Report http://www.wbionline.de/

Weisbrod N., Alon-Mordish C., Yechieli Y., 2012. Dynamic dissolution of halite rock during flow of diluted saline solutions. Geophysical Research Letters, 39, L09404, 7pp, doi:10.1029/2012GL051306, 2012

Welton J.E., 1984. SEM petrography Atlas. The Am. Assoc. of Petrol. Geologists. Tulsa, Oklahoma, USA, 227pp.

Yoshino, T., 1991. Low frequency seismogenic electromagnetic emissions as precursors of earthquakes and volcanic eruption in Japan. Journal of Scxientific Exploration. V.5., No.1, 121-144

Yaramanci U. 1994. Relation of in-situ resistivity to water content in salt rocks.

Zaslavsky Y., A. Shapira, G. Ataev, M. Gorstein, T. Aksinenko, M. Kalmanovich, N. Perelman, and R. Hofstetter, 2009. Using Ambient Noise Measurements in the Process of Assessing Earthquake Hazards in Urban Areas: Examples from Israel, Authors / Editors: T. Miura and Y. Ikeda, Earthquake Engineering: New research, Nova Publisher, pp. 155-218

Zheludev, V. and Alperovich, L., 1999. Wavelet analysis as a tool for revealing geomagnetic precursors of an earthquake. *Seismo-Electromagnetics, TERRAPUB*, **255**, Tokyo, Japan. *Geophysical Prosp*ecting, 41, 229-239

Yaramanci, U., G. Lange, and M. Hertrich, 2002, Aquifer characterization using surface NMR jointly with other geophysical techniques at the Nauen/Berlin test site: J. Appl. Geophys, **50**, 47–65.

Yechieli.Y., 2000. Fresh-Saline ground water interface in the western Dead Sea area. *Ground Water, vol. 38, N°4, pp. 615-623.*

Yechieli, Y., 2007, Geochemical monitoring of groundwater in boreholes at the Dead sea coastal area – project of sinkholes, *GSI Report TR-GSI/18/2007*.

Yechieli, Y., Ronen, D. and Berkowitz, B., 1995, Are sedimentary salt layers always impermeable?. Geophysical Research Letters, **22**, No. 20, 2761-2764.

Yechieli, Y., Kafri, U, Goldman, M. and Voss, C.I., 2001. Factors controlling the configuration of the fresh-saline water interface in the Dead Sea coastal aquifers: synthesis of TDEM surveys and numerical groundwater modeling. *Hydrology Journal*, 9:367-377.

Yechiely, Y., Wachs, D, Shtivelman, V., Abelson, M., Onn, C., Raz, E. and Baer, G., 2002. Formation of sinkholes along the shore of the Dead Sea – summary of the first stage of investigations, *Geological Survey of Israel, Current Research*, 13: 1-6.

Yechieli, Y., Abelson, M., Bain, A., Shtivelman, V., Onn, C., Wacks, D., Bar, G., Kalbo, R., and Lyachovski, V., 2004, Sinkhole phenomena along the Dead Sea shore line: GSI *Report No. GSI/21/04 (in Hebrew).*

Yechieli, Y., Abelson, M., Bein, A. and Crouvi, O., 2006. Sinkhole "swarms" along the Dead Sea coast: reflection of disturbance of lake and adjacent groundwater systems. GSA Bulletin, v.118, 9/10, 1075-1087 doi: 10.1130/B25880.1.

Yoshino, T., 1991. Low frequency seismogenic electromagnetic emissions as precursors of earthquakes and volcanic eruption in Japan. Journal of Scxientific Exploration. V.5., No.1, 121-144

Zhou,W., Beck, B.F. and Stephenson, J.B., 1999. Application of electrical resistivity tomography and natural-potential technology to deliniate potential sinkhole collapse areas in a covered karst terrane. *Hydrogeology and engineering geology of sinkholes and karst*, Beck,Pettit & Herring (eds),Balkema, Rotterdam: 187-193.

4. IMPACT, RELEVANCE AND TECHNOLOGY TRANSFER

How will it be found useful in the Middle East region

The Project has been performed in the region where an intensive industrial activity (Potash Facilities in Jordan and Dead Sea Work in Israel) takes place. The agricultural activity takes place along the Dead Sea shore (Qalia, Ein Gedi, Mizpe Shalem, etc). Archeological and Historical objects are being visited by numerous tourists. In addition, the Dead Sea region is an international resort zone, where buildings of numerous hotels have been constructed and exploited. At the same time, the sinkhole developing along the DS shore in Israel and Jordan has already caused considerable damage to the infrastructure, and at least four people have fallen into sinkholes which collapsed under their feet. There is an obvious potential for further collapses beneath the main highways and other human structures. Thus, high sinkholes hazard threatens human lives and economic development in the Dead Sea basin. In addition the drop in the Dead Sea level accelerates the sinkhole developing. If to add here the seismic hazards from earthquakes it will be clearly the interest of the business community, local administrations and different researchers to the sinkhole hazard assessment that should play a crucial role in planning and development of areas susceptible to sinkhole formation.

In order to protect human life and infrastructure, it is necessary to understand how sinkholes form and to produce a reliable sinkhole susceptibility and hazard maps, identifying the most dangerous areas that should be avoided or properly engineered.

That is why the cooperation between the Israeli and Jordanian researchers has a significant scientific impact to the problem decision. The studying of the sinkhole phenomena through the whole DS region generalizes the knowledge on the problem mechanism and the new methodologies will allow the delineating of the dangerous zones.

The Project's impact on individuals, laboratories, departments, and institutions

The new knowledge and methodology obtained during the Project meet the interest of scientists and parallel programs which are carried out in the Dead Sea region. Based on our results, The Geological Survey of Israel specifies the maps of sinkhole hazard generated intuitively through the areas where the sinkholes have been formed, whereas no maps were generated throughout areas where no sinkholes are visible at the surface.

Use of the Project result

We have advised the Leading Researcher, Dr. G. Shamir who is dealing with the Program of Defense of the Dead Sea Hotels (HELI). Our results will be used by the Geological Survey of Israel (Dr. A. Salomon) and the Ben-Gurion University (Prof. Y. Hatzor), in estimation of the liquefaction potential of the Dead Sea area. The MSc thesis by E. Livne (2012) was written based on the boreholes data. The Israel National Roads Company Ltd (MAATZ) ordered from GII in 2011 seismic surveys in the Mineral Beach and Ein Gedi areas to search salt and estimate sinkhole hazards

Warrants.

All the boreholes drilled with respect to our results confirm our conclusions. The study carried out by GSI also confirms GII prediction (Abelson et al., 2013).

New capacity, equipment or expertise that will be left behind in the target countries

During the Project life, participants purchased new equipment, new software and upgraded the available one:

GII:

1. OYO SonicViewer-SX Model 5251C (GII) was used for ultrasonic measurements on specimens;
2. Resistance Meter Nilsson #400 (Farwest Corrosion Control Company, USA) (GII) was used for resistance measurements of soil and salt specimens;
3. Low frequency geophones SN4_2.5Hz (Gisco Ltd, Minneapolis, USA) (GII) were used for the MASW measurements in the field.
4. Software RadExPro (Deco Ltd, San Petersburg, Russia) (GII); PC software for reflection data processing.
   GII has upgraded also SurfSeis 3 software for MASW data processing and RadExPro
5. Magnetic susceptibility meter (TAU) was used during the field magnetometric mapping of the Mineral Beach area.
7. Densitometer (TAU) was used for determining of salt sample density in laboratory conditions
8. BAU (Jordan) received the CG-5 Gravity Meter (by Scintrex a division of LRS, Canada) and investigated the north of the Ghor Al-Haditha area.
9. The equipment produced at GII (7-transducered Ultrasonic Probe for borehole) was successfully used during the borehole investigations.

There are some ways to improve the cooperation between Middle East scientists. The first one is organization of trainings in the framework of current scientific meetings. Example of such meetings are these organized in Larnaka and Athens, where in addition to current results of studies lectures of leading researchers, and practical teaching took place. The second one is on-line Internet lectures presented by leading scientists for students of cooperating institutions. We tried to organize such lectures but it was not possible due to a very complicated political situation.

5. PROJECT ACTIVITIES/OUTPUTS: LIST OF MEETINGS ATTENDED AND HELD FOR THE ENTIRE PROJECT

5.1. Presentation of the Project results at scientific meetings.

Generally, results of the Project studies were presented at different International and Local meetings listed in the Appendix 1. EAGE meetings were held in Zurich, Switzerland (2 papers), Barcelona, Spain (1); Vienna, Austria (1), Leicester, UK (3 papers), Paris, France (1); London, UK (1), Bohum, Germany (1), SAGEEP Denver, Colorado, U.S.A.(1). Note all presentations were subjected to peer review and have status of publications. Nine publications were presented at the EGU 2012, Vienna, Austria. Finally, 1 paper has been accepted for presentation at the XII IAEG Congress and the paper has been submitted.

We have submitted also 3 papers at the annual local meetings of the Israeli Geological Association (IGS).

All the presentations are with thanks to USAID MERC program. Note also that participations in meetings were mostly covered by the participants. The use of the Project budget for traveling abroad was used only upon permission of the MERC Office.

5.2. Training, publications and patents for the entire project

In spite of the political situation in our region (which is constantly worsened) the Israeli and Jordanian participants of the Project continued the contact during the entire period. Our usual communications are done by regular means and phone conversations between the leaders of the collaborating groups. E-mails are also an important element of communicating. However, the situation in Jordan makes difficult even phone conversations and e-mail communication. Therefore, the meetings with the partners were the most effective means of fast exchange of materials, ideas, plans and publications. In addition, the training of the post-graduate students is possible only during such a meeting.

Three joint meetings were held jointly by the Israeli and Jordanian partners: (1) at Larnaka City, Cyprus on August 2010; (2) at the Athens, Greece on June 19-21, 2011 (Both, Second Progress Report); (3) at Vienna, Austria (April 21-27, 2012), where a Special Session GI3.7. "An Integrated Geophysical Examination of Karst Phenomenon in Arid Environ*ments". (Conveners: L.V. Eppelb*aum, M. E*zersky, S. Keydar, A. Al-Zoubi*) was organized in the framework of the General Assembly of European Geophysical Association (EGU). The results of our studies during MERC Project were reported in 8 oral and Poster presentations by Israeli and Jordanian researchers (see list of publications in the Appendix 1). All the presentations were devoted to the Dead Sea sinkhole problem. The French researchers dealing with the DS sinkhole problem participated in this session as well. Totally 17 oral presentations and posters were presented.
In these three meeting participated: (from Israel) Prof. L. Eppelbaum, Drs. M. Ezersky, and S. Keydar, E. Levi and B. Medvedev (both, Post-graduate students); (from Jordan) Prof. A. Al-Zoubi, Dr. E.Akkawi, A.-R. Abuelades (Post-graduate student). Some photos presented in Figs. 108, and 109 give imagination on EGU meeting.

Figure 108. Session of the Dead Sea sinkholes. Presentation of Dr. E. Akkawi (BAU)

Figure 109. Working moments of the meeting in the oral presentation hall and poster area: (clockwise) L. Eppelbaum, M. Ezersky, S. Keydar and E.Akkawi, general view of the DS Poster area.

Note joint publications that include both Israeli and Jordanian researchers

a. In scientific Journals (Totally 6)

1. Al-Zoubi A., L. Eppelbaum*, A. Abueladas, M. Ezersky and E. Akkawi 2013. Removing regional trends in microgravity in complex environments: Testing on 3D model and field investigations in the eastern Dead Sea coast (Jordan). International Journal of Geophysics. Special Issue. Vol. 2013. Article ID341797, 13pp. http://dx.doi.org/10.155/2013/341797
2. Frumkin, A., Ezersky, M., Al-Zoubi, A., Akkawi, E., Abueladas, A.-R. 2011. The Dead Sea hazard: geophysical assessment of salt dissolution and collapse. *Geomorphology* (2011), v.134, 102-117 doi: 10.1016/j.geomorph.2011.04.023
3. Ezersky, M., Legchenko, A., Al-Zoubi, A., Levi, E., Akkawi E., Chalikakis, K, 2011. TEM study of the geoelectrical structure and groundwater salinity of the Nahal Hever sinkhole site, Dead Sea shore, Israel. Journal of Applied Geophysics, 75, 99-112 doi: 10.1016/j.jappgeo.2011.06.011
4. Ezersky, M.G., Eppelbaum, L.V., Al-Zoubi, A., Keydar S., Abueladas, A-R., Akkawi E., and Medvedev, B. 2013. Geophysical prediction and following development sinkholes in two Dead Sea areas, Israel and Jordan. *Environ Earth Sci*, 70 (4) 1463-1478,DOI: 10.1007/s12665-013-2233-2 (in press)
5. Keydar S., Medvedev B., Al-Zoubi A., Ezersky M., and Akkawi E., 2013. 3D Imaging of Dead Sea Area Using Weighted Multipath Summation: A Case Study. International Journal of Geophysics, Special Issue. Vol. 2013, Article ID 692452, 7 pp. http://dx.doi.org/10.155/2013/692452
6. M. Ezersky, L. Bodet, A. Al-Zoubi, E. Akkawi, C. Camerlynck, A. Dhemaied, P-Y. Galibert. 2013a Seismic surface-wave prospecting methods for sinkhole hazard assessment along the Dead Sea shoreline (Special issue of NSG-JEEG, April, 2013)

b. In peer reviewed proceedings of International Symphosiums (Totally 7)

1. Ezersky, M., Eppelbaum, L, Al-Zoubi, A., Medvedev, B. 2010. Geophysical prediction and following analysis of the Dead Sea sinkhole development through the Ein Gedi – Arugot area. EAGE-*ES 16h Meeting, Zurich, Switzerland, 6-8 September*, 2010, P74
2. S. Keydar (1), L. Bodet (2), C. Camerlynck (2), A. Dhemaied (2), P-Y. Galibert (2), M.G. Ezersky (1), E. Oz Dror, E. Akkawi (1) and A. Al-Zoubi (3), 2011. A new approach for shallow subsurface imaging and its application to the Dead Sea sinkhole problem. 73rd EAGE Conference and Exhibition, Vienna, Austria, April, 2011. A401, 4pp
3. Ezersky M., Frumkin A., Al-Zoubi A., Abueladas A-R., Keydar S., Eppelbaum L., Akkawi E., Medvedev B., and Levi E. 2011. Geophysical assessment of salt sinkholes hazard along the Dead Sea shore in Israel and Jordan. EAGE-*ES 17 th Meeting*, 12-14 September 2011., Lechester, UK., P078, 4pp.
4. Levi E., Ezersky M., Al-Zoubi A., Eppelbaum L., 2011. Study of the salt layer environments using TEM method in the Dead Sea sinkhole problem. EAGE-*ES 17 th Meeting*, 12-14 September 2011., Lechester, UK., P29, 4pp.
5. Al-Zoubi A., Eppelbaum L., Abueladas A., Ezersky M., Akkawi E. 2011. Preliminary magnetic data analysis in the eastern Dead Sea shore for identification of subsurface inhomogeneties and sinkholes EAGE-*ES 17 th Meeting*, 12-14 September 2011., Lechester, UK., P30, 4pp.
6. M. Ezersky, S. Keydar, A. Al-Zoubi, B. Medvedev, L. Eppelbaum. 2012. Relations between Dead Sea sinkholes and faults. EAGE Near Surface Geosciences, 3-5 September 2012, Paris, France, P18, 4pp
7. Keydar S., Ezersky M., Al-Zoubi A., Medvedev B., Abueladas A-R., Akkawi E. 2013. 3D imaging of shallow subsurface at Dead Sea area (Case study). 75th EAGE Conference & Exhibition incorporating SPE EUROPEC 2013, London, UK, 10-13 June 2013. Tu-P05-03, 4pp.

c. Abstracts(non-reviewed) in proceedings of International Symphosiums (Totally 9)

8. Akawwi E, Al-Zoubi A, Abueadas A, Eppelbaum L, Ezersky M, Levi E, Legchenko A, and Boucher M. 2012. Mechanism of Sinkhole Formation in the Ghor Al-Haditha Based on

Geophysical Data. Geophysical Research Abstracts Vol. 14, EGU2012-2244, EGU General Assembly 2012
9. Al-Zoubi A, Akkawi E, Abueladas A, Eppelbaum L, Keydar S, Medvedev B, Levi E, and , and M. Ezersky. 2012. Integrated Geophysical Tools for Sinkholes Study along the Dead Sea shoreline. Geophysical Research Abstracts Vol. 14, EGU2012-1980, EGU General Assembly, 2012
10. Al-Zoubi A, Abueladas A, Akkawi E, Eppelbaum L, Levi E, and Ezersky M. 2012 Use of Microgravity survey in the Dead Sea areas affected by the sinkholes hazard. Geophysical Research Abstracts, Vol. 14, EGU2012-1982, EGU General Assembly 2012
11. Eppelbaum LV, Alperovich LS, Zheludev V, Ezersky M, Al-Zoubi A, and Levi E (2012) Integration of potential and quasi potential geophysical fields and GPR data for delineation of buried karst terrains in complex environments. Geophysical Research Abstracts, Vol. 14, EGU2012-3418-1, EGU General Assembly 2012
12. Ezersky M, Al-Zoubi A, Eppelbaum L, Keydar S, Akkawi E, Medvedev B, Levi E, and Legchenko A (2012) Mechanism of sinkhole formation along the Dead Sea shores –geophysical evidences. Geophysical Research Abstracts, Vol. 14, EGU2012-1450, 2012, EGU General Assembly 2012
13. Ezersky M, Bodet L, Al-Zoubi A, Camerlynck C, Dhemaied A, Galibert P-Y, and Keydar S. 2012. Seismic surface-wave prospecting methods for sinkhole hazard assessment along the Dead Sea shoreline Geophysical Research Abstracts Vol. 14, EGU2012-3959, EGU General Assembly 2012
14. Keydar S, Medvedev B, Al-Zoubi A, and Ezersky M. 2012 Another look of imaging of shallow subsurface: Real examples from the Dead Sea sinkhole development areas. Geophysical Research Abstracts, Vol. 14, EGU2012-1432, EGU General Assembly 2012
15. Levi E, Abueladas A, Al-Zoubi A, Akkawi E, and Ezersky M. 2012. Application of geoelectrical methods in the DS sinkhole problem, Israel and Jordan Geophysical Research Abstracts Vol. 14, EGU2012-4695, EGU General Assembly 2012
16. Medvedev B, Keydar S, Al-Zoubi A, Abueladas A, and Ezersky M. 2012. 3D reflection on the edge of a sinkhole: Evidence from the western Dead Sea shore. Geophysical Research Abstracts, Vol. 14, EGU2012-3473-1, EGU General Assembly 2012

6. Project Productivity:

6.1. Project accomplishments.

1. We have developed 2-D and 3-D seismic reflection techniques based on the multipath summing and applied these techniques to fault investigations (Keydar and Mikenberg, 2010; Keydar et al., 2011, Keydar et al., 2012, Keydar et al., 2013a, Keydar et al., 2013b; Medvedev et al., 2012).

2. We have suggested Vs estimation using surface-wave prospecting methods, based on the surface-wave dispersion measurements and inversion. Along the Israeli shoreline, Vs mapping has been performed to discriminate weak and hard zones within the salt layers, after the calibration of inverted Vs near boreholes. It has been shown that there is a Vs increase in the DS direction. Initially examined weak zones, located near the salt edge, associated with karstified salt, are characterized by Vs values of 760-1050 m/s, and extend 60 -100m from salt edge in the DS direction. Hard salt zones with velocity Vs values greater than 1500 m/s are located at distances of more than 100-220m from salt edge. Finally, transition zones (1050 <Vs <1500 m/s) have a 40-160m spread. On a Jordanian site, we used previous studies including roll-along acquisition and dispersion stacking. Inverted pseudo-2D Vs sections present low Vs anomalies in the vicinity of existing sinkholes and made it possible to detect decompacted sediments associated with potential sinkholes occurrences. Moreover, Vs profiles showed a high velocity unit at 40-50m depth that can be interpreted as a salt layer. (Ezersky et al., 2012; 2013a)

3. As a result of two above studies we have proved the salt presence in the Ghor Al-Haditha (Frumkin et al., 2011) and proposed general model of the Dead Sea sinkhole formation based on salt distribution around the DS (Ezersky et al., 2013b, Ezersky and Frumkin, 2013).
Sinkholes are formed along the edge of the salt layer that, in his turn, is formed either along faults or sediments brought by wadies (Ezersky 2006; Frumkin et al., 2011; Ezersky et al., 2012c; Ezersky and Frumkin, 2013).

4. We suggested a new approach to use the Transient Electromagnetic (TEM) method in its FAST modification. This approach is based on a separate studying of both characteristics of the salt layer and evaluation of groundwater salinity. The key point of the new methodology is delineating salt distribution, in particular the salt edge, using seismic refraction method (Ezersky et al., 2010). Then we can separate the investigation area into two "sub-areas" (Levi et al., 2011): (1) "salt" area, where the measured resistivity is influenced by the salt porosity (estimated from the Archie's law); (2) "no-salt" area, where the measured resistivity is influenced by the groundwater salinity estimated using the resistivity-salinity inter-relations obtained for the Dead Sea region (Ezersky and Levi, 2013). In Israel, west of the salt edge resistivity of aquifer associated with the aquifer salinity, whereas east of that salt layer resistivity related to its porosity is mapped. In Jordan it works reversely. New methodology enables the avoiding of 3-D effects in vicinity of salt edge. We have mapped areas in the Mineral Beach, Nahal Zeelim and Ghor Al-Haditha sites.

5. We have tested a number of transformation methods (including computing gravity field derivatives, self-adjusting and adaptive filtering, Fourier series, wavelet, and other procedures) on a 3D model (complicated by randomly distributed noise) (Al-Zoubi et al., 2011, Al-Zoubi et al., 2013; Eppelbaum, 2013). Field Microgravity and Micromagnetic investigations were carried out in Ghor Al-Haditha (Jordan). We show that the most effective methods for regional trend removal (at least for the theoretical and field cases here) are the bilinear saddle and local polynomial regressions. Application of these methods made it possible to detect the anomalous gravity effect from buried targets in the theoretical model and to extract the local gravity anomaly at the Ghor Al-Haditha site. The local anomaly was utilized for 3D gravity modeling to construct a physical-geological model (PGM) **(**Al-Zoubi et al., 2012, Eppelbaum, 2013). Al-Zoubi et al. (2012) integrated Microgravity and Micromagnetic methods into surface geophysical methods to reveal sinkhole hazards. Electromagnetic Radiation (EMR) method was tested through the Ghor Al-Haditha area (Akkawi et al., 2012). Electrical Resistivity Tomography (ERT) in 2D and 3D mode was applied in Jordan (Frumkin et al., 2011).

6. (a) Two types of lithology were studied in-situ and laboratory conditions to reveal geotechnical and geophysical properties of these soils. Two boreholes MN-5E and EB-3E, of clayey and sandy-gravel, respectively lithology, were drilled in the Mineral Beach and Ein Boqeq sites.
We have revealed the following features of the DS soil properties (Ezersky, 2013; Ezersky and Livne, 2013). Sandy-gravel sediments are presented by coarse sands, which are characterized by Vs = 300 – 650 m/s. Such increased shear wave values can be caused by increased the DS soil stiffness described in the literature. Brine saturated lime carbonates (DS mud) are characterized by low Vs values of 120 – 250 m/s. They do not exhibit cohesion when saturated in the DS brine. It is explained by mineralogical composition of the Dead Sea material, composed predominantly of calcite and not clay minerals, whereas other Israeli clays are comprised largely of montmorillonite (spectite) clay minerals. This feature allows considering of saturated lime carbonate as cohesionless soil like fine sands. Lime carbonates demonstrate also very low cation exchange capacity (CEC) that allows the use of TEM resistivity method for determining of porosity of both sands and DS mud (Ezersky 2013c). Note also that significant difference of Vs in sands and lime carbonates allows the mapping of different lithology along DS coastal areas.
(b) Salt porosity-permeability, their mutual inter-relationships and correlations with ultrasonic compression wave velocity (Vp), shear wave velocity (Vs) and resistivities (ρ_x) were studied in laboratory conditions (Ezersky and Goretsky 1 and 2, 2013). These relationships were interpolated into range of in-situ values using MASW method and Magnetic Resonance Sounding (MRS) permeability, carried out in past. Thus, mapping of salt permeability based on Vs values was performed in 3 sites under investigation. (Ezersky and Legchenko, 2013).

7. The results of the study were implemented at the Dam 5/8 separating southern DS basin from the northern one. This study shows that now we have a method to evaluate salt properties (based on Vs values) in the DS region.

6.2. Future work

(1) We see future researches in the check of salt mechanical properties and permeability in-situ conditions using joint testing of in-situ salt layers by MASW method and pumping tests. (2) We are planning to check dependence of water salinity evaluation using aquifer porosity measurements by geotechnical testing; (3) We plan to map salt unit depth a thickness using TEM method. Latter will enable us to locate young faults between salt units along the DS shore.

Acknowledgements

This study was made possible thanks to the support provided by the U.S. Agency for International Development, under the terms of Award No M27-050. The opinions expressed herein are those of the author(s) and do not necessary reflect the views of the USAID. We are also grateful to the Ministry of Infrastructure of Israel for supporting this investigation. We would like to thank also the MERC office at the American Embassy for the support and assistance in resolving the current problems. We are grateful to the GII Administration and staff for the efficient organization of the field work. We thank the field crews of BAU and GII who helped to acquire the data in complicated climate conditions, as well as in dangerous sinkhole areas. Thanks to the Tamar Regional Council for supporting this study. We thank Dead Sea Works Ltd. for the permission to carry out field studies at the DS Dam 5/8. The authors thank the geophysical team at UPMC (Université Pierre et Marie Curie, Paris, France), which provided the seismic data of Ghor Al-Haditha, originally collected during an integrated geophysical survey carried out in the framework of the NATO Science for Peace Program (project SfP 981128).
Thanks to A. Frumkin (Hebrew University of Jerusalem) for the fruitful cooperation in the framework of the Project. We are grateful to A. Salomon (GSI), Y. Hazor, E. Livne (Ben Gurion University of Negev) for the cooperation in the Drilling Program. Thanks to Y. Goretsky, (Geotechnical Laboratory, Haifa) and D. Blechman (ISI, Tel-Aviv) for the testing of salt and soil samples. We more particularly would like to thank A. Abueladas, R. Al-Ruzouq, L. Sobolevsky and P. Trachtman and M. Boucher for assisting in data processing. A. Legchenko is thanked for the organisation of a Session at the EGU GA in Vienna and the cooperation in the paper writing**.** Eli Raz (Kibbutz Ein Gedi) has provided useful information about recent sinkhole development. Our thanks to L.Kirzhner and S. Nasihi (National Roads Company of Israel) for the geological information on sinkhole sites.

Appendix I. List of Publications and presentations

MERC Publications NEW

Ezersky M., Al-Zoubi **A.,** Keydar S., Eppelbaum L., 2013. Sinkhole Hazard Assessment of the Dead Sea area in Israel and Jordan: Multidisciplinary Study. **Final Report. MERC Project No M27-050**

MERC Publications NEW

Ezersky M., Al-Zoubi A., Keydar S., Eppelbaum L., 2013. Sinkhole Hazard Assessment of the Dead Sea area in Israel and Jordan: Multidisciplinary Study. Final Report. MERC Project No M27-050

1. REPORTS

GII REPORTS

1. Ezersky, M. 2011. Sinkhole Hazard Assessment. **Part I.** Results of the combined geological-geophysical investigations in two boreholes EB-3E and MN-5E at Ein Boqeq and Mineral (Shalem-2) sites. Report MERC_1/M27-050 (In preparation)
2. Keydar, S., Medvedev B. Ezersky M. 2013. Sinkhole Hazard Assessment. **Part II.** Report: MERC Project 2/M27-050. MERC_2/M27-050 New reflection technique in the sinkhole problem
3. Ezersky M., Frumkin A, Keydar S., Medvedev B., 2013. Sinkhole Hazard Assessment. **Part III.** Report: MERC_3/M27-050 Fault – sinkhole relations.

4. Ezersky, M. et al 2012. Sinkhole Hazard Assessment. **Part IV.** Results of the salt mapping using MASW method Report MERC_4/M27-050 (In preparation)
5. Ezersky, M. and Eppelbaum 2013. Sinkhole Hazard Assessment. **Part V**. Dead Sea salt porosity and permeability and their inter-relations with geophysical parameters. MERC_5/M27-050.
6. Ezersky M.G. 2013. Sinkhole Hazard Assessment. **Part VI**. Geotechnical and geophysical properties of soils in the Dead Sea sinkhole problem. MERC_6/M27-050
7. Ezersky M., and Levi E., 2013. Sinkhole Hazard Assessment. **Part VII**. TEM method for groundwater salinity and salt parameters study. Report MERC_7/M27-050 (In preparation)

TAU REPORTS

8. Eppelbaum L., Al-Zoubi A., Abueladas A-R., Ezersky M.G., 2013. Sinkhole Hazard Assessment. **Part VIII**. Analysis of potential fields in the Dead Sea Sinkhole problem. TAU Final Report: MERC 8/M27-050, June, 2010. 89 pp.
9. Eppelbaum L. 2013. Sinkhole Hazard Assessment. **Part IX**. Measurements of Density of Salt Samples using densitometer. TAU separate report: MERC 9/M27-050, April 2013, 8pp.

BAU REPORTS

10. Abueladas A-R., and Eppelbaum L., 2011. Sinkhole hazard assessment Part X. Magnetic field processing and analysis. Report MERC 10/M27-050, January 2011, 15pp.
11. Al-Zoubi A., Akkawi E., Abueladas A. 2013. Sinkhole hazard assessment **Part XI**. Electromagnetic Radiation Method (EMR) for sinkhole detection. Report MERC 11/M27-050, April 2013, 9pp.
12. Al-Zoubi A. Akkawi E., Abueladas A-R., Ezersky M.G. 2013. Sinkhole hazard assessment. **Part XII**. Surface Geophysical Methods in the sinkhole problem. Report MERC 12/M27-050, January 2011, 15pp.
13. Al-Zoubi A., Abueladas A-R., Al-Ruzoug, R.I., Akkawi, E., 2010. MERC Sinkhole Project. ERT and EMR surveys. BAU, Salt, Jordan.
14. Akkawi E., 2010. Electrical Time Domain Method. Progress report for the sinkholes at the southern part of the Dead Sea. BAU, October, 2010, 17p.p.
15. Al-Zoubi A, Abueladas A-R, Akawi E., 2012. MERC Sinkholes Project. Al-Balqa Applied University, Progress Report January 2012

2. ARTICLES IN SCIENTIFIC JOURNALS

Published:

1. Frumkin, A., Ezersky, M., Al-Zoubi, A., Akkawi, E., Abueladas, A.-R. 2011. The Dead Sea hazard: geophysical assessment of salt dissolution and collapse. *Geomorphology* (2011), v.134, 102-117 doi: 10.1016/j.geomorph.2011.04.023, IF2.52
2. Ezersky, M., Legchenko, A., Al-Zoubi, A., Levi, E., Akkawi E., Chalikakis, K, 2011. TEM study of the geoelectrical structure and groundwater salinity of the Nahal Hever sinkhole site, Dead Sea shore, Israel. Journal of Applied Geophysics, 75, 99-112 doi: 10.1016/j.jappgeo.2011.06.011 IF 1.44
3. Keydar, S., Medvedev, B., Ezersky, M., and Sobolevsky, L. 2012. Imaging shallow subsurface of Dead Sea area by Common Shot Point stacking and diffraction method using weighted multipath summation *Journal of Civil Engineering and Science (JCES)*. **1,** (2): 75-79. http://www.ij-ces.org/Issue.aspx?Abstr=false
4. Ezersky, M.G., Eppelbaum, L.V., Al-Zoubi,A.3, Keydar S., Abueladas, A-R., Akkawi E., and Medvedev, B. 2013. Geophysical prediction and following development sinkholes in two Dead Sea areas, Israel and Jordan. *Journal of Environmental Earth Sciences* DOI: 10.1007/s12665-013-2233-2 (in press, IF 0.756)
5. Al-Zoubi A., L. Eppelbaum*, A. Abueladas, M. Ezersky and E. Akkawi 2013. Removing regional trends in microgravity in complex environments: Testing on 3D model and field investigations in the eastern Dead Sea coast (Jordan). International Journal of Geophysics. Special Issue. Vol. 2013. Article ID341797, 13pp. http://dx.doi.org/10.155/2013/341797
6. Keydar S., Medvedev B., Al-Zoubi A., Ezersky M., and Akkawi E., 2013. 3D Imaging of Dead Sea Area Using Weighted Multipath Summation: A Case Study. International Journal of Geophysics, Special Issue. Vol. 2013, Article ID 692452, 7 pp. http://dx.doi.org/10.155/2013/692452

7. Ezersky, M., Bodet, L., Akkawi, E., Al-Zoubi, A., Camerlynck, C., Dhemaied, A., and Galibert, P-Y., 2013, Seismic Surface-wave prospecting methods for sinkhole hazard assessment along the Dead Sea shoreline: 201, 35-44. DOI: 10.1016/j.geomorph.2013.06.002,
8. Ezersky M., and Frumkin 2013. Faults – dissolution front relations and the DS sinkholes problem. Geomorphology, 201, 35-44. DOI: 10.1016/j.geomorph.2013.06.002,

Submitted

9. Ezersky M.G. and Goretsky I.., 2013 Permeability porosity inter-relations in the Dead Sea salt samples: 1 (ENGEO5214, submitted to Engineering Geology, 15-05-2013, IF 1.402)
10. Ezersky, M.G., and Goretsky I., 2013 Pore space properties – geophysical parameters inter-relations in the Dead Sea salt samples: 2 **(**ENGEO5215, submitted to Engineering Geology, 15-05-2013**,** IF 1.402**)**
11. Ezersky M., Legchenko A., 2013. In-situ Shear Wave Velocity versus Hydraulic Conductivity Inter-relationships in the Dead Sea Salt Layers (2013, Geomorphology, 23.05.2013, IF 2.52)

Comments: Papers 9 and 10 have been revised and recommended to publishing after major revision.

3. Presentations at International Meetings

1. Eppelbaum, L., Yakubov, Ya., and Ezersky, M., 2010. Method for comprehensive computing of water flows geodynamics in the Dead Sea basin. *Trans. of the **XXXV** EGS Meet.*, Zurich, Switzerland, P24, 4 pp.*)
2. Ezersky, M., Eppelbaum, L, Al-Zoubi, A., Medvedev, B. 2010. Geophysical prediction and following analysis of the Dead Sea sinkhole development through the Ein Gedi – Arugot area. EAGE-*ES 16^{h} Meeting, Zurich, Switzerland, 6-8 September*, 2010, P74
3. Keydar, S. and Mikenberg, M. 2010. Prestack Time Migration using the Kirchhoff Sum along a new approximation of the reflection travel time curve. 72nd EAGE Conference and Exhibition incorporating EUROPEC 2010, Barcelona, Spain, 14-17 June, 2010, P401*)
4. S. Keydar, L. Bodet, C. Camerlynck, A. Dhemaied, P-Y. Galibert, M.G. Ezersky, Oz Dror, E. Akkawi, and A. Al-Zoubi, 2011. A new approach for shallow subsurface imaging and its application to the Dead Sea sinkhole problem. 73rd EAGE Conference and Exhibition, Vienna, Austria, April, 2011. A401, 4pp

*) Acknowledgement to MERC was written in the Presentation (Oral or Poster)

5. Ezersky M., Frumkin A., Al-Zoubi A., Abueladas A-R., Keydar S., Eppelbaum L., Akkawi E., Medvedev B., and Levi E. 2011. Geophysical assessment of salt sinkholes hazard along the Dead Sea shore in Israel and Jordan. EAGE-*ES 17 th Meeting*, 12-14 September 2011., Lechester, UK., 4p.p. P078

6. Levi E., Ezersky M., Al-Zoubi A., Eppelbaum L., 2011. Study of the salt layer environments using TEM method in the Dead Sea sinkhole problem. EAGE-*ES 17 th Meeting*, 12-14 September 2011., Lechester, UK., P29, 4pp.

7. Al-Zoubi A., Eppelbaum L., Abueladas A., Ezersky M., Akkawi E. 2011. Preliminary magnetic data analysis in the eastern Dead Sea shore for identification of subsurface inhomogeneties and sinkholes EAGE-*ES 17 th Meeting*, 12-14 September 2011., Lechester, UK., P30, 4pp.

Following 9 Papers were presented in framework of the MERC Project M27-050 at the EGU General Assembly, **Session GI3.7. Integrated Geophysical Examination of Karst Phenomenon in Arid Environments.** Convener: L.V. Eppelbaum, Co-Conveners: M. Ezersky, S. Keydar, A. Al-Zoubi, A. Legchenko

8. Akawwi E, Al-Zoubi A, Abueadas A, Eppelbaum L, Ezersky M, Levi E, Legchenko A, and Boucher M. 2012. Mechanism of Sinkhole Formation in the Ghor Al-Haditha Based on Geophysical Data. Geophysical Research Abstracts Vol. 14, EGU2012-2244, EGU General Assembly 2012

9. Al-Zoubi A, Akkawi E, Abueladas A, Eppelbaum L, Keydar S, Medvedev B, Levi E, and , and M. Ezersky. 2012. Integrated Geophysical Tools for Sinkholes Study along the Dead Sea

shoreline. Geophysical Research Abstracts Vol. 14, EGU2012-1980, EGU General Assembly, 2012

10. Al-Zoubi A, Abueladas A, Akkawi E, Eppelbaum L, Levi E, and Ezersky M. 2012 Use of Microgravity survey in the Dead Sea areas affected by the sinkholes hazard. Geophysical Research Abstracts, Vol. 14, EGU2012-1982, EGU General Assembly 2012

11. Eppelbaum LV, Alperovich LS, Zheludev V, Ezersky M, Al-Zoubi A, and Levi E (2012) Integration of potential and quasipotential geophysical fields and GPR data for delineation of buried karst terrains in complex environments. Geophysical Research Abstracts, Vol. 14, EGU2012-3418-1, EGU General Assembly 2012
12. Ezersky M, Al-Zoubi A, Eppelbaum L, Keydar S, Akkawi E, Medvedev B, Levi E, and Legchenko A (2012) Mechanism of sinkhole formation along the Dead Sea shores –geophysical evidences. Geophysical Research Abstracts, Vol. 14, EGU2012-1450, 2012, EGU General Assembly 2012
13. Ezersky M, Bodet L, Al-Zoubi A, Camerlynck C, Dhemaied A, Galibert P-Y, and Keydar S. 2012. Seismic surface-wave prospecting methods for sinkhole hazard assessment along the Dead Sea shoreline Geophysical Research Abstracts Vol. 14, EGU2012-3959, EGU General Assembly 2012
14. Keydar S, Medvedev B, Al-Zoubi A, and Ezersky M. 2012 Another look of imaging of shallow subsurface: Real examples from the Dead Sea sinkhole development areas. Geophysical Research Abstracts, Vol. 14, EGU2012-1432, EGU General Assembly 2012
15. Levi E, Abueladas A, Al-Zoubi A, Akkawi E, and Ezersky M. 2012. Application of geoelectrical methods in the DS sinkhole problem, Israel and Jordan Geophysical Research Abstracts Vol. 14, EGU2012-4695, EGU General Assembly 2012
16. Medvedev B, Keydar S, Al-Zoubi A, Abueladas A, and Ezersky M. 2012. 3D reflection on the edge of a sinkhole: Evidence from the western Dead Sea shore. Geophysical Research Abstracts, Vol. 14, EGU2012-3473-1, EGU General Assembly 2012
17. M. Ezersky, S. Keydar, A. Al-Zoubi, B. Medvedev, L. Eppelbaum. 2012. Relations between Dead Sea sinkholes and faults. EAGE Near Surface Geosciences, 3-5 September 2012, Paris, France, P18, 4pp
18. Keydar S., Ezersky M., Al-Zoubi A., Medvedev B., Abueladas A-R., Akkawi E. 2013. 3D imaging of shallow subsurface at Dead Sea area (Case study). 75th EAGE Conference & Exhibition incorporating SPE EUROPEC 2013, London, UK, 10-13 June 2013. Tu-P05-03.
19. Ezersky M and Livne E. 2013. Geotechnical and geophysical properties of soils in the Dead Sea sinkhole problem, EAGE Annual Meeting of Near Surface Geoscience, 9-12 September, 2013, Bohum Mo P 13
20. Eppelbaum, L.V., 2013. Interpretation of magnetic anomalies due to archaeological and environmental targets classified as “quasi thick bed bodies” in complex physical-geological environments. Proceed. of the 2013 SAGEEP Conference, Denver, Colorado, USA, 26, No. 1, 1-10.
21. Ezersky M., and Legchenko A., 2014. Mapping of salt consolidation and permeability using MASW method in the Dead Sea sinkhole problem. Proceedings of VII IAEG Congress, Torino 2014, Springer, 6pp. (In press)

4. Presentations at National Meetings

Levi, E., Ezersky, M., Eppelbaum, L., 2011. TEM study of the salt layer conditions at the Shalem-2 sinkhole development site, Dead Sea. Annual GIS Meeting, 22-24 March 2011, Mizpe Ramon, Israel , 100

Ezersky, M., Frumkin A., Keydar, S., Eppelbaum, L., Levi, E., Medvedev, B., 2011. The Dead Sea hazard: geophysical assessment of salt sinkholes hazard in Israel. Annual GIS Meeting, 22-24 March 2011, Mizpe Ramon, Israel, 66

Ezersky M. 2013. Mapping of salt layers through Dead Sea sinkhole development areas using MASW method. GIS Meeting, 28-30 May 2013, Ako, Israel

5. Progress reports

1. Ezersky M., Keydar S., Eppelbaum L., and Al-Zoubi A., 2010 First semi-annual Progress Report (December 1, 2009 – June 1, 2010). 2010. Sinkhole hazard assessment of the Dead Sea area in Israel and Jordan: multidisciplinary study. Grant No.TA-MOU-07-M27-050, MERC Project M27-050. USAID.
2. Ezersky M., Al-Zoubi A., Keydar S., Eppelbaum L. 2010. Second semi-annual Progress Report (June 1, 2010-December 10, 2010). 2010. Sinkhole hazard assessment of the Dead Sea area in Israel and Jordan: multidisciplinary study. Grant No.TA-MOU-07-M27-050, MERC Project M27-050. USAID.
3. Ezersky M., Al-Zoubi A., Keydar S., Eppelbaum L. 2011. Third semi-annual Progress Report (December 10, 2010 – June 31, 2011). 2011. Sinkhole hazard assessment of the Dead Sea area in Israel and Jordan: multidisciplinary study. Grant No.TA-MOU-07-M27-050, MERC Project M27-050. USAID.
4. Ezersky M., Al-Zoubi A., Keydar S., Eppelbaum L. 2011. Fourth semi-annual Progress Report (June 31, 2011-February 29, 2012). 2012. Sinkhole hazard assessment of the Dead Sea area in Israel and Jordan: multidisciplinary study. Grant No.TA-MOU-07-M27-050, MERC Project M27-050. USAID.
5. Ezersky M., Al-Zoubi A., Keydar S., Eppelbaum L. 2012. Fifth semi-annual Progress Report (March 1, 2012-August 31, 2012). 2012. Sinkhole hazard assessment of the Dead Sea area in Israel and Jordan: multidisciplinary study. Grant No.TA-MOU-07-M27-050, MERC Project M27-050. USAID.